Evaluation of High Temperature Performance of the Co-Cr-C Coated P92 Steel

Thomas Michael Hoey

BSc (Hons)

Thesis submitted to the University of Nottingham for the degree of Doctor of Engineering (EngD)

September 2016

For Eve

ABSTRACT

The motivation to increase the operation temperatures of fossil fuel power plant is primarily to improve power plant efficiency and reduce the negative environmental impact of fossil fuel power plant emissions. A main limitation to higher temperature operation is the enhanced oxidation damage of materials at increased temperatures. One of the most concerning areas of enhanced damage is on the inside surface of P92 ferritic steel (~ 9 % Cr) pipework which is used primarily to carry high temperature steam from the boiler.

To combat the oxidation damage of P92 the energy industry has recently begun investigating the application of oxidation resistant coatings to P92 to enable higher temperature operation. Aluminium diffusion coatings have been the focus to date but they have been found to have a number of limitations, including coating degradation/porosity and a detrimental effect on the creep properties of the substrate, in part due to the high temperature coating process. Although other lower temperature coating methods, such as thermal spraying, have been considered these are limited by the practicalities and economics of spraying on the inside surface of P92 pipework. Therefore there is a real industrial need for consideration of a new coating type, for the inside of P92 pipework, which can be applied at low temperature and is also economical at full scale. This is where this thesis contributes by considering an electro-deposited Co-Cr-C coating never previously considered for this application.

The Co-Cr-C type coating is electro-deposited to ~ 34-37 µm onto P92 ferritic steel. The coating is composed of ~ 35 wt % Cr_3C_2 electro-deposited within a cobalt matrix. The free-standing coating material and coated P92 system were subjected to isothermal oxidation in air and the oxidised state was characterised by a range of microstructural techniques. Oxidation behaviour, microstructural evolution and inter-diffusion between coating and substrate have all been considered. Thermo-Calc thermodynamic software has been used to make predictions about the long term evolution of the system. A series of uncoated and coated mechanical tests (creep, fatigue, creep-fatigue) have also been performed to assess the effect of coating application on the mechanical properties of P92 steel. This research has been motivated by industry at all stages and close collaboration has allowed for the most industrially relevant test conditions to be determined.

Overall the Co-Cr-C coating is shown to be an industrially promising coating technology for application to P92. The study within this thesis shows that the good oxidation properties, interface behaviour and mechanical properties, combined with low temperature deposition and easy scale up, make this a viable coating for further development. It also has a number of advantages over the current aluminium coatings. The work within this thesis serves as a detailed feasibility and industry case study for further in-house testing by industrial sponsors, before future commercialisation of the product. A discussion of potential future work is also included at the end of the thesis.

ACKNOWLEDGEMENTS

First and foremost, I would like to thank my academic supervisors: Professor Wei Sun and Professor Graham McCartney. Their support and input to my research for the last four years has been crucial for the success of this project. My industrial supervisor, Jeremy Mansfield (Doosan Babcock Ltd), and my industrial contact, John Foster (Praxair Surface Technologies Ltd), have also provided invaluable industrial direction for my work.

I would like to give special thanks to the EPSRC (Engineering and Physical Sciences Research Council) and BF2RA (Biomass and Fossil Fuel Research Alliance) who have funded my research through the Efficient Fossil Energy Technologies (EFET) engineering doctoral training centre (DTC) at the University of Nottingham.

I would like to extend my thanks to all of the technical staff and researchers in the Wolfson building at the University of Nottingham for their support and expertise that has allowed this project to reach completion.

Thanks must go to my family, in particular my parents and siblings. They have always supported my studies and have encouraged me in all aspects of my life.

Finally my biggest debt of gratitude is to my partner, Eve. Your enduring love and support is what motivates me every day and without you this work would never have been completed. I therefore dedicate this thesis to Eve.

SELECTED PUBLICATIONS

During this research period, the following conference papers have been published:

- Hoey, T., Chen, R., McCartney, D., Sun, W., Mansfield, J., Barnard, P. and Foster, J. (2015). Requirement for and use of coated P92 steel for enhanced structural integrity at high temperature, In: *13th International Symposium on the Physics of Materials*, Prague, Czech Republic, ISPMA 13.

During this research period, the following journal papers have been published in peer reviewed journals:

- Hoey, T., Chen, R., McCartney, D., Sun, W., Mansfield, J., Barnard, P. and Foster, J. (2015). Requirement for and use of coated P92 steel for enhanced structural integrity at high temperature, *Acta Physica Polonica: A*, 128(4), pp. 514-519.

Details of additional poster and oral presentations throughout the research project can be provided upon request. A series of additional journal papers are planned/in preparation to disseminate the thesis findings.

TABLE OF CONTENTS

LIST OF FIGURES

LIST OF TABLES

LIST OF ABBREVIATIONS

Item	Description
ACC.V	Accelerating Voltage
ASM	American Society of Metals
ASME	American Society of Mechanical Engineers
ASTM	American Society for Testing and Materials
BCC	Body Centred Cubic
BCF	Chamber Furnace
BCT	Body Centred Tetragonal
BF2RA	Biomass and Fossil Fuel Research Alliance
BSE	Backscattered Electrons
C	Coated
CALPHAD	Calculation of Phase Diagrams
C-F	Creep-Fatigue
COMP	Compressed
CPS	Counts per Second
CSEF	Creep Strength Enhanced Ferritic
CVD	Chemical Vapour Deposition
DB	Doosan Babcock Ltd
DBTT	Ductile to Brittle Transition Temperature
DECC	Department of Energy and Climate Change, UK Government

DET	Detector
DICTRA	Diffusion Controlled Transformations
DTC	Doctoral Training Centre
EB-PVD	Electron Beam – Physical Vapour Deposition
EBSD	Electron Backscatter Diffraction
ECCC	European Creep Collaborative Committee
EDM	Electric Discharge Machining
EDX	Energy Dispersive X-Ray Spectroscopy
EFET	Efficient Fossil Energy Technologies
EngD	Engineering Doctorate
EPRI	Electric Power Research Institute, USA
EPSRC	Engineering and Physical Sciences Research Council
ESEM	Environmental Scanning Electron Microscope
EVA	Diffractometer Analysis Software
FCC	Face Centred Cubic
FD	Finite Difference
FE	Finite Element
FEG	Field Emission Gun
FEI	Field Electron and Ion Co.
HCF	High Cycle Fatigue
HCP	Hexagonal Close Packed
HP	Hollomon-Jaffe Parameter
HV	Vickers Hardness
HVOF	High Velocity Oxy-Fuel Spraying

ICDD	International Centre for Diffraction Data
IDZ	Inter-Diffusion Zone
IMS	Industrial Methylated Spirit
LCF	Low-Cycle Fatigue
MAGN	Magnification
MMC	Metal Matrix Composite
MMT	Micro-Hardness and Micro-Indentation Tester
MSR	Minimum Strain Rate
NIST	National Institute of Standards and Technology
OM	Optical Microscopy
P	Pipe
PAGB	Prior Austenite Grain Boundary
PST	Praxair Surface Technologies Ltd
PVD	Physical Vapour Deposition
R&D	Research and Development
SE	Secondary Electrons
SEM	Scanning Electron Microscopy
SPOT	Spot Size
SSOL5	Thermo-Calc Alloys Database
T	Tube
TBC	Thermal Barrier Coating
TBD	To Be Determined
TCFE7	Thermo-Calc Steels Database
TEM	Transmission Electron Microscopy

TMF	Thermo-Mechanical Fatigue
TWI	The Welding Institute
U	Uncoated
UK	United Kingdom
UoN	University of Nottingham
USC	Ultra-Supercritical
V&M	Vallourec and Mannesmann
VPA	Vapour Phase Aluminising
WD	Working Distance
XRD	X-Ray Diffraction

NOMENCLATURE

Symbol	Description
a	Activity
A	Material constant in Norton and Kachanov creep model
A_f	Frequency factor constant
Ae_1	Ferrite to austenite transformation temperature
B	Material constant in Kachanov creep model
C	Total number of components
C_{LM}	Material constant in the Larson-Miller relationship
C_{HP}	Constant for the Holloman-Jaffe parameter
C_o	Oxidation Constant
d	Grain size
d_{ps}	Plane spacing
d_o	Oxide thickness
D	Diffusivity
D_o	Temperature independent pre-exponential
E	Modulus of elasticity
F	Load
F_{DF}	Degrees of freedom
G	Gibbs free energy

G_x	The fraction of total diffracted intensity
H	Enthalpy
J	Diffusion flux
k_p	Parabolic rate constant
m	Material constant in Kachanov creep model
M	Material constant in Kachanov creep model
n	Material constant in Norton and Kachanov creep model
N	Number of cycles
N_f	Number of cycles to failure
P	Number of phases
P_{LM}	Larson-Miller parameter
Q	Activation energy
R	Gas constant
R_f	Fatigue stress ratio (= σ_{min} /σ_{max})
R^2	Coefficient of determination (variance)
R_A	Surface roughness
S	Entropy
t	Time
t_f	Time to failure
t_u^*	Predicted rupture time - ECCC
t_{eqv}	Equivalent time
T	Thermodynamic temperature
T_o	Thermodynamic temperature constant
U	Internal energy of a system

V	Volume
x	X-ray penetration depth
x_m	Mass gain per unit area
…….....	
α	Multiaxial parameter material constant
ε	Strain
ε^c	Creep strain
$\dot{\varepsilon}$	Creep strain rate
$\dot{\varepsilon}_{ave}$	Average creep strain rate
$\dot{\varepsilon}_{min}$	Minimum creep strain rate
ϕ	Material constant in the Kachanov creep damage model
σ	Stress
σ_0	ECCC Stress
σ_r	Rupture stress
σ_{min}	Minimum peak stress
σ_{max}	Maximum peak stress
ω	Damage parameter
χ	Material constant in the Kachanov creep damage model
μ_{cp}	Chemical potential
μ	Mass absorption coefficient
β_o	ECCC mean data constant
β_1	ECCC mean data constant
β_2	ECCC mean data constant
β_3	ECCC mean data constant

β_4	ECCC mean data constant
β_5	ECCC mean data constant
λ	Incident wavelength
ρ	Density
θ	Scattering angle - XRD
…….....	
at %	Atomic percentage
wt %	Weight percentage

CHAPTER 1

INTRODUCTION

1.1 Background

The need to limit the amount of carbon dioxide emitted into the atmosphere is becoming increasingly important around the world, primarily to limit the effects of climate change. This presents a considerable challenge as the energy supply must be secure, reliable and economically viable, whilst simultaneously meeting international carbon reduction obligations. Due to limitations of renewable energy generation it seems clear that fossil fuel generation, especially coal, is going to remain a part of the world energy mix for the foreseeable future. Therefore it is vitally important that research into making fossil fuel generation more efficient is conducted [Bugge et al., 2006].

One way in which this can be done is to increase the temperature and pressure of the steam cycle of fossil fuel power stations. This will result in an overall increase in the efficiency of energy generation. This means that more energy can be generated per unit of fuel whilst simultaneously reducing the amount of carbon dioxide that is released to the atmosphere. The current fleet of UK coal

plant, largely built in the 1960s and 1970s, are pushed to their limits at these higher temperatures with expensive modifications/repairs being needed. Whilst in developing countries, such as China and India, USC power plant are being built specifically for this higher temperature operation regime [Clark, 2015; Viswanathan and Bakker, 2001].

One of the greatest challenges to achieving this higher temperature and more efficient operation is the materials technology. In particular, the alloys used within the power station to transport high temperature steam must have a good service life under these higher operation temperatures, whilst also being cost-effective to manufacture [Viswanathan et al., 2005]. At present, the most commonly used ferritic steel for steam carrying pipework is P92, ~ 9 % Cr steel that was developed for its combination of good mechanical properties and oxidation resistance. It has been used extensively for this application in power stations for around the last 20 years.

One of the limitations with continuing to use P92 for steam carrying pipework, as this operation temperature is increased, is that the oxidation damage on the inside surface of the pipework is significantly increased. This causes brittle iron rich oxides to form that can spall from the surface [Laverde et al., 2004]. This not only damages the pipework integrity itself but the spalled oxide can also cause erosion throughout the rest of the system, especially in expensive turbine components. This increased oxidation means that P92 (at least in the UK) is currently limited to upper operation temperatures of ~ 620 ^{o}C [Viswanathan and Bakker, 2001]. This presents a problem if higher temperature steam cycles and higher efficiencies are to be achieved. Some

authors have reported that USC power stations of the future could operate at anything up to 700 - 760 ^{o}C [Viswanathan et al., 2005].

The first and most ideal solution to this enhanced oxidation would be to completely replace all of the P92 ferritic steel with alloys richer in chromium and nickel (i.e. austenitic steels), as some of the most high temperature parts of the system already are. This would vastly improve the oxidation and mechanical properties of the steam carrying pipework. However this solution is unrealistic because nickel and chromium richer alloys are more expensive than ferritic steels and are uneconomical to use on large scale for all of the pipework in a power station. They are reserved for only the highest temperature and stress components (i.e. turbine blades and super-heater pipework).

Secondly there is the possibility that the P92 composition can be further alloyed to provide higher temperature oxidation resistance and good mechanical properties. However, as the literature shows [Danielsen and Hald, 2006], P91 and P92 have been very carefully designed over a number of years to give the best combination of oxidation and mechanical properties. Any further alloying attempt to increase oxidation resistance, for example increasing the content of chromium, has a detrimental effect on the mechanical properties (i.e. formation of a brittle Z phase).

Therefore industry is now beginning to consider a more novel solution, by applying an oxidation resistant coating to the inside surface of the ferritic steel pipework. The principle of applying the oxidation resistant coating is that the coating material, on exposure to high temperature steam conditions, forms an adherent and slow growing oxide that protects the P92 substrate below from excessive oxidation damage [Aguero et al., 2001; Nicholls, 2000].

As the literature review details (chapter 2) most of the current coated P92 work has considered aluminide type coatings, which are aluminium rich diffusion coatings. A significant amount of work has been conducted on these aluminide type coatings with mixed results. Most authors find that the aluminide type coatings have a negative effect on the mechanical properties of the substrate material, which is mainly as a result of the high temperature coating process. Also the inter-diffusion processes between the coating and the substrate result in porosity, AlN particles precipitating and cracking forming beneath the coating. Both of these effects are detrimental to the integrity of the coated system.

Therefore industry is now starting to look towards new types of oxidation resistant coating, which have good oxidation properties and less detrimental effect on the P92 substrate during its service life.

1.2 Aims and Objectives

This thesis focused on one such coating; a Co-Cr-C type coating that is composed of Cr_3C_2 particles that have been electro-deposited within a cobalt matrix. This is a standard 'off-the-shelf' coating that has been used for many years for its wear resistance and belongs to the Tribomet family of coatings manufactured by Praxair Surface Technologies Ltd [Foster, 2012a; 2012b; 2007]. This coating was selected as a promising candidate for application to P92 because the cobalt and chromium rich oxide produced on the coating are shown to be slow growing and adherent [Hoey et al., 2015]. Also the low temperature electro-deposition method makes it economical and practical to coat pipework components. Previous work on the Co-Cr-C coating has been

performed at high temperature (1000 ^{o}C) when applied to gas turbine components. No work has been performed to study the coating at lower temperature (600-700 ^{o}C) or when applied to ferritic steel substrates. This is the gap in the understanding that this thesis considered. This thesis has served as a detailed feasibility study for Co-Cr-C coated P92 steel. The work presented in this thesis therefore considered several key themes:

- The oxidation and microstructural evolution behaviour of the Co-Cr-C free-standing coating when exposed to high temperature oxidation, typical of power plant conditions. This provided baseline understanding of the Co-Cr-C coating behaviour without the effects of stress or a substrate.
- The effect that Co-Cr-C coating application has on the mechanical properties of the substrate P92 steel, namely high temperature creep and fatigue at typical power plant conditions. The mechanical properties of the coated system were found to be a major limitation of the previous aluminide coating so it was important to characterise Co-Cr-C coated P92.
- The oxidation, microstructural evolution and inter-diffusion behaviour of Co-Cr-C coated P92 when exposed to high temperature oxidation and/or mechanical loading, typical of power plant conditions. The effect of the substrate was found to be another limitation of the previous aluminide type coating so it was important to characterise this for Co-Cr-C coated P92.

These three research themes have been investigated experimentally through high temperature testing in air, including oxidation and mechanical testing. Microstructural characterisation was carried out using XRD, OM, SEM and

EDX. Mechanical testing included tensile, creep and fatigue/creep-fatigue testing. In addition computational modelling of certain systems was also conducted using the thermodynamic modelling software, Thermo-Calc, to provide further understanding of the diffusion behaviour and microstructural evolution.

1.3 Thesis Outline

The thesis contains the following key chapters to investigate the overall feasibility of the Co-Cr-C coated P92 system. This thesis acts as a detailed feasibility study which provides the basis for further industrial R&D and hopefully future commercialisation of the technology. Results chapters 4, 5, 6 and 7 all include detailed discussion sections that compare the findings of the chapter to the literature and also to other chapters within this thesis. These findings are brought together into a series of conclusions in chapter 8. Suggestions are also made as to how this research work can be continued by industry in the future.

Chapter 2: Literature Review – in which the current literature in this area is presented with the gaps in the understanding being highlighted. The novelty of the research work in this thesis is highlighted.

Chapter 3: Experimental Methods – in which the high temperature oxidation and mechanical testing is described, as well as full details of the sample preparation and characterisation methods used. Modelling methodologies are presented in appendix C.

Chapter 4: Effect of High Temperature Oxidation on the Co-Cr-C Free-standing Coating (results and discussion) – in which the work undertaken to characterise the Co-Cr-C free-standing coating, following high temperature oxidation, is presented. This considers oxidation and microstructural evolution of the coating.

Chapter 5: Microstructural and Mechanical Characterisation of P92 Steel (results and discussion) – in which the microstructural and mechanical characterisation of the P92 substrate material, used in this project, is presented. Comparisons are made with the literature to determine if the specific material used in this thesis is typical for P92.

Chapter 6: Mechanical Characterisation of Coated P92 (results and discussion) – in which the high temperature mechanical testing of coated P92 is presented to assess the effect of Co-Cr-C coating application on the mechanical properties of the P92 substrate steel.

Chapter 7: Oxidation and Microstructural Study of Coated P92 (results and discussion) – in which the work undertaken to characterise the Co-Cr-C coated P92 is presented. This includes industrially relevant high temperature oxidation, both coated P92 coupons and failed creep specimens. It studies oxidation, microstructural evolution and inter-diffusion of the coated P92 system. Other industrial considerations of the coating technology are also discussed.

Chapter 8: Conclusions and Future Work: in which the findings of the proceeding chapters are summarised and brought together into a series of conclusions about the Co-Cr-C coated P92 system. Conclusions are also drawn about the overall suitability of the Co-Cr-C coating for this application. Details of future research work to be conducted by industry sponsors is also included.

Appendix A: in which the published diffraction data for the XRD identified phases is included for reference.

Appendix B: in which the XRD penetration depths of coating samples are included for reference.

Appendix C: in which the Thermo-Calc CALPHAD modelling methodology is included.

Appendix D: in which the initial feasibility work for MCrAlY coated P92 is included.

1.4 Industrial Relevance of the Thesis

The research presented in this thesis has been conducted as part of the EFET DTC at the University of Nottingham. This EngD centre collaborates with a large number of industrial partners in the energy industry. This includes; energy generators (e.g. E.ON, EDF etc.), service providers (e.g. Doosan Babcock, GE Power etc.) and large net users of energy (e.g. British Sugar, Tata Steel etc.). Therefore industrial direction and relevance of this EngD research

has been paramount. The testing in this thesis was designed with industry input at all stages and therefore ensures that the main industry questions for this research are being answered.

The original motivation for this work was provided by Doosan Babcock Ltd and BF2RA. Doosan Babcock are a large international engineering company that has numerous contracts around the world to build and maintain fossil fuel power plants. They have been investigating for many years how to improve the oxidation properties of the ferritic steels used for steam carrying pipework in order to allow higher temperature and more efficient operation. As part of this work Doosan Babcock and collaborators have used their expertise to investigate the viability of coated P92, with much of the work to date being focused on aluminide coated P92. Like other investigations they have identified a number of limitations of using aluminide type coatings.

However working alongside the market-leading coating manufacturer, Praxair Surface Technologies Ltd, they identified an electro-deposited Co-Cr-C type coating as a potentially promising coating for P92 oxidation resistance. The low cost electro-deposition method makes this a commercially viable technology. Following some initial in-house feasibility work and proof of concept this four year engineering doctorate research project was created to focus on a more detailed feasibility study of this Co-Cr-C coated P92 system. This project is designed to provide the basis for a wider portfolio of projects going forward which are being conducted in-house at Doosan Babcock. The ultimate aim would be full scale commercialisation of the Co-Cr-C coating when applied to P92.

Doosan Babcock and Praxair Surface Technologies also suggested an MCrAlY type electro-deposited coating for application to P92 substrate. However when this coating was studied in the early stages of the research project its oxidation properties were insufficient for this application (as discussed in appendix D). Therefore the Co-Cr-C coating was instead the focus for this thesis as it showed much more promising properties for P92 application.

The funding for this work was provided partly by the EPSRC and partly by BF2RA, of which Doosan are a long standing member, along with other large engineering companies and energy generators. BF2RA ensured that the progress of this research was shared with all of the main stake-holders in the UK energy industry, from generators to service providers. This ensured maximum impact of this research within the energy industry. This typically took the form of 6 monthly technical progress reports, oral presentations and regular stakeholder meetings.

CHAPTER 2

LITERATURE REVIEW

2.1 Introduction

This chapter includes a review of the published work relating to the integrity of coated ferritic steels. This includes details of common power plant ferritic steels and highlights the need for oxidation resistant coatings to enable higher temperature and more efficient power plant operation. The previous work on the coated ferritic steel system is considered and the limitations of the current technology highlighted. Finally a Co-Cr-C coating, with promising oxidation properties, is discussed for potential future application to ferritic steel.

The overall aim was to assess the current state of the art and provide context to the research work that is presented within this thesis. It highlights the gap in the understanding of coated ferritic steel that this thesis aimed to address.

2.2 Principles of Power Plant Operation

Power generation and production of electricity is one of the fundamental requirements for a modern society. Finding a way to produce this electricity in

a reliable but also sustainable way is something that has long been a significant challenge for countries around the world. With the economic, political, reliability and efficiency problems associated with many renewable technologies, most researchers are in agreement that fossil fuel energy (especially coal) is going to remain part of the world energy mix for the foreseeable future, especially in developing countries such as China and India. Therefore ways to make fossil fuel generation more efficient is important for the future of our environment [Yeh and Rubin, 2007; Bugge et al., 2006].

Thermodynamics tells us that the efficiency of a fossil fuel power plant is strongly dependent on both the temperature and pressure at which the steam cycle operates [Bugge et al., 2006]. In recent years there have been a number of advances in increasing both temperature and pressure in order to increase the efficiency [Viswanathan and Bakker, 2001]. This development has been driven in part by the need for countries to address their carbon emissions and also for power generation companies to reduce the costs associated with generating electricity in an increasingly competitive global market. According to Viswanathan and Bakker [2001] steam temperatures in the most efficient fossil fuel power plant are now close to ~ 620 ^{o}C with steam pressures of up to 25 MPa. This represents an increase of 60 ^{o}C in the last 30 years. It is also predicted that these temperatures will increase by a further 50-100 ^{o}C in the next 30 years. Currently UK coal-fired power plant efficiencies are around 30-40 % [Rosen, 2001], dependent on size, with future USC boilers (steam: 600-700 ^{o}C, > 25 MPa) expected to achieve close to 50 % efficiency [Viswanathan et al., 2005]. Developing countries such as China and India are leading the world in USC power generation with a number of construction projects

underway or planned for the future. This new generation of power plant are being specifically designed for USC operation.

When the UK's current fleet of coal fired power stations were originally constructed in the 1960s and 1970s they were intended to provide predominantly base load generation. This means that the plant would be operating at maximum output with very limited shut down, other than for essential maintenance. However in recent years this ageing power plant fleet is being required to operate much more flexibly, in order to accommodate the intermittency of renewables on the power grid. This means that they are often being required to come on-line at short notice and provide top-up generation when the input from renewables to the grid reduces [DECC, 2014]. This means that many conventional UK power plants, which were not originally designed for such cycling, are operating under harsher cycling conditions [Bugge et al., 2006; Lefton and Besuner, 2006]. They are also being required to operate at higher temperatures and pressures to increase generation efficiency, far above the conditions that they were originally designed for. This pushes the UK's current coal fired fleet to their limits [Clark, 2015].

One of the main areas that must be addressed to allow this higher temperature and more flexible operation is the materials technology, especially high temperature steels and super-alloys. Work by Viswanathan et al. [2005] shows that commonly used power plant steels suffer enhanced damage at higher temperature operation and that this is a significant barrier to future development. Increased material degradation is blamed for increasing the occurrence of unplanned outages. Industry sponsors suggest the financial penalty for unplanned outages on a coal plant can be up to £100,000 per day.

2.3 Introduction to Power Plant Steels

In a coal-fired power plant there are two main areas of interest for power plant metallurgists. Firstly, steam turbine materials which utilise both ferritic and austenitic (higher alloy) steels. Secondly, the boiler system itself which includes both fireside and steam-side components. The boiler system typically utilises lower value, lower alloy steels (ferritic steels mainly and austenitic steels for very high temperature parts such as superheaters).

Materials used in all areas of a fossil fuel power plant have got to satisfy a number of criteria [Callister and Rethwisch, 2007; Viswanathan et al., 2005], these include:

- Sufficient strength to resist mechanical loading
- Sufficient toughness to resist brittle failure
- Sufficient resistance to creep failure (high temperature, constant stress loading)
- Sufficient resistance to fatigue failure (high temperature, cyclic stress loading)
- Good steam oxidation resistance (at enhanced temperatures and during cyclic loading)
- Good corrosion resistance (this is becoming more important as biomass combustion significantly enhances this mechanism)
- Good component lifetimes in service (to minimise costly unplanned power plant outages and reduce cost)

It is important that all of these criteria are satisfied whilst also keeping the cost of these materials economical and the manufacturing methods straightforward. Therefore because of its ready availability, and ability to include alloying elements, steel of various grades is the material of choice for power plant engineering. The mechanical properties and oxidation properties of steel are both expected to be negatively influenced by an increase in operating temperature and pressure [Bhadeshia and Honeycombe, 2006; Birks et al., 2006].

2.3.1 Steel Metallurgy

The Fe-C phase diagram (figure 2.1) is the basis for understanding complex multi-component steels and can be a useful tool for predicting the behaviour of steel at temperatures of interest. Steel without any elemental additions will contain carbon as its only alloying element (Fe-C). This simple form of steel, upon heating, experiences two changes to its crystal structure before it melts. At room temperature this steel is considered to be in a stable form, α-ferrite, and has a BCC crystal structure. As the temperature is increased the α-ferrite experiences a polymorphic transformation and forms a new stable form called γ-austenite at 912 ^{o}C, with an FCC crystal structure. γ-austenite remains up to 1394 ^{o}C, at which the austenite transforms to BCC δ-ferrite before finally melting at 1538 ^{o}C. Figure 2.1 shows that at 6.70 wt % carbon the intermediate iron carbide, Fe_3C, called cementite is formed. Virtually all the carbon in steel will be in the form of cementite instead of graphite. For compositions greater than 6.70 wt % graphite will be the dominant phase [Callister and Rethwisch, 2007: pp. 319-321; Gale and Totemeier, 2004].

Carbon has a low solubility in ferrite, so when the steel is cooled slowly from the austenite phase to the ferrite phase the structure is then composed of alternating layers of ferrite and cementite (as the carbon precipitates); this structure is referred to as pearlite. These cementite layers have positive effects on the strength of the steel and improve the mechanical properties [Callister and Rethwisch, 2007; Bhadeshia and Honeycombe, 2006].

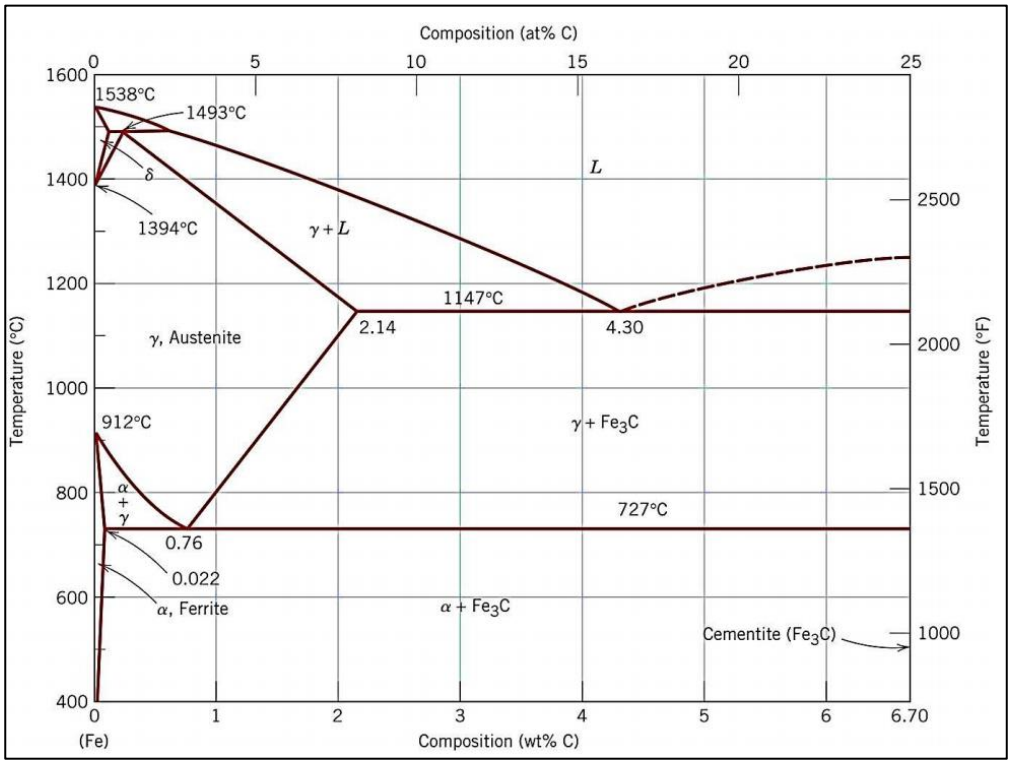

Figure 2.1: The iron-iron carbide phase diagram to show the equilibrium phases of the Fe-C system [Callister and Rethwisch, 2007: p.319].

The scenario discussed above is an idealised situation and considers when the system has been allowed to reach a natural equilibrium point under slow cooling. If the austenite is cooled much quicker then martensite will be formed via a martensitic transformation. Martensite is a non-equilibrium single phase structure with a BCT crystal structure and a high dislocation density. It occurs by the diffusion-less transformation of austenite, essentially it forms when the

cooling is fast enough such that carbon diffusion does not occur. Martensite can negatively affect the mechanical strength of the steel because of its brittle properties. Typically martensite will be formed during casting and welding processes and can be observed using optical microscopy as characteristic martensitic laths [Meyers and Chawla, 2009; Bhadeshia and Honeycombe, 2006; Callister and Rethwisch, 2007]. The final structure will contain martensitic laths forming within prior austenite grains; the prior austenite grain boundaries are retained and can be observed using microscopy. Heat treatment can be used to relax some of the stresses that are caused by this brittle martensitic structure. This heat treatment can also allow some diffusion to occur which can soften the martensite, this is known as tempering. P92 and P91 steel, ferritic steels that are of interest to this project, both have a tempered martensitic structure [Callister and Rethwisch, 2007].

The pearlite reaction can be considered a high temperature reaction (550-720 ^{o}C) and the martensite reaction is considered low temperature. Therefore there is a large range of temperatures (250-550 ^{o}C) where neither of the above processes is dominant. This middle temperature range is dominated by a phase called bainite and is characterised by the formation of fine aggregates of ferritic plates (laths) and cementite particles around them. Bainite is termed upper or lower depending on the temperature of the reaction [Bhadeshia and Honeycombe, 2006]. These bainitic structures have been shown to have superior creep properties when alloyed with other elements [Abe, 2004]. Bainite has a BCT structure and high dislocation density like marteniste; however it forms at slower cooling rates and is generally softer than martensite [Callister and Rethwisch, 2007].

2.3.2 The Role of Alloying Elements in Steel

The addition of a number of different alloying elements to Fe-C can significantly increase the strength and make it more useful for industry. This increase in strength is achieved through solid solution strengthening, precipitate strengthening and dispersion strengthening, primarily by preventing dislocation motion [Callister and Rethwisch, 2007]. Elements can also be added to aid oxidation or corrosion resistance by forming protective oxide scales. Some of the most important alloying elements are detailed below [Bhadeshia and Honeycombe, 2006; Agyakwa, 2004].

- Carbon is present in all steels due to production methods. Carbon occupies interstitial sites in the metal matrix until it reaches its solubility limit, after which the remaining carbon will precipitate as carbides [Taneike et al., 2003; Taneike et al., 2004; Llewelyn and Hudd, 1998]. Carbon is very effective at sold solution strengthening as it introduces lattice strains that prevent dislocation movement and significantly improve the mechanical properties. A fine distribution of carbides also strengthens the steel by pinning dislocations and grain boundaries [Masuyama, 2001; Ennis et al., 1997].
- Nitrogen, as an alloying element, is very similar to carbon and can also produce precipitates; namely carbo-nitrides and nitrides [Beeghly, 1952]. Nitrogen atoms again occupy interstitial sites on the lattice until it reaches its solubility limit, after which it forms precipitates [Bhadeshia and Honeycombe, 2006].
- Chromium additions provide solid solution strengthening and also precipitation strengthening through the precipitation of carbides, most

commonly $M_{23}C_6$ ($Cr_{23}C_6$). These precipitates form predominantly at dislocations and grain boundaries, preventing slip and grain boundary sliding and improving the mechanical properties [Ennis and Czyrska-Filemonowicz, 2003]. However the most useful effect of chromium addition is improvement in the oxidation resistance. Iron that does not contain chromium will form thick and potentially brittle iron oxides (e.g. FeO, Fe_2O_3, Fe_3O_4) [Chen and Yeun, 2003]. When chromium is present it will preferentially form the slow-growing and adherent $(Fe, Cr)_3O_4$ or Cr_2O_3, thus protecting the steel below from oxidation [Birks et al., 2006].

- Molybdenum is an extremely effective solid solution strengthener and can also form carbide phases within the steel during precipitation (MX type and Laves phase) [Vyrostkova et al., 2008]. Molybdenum is reported to increase the creep strength of the steel up to a certain critical value, after this critical value delta-ferrite forms thus causing a marked decrease in the creep strength. Molybdenum is also reported to enhance the corrosion resistance of steels [Masuyama, 2001].
- Tungsten has very similar properties to molybdenum and is also an extremely effective solid solution strengthener. The tungsten is a desirable addition when the steel is to be used at high temperatures because it remains stable for longer at elevated temperature [Agyakwa, 2004]. Like molybdenum, tungsten is also shown to have a positive effect on creep properties, although the effect of tungsten is approximately half that of molybdenum. Tungsten also has a critical concentration after which it begins to decrease the creep life [Masuyama, 2001].

- Nickel and manganese both lower the temperature at which ferrite transforms to austenite and are said to be austenite stabilisers. Steels that are austenite stable have improved toughness and strength. Nickel and manganese show an increased strength by solid solution strengthening. Neither elements are shown to cause the formation of carbides [Clark, 2015; Ennis and Czyrska-Filemonowicz, 2003].
- Vanadium and niobium ensure that small finely dispersed precipitates are produced by their reaction with carbon and nitrogen. Namely they produce carbides, nitrides and carbo-nitrides [Taneike et al., 2004]. These particles are very fine and precipitate coherently on the ferritic matrix. For precipitation strengthening these small particles are highly desirable.

Power plant metallurgists have spent many years perfecting the combinations of these elements to produce power plant steels that have good oxidation and mechanical properties and are also economical to produce.

2.3.3 Austenitic and Ferritic Steels

In power plant engineering for boiler system components there are currently two main steel alloy types used; austenitic and ferritic steels [Oakey et al., 2003].

Austenitic steels (18-25 % Cr, 8-32 % Ni) are generally used for super-heater tubes and header sections of the boilers (the hottest sections), as shown in figure 2.2. They have excellent oxidation, corrosion and mechanical properties which are superior to ferritic steels. However due to the expense of adding large quantities of the alloying elements (Cr, Ni) they are only used for areas that experience very high steam temperatures; therefore they are often found

welded to less expensive ferritic steels [Clark, 2015; Masuyama, 2001; Eiselstein and Tillack, 1991].

Ferritic steels are the focus for this thesis and come in a number of different forms including; carbon steels, low alloy steels (2.25 % Cr), intermediate alloy steels (9-10 % Cr) and high alloy steels (12-18 % Cr) [Masuyama et al., 2001]. Compositions of some common ferritic steels are included below in table 2.1. The ferritic steels are used extensively for the main steam carrying pipework sections as they have good mechanical and oxidation properties as well as being relatively economical to produce. The current 'best-in-class' ferritic steel for steam carrying pipework is P92, an ~ 9 % Cr steel that has been developed for its superior creep and oxidation resistance. P92 will be the focus of this current research project. The evolution of ferritic steels in recent times is summarised in figure 2.3 [David et al., 2013].

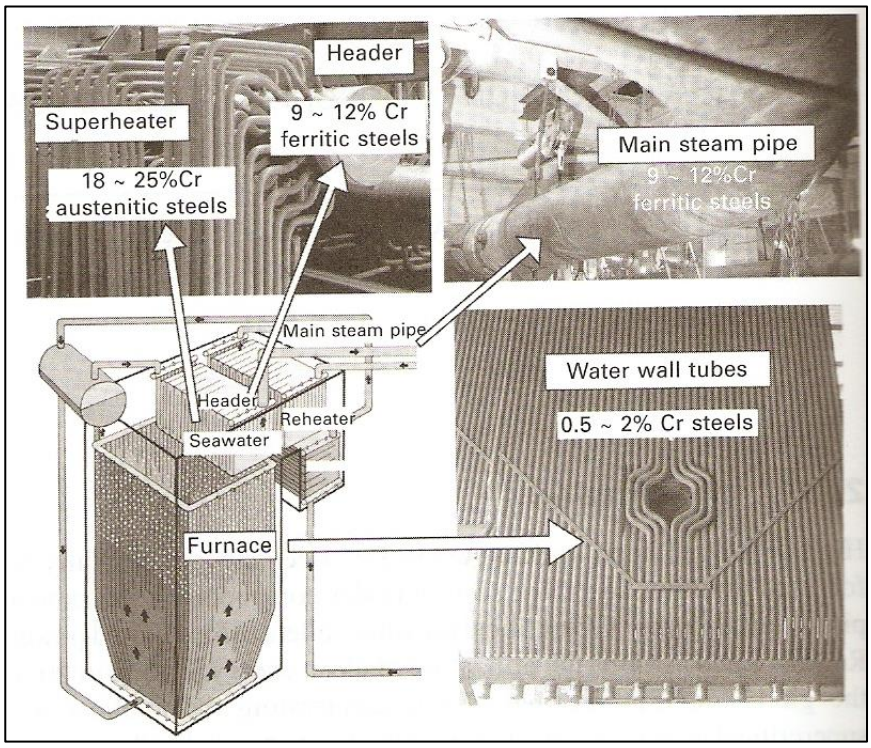

Figure 2.2: A schematic to show the typical steels used in a fossil fuel power plant boiler [Abe et al., 2008: p.15].

Table 2.1: Compositions (wt %) of common power plant ferritic steels, adapted from Vaillant et al. [2008: p.39].

Grades	C	Mn	P	S	Si	Cr	W	Mo	V	Nb	Ti	N	B	Al	Ni
T/P22	0.05 – 0.15	0.30 – 0.60	-	-	-	1.90 – 2.60	-	0.87 – 1.13	-	-	-	-	-	-	-
T/P23	0.04 – 0.10	0.10 – 0.60	0.030	0.010	0.50	1.90 – 2.60	1.45 – 1.75	0.05 – 0.30	0.20 – 0.30	0.02 – 0.08	-	0.030	0.0005 – 0.006	0.030	-
T/P24	0.05 – 0.10	0.30 – 0.70	0.020	0.010	0.15 – 0.45	2.20 – 2.60	-	0.90 – 1.10	0.20 – 0.30	-	0.06 – 0.10	0.012	0.0015 – 0.0070	0.020	-
T/P91	0.08 – 0.12	0.30 – 0.60	0.020	0.010	0.20 – 0.50	8.00 – 9.50	-	0.85 – 1.05	0.18 – 0.25	0.06 – 0.1	-	0.030 – 0.070	-	0.04	0.40
T/P911	0.09 – 0.13	0.30 – 0.60	0.020	0.010	0.10 – 0.50	8.50 – 9.50	0.90 – 1.10	0.90 – 1.10	0.18 – 0.25	0.06 – 0.10	-	0.04 – 0.09	0.0003 – 0.006	0.04	0.40
T/P92	0.07 – 0.13	0.30 – 0.60	0.020	0.010	0.50	8.50 – 9.50	1.5 – 2.00	0.30 – 0.60	0.15 – 0.25	0.04 – 0.09	-	0.03 – 0.07	0.001 – 0.006	0.04	0.40

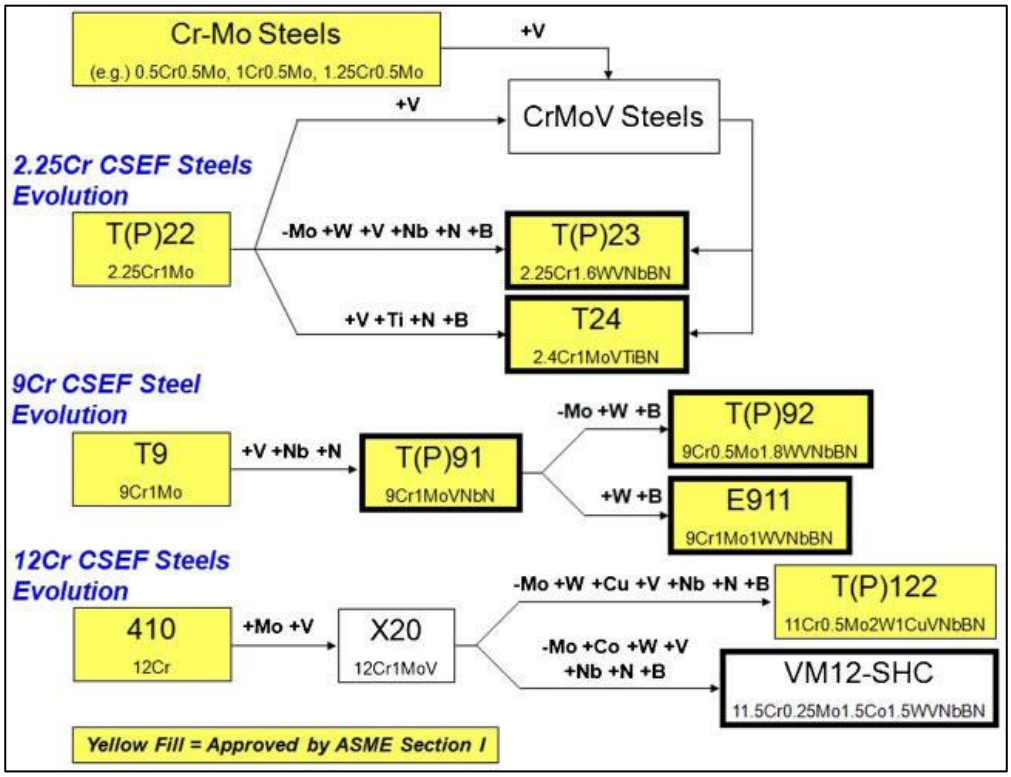

Figure 2.3: Schematic to show the evolution of ferritic steels in recent years [David et al., 2013: p.635].

2.4 P92 Ferritic Steel

2.4.1 Microstructural Features of P92

The microstructure of P92 steel (with composition given in table 2.1) in power plant components consists of purely tempered martensite with a high dislocation density and a number of finely distributed carbides, nitrides and carbo-nitrides [Czyrska-Filemonowicz et al., 2006]. In order to produce this desired microstructure a series of controlled heat treatments are performed. Firstly, once the steel has been extruded/forged it is heated up to ~ 1100 ^{o}C so that austenite forms, this is known as normalising or austenitising. Secondly, the steel is cooled to room temperature, by quenching in oil, to form the martensitic structure. As mentioned previously, it is not desirable to have a

brittle martensitic structure. Therefore a final tempering heat treatment of ~ 780 ^{o}C for ~ 2 hours is applied. This heat treatment relaxes stresses (by annihilating dislocations) causing increased ductility and also inducing the formation of desirable precipitates ($M_{23}C_6$ and MX) for creep resistance. This final temper then makes the steel suitable for service [Chalk, 2013; Li and Mitchell, 2013; Ennis et al., 2000]. The presence of dislocations, solutes and precipitates all contribute to the overall hardness of the material by pinning and preventing dislocation movement and are vital to stabilise the sub-grain structure and prevent coarsening [Yoshizawa et al., 2009; Abe, 2004; Ennis and Czyrska-Filemonowicz, 2003].

The main precipitates in P92 ferritic steel are MX (where X is C and/or N and M is V and/or Nb), $M_{23}C_6$ (M = Cr, Mo, Fe, W) and Laves phases ((Fe, Cr)$_2$(Mo, W)). $M_{23}C_6$ carbides are normally located at grain and lath boundaries while MX are distributed homogeneously throughout the grains and are found at grain boundaries [Yoshizawa et al., 2009; Ennis et al., 1997]. The distribution of these precipitates is best represented in figure 2.4. $M_{23}C_6$ and MX particles precipitate during tempering and the Laves phase may precipitate during the service life of the component (during creep exposure or isothermal ageing) at temperatures below the final tempering temperature. Laves phase is unstable at the tempering temperature [Hald, 2008].

$M_{23}C_6$ is the main precipitate that can be experimentally observed in the tempered martensitic microstructure of P92 using OM and SEM. Work by Ennis et al. [2000] shows that during austenitisation the $M_{23}C_6$ is completely dissolved but will form again during the tempering treatment. $M_{23}C_6$ will mainly be observed along the edges of PAGB's and typically has a size of less

than 90 nm [Anderson et al., 2003]. The literature review by Sourmail [2001] and Chalk [2013] shows that $M_{23}C_6$ is most commonly $Cr_{23}C_6$ with an FCC crystal structure. $M_{23}C_6$ is shown to coarsen following high temperature exposure (isothermal ageing and creep) for long duration [Ennis et al., 1997]. $M_{23}C_6$ is beneficial to mechanical properties by pinning dislocation and preventing grain coarsening.

TEM can be used to observe the MX precipitate that is also present within P92 and is usually found within the sub-grain interior or at grain boundaries. Sourmail [2001] and Chalk [2013] show that it can take a number of forms, where M = Nb and/or V and X = C and/or N. There are three main types of MX precipitates. The first is coarse spherical NbX randomly distributed within the material, approximately 100 nm in diameter, which remain after austenitisation. Secondly is fine NbX and VX precipitates that are distributed uniformly within the sub-grains with a diameter of 10-20 nm and which precipitate during the tempering heat treatment. The final type is a V-wing complex where the large coarse NbX particles that are present following austenitisation act as nucleation sites for VN during tempering [Chalk, 2013; Zielinska-Lipiec and Czyrska-Filemonowicz, 2007; Sourmail, 2001]. Fine MX particles are desirable in P92 as they pin dislocations, therefore improving the creep properties. Coarser MX particles are also desirable in small amounts as they can limit the size of austenite grains. MX phase is seen to coarsen rapidly during creep [Klueh, 2005].

The intermetallic Laves phase will precipitate during creep or isothermal ageing at high temperature on PAGB's, close to the $M_{23}C_6$ particles. There is some disagreement in the literature as to whether Laves phase is beneficial or

detrimental to the creep properties of P92. Traditionally it was always thought that Laves phase would be detrimental because it depletes the molybdenum and tungsten from solid solution, both of which are vital for the solid solution strengthening that gives P92 its good creep properties [Chalk, 2013; Hosoi et al., 1986]. However more recently a number of authors have suggested that a fine distribution of Laves phase may in fact be beneficial for the creep strength by precipitation strengthening [Chalk, 2013; Hald, 1996].

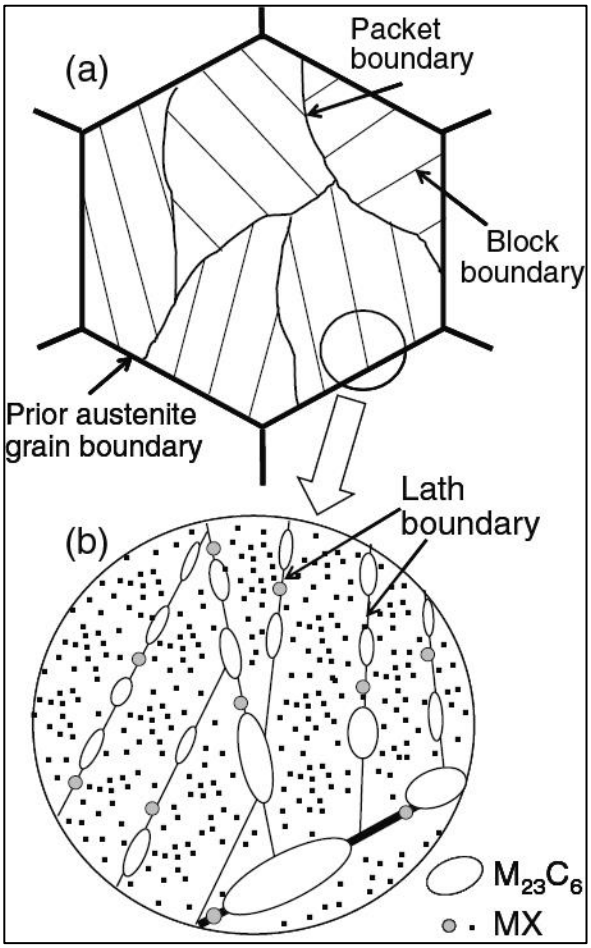

Figure 2.4: Illustration of the P92 steel microstructure following tempering heat treatment (a) sub-grain structure (b) distribution of $M_{23}C_6$ and MX phase [Abe et al., 2007: p.4].

2.4.2 Mechanical Properties of P92

The two most important mechanical loadings that P92 steel will experience in a power plant are creep and fatigue. Both of these mechanical properties become increasingly important as P92 is expected to operate in more aggressive environments.

Creep is a load, material properties, temperature and time dependent mechanism that results in the deformation and ultimately failure of components. At high temperatures, materials under constant loads, which caused no permanent deformation at room temperature, start to deform by creep. Creep stress in high temperature components is usually below the yield stress of the material. Creep is characterised by a slow flow of the material almost as though the material was viscous and occurs at a temperature > 0.4 times the melting temperature [Ashby and Jones, 2013; Meyers and Chawla, 2009; Evans and Wilshere, 1993; Evans and Wilshere, 1985].

Fatigue is defined as the repeated application of a load that is not sufficient to cause failure of the material with a single load. Cyclic loading (fatigue and creep-fatigue interaction) is representative of the types of load that power plant steels experience during ramp up and ramp down as they are being required to operate increasingly flexibly [DECC, 2014; Meyers and Chawla, 2009; Callister and Rethwisch, 2007]. Cyclic testing is often considered more industrially relevant.

2.4.2.1 Creep

Creep testing of P92 has been extensively investigated by a number of different authors over the last 20 years and a very good understanding of the materials

behaviour has been achieved [Vaillant et al., 2008; Viswanathan and Bakker, 2001]. One of the most respected sources for creep data of P92 is the ECCC. This collaboration of more than 40 European industries and research institutes is designed to bring together all of the creep testing being conducted throughout Europe into one easy to use database. The ECCC has produced a master equation from experimental testing for the creep behaviour of P92 that can be used to predict the creep failure time for a particular set of test conditions [ECCC, 2005]. The ECCC master equation is as follows:

$$t_u^* = \exp\{(\beta_0 + \beta_1.\log(\sigma_0) + \beta_2.\log(\sigma_0)^2 + \beta_3.\log(\sigma_0)^3 + \beta_4.\log(\sigma_0)^4).(T - T_0) + \beta_5\} \quad \text{[Equation 2.1]}$$

In equation 2.1, t_u^* is the predicted rupture time (h), T is the absolute temperature (K), σ_0 is the stress (MPa) and β_0, $\beta_1, \beta_2, \beta_3, \beta_4, \beta_5$ and T_0 are constants. For P92, β_0 = -0.921, β_1 = 1.942, β_2 = -1.629, β_3 = 0.604, β_4 = -0.085, β_5 = 40.512 and T_0 = 500. Although this is a general equation for P92 and does not refer to a specific set of manufacture conditions or composition it is a very useful tool to predict the approximate life of P92 steel in the austenitised and tempered condition. The majority of P92 creep testing to formulate this equation has been conducted at 550-650 ^oC, there is very limited work at above 650 ^oC.

Vallourec and Mannesmann Tubes, one of the world's leading P92 manufacturers, have published a series of standard P92 creep tests [Richardot et al., 2000]. This is presented in figure 2.5 and shows that as the stress of the creep test is reduced the time to failure increases. Also that as the temperature

is increased the stress to produce a given failure time reduces. Richardot et al. [2000] has also presented the maximum allowable stress for P92 pipework, as shown in table 2.2.

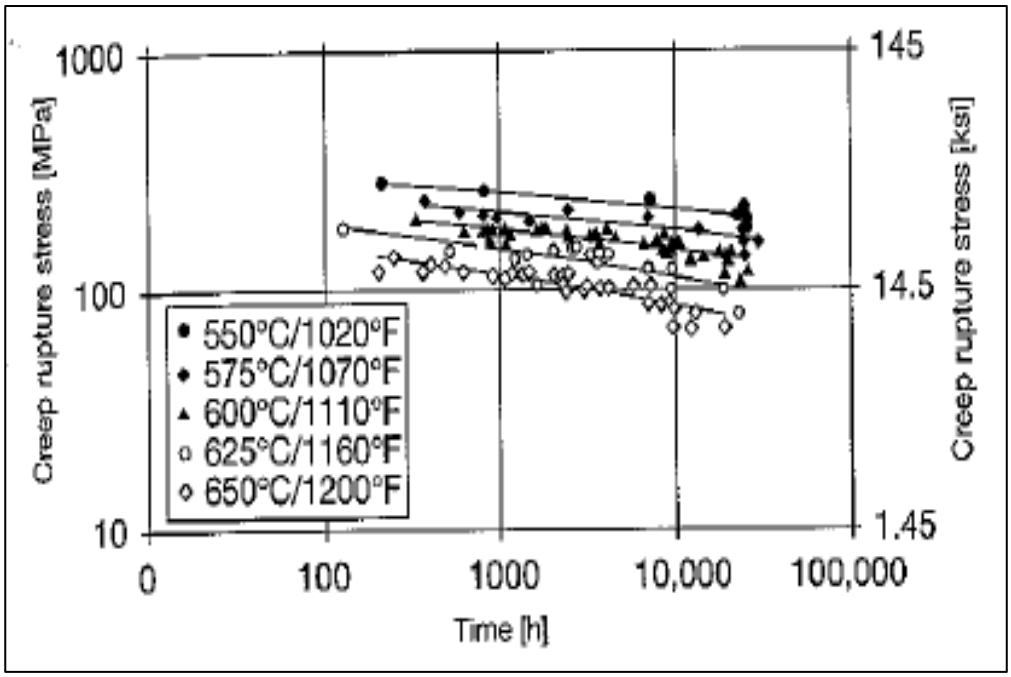

Figure 2.5: Vallourec and Mannesmann creep testing results for P92, conducted at 550-650 ºC [Richardot et al., 2000: p.25].

Table 2.2: Maximum allowable stresses for standard dimension P92 pipework according to ASTM/ASME code standards (code case 2179), adapted from Richardot et al. [2000: p.6].

Temp [ºC]	371	399	427	454	482	510	538	566	593	621	649
Stress [MPa]	154	151	147	143	138	132	126	119	94	70	48

2.4.2.2 Fatigue

Review of the literature suggests that both stress and strain controlled fatigue testing has been studied for P92. The extensive literature review conducted by

Fournier et al. [2008], Fournier et al. [2010] and Fournier et al. [2011] shows that the vast majority of cyclic testing conducted on 9-12 % Cr ferritic steels at high temperature is pure fatigue with only a few authors considering creep-fatigue interaction. LCF is the most common fatigue testing for P92 as it is relatively short duration. To make the fatigue testing of P92 more industrially relevant the overall number of cycles should be increased (strain reduced) and the individual cycles should be slow to represent real power plant cycling conditions.

The fatigue properties of bulk P92 have been investigated previously by a number of authors. Junak and Ciesla [2011] evaluated the low cycle fatigue behaviour of P92 and P91 steels for strain controlled operation at room temperature. Higher temperature strain controlled work was also performed and it was found that P91 and P92 both showed very similar fatigue characteristics at temperatures of 550 and 600 ^{o}C [Kannan et al., 2013]. Figure 2.6 presents the peak tensile stress reduction of P91 and P92 fatigue tests at 600 ^{o}C for strain of 0.25-0.6 %. Using the Palmgren-Miner hypothesis it can be shown that the materials fatigue life depends on the strain history (cumulative damage), in both cases cyclic weakening of the material was observed. This weakening or softening was studied in detail by Giroux et al. [2010] and is shown to be due to microstructural evolution; specifically a decrease in the kinematic component of hardening and significant precipitate coarsening. Also it has been shown by Armas et al. [2004], when considering low cycle fatigue failed specimens of P92, that there is significant coarsening of grain size and a decrease in dislocation density during cyclic loading. Fatigue failure is

dominated by an initial crack initiation phase, then crack propagation before finally fatigue failure.

A small number of authors have also studied the strain controlled creep-fatigue interaction behaviour of P92 steel. This is where a dwell or holding period is introduced either at peak tensile or compression. Fournier et al. [2008] shows that a compressive holding period is more deleterious to the overall fatigue lifetime than a tensile one. This work also found that oxidation has a strong influence on the fatigue lifetime; in some cases the environmental degradation by oxidation is sufficient to cause sites for fatigue crack initiation.

Overall there would appear to be gaps in the literature for further cyclic testing of P92, especially for long duration industrially relevant cycles. There is also very limited work at temperatures exceeding 650 ^{o}C.

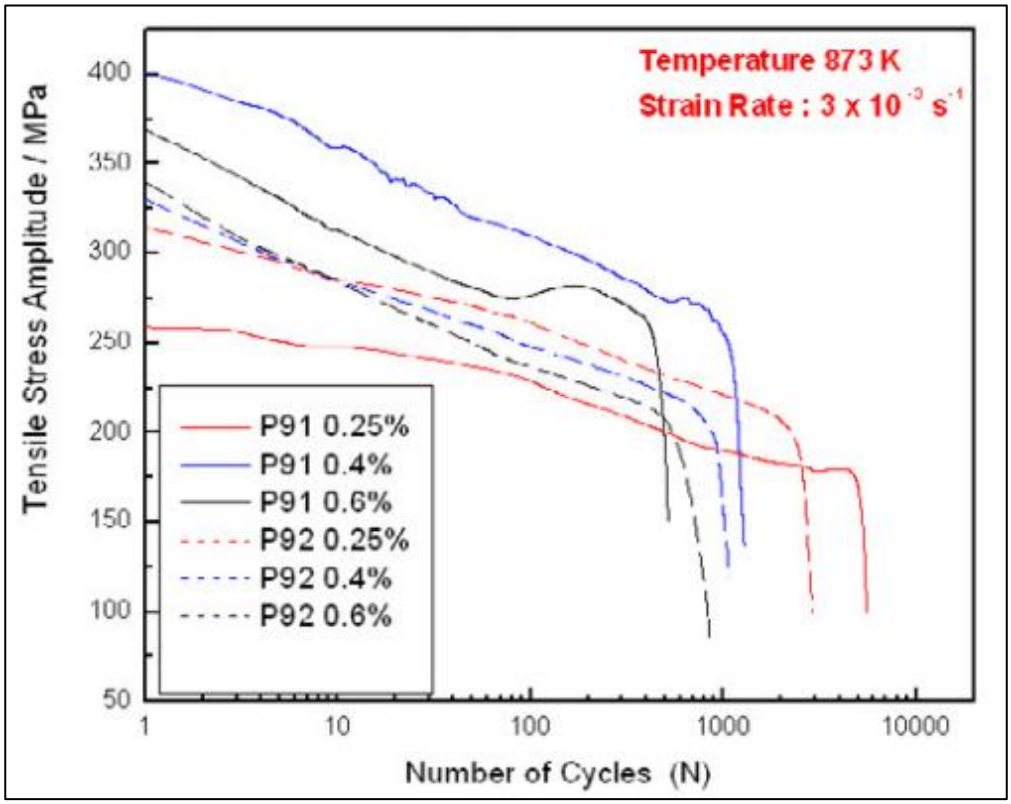

Figure 2.6: Cyclic stress responses of P91/P92 at 650 ^{o}C [Kannan et al., 2013: p.151].

2.4.3 Oxidation Behaviour of P92/P91

Steam oxidation has the potential to cause degradation and failure of the P92 pipework as the steam temperatures are increased. This can subsequently lead to unplanned shutdown, as pipework is damaged, which can be costly to power plant operators. The spalling oxide can also cause erosion of other components within the power plant, for example turbine blades.

Zurek et al. [2014], Viswanathan et al. [2006] and Laverde et al. [2004] have studied in detail the isothermal steam oxidation of P92/P91 steel within the temperature range 575-700 ^{o}C. Mogire et al. [2011] and Vaillant et al. [2008] show that the oxides formed on P91 and P92 in steam are the same providing the chromium and silicon contents are similar, although the oxide on P92 is shown to be thicker compared to P91. The rate of oxide formation is faster on P92 than on P91, usually around twice as fast. This is explained by the rapid oxidation of tungsten, which is included in larger concentrations in P92 [Mathiazhagan and Khanna, 2011; Ehlers et al., 2006]. Three clearly defined oxide layers have been identified on P91 and P92 following steam exposure:

- Innermost spinel type oxide – $(Fe, Cr)_3O_4$
- Intermediate layer of porous magnetite – Fe_3O_4
- Thin outermost layer of compact hematite – Fe_2O_3

It has been shown that the majority of the oxide scale thickness is composed of the inner spinel layer and the intermediate magnetite layer, as shown in figure 2.7. The oxidation kinetics of P91 and P92 are shown to be parabolic in nature [Ennis and Quadakkers, 2007]. At elevated temperatures this oxidation process

is accelerated resulting in the formation of thicker oxide scales. For P91/P92 currently, the operation temperature limit for live steam is 605 ^{o}C and 620 ^{o}C for reheat steam [Viswanathan and Bakker, 2001]. At these temperatures the oxidation damage and spallation is acceptable to industry [Vaillant et al., 2008]. As the temperature is increased beyond these levels to increase efficiency the oxide layer becomes thicker and more likely to spall.

There are a number of problems with thicker oxide scales on P91 and P92 [Ennis and Quadakkers, 2007; Nieto Hierro et al., 2005]. Firstly, the scale can insulate the tube reducing heat transfer. This induces residual stresses and affects the composite conductivity of the metal meaning higher metal temperatures and thus higher creep rates. Secondly, the thicker scale can spall much more easily from the wall of the pipe meaning that, in certain pipe designs, it can travel through the steam system causing erosion and damage of components [Viswanathan et al., 2006]. The integrity of the pipework is also compromised by the loss of wall thickness. Spallation is caused principally by the stress within the scale as it grows and differences in the thermal expansion of the scale and the substrate during cyclic operation. Spallation can occur between the different layers of the oxide and also at the steel-oxide interface [Ennis and Quadakkers, 2007]. An example of oxide spallation within P92 pipework is shown in figure 2.8.

Birks et al. [2006] and Laverde et al. [2004] have also shown that the oxide produced following high temperature air exposure contains the same three layered structure as in steam. The main difference is that in air the oxidation is slower to occur and steam conditions have been shown to significantly enhance the oxidation rate of the P91 steel. Also in steam exposure the outer Fe_2O_3 is

more discontinuous than in air. [Shibli and Starr, 2007; Ehlers et al., 2006]. It is common in the literature for P92 oxidation tests to be performed in air, mainly because of the limited availability of steam testing facilities.

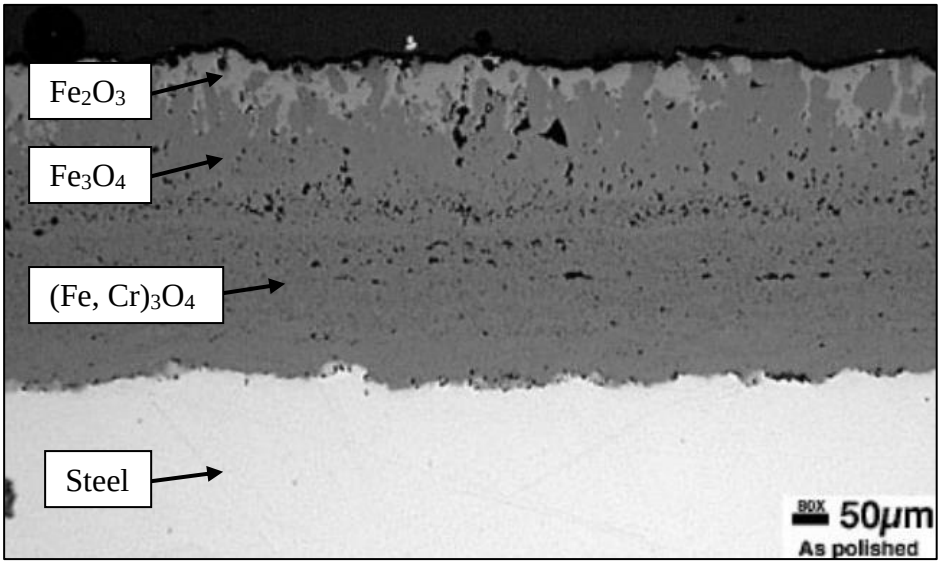

Figure 2.7: SEM micrograph to show the multi-layered oxide formed on P91 following 63,000 hours at 566 ºC in steam [Wright and Dooley, 2010: p.143].

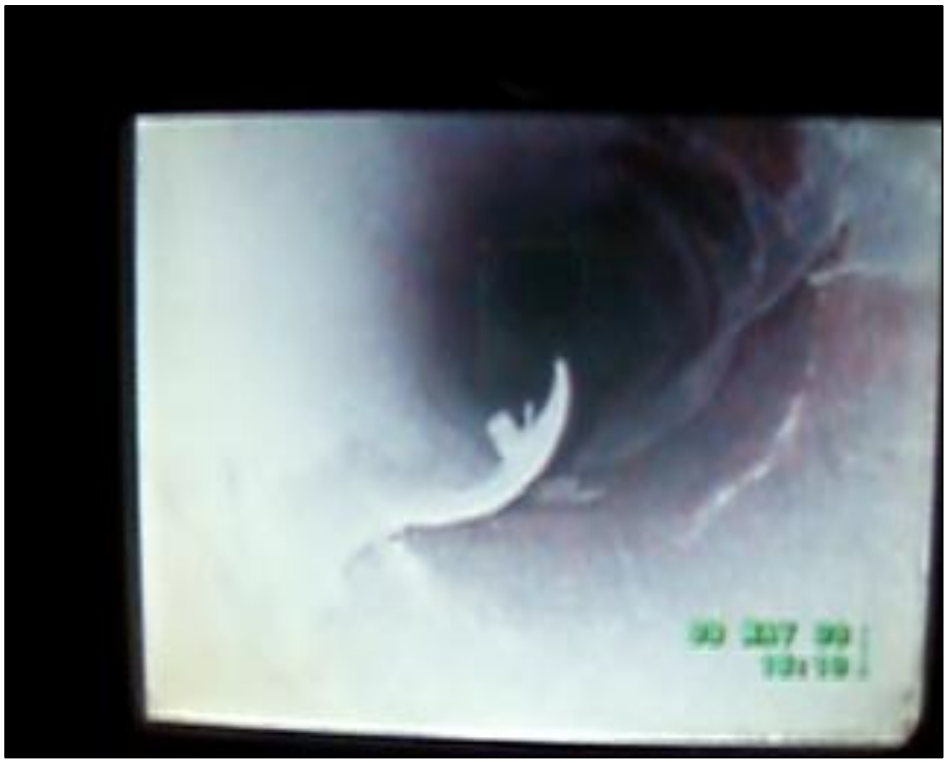

Figure 2.8: Digital photography provided by Doosan Babcock of the spallation on the inside surface of a typical P92 pipe [Chi and Barnard, 2012].

To protect ferritic steels from excessive oxidation the general principles of alloy design rely on the selective oxidation of alloying elements to form a protective oxide layer. This oxide layer must be slow growing and resistant to spallation so that pipework damage and erosion is kept to a minimum [Young, 2008; Birks et al., 2006; Ennis and Czyrska-Filemonowicz, 2003].

Currently P91 and P92 ferritic steels are based around 8-9.5 wt % Cr and studies show that if the percentage can exceed 13 wt % then a significant reduction in the scale thickness can be achieved [Chi and Barnard, 2012; Danielsen and Hald, 2008; Richardot et al., 2000]. Chromium additions will oxidise preferentially by selective oxidation and form a Cr_2O_3 or $(Fe, Cr)_3O_4$ protective scale. $(Fe, Cr)_3O_4$ is less protective compared to Cr_2O_3 but they are both slow growing and improve the steam oxidation properties of the material [Birks et al., 2006]. Cr_2O_3 can be achieved by increasing the steel chromium content. However, increasing the chromium percentage above its current values (8-9.5 wt %) has a detrimental effect on the mechanical properties by the formation of a brittle Z-phase [Danielsen and Hald, 2008]. The higher the chromium content the faster the brittle Z phase precipitates. Precipitation of the Z-phase is associated with dissolution of MX carbo-nitrides and specifically causes a breakdown in the long term creep properties.

For P92 it is not only the content of chromium within the material that effects steam oxidation but also the addition of other elements. Additions of silicon and aluminium can be very beneficial to the oxidation resistance as they can form protective silicon and aluminium oxides. However these additions are known to make the materials brittle and give poor creep properties. Therefore the content of such additions has to be kept low and be carefully controlled

[Brett et al., 2004]. Sulphur has been found to be a more effective addition to improve oxidation resistance than silicon when tested at 650 ^{o}C. However this sulphur level must also be carefully controlled to prevent adverse mechanical properties [Viswanathan et al., 2006]. Also; manganese, molybdenum and tungsten can all be beneficial to oxidation of P92 if carefully controlled [Viswanathan et al., 2006].

2.5 Coated Ferritic Steel System

Overall the literature suggests that P92 ferritic steel is fairly well optimised for both oxidation resistance and mechanical properties and that it is very difficult to further improve the oxidation resistance without having a detrimental effect on the mechanical properties. From the literature it seems unlikely that further adjustment of the alloying elements would allow for a significant increase in the operation temperature of P92.

Therefore in the meantime industry is beginning to look for other methods to achieve these higher temperatures for P92. A particularly important area is the application of oxidation resistant coatings to allow P92 to operate at higher temperatures without the formation of such thick and brittle oxide phases [Nicholls, 2000]. The primary function of any oxidation resistant coating is to produce a stable and slow growing oxide that creates a barrier between the coating alloy and the oxidising environment, which provides protection to the substrate material below [Scheefer et al., 2005; Aguero et al., 2001]. Nicholls [2000] states that oxidation resistant coatings can be split into two broad categories, namely diffusion and overlay type coatings.

Diffusion coatings are formed by enriching the surface of the material with aluminium, chromium or silicon. This then allows a protective scale to form (e.g. Al_2O_3, Cr_2O_3, and SiO_2). Typically methods of applying diffusion coatings include pack and slurry cementation and CVD.

Overlay coatings are different to diffusion coatings as the substrate and coatings only interact enough to be bonded together. This allows for more flexibility of coating composition as elements that are harder to incorporate into diffusion coatings, because of their high melting temperatures, can be included, for example chromium. Typical methods of deposition include EB-PVD, HVOF – thermal spraying, plasma spraying and electro-plating.

Some of the most common coated P92 systems studied in the literature will now be presented. The majority of work conducted to date has considered aluminide diffusion coatings. However a series of overlay coatings have also be considered and detailed in this section.

2.5.1 Aluminide Diffusion Coatings

2.5.1.1 Deposition Methods

Aluminide diffusion coatings were one of the first coatings to be investigated when coated P92 was first suggested. They were typically deposited with a thickness of 40-130 μm. The majority of work studying aluminide diffusion coatings on P92 has considered the slurry deposition process. Essentially this involves the slurry deposition of aluminium onto the surface of the P92, followed by a curing heat treatment (usually around ~ 350 ^oC). A layer of Al_5Fe_2 can then be produced using a secondary heat treatment at ~ 700 ^oC in argon for approximately 10 hours. This heat treatment acts as the thermal

activation stage. An example of the as-deposited coating is shown in figure 2.9. On exposure to air and steam at service like conditions the Al_5Fe_2 goes on to form the protective and slow growing Al_2O_3, accompanied by a thin layer of FeAl close to the substrate [Bellucci et al., 2015; Aguero et al., 2007]. This Al_2O_3 scale is desirable over silica or chromia scales because it remains chemically stable in supercritical steam at high temperatures [Xiang and Datta, 2006].

The pack cementation method has also been considered by a number of authors but not as extensively as slurry deposition. Bates et al. [2014] showed that pack cementation can be performed at a variety of temperatures ranging from 650-1050 ^{o}C. However the high temperature nature of this deposition is a problem when coating ferritic steels.

CVD for aluminide deposition has also been suggested by Sanchez et al. [2008] as well as HVOF thermal spraying by Aguero et al. [2008]. Aguero et al. [2008] suggests that thermal spraying is one of the most effective methods. However the practicalities of thermal spraying on the inside surface of a P92 pipe makes this a method that is unlikely to be utilised for the aluminide coated P92 pipework application.

2.5.1.2 Coated P92 Integrity/Oxidation

Slurry aluminide coatings have been shown to be protective for at least 41,000 hours at 650 ^{o}C in pure steam by the formation of adherent and slow growing Al_2O_3. Degradation occurs by coating-substrate inter-diffusion leading to a decrease in aluminium in the coating as it diffuses into the substrate and causes precipitation of AlN precipitates within the substrate. Evidence of Kirkendall

porosity forming at the coating-substrate interface is also observed. This is a particularly concerning feature as it could potentially cause cracking or failure of the coating [Aguero et al., 2007]. This is illustrated in figure 2.10.

Bose [2011] and Durham et al. [2008] show that the composition difference between the substrate and the coating provides the driving force for the inter-diffusion of elements. As the temperature is increased the degradation due to inter-diffusion becomes more pronounced as the elements that are diffusing become more mobile at higher temperature. The diffusion can result in the surface concentration of aluminium decreasing due to aluminium inward diffusion into the substrate, offering increasingly limited oxidation protection and causing aluminium rich particles to precipitate in the substrate.

Hoglund and Agren [2001] suggest that the difference in the diffusion rates of the coating and the substrate can result in the formation of Kirkendall pores. In other words the inward diffusion rate for aluminium and the outward diffusion rate for iron are different meaning that voids form beneath the coating which can significantly affect the mechanical properties of the coating [N'Dah et al., 2007]. Chemical potential and atomic size are the main factors influencing diffusion of elements. Aguero et al. [2007] and Aguero et al. [2008] also confirm that for a ferritic-aluminide system the difference in the diffusion rates of iron and aluminium is very large resulting in extensive Kirkendall porosity below the coating. Pint and Zhang [2011] agree with this and suggest that the porosity can cause cracking when the system is thermally cycled very rapidly. Thinner coatings with lower aluminide content have been shown to reduce crack formation as they introduce less residual stress, are cheaper to produce and have less of an effect on pipework dimensions.

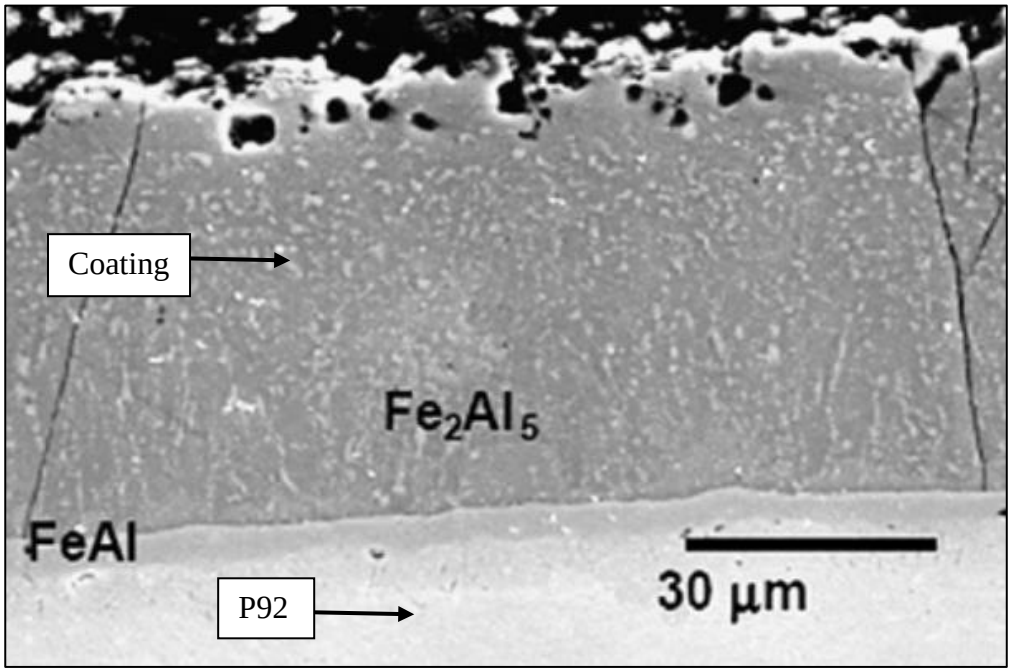

Figure 2.9: SEM cross-section of slurry deposited aluminium on P92 following diffusion activation heat treatment [Aguero et al., 2007: p.6253].

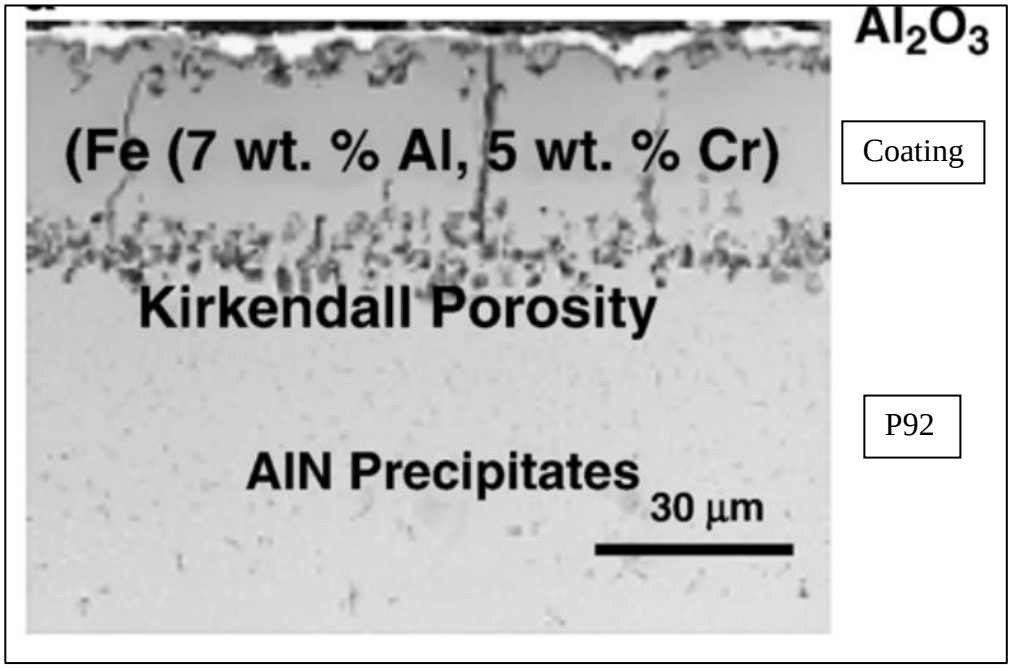

Figure 2.10: SEM cross-section of slurry aluminide coated P92 following isothermal oxidation in steam for 40,000 hours at 650 ^{o}C [Aguero et al., 2007: p.6255].

Very little work has been conducted to consider silicon and chromium based diffusion coatings on ferritic steel. Theoretically silicon and chromium coatings should be more resistant to inter-diffusion degradation because the atomic size is larger meaning that diffusion occurs less readily [Birks et al., 2006]. However chromising has never been seriously considered as it requires such high chromising temperatures that the substrate steel would be irreversibly transformed (although formation of chromia from an overlay coating would still be viable). Siliconising can be performed at lower temperatures but the work by Scheefer et al. [2005] suggests that the protective SiO_2 formed on the coatings are very soluble in high pressure steam. Therefore aluminising is the only diffusion coating that has been investigated for P92.

2.5.1.3 Coated P91/P92 Mechanical Behaviour

For an aluminide type coating to be accepted for use in service it is necessary to demonstrate that the aluminide coating does not adversely affect the mechanical performance of the substrate material. Aguero et al. [2005] showed that aluminide coatings on ferritic steel have reasonable ductility (~ 1.6 % when stressed in tension between room temperature and 400 ^{o}C) that increases at higher temperatures. This is encouraging as a brittle coating would spall easily from the substrate under stress. According to Nicholls [2000] aluminide coatings have the highest DBTT of any coating that could be applied to P92 (600-1000 ^{o}C).

The effect of coating application on the creep properties of the substrate are determined by conducting coated and uncoated creep tests at the same test conditions (stress, temperature, environment). The aluminide coating process

was applied to the P91/P92 creep test specimen to a service relevant thickness (40-130 µm) and compared directly to an uncoated specimen. This coating thickness was not considered to be load bearing compared to the substrate specimen gauge diameter. Most mechanical work has been conducted with a P91 substrate, however this will still be representative of P92 as the compositions and mechanical properties are very similar.

Early work performed by Aguero et al. [2007] shows a 10% drop in creep failure time as a result of the aluminide slurry deposition process onto P91 (700 ^{o}C deposition temperature) following creep tests performed in air at 600-650 ^{o}C. It was also shown that this reduction in life is greater following longer creep testing, as shown in figure 2.11. Aguero et al. [2007] suggests that the high temperature nature of the slurry deposition process (700 ^{o}C) accounts partially for the loss of creep strength (4-7 %) as the P92 microstructure is changed. The presence of the diffusion zone is responsible for the remaining reduction as this is assumed to have no creep strength. Aguero et al. [2007] suggests that this inter-diffusion effect is limited as wall thickness is increased and can be neglected for common component wall thicknesses.

Bates et al. [2014] has given similar consideration to an aluminide coating deposited by pack deposition onto P91. Bates et al. [2014] found that decreases in creep life at 650 ^{o}C were observed for all samples coated with pack cementation aluminide coatings, as shown in figure 2.12. For specimens aluminized at 650-700 ^{o}C with coating thickness of 18-125 µm a reduction in creep life of 16-34 % was measured. Specimens aluminized at 1050 ^{o}C with a coating thickness of ~ 290 µm show a decrease in the rupture life of ~ 51 %. Bates et al. [2014] concludes that differences in the creep life are caused by the

high deposition temperatures causing irreversible transformations in the P91 (martensite forms as carbon diffuses from the coating into the substrate).

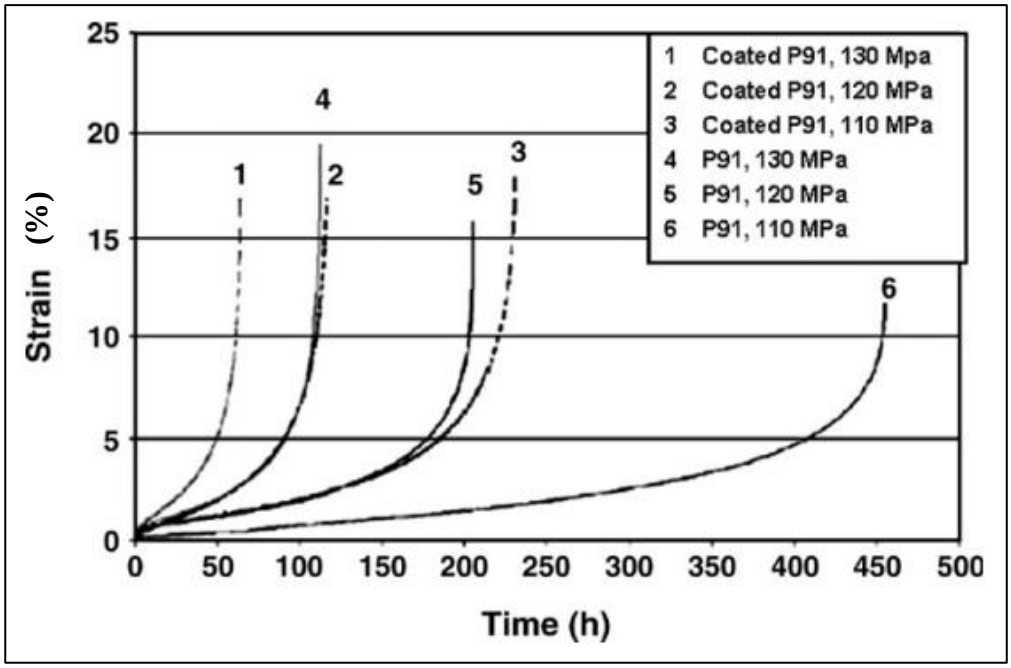

Figure 2.11: Creep strain curves for uncoated and slurry aluminide coated P91 for creep testing performed at 650 ºC [Aguero et al., 2007: p.6256].

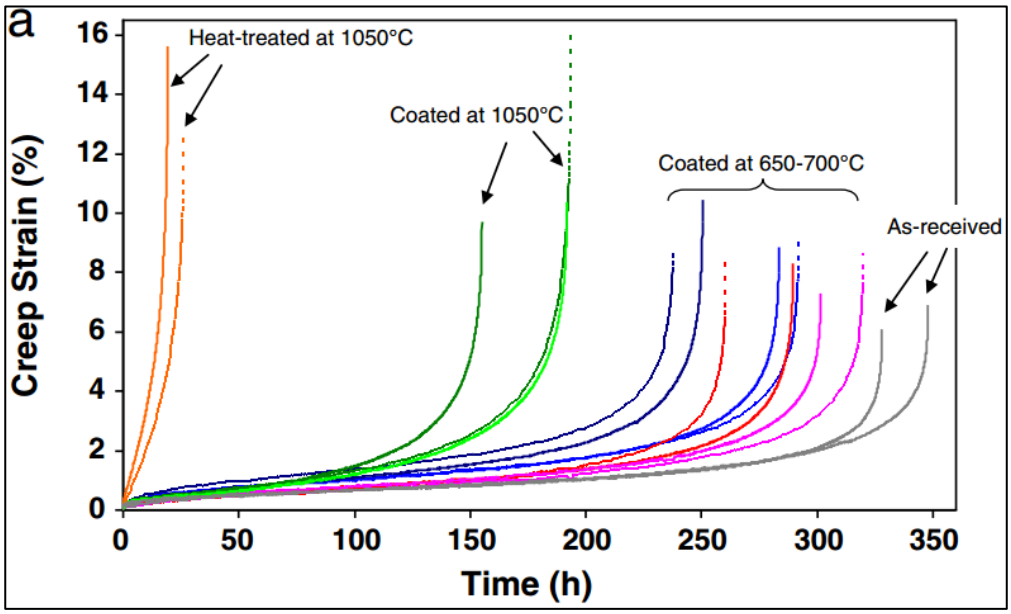

Figure 2.12: Creep strain curves for uncoated and pack aluminide coated P91 creep testing performed at 100 MPa at 650 ºC [Bates et al., 2014: p.35].

For martensitic steels the maximum allowable coating deposition temperature is suggested to be no higher than 650 ^{o}C to avoid detrimental microstructural transformation [Ennis et al., 1997; Saroja et al., 1995]. This is a fundamental challenge for aluminising of P92 because the melting point of aluminium is 660-700 ^{o}C [Callister and Rethwisch, 2007] and therefore this is a minimum requirement for the thermal activation heat treatment. Researchers have tried lower temperature thermal activation but have found that this limits the thickness of the aluminide coating and therefore its effectiveness. Much more recent work presented by Bellucci et al. [2015], Xiang and Datta [2006] and Xiang et al. [2006] suggests that pack cementation may still be an option and that by careful control and optimisation of the deposition process it is possible to control the grain size coarsening and therefore limit any negative effect seen previously on the mechanical properties. Pack cementation is an interesting area for further future development.

A small amount of work has been conducted considering the effect of aluminide coating deposition on the fatigue properties of P92/P91 substrate. Aguero et al. [2007] has performed TMF testing of aluminide coated alloy 122 (considered representative of P91 and P92). The comparison testing was again performed by running an uncoated specimen and a coated specimen (specimen coated to thickness of 40-130 μm) at the same conditions. The specimens were tested with an out of phase cycle, temperature range of 200-650 ^{o}C (5 Ks^{-1}) and a strain up to 0.6 %. This work shows that at high strain ranges the TMF performance of aluminide coated P92 is enhanced, as shown in figure 2.13. The beneficial effect is reduced as strain is reduced. Figure 2.14 shows that for a high strain test the final drop in stress occurs over a much larger number of

cycles. This suggests that the crack growth is occurring more slowly, probably because the coated sample surface is more resistant to crack initiation or the coating-substrate interface retards crack growth. Examination of the failed samples shows that cracking occurs and that the coating-substrate interface appears to slow them. This is most likely due to changes in alloy chemistry and fracture toughness in the IDZ [Aguero et al., 2007].

Overall the current state of the literature seems to suggest that although aluminides provide the desired oxidation protection for long term exposures and potentially improve the fatigue crack initiation and propagation properties at high strain, there are a number of potential limitations. This includes Kirkendall porosity forming beneath the coating and the apparent decrease in the creep life caused by the high temperature deposition process. It appears from the literature that most of the problems with aluminides are caused by the high temperature heat treatments needed for deposition/thermal activation and differences in the composition and diffusion properties of the coating and the substrate. The literature suggests that further work is needed for aluminide coatings to limit the microstructural effects that the high temperature deposition has on P92. However it seems that a more straightforward solution would be to develop a much lower temperature coating deposition process. Therefore lower temperature overlay coatings need to be considered. The most promising type would be those that utilise Cr_2O_3 or Al_2O_3 without the need for high temperature diffusion heat treatments.

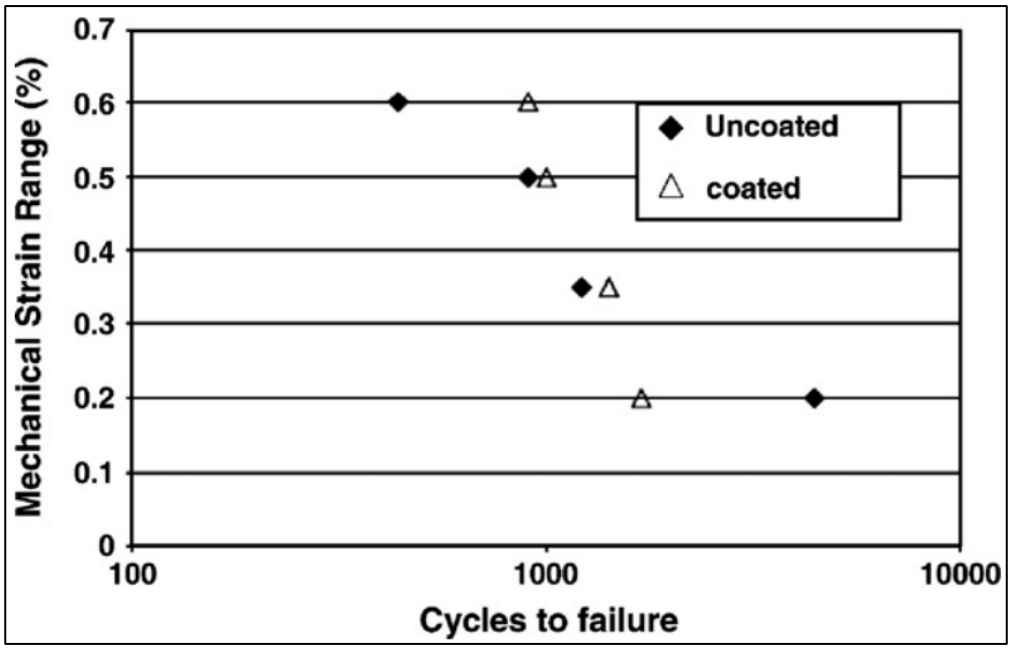

Figure 2.13: TMF testing cycles to failure for uncoated alloy 122 and slurry aluminide coated alloy 122 [Aguero et al., 2007: p.6259].

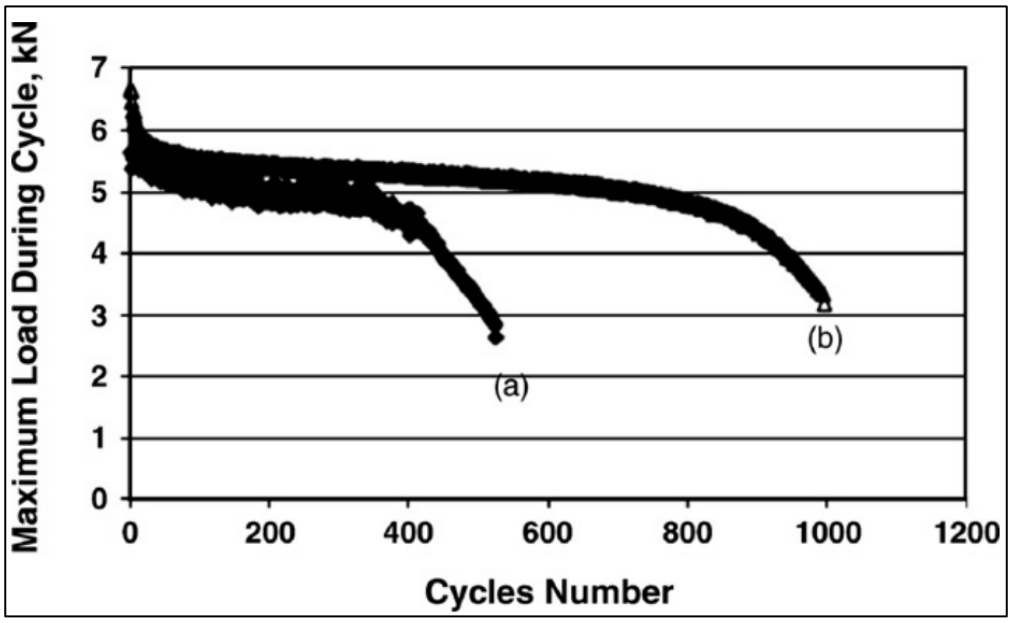

Figure 2.14: Maximum load reduction during TMF testing at 0.6 % strain for (a) uncoated alloy 122 and (b) slurry aluminide coated alloy 122 [Aguero et al., 2007: p.6259].

2.5.2 Overlay Type Coatings

In addition to diffusion coatings a small amount of work has also been conducted to consider overlay coatings for ferritic steels, deposited by a variety of techniques.

Thermal spraying has been investigated by a number of authors as shown in the review by Aguero et al. [2001]. Thermal spraying involves accelerating fine molten or semi-molten droplets towards the surface of a substrate material. When the droplets coalesce and cool they form a coating. Some of the most common coatings that have been investigated in the literature are: FeAl, FeCrAl, NiCr and AlFeCoCr. Some of the most in-depth work has been conducted by Sundararajan et al. [2004; 2003a; 2003b] considering Ni-Cr type coatings. Cermet coatings have also been considered which gave satisfactory oxidation protection [Ding et al., 2015; Ding, 2009]. The thermally sprayed coatings considered all aimed to produce aluminium or chromium based protective oxides, or a combination of both. In almost all cases the coatings were shown to be resistant to high temperature air/steam. All of the methods were also low temperature and did not require a post deposition heat treatment, therefore the substrate material remained unaffected (apart from localised surface heating of some spray techniques). The main disadvantages of thermal spraying are its high cost and also the fact that it is a line of site method only. This means that it is very hard to coat complex geometries and the inside of pipework. Further work would be needed to develop smaller thermal spray systems for this application.

The review by Aguero et al. [2001] also reports that electro-less nickel coatings have been considered for ferritic steels. This work suggests that although

exposure tests at high temperature suggest a good oxidation stability of these coatings, through cracks have been observed in the coating that reach the substrate material. These are most likely due to the brittle nature of the nickel coating.

Overall a number of different overlay coatings have been considered, mainly produced by thermal spraying. A variety of different coating compositions have been considered without a clear focus on one type. Although most of the thermal spray coatings studied gave good oxidation protection the deposition method makes it limited for P92 pipework. Therefore work to find a more suitable coating method is needed. This needs to be low temperature and also practical for easy application to the inside surface of P92 pipework.

2.6 Co-Cr-C Oxidation Resistant Coating for Ferritic Steel

Having reviewed the current literature for coated ferritic steels it is clear that the majority of work has been focused on diffusion coatings, mainly the aluminide diffusion type coating. These coatings are shown to have a number of potential problems, mainly due to the high temperature coating process. Thermally sprayed overlay coatings have also been considered, however the limitations of thermally spraying the inside of a P92 pipe make this method limited. Industry is therefore beginning to research lower temperature deposition overlay type coatings, which can easily coat the inside surface of P92 pipes. Overlay coatings that form adherent and slow growing chromium based oxides are one of the most desirable [Nicholls, 2000].

The specific coating being considered in this thesis is an ‘off the shelf’ Co-Cr-C type which is part of the Tribomet family of coatings manufactured by Praxair Surface Technologies Ltd. On exposure to high temperature this coating forms slow growing and adherent chromium and cobalt based oxides [Hoey et al., 2015].

Tribomet coatings are electro-deposited composites which are applied by a patented deposition process (chapter 3). The literature shows that there are several existing patents for Tribomet coatings [Payne et al., 2013; Datta, 2010; Newman, 1977] and the original work for the Tribomet family of coatings is presented by Kedward [1973], Kedward et al. [1974], Kedward and Addison [1976] and Honey et al. [1986]. Tribomet coatings are produced when particles which are kept in suspension in an electro-plating bath, settle onto the component and become trapped by the depositing material, as shown in figure 2.15. The Co-Cr-C type Tribomet coatings are produced from electro-plated cobalt and fine particles of Cr_3C_2. There are two versions of the Co-Cr-C coating, T104C and T104CS (tradenames). T104C has a carbide content of 12-28 wt %, hardness of 300 HV and a maximum operating temperature of 700 ^{o}C. T104CS has a carbide content of 30-40 wt %, hardness of 450 HV and a maximum operating temperature of 900 ^{o}C. T104CS can also be supplied in heat treated form (1000 ^{o}C) which has the effect of increasing the hardness of the coating.

The Tribomet coatings have been used very successfully for many years by Praxair Surface Technologies for application to super-alloy substrates for fretting and abrasive wear resistance in turbine engines [Brooman, 2004; Kedward and Wright, 1978]. The aim of a wear resistant coating is to form an

adherent slow growing oxide as an inner layer and an outer layer which readily produces a glaze on sliding contact [Mellor, 2006].

There are a number of features of Tribomet coatings that make them promising for high temperature oxidation resistance for application to ferritic steel substrates. The most important of which is the adherent and slow growing oxide which forms at high temperature [Birks et al., 2006]. Foster [2012a] suggests a number of other advantages of using T104CS:

- Non line of sight areas and internal bores can be coated easily using electro-plating. This is much easier than thermal spraying inside ferritic steel pipework.
- Excellent adhesion (> 30,000 psi) to metallic substrates
- Operating temperatures of up to 900 ^{o}C for T104CS
- Very little porosity introduced during deposition
- Low temperature coating (45 ^{o}C) will avoid any thermal distortion of the substrate steel.
- Praxair Surface Technologies have 40 + years of experience coating T104CS onto super-alloy substrates for gas/steam turbine components.

For this thesis the un-heat treated version of T104CS was considered as it was expected that the higher chromium content would be beneficial to produce more adherent chromium rich oxides [Birks et al., 2006]. Also the un-heat treated version was studied as consultation with industrial sponsors concluded that application of a post-deposition heat treatment would significantly increase the cost of coated P92.

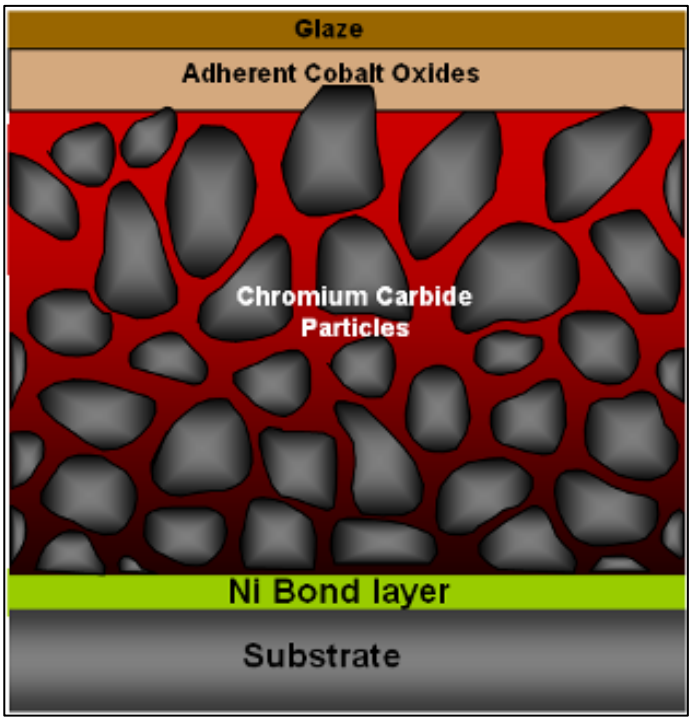

Figure 2.15: Schematic published by Praxair Surface Technologies Ltd to show the formation of the T104CS coating [Foster, 2012a: p.1].

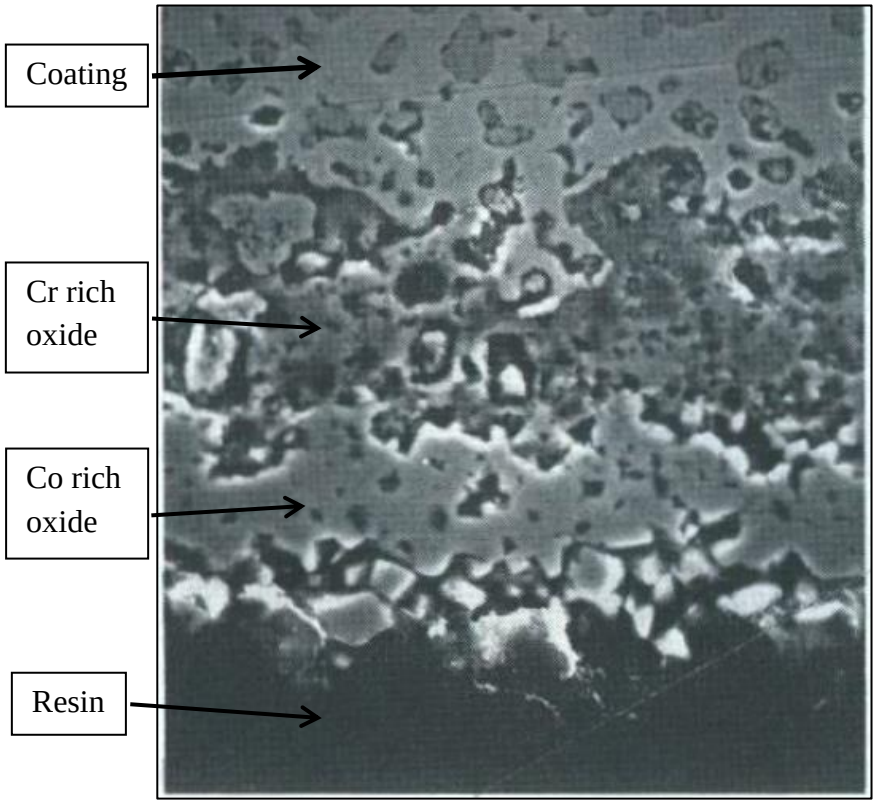

Figure 2.16: T104CS coating following high temperature oxidation in air at 1000 ^{o}C for 1 hour [Cameron et al., 1979: p.1].

2.6.1 Oxidation Properties

El Dahshan et al. [1975] concludes that the oxidation kinetics of the homogenised cast Co-Cr-C ternary system (Co-(5-35)Cr-(0.5-1.0)C) in air can be described by a parabolic rate law up to 1000 ^{o}C. The oxide formed on the ternary system is thin and contains mainly Cr_2O_3 and $CoCr_2O_4$. Durham et al. [1998a] has continued much of the work of El Dahshan et al. [1975] and has focused on high temperature (up to 1000 ^{o}C) exposure in air (Co-25Cr-(0.5-1.0)C). In this study, reaction rates were insensitive to carbon and when silicon was present chromium oxidised selectively leading to a protective scale of Cr_2O_3 and $CoCr_2O_4$. Under these circumstances Cr_3C_2 beneath the alloy surface dissolved and chromium diffused to the surface, sustaining the growth of protective Cr_2O_3. They also suggested that the size of the carbides is important in protecting the alloy from high temperature oxidation. Further work by Durham et al. [1998b] investigated both coarse and fine carbides and it was reported that the fine carbides can dissolve fast enough to provide the chromium flux needed to form and maintain Cr_2O_3 scales. The high surface area to volume ratio of finely dispersed particles facilitates the formation of protective Cr_2O_3 scales, as more chromium can be released from smaller particles on a per volume basis. Smaller particles are seen to dissolve faster than larger particles.

Another important consideration is the method by which coarse Cr_3C_2 might oxidise. There is limited work in this area but Clark et al. [1986] has investigated the mechanism. It has been reported that oxidation of Cr_3C_2 leads to decarburisation to form stable films of Cr_2O_3 at high temperatures around the carbide particles, inhibiting further oxidation. Some researchers have reported

that oxidation of Cr_3C_2 leads to formation of Cr_7C_3 (orthorhombic) and $Cr_{23}C_6$ (FCC) phases at 900 ^oC [Kamal et al., 2009; Kosolapova, 1971].

Finally the limited work that specifically relates to the T104CS Co-Cr-C coating has been reviewed. Cameron et al. [1979] performed a series of tests on the Co-Cr-C free-standing coating at 1000 ^oC and have found that the oxide formed is greatly influenced by the breakdown of the Cr_3C_2 particles within the coating. The oxidation protection is provided by the supply of chromium to the oxide as the Cr_3C_2 particles breakdown and a coating with a higher Cr_3C_2 content will give better oxidation resistance. Cameron et al. [1979] suggests that the examined scale structures of the coating samples are similar to those of conventional Co-Cr alloys [Birks et al., 2006]. They exhibit porosity and they have a double layered oxide. Typically this double layered oxide, shown in figure 2.16, has an outer layer consisting of cobalt rich oxide (Co_3O_4) (outward growth) and an inner layer (inward growth) containing chromium oxide (Cr_2O_3), spinel ($CoCr_2O_4$) and a cobalt oxide network. It is reasoned that this cobalt oxide network exists to facilitate the continual growth of the outer oxide layer.

Cameron et al. [1979] also considers the oxides formed on T104CS free-standing samples which received heat treatment (24 hours at 1000 ^oC in argon) prior to being oxidation tested at 1000 ^oC. The oxide structure formed in this case is different to the oxidised non-heat treated samples. These oxides are not as porous and they do not contain an outer Co_3O_4 layer, but consist instead of $CoCr_2O_4$ and a Cr_2O_3 layer. This is consistent with the homogenised samples discussed previously. The adhesion of the oxide scales is also improved by the pre-test heat treatment. Foster [2007] has investigated the oxidation behaviour

of the T104CS Co-Cr-C coating both with and without a prior heat treatment and shows that the application of a heat treatment results in a denser oxide with less porosity being observed. It was also seen that increasing the weight percentage of Cr_3C_2 in the Co-Cr-C coating results in slower oxidation rates. Also when T104CS is compared to standard Co-Cr alloys the oxidation rate is significantly reduced.

In the published literature there is no oxidation/ageing study of the T104CS coating when applied to steel substrates of any kind. From consultation with the coating manufacturer extensive work will have been conducted to consider the T104CS coating when applied to nickel super-alloy substrates for turbine engines. However due to the commercially sensitive nature of this work it is not available in the public domain. There has been no consideration of T104CS applied to ferritic steels, either in the literature or by the coating manufacturer.

2.6.2 Mechanical Properties

Foster [2012a] has measured the micro-hardness of the T104C and T104CS Co-Cr-C coating. T104C (lower Cr_3C_2 content of 12-28 wt %) quotes a nominal hardness value of 300 HV for the bulk coating. Unsurprisingly the hardness of the T104CS coating (30-40 wt % Cr_3C_2) quotes a nominal hardness of 450 HV. This suggests that the more Cr_3C_2 is added to the coating system the harder the bulk coating becomes. Foster [2012a] has also stated the hardness values for heat treated T104CS of 700 - 800 HV when heat treated at ~ 1000 ^oC for 24 hours. As heat treatment of the composite coating is applied and alloying occurs between Cr_3C_2 particles and the cobalt matrix the hardness

of the coating is increased. Pre-heat treatment can increase hardness of T104C and T104CS by improving the particle/matrix cohesion and by alloying.

Walton [1990] has also considered the tensile properties of the T104CS type coating. This work found that prior heat treatments in hydrogen or argon significantly increase the ductility, tensile strength and micro-hardness. These changes in the mechanical properties are associated with recrystallization and solid solution strengthening of the cobalt matrix by the gradual dissolution of the Cr_3C_2 particles. Maximum strength of the composites is associated with material that has received a prior heat treatment in argon. The ideal strength microstructure will have a significant level of retained carbide which is capable of reinforcing the strength of the structure. As the carbide percentage in the coating is reduced strength decreases but the ductility of the coating increases.

2.7 Conclusions of the Literature Review

- There appears to be a reasonable body of work examining the microstructure and the mechanical properties of P92 ferritic steel. The vast majority of this work has been conducted at 550-650 ^{o}C as this has traditionally been the standard operation temperature for P92 in power plant applications. Far less work has been conducted to study the properties (mechanical behaviour) at temperatures exceeding 650 ^{o}C. The literature shows that the future drive towards USC power plant makes this higher temperature range 650-760 ^{o}C more industrially relevant. Therefore there is a gap in the current literature for higher temperature creep testing.
- This literature review also shows there is a need to coat the inside surface of P92 steam carrying pipework with oxidation resistant coatings to allow

for higher temperature operation. However there is very limited previous work examining coated P92. The work that has been carried out is mainly concerned with aluminide diffusion coatings. However they have been shown to have a number of limitations when considered for long term industrial service. This includes porosity forming beneath the coating due to inter-diffusion and the coating application having a detrimental effect on the creep life of the P92. The main disadvantage of these coatings is the high temperature coating process causing irreversible damage to the P92 substrate steel. Thermal spray coatings have also been considered but the difficulty of thermal spraying the inside of a P92 pipe makes this method unviable with current technology. Therefore there appears to be an industry need for consideration of a new overlay type coating that is deposited at low temperature by a method that can be scaled easily for coating full size P92 pipework. The production of a chromium rich protective oxide seems the most promising area to investigate. This is where this thesis aims to contribute.

- The commercially available electro-deposited Co-Cr-C T104CS Tribomet coating, currently used as a wear resistant coating, appears to be a very promising coating technology for P92 oxidation resistance. The main advantages of this coating are:

(1) The adherent and slow growing cobalt and chromium rich oxide formed is ideal for oxidation resistance.

(2) The electro-deposition method is non-line of sight allowing pipework and complex geometries to be coated.

(3) Operation temperatures of up to 900 ^{o}C are possible.

(4) The deposition process is low temperature (45 ^{o}C) meaning the P92 substrate is unaltered by the coating process.

The majority of existing work considering T104CS has always been concerned with application to super-alloy substrates for service temperatures of up to 1000 ^{o}C. There has been no consideration of the lower temperature behaviour of the T104CS coating (600-700 ^{o}C) and no consideration of the coating when applied to ferritic steel substrates. This thesis aims to address the gaps in the current understanding for T104CS and to assess the overall suitability of T104CS for application to P92.

- Having reviewed all of the previous coated P92 work, especially considering the limitations of aluminide diffusion coatings, there are several key areas that must be understood in this thesis if the T104CS coated P92 system is to be considered suitable for service. These include:

(1) **Oxidation Behaviour**: To determine the integrity of oxides formed under service relevant exposures (~ 650-700 ^{o}C) and what effect the substrate has on oxidation.

(2) **Microstructural Evolution**: To determine how the coating material evolves at lower temperature and what this means for coating integrity.

(3) **Inter-diffusion Behaviour**: To determine how inter-diffusion between the coating and the substrate steel affects the overall integrity of the coated system under service relevant exposures.

(4) **Mechanical Behaviour**: To determine how the application of the coating affects the mechanical properties of the substrate steel beneath, especially considering creep and LCF.

CHAPTER 3

EXPERIMENTAL METHODS

3.1 Introduction

This chapter presents a detailed description of the experimental methods that were used within this thesis. Firstly the substrate steel and coating materials are outlined, as well as the coating process. Secondly the exposure conditions are detailed, including the high temperature oxidation studies and the high temperature mechanical testing. Thirdly details of the microstructural characterisation techniques are included. Thermo-Calc thermodynamic modelling methods have been presented separately in appendix C.

3.2 Materials and Sample Preparation

For this thesis two main materials have been considered; P92 ferritic steel and the Co-Cr-C T104CS Tribomet coating manufactured by Praxair Surface Technologies. All coating has been performed by Praxair Surface Technologies to specifications defined by Doosan Babcock and the University of

Nottingham. The sample preparation methods and details of both materials are included below.

3.2.1 P92 Steel

The substrate material that has been studied in this experimental work is P92 ferritic steel. The particular sample of P92 used for this project was provided by Doosan Babcock and will therefore be referred to throughout this thesis as 'DB P92'. A large as-cast half section of pipe was supplied (wall thickness = 80 mm, inner diameter = 300 mm, axial length = 200 mm), as shown in the schematic below in figure 3.1. This is a representative sample of the P92 steel that Doosan Babcock have used for high temperature steam carrying pipework in fossil fuel power plant installations. Following the extruding/forging process this DB P92 was austenitised at ~ 1070 ^{o}C and tempered at ~ 775 ^{o}C to produce a creep resistant martensitic structure. No further heat treatment was performed on DB P92 following austenitising and tempering. The exact elemental composition of DB P92 is detailed in table 3.1, determined experimentally.

The DB P92 pipe section was then machined using EDM. This technique was used as it allows very strong materials to be cut easily and it also introduces less heat to the material when compared to traditional cutting methods, for example abrasive cutting wheels. Part of the pipe section was cut into a number of square P92 coupons, approximately 25 x 25 x 10 mm, which would be used for oxidation testing of coated and uncoated P92. Also a number of mechanical test specimen blanks were also machined, approximately 140 x 20 x 20 mm. These blanks could then be machined in a lathe to form the mechanical test specimens for creep and fatigue testing. Figure 3.1 shows where the samples

were machined from the DB P92 pipe section. All of the samples were taken from the axial direction of the pipe section. The mechanical specimens machined included: tensile, uniaxial creep and uniaxial fatigue. Dimensions for these specimens are given below in figures 3.2 and 3.3.

Following initial machining all DB P92 coupons and mechanical specimens were ground to a surface roughness (R_a) of ~ 0.2 µm, which is considered to be a ground/polished surface. A silicon carbide grinding wheel was used to achieve this finish. This was the surface finish specified by Praxair Surface Technologies for coating application as it ensures a smooth, clean surface which is ideal for depositing the coating onto. Surface finish specifications will need to be investigated by Praxair when depositing onto full size P92 pipework in the future. The final gauge dimensions of the specimens have a tolerance of ± 0.02 mm.

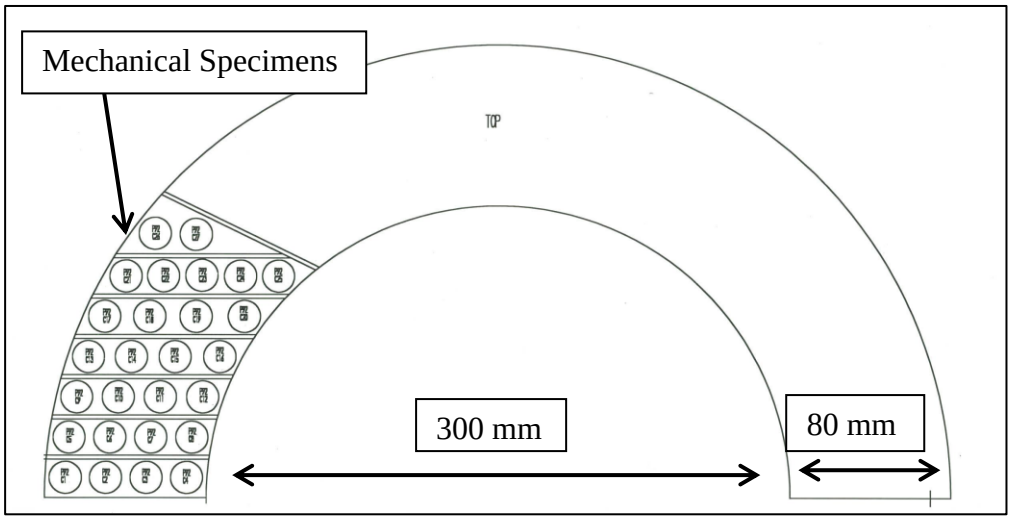

Figure 3.1: A schematic of the original DB P92 pipe section (top-down view). The axial dimension, not shown, is 200 mm.

Table 3.1: DB P92 elemental composition.

Element	Weight Percentage [%]
C	0.10
Si	0.19
Mn	0.46
P	0.013
S	<0.002
Cr	8.72
Mo	0.51
Ni	0.14
Al	<0.02
Cu	0.17
N	0.051
Nb	0.05
V	0.18
W	1.70
B	0.003

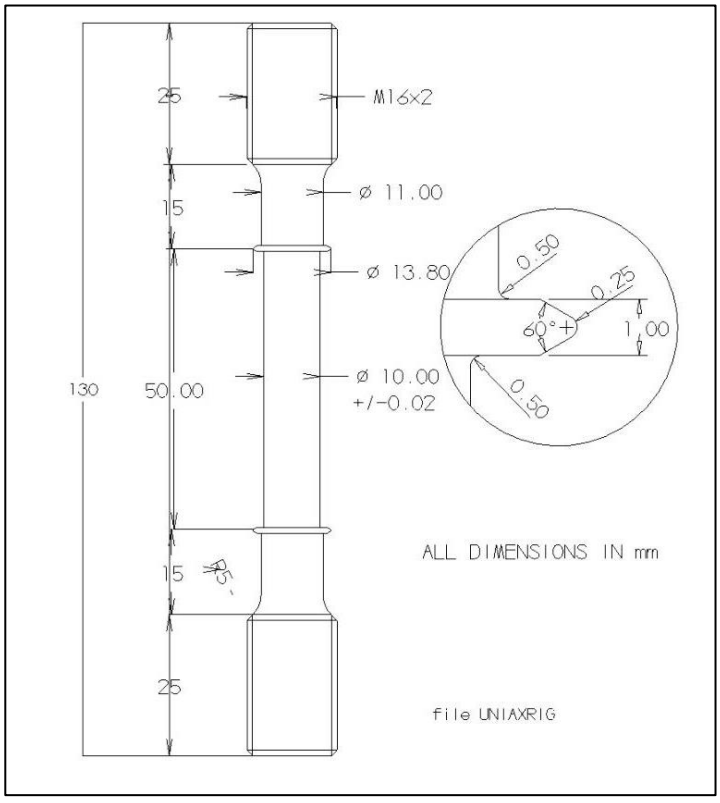

Figure 3.2: DB P92 tensile and uniaxial creep specimen dimensions.

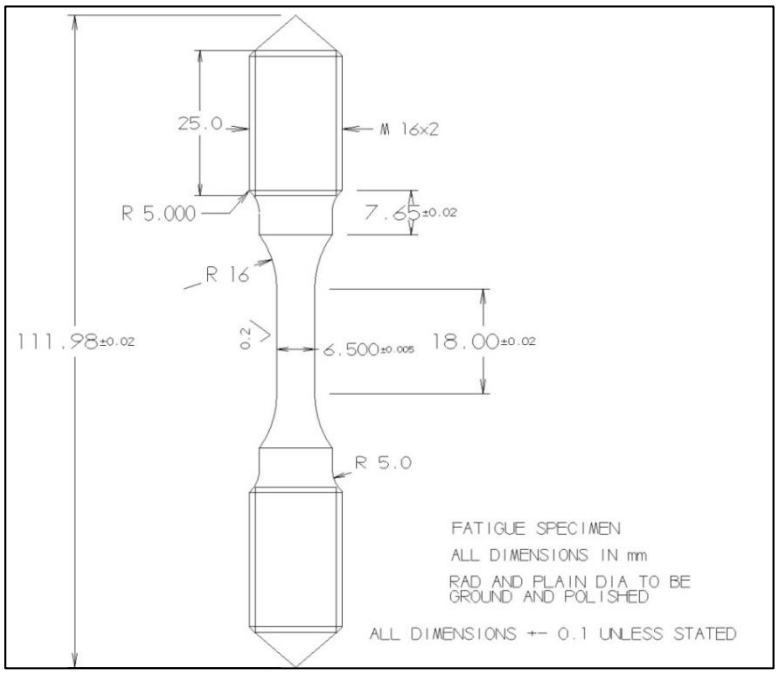

Figure 3.3: DB P92 uniaxial fatigue specimen dimensions.

3.2.2 Co-Cr-C Coating Deposition Method and Samples

The DB P92 oxidation samples (square coupons) and the DB P92 mechanical specimens (creep and fatigue testing) could then be coated with the Co-Cr-C T104CS Tribomet coating.

3.2.2.1 Electro-Deposition Methodology

The coating studied within this work is the commercially available Co-Cr-C T104CS Tribomet coating manufactured and supplied by Praxair Surface Technologies. For simplicity the T104CS Tribomet coating, which is a tradename, will just be referred to as the 'Co-Cr-C coating' throughout the rest of the thesis. The Co-Cr-C coating is a composite that consists of Cr_3C_2 particles that have been electro-deposited within a cobalt matrix. Typically the Co-Cr-C coating would contain 30-40 wt % Cr_3C_2 particles which have an average diameter of 5-10 μm. The remaining microstructure is made up of a

cobalt matrix. The typical electro-deposited microstructure of Co-Cr-C coating is shown in figure 3.4.

The machined DB P92 samples (square coupons) and the DB P92 mechanical specimens (creep and fatigue testing) could then be coated with the Co-Cr-C coating. As mentioned previously all P92 samples were machined with a surface roughness (R_a) of 0.2 µm (ground and polished surface). Prior to coating the samples were then slurry grit blasted with alumina (120 grade alumina) or chemically etched (10% sulphuric acid) to remove debris and prepare the surface. The samples were then rinsed in IMS and distilled water to remove any final debris from the surface. Batch 1 samples received the alumina slurry grit blast and batch 2 received the chemical etch. There are no other differences between batch 1 and batch 2. The alumina grit blast in batch 1 often resulted in alumina grit entrapment at the interface; this is specified by the manufacturer as being less than 20 % of the interface. However in practice this is often less than 5 %. Different batches were manufactured to assess any effect of the alumina grit, especially on the mechanical samples. A very thin nickel strike layer (2-3 µm) was then electro-deposited onto the P92 substrate for both batches to aid in the deposition of the Co-Cr-C coating.

Once prepared the samples could be subjected to the electro-deposition process, as detailed extensively by Walton [1990]. The plating tanks are constructed from polypropylene and the design is based on the weir/hopper style (figure 3.5). The general principle of operation is that compressed air is fed through the base of the plating tank and carries with it the powder (Cr_3C_2) slurry mixture, which, once it has reached the top of the tank will fall back down past the cathode to the bottom where it is recirculated. The plating tank is

shaped so that it is angled towards the compressed air inlet nozzle. This helps with recirculation and prevents the powder from forming sediment in the base of the tank [Walton, 1990]. Figure 3.5 also shows the various additional equipment that is required for electro-deposition. Firstly a water heater to ensure the plating solution is kept at 45 ^{o}C. Secondly the power supplies for the plating tank and the motors for the sample holding jig. Cobalt chips were placed in the anodic basket to maintain the bath composition throughout electro-plating. The plating jigs are a vital part of the plating system as they allow the cathode (the P92 samples) to be rotated during plating. This is especially important when coating particularly unusual or complex shapes. The plating solution consists of a traditional cobalt electrolyte, with approximately the following composition:

- Cobalt sulphate: 450 g/l
- Sodium chloride: 13 g/l
- Boric acid: 30 g/l

The overall pH of the plating solution was maintained between 4.5 and 5.0. Sulphuric acid or sodium hydroxide can be used to correct the pH if it varies too much during plating. The Cr_3C_2 powder is washed in dilute sulphuric acid and washed several times in distilled water prior to coating. The size of particles can be selected using a variety of particle size determination techniques [Walton, 1990]. Exact details of the coating method are not provided as this is a commercially sensitive process which is not made publically available. For further details contact Praxair Surface Technologies.

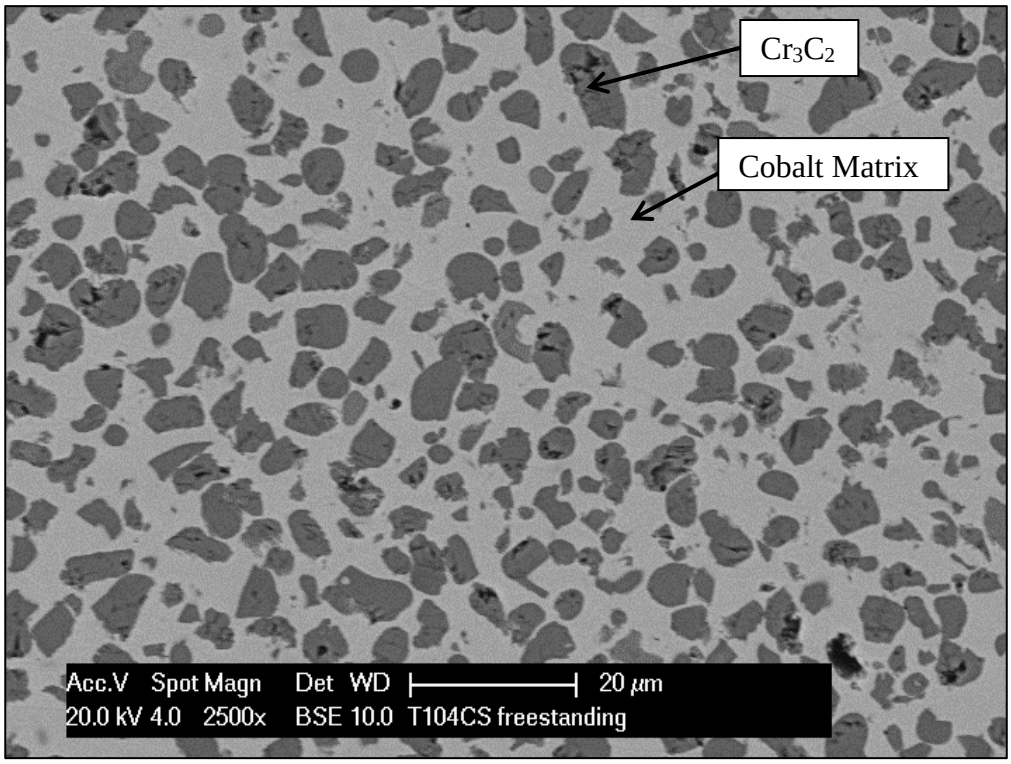

Figure 3.4: SEM micrograph of the typical microstructure of the polished Co-Cr-C coating.

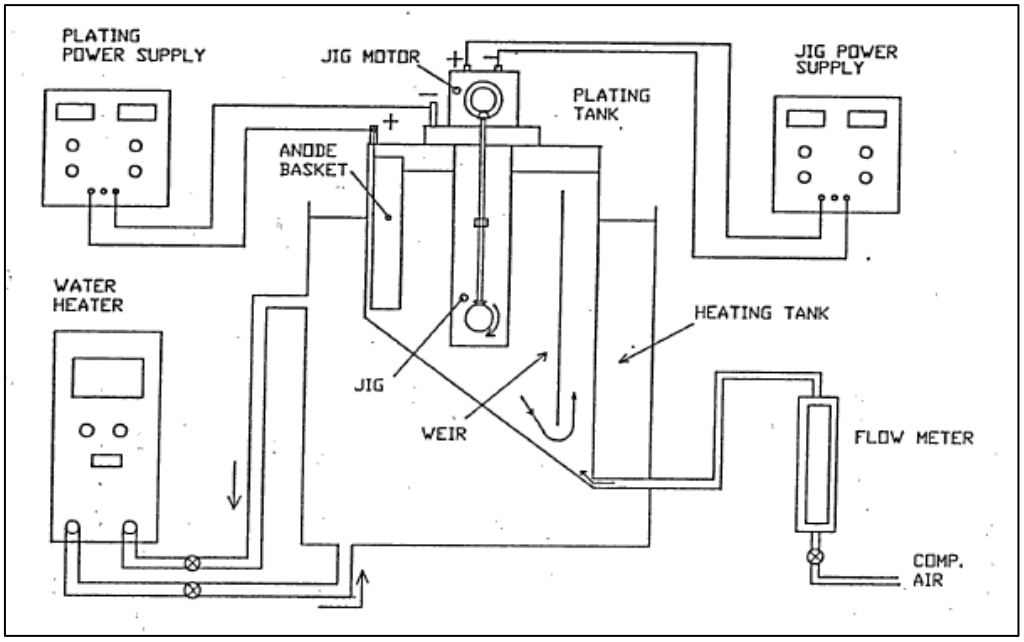

Figure 3.5: A schematic from Walton [1990: p.119] of the composite plating tank used for the deposition of the Co-Cr-C coating.

The DB P92 samples (square coupons and mechanical specimens) were coated to a thickness of 34-37 µm as this is the expected in service thickness specified by Doosan Babcock. The coating thickness is a function of time, powder volume fraction and current density. The as-plated coating surface has a surface roughness (R_a) of 1-2 µm. The surface roughness can be further improved by grinding. However in this case it was left in the as-plated condition.

3.2.2.2 Co-Cr-C Coated P92

The DB P92 coupons (25 x 25 x 10 mm) had the 34-37 µm Co-Cr-C coating applied to one face only (25 x 25 mm) whilst the other 5 faces were masked off. All of the coated coupons are batch 1 with an alumina grit blast pre-treatment. These samples were used primarily to study the oxidation, microstructural evolution and inter-diffusion behaviour of the coated P92 system following high temperature oxidation. Batch 1 samples are particularly good for investigating inter-diffusion as the entrapped alumina grit acts as inert markers of the original interface. Following coating no additional heat treatment was applied to any of the coated coupons.

The DB P92 creep specimens were also coated to a thickness of 34-37 µm around the entire circumference of the gauge length. The only areas not coated were the screw threads, which were masked off, to ensure the specimens would still fit into the creep and fatigue machine holders. Following coating no additional heat treatment was applied to any of the specimens. The creep specimens were coated in two batches. Batch 1 were alumina slurry grit blasted

before coating and batch 2 were chemically etched with sulphuric acid before coating.

The DB P92 fatigue specimens were also coated with the Co-Cr-C coating to a thickness of 34-37 μm around the entire circumference of the gauge length. The only areas not coated were the screw threads, which were masked off. Following coating no additional heat treatment was applied to any of the specimens. All of the fatigue specimens were prepared with a chemical etch pre-treatment (batch 2).

Figure 3.6 shows the coated P92 coupon (batch 1) following a short adhesion check heat treatment of 6 hours at 650 ºC. The coating is seen to deposit uniformly onto flat and curved samples with an even distribution of Cr_3C_2 throughout the coating. The coating shows good adherence with no evidence of porosity at the coating-substrate interface.

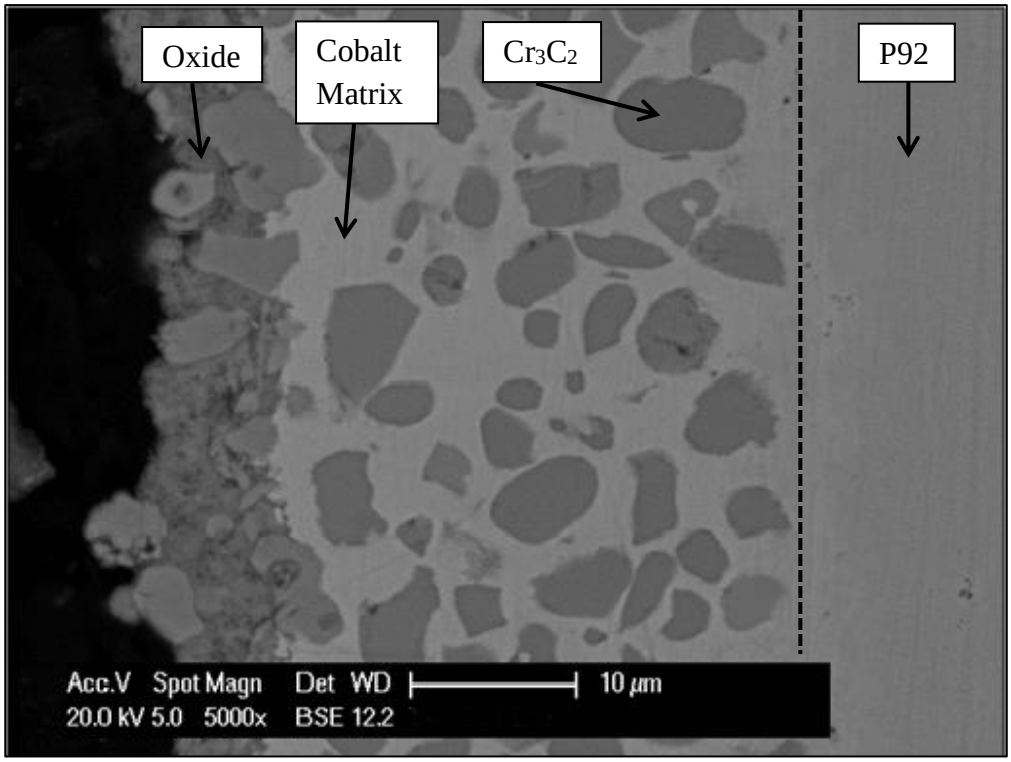

Figure 3.6: SEM micrograph to show the coated cross-section of the P92 coupon (batch 1) following a heat treatment of 6 hours at 650 ºC.

3.2.2.3 Co-Cr-C Free-Standing Coating

As well as the 34-37 µm coated P92 samples (coupons and mechanical specimens), a number of Co-Cr-C free-standing coating sheets were also prepared, with a thickness of ~ 1 mm. This sheet is primarily used to study evolution of the Co-Cr-C free-standing coating after oxidation.

In order to produce these samples a substrate of aluminium was initially used, with a dimension of approximately 150 x 70 x 5 mm. The same coating procedure as detailed above for P92 was used, however this time the coating process was allowed to run until approximately 1 mm of Co-Cr-C coating has been deposited. The samples were alumina grit blasted as a pre-treatment (batch 1) and did not receive additional heat treatment following coating.

The Co-Cr-C free-standing coating sheet can then be prepared from these large coated aluminium plates. Firstly the edge build up is removed using a standard silicon carbide abrasive cut off wheel. This reduces the amount of grinding that needs to be done and produces square sheets. The sheets were then ground on a magnetic flat bed grinder down to a uniform thickness of 1 mm. A diamond edged abrasive cutting wheel was then used to section the large sheet of coated aluminium into smaller square samples (20 x 20 mm). The samples with aluminium substrate are then placed into a vessel (5 litre beaker) containing 50 % solution of sodium hydroxide; this causes the aluminium to dissolve away by a simple exothermic reaction. The samples are stood upright in the beaker to ensure the maximum reaction area and a water jacket was used to cool the beaker. When the reaction is finished the Co-Cr-C free-standing coating samples are removed and rinsed with distilled water and IMS. The sample top surface is left in the as-plated condition (surface roughness of 1-2 µm) to be

consistent with the coated P92 samples. This is the surface that is used for any comparisons. For the free-standing sheet used for the oxidation kinetics study the samples were given a light grind on all faces with 1200 grit (15.3 µm) silicon carbide paper. This ensured a uniform oxidation surface on all faces.

Table 3.2: Oxidation conditions for Co-Cr-C free-standing coating study in air.

Sample Number	Temperature [ºC]	Exposure Duration [h]
1	650	96
2	650	240
3	650	288
4	650	336
5	700	96
6	700	168
7	700	240
8	700	336
9	750	72
10	750	168
11	750	240
12	750	336
13	650	2383
14	650	2691
15	650	3764
16	675	2659
17	700	1006

Table 3.3: Oxidation conditions for Co-Cr-C coated P92 coupon study in air.

Sample Number	Temperature [ºC]	Exposure Duration [h]
1	650	1377
2	650	1993
3	650	2383
4	650	2691
5	650	3764
6	675	2659
7	700	1006
8	700	1403

3.3 Oxidation Testing

Oxidation testing of the Co-Cr-C free-standing coating and Co-Cr-C coated P92 coupons is intended to simulate future operation conditions within fossil fuel power plant. Oxidation, microstructural evolution and inter-diffusion of the samples are then studied. Industrial sponsors for this research have provided invaluable industrial direction when selecting the precise conditions to use for this study. The majority of experimental facilities available for this work are limited to high temperature exposure in air, rather than steam. The literature for uncoated P92 suggests that oxidation mechanisms will be comparable but that in steam the oxidation will be more rapid [Laverde et al., 2004]. This is discussed in more detail in the discussion section of chapter 4.

The high temperature oxidation testing (tables 3.2 and 3.3) was performed using two different isothermal air furnaces (both using lab air). The short duration testing (96-336 hours), for the oxidation kinetics study of Co-Cr-C free-standing coating, was performed in an Elite BCF furnace at temperatures between 650 and 750 ^{o}C. The longer duration exposures (1000 hours +), for Co-Cr-C free-standing coating and Co-Cr-C coated P92 coupons, were performed by placing the samples within the free space in the top of the creep rig furnace. Therefore the durations of these samples were determined by the durations of the coated creep tests presented in chapter 6. This ensured the free-standing coating and coated coupons were exposed to exactly the same conditions as the coated creep tests. The oxidation test conditions for the Co-Cr-C free-standing coating and the Co-Cr-C coated P92 coupons are included in tables 3.2 and 3.3 respectively.

All samples were placed into the furnaces inside new clean recrystallized alumina crucibles. This ensured no contamination of the samples while in the furnace as well as ensuring that any spalled material was collected in the crucibles for examination after testing (high sided crucibles). The samples were orientated in the crucibles so that the maximum amount of coating area was exposed to the furnace conditions. In the case of Co-Cr-C coated P92 coupons this involved orientating the one coated face so that it was facing upwards. For the Co-Cr-C free-standing coating samples this involved placing the small thin samples into smaller round crucibles so that they would stand up on the thinnest edge, therefore exposing the maximum surface area. In all cases (all samples) the temperature was monitored using a thermocouple placed approximately 1 cm away from the sample. Once the test had finished the samples were allowed to cool down slowly within the furnace. This ensured there was no sudden thermal shock to the samples that could cause damage.

The Co-Cr-C coated P92 coupons (25 x 25 x 10 mm) were left in the as-coated state for oxidation testing as would be expected in service (1-2 μm finish). The Co-Cr-C free-standing coating samples (20 x 20 x 1 mm), not used for oxidation kinetics (1000 hours +), were also left in the as-coated condition to be consistent with the coated P92 samples (1-2 μm finish). The Co-Cr-C free-standing coating samples (20 x 20 x 1 mm), for oxidation kinetics study (96-336 hours), were ground down using the 1200 grit silicon carbide grinding paper (15.3 μm finish) to ensure a consistent oxidation surface on all faces. The samples for oxidation kinetics (96-336 hours) had their weight (± 0.0001 grams) and dimensions (± 0.01mm) accurately measured prior to testing. This would allow the oxidation kinetics to be accurately studied.

3.4 Mechanical Testing of Uncoated and Coated P92

3.4.1 Tensile Testing

Tensile testing was conducted on a MAYES universal 250 kN servo-hydraulic testing machine. The same specimen dimensions were used as for creep testing (figure 3.2). Tensile tests were performed by applying an increasing load until the specimen deformation was so large that the specimen failed. Failure was dominated by high ductility as the load caused the specimen to plastically deform. Tensile testing was performed on uncoated DB P92 to determine the yield stress, ultimate tensile stress and the modulus of the P92. It was a crucial test to perform before creep testing so that the ideal creep test regime could be approximated and appropriate stresses selected. The elastic and plastic regimes of the material could be determined by this testing. Tests have been performed at room temperature (20 ^{o}C), 650 and 675 ^{o}C, at a speed of ~ 0.1 mm/s for DB P92.

Heating of the specimen was provided by a three stage furnace which encloses the entire specimen length. The temperature was monitored by three thermo-couples attached to the test specimen in the middle and at either end; this ensures the temperature is consistent in each area of the furnace and therefore along the entire length of the sample. When the furnace was switched on it took approximately 2 hours for the furnace to reach temperature. During this time the machine was set to ensure that no load is applied, even as the sample expands at high temperature. Once the temperature had stabilised the tensile test could begin. The strain of the specimen was measured using high temperature extensometers attached to the ridges on the test specimens, shown in figure 3.2. The stress value was measured directly from the 250 kN load cell

in the form of voltage and could be converted to a stress value. Data was logged at 20 data points per second using a National Instruments data logger.

3.4.2 Uniaxial Creep Testing

Uniaxial creep tests have been performed at three different temperatures in air (lab air) for both the coated and uncoated samples (650, 675 and 700 ^{o}C). A range of stresses have been chosen to give failure times ranging from 165 (ductile failure)-3764 (brittle failure) hours. In all cases the coated creep testing has been a repeat of the conditions used for uncoated creep testing. This allows for any effect of coating application to be seen. Batch 1 and batch 2 tests have been conducted to assess the effect of pre-coating processing. The temperature and stress conditions for uncoated and coated tests are given below in table 3.4.

Table 3.4: Uncoated and coated P92 creep test parameters.

Temperature [^{o}C]	**Stress [MPa]**	**Uncoated**	**Coated – Batch 1**	**Coated – Batch 2**
650	105	✓	✓	
650	110	✓	✓	✓
650	120	✓	✓	
650	130	✓		
650	140	✓		
675	80	✓	✓	✓
675	90	✓	✓	
675	100	✓	✓	
700	65	✓	✓	
700	70	✓	✓	
700	75	✓		
700	80	✓		

The uniaxial creep tests have been performed using a Denison creep testing machine, which is made up of a basic frame with a 2 x 2 m ‘L-shape’. This

frame basically consists of a vertical section made up of four vertical columns, which houses the furnace and specimen holder, and a horizontal section that contains the lever system that is responsible for applying the load to the specimen. All Denison creep testing machines at the University of Nottingham are situated within a temperature controlled laboratory to ensure no environment effects are seen on the frame. The specimen was screwed into the holder within the furnace and allowed to heat up before any load was applied. Once the temperature had stabilised the constant load could be applied by attaching the load bar. This heat up period usually took around 2 hours meaning the specimen experienced a short heat treatment before any load was applied. During this time some slight alloying of the composite coating will begin to occur and also inter-diffusion with the P92 substrate. This is likely to be beneficial to the coating as it will allow for good adherence before the load is applied. This is representative of the heat up time when re-starting a power plant following an outage [Chalk, 2013].

Constant tensile stress was applied to the specimen in the uniaxial direction of the specimen axis. The temperature was maintained by a three stage furnace that completely covered the specimen length. Temperature was controlled and monitored throughout the test using three thermo-couples attached to the specimen. Thermocouples were attached to the middle of the specimen and at either end. This ensured that the temperature of the specimen in all three areas of the furnace was constant. The strain over the gauge length of the specimen was measured using high temperature extensometers that were attached to the specimen via the specimen ridges shown in figure 3.2, these ridges prevented slipping of the extensometers during the test. The data from the extensometers

was logged at regular intervals using a National Instruments data logger. During the steady state (secondary creep) part of the creep test, where the test spends most of its duration, the data was logged at 1 data point per 15 minutes as the strain was varying very slowly, therefore limiting the computing power that was needed during this part of the test. During the primary and tertiary stages this data collection speed was increased to 1 data point per second. This was important in order to accurately record the rapid changes in strain during the early (primary) and late stages (tertiary) of the creep test.

3.4.3 Low Cycle Strain Controlled Fatigue Testing

LCF usually refers to the total number of cycles to failure being less than 10,000. The LCF tests were also performed on a MAYES universal 250 kN servo-hydraulic testing machine, with fatigue specimen dimensions shown in figure 3.3. The test conditions for uncoated and coated testing are summarised in table 3.5.

The fatigue testing has been performed at 650 ^{o}C (isothermal for the duration of the test), where the heating was provided by a three stage furnace and temperature monitored by three thermo-couples attached to the specimen in the middle and at either end. The specimen was again screwed into the holder within the furnace and the temperature allowed to stabilise before any load was applied. Therefore, as for the creep specimens, the fatigue specimens also received an approximately 2 hour warm up heat treatment. The testing was performed in strain controlled mode, where the strains were monitored by high temperature extensometers clamped to the specimen gauge. The test started at zero strain and took the specimen to the required strain percentage, then

immediately it returned back to zero strain, all at the given strain rate. This is defined as one loop and this loading was repeated until the specimen failed or there was greater than a 50 % stress drop. The stress required to achieve the given strain percentage decreased with each cycle until the sample failed. An example loading wave form for three consecutive loops at 0.3 % strain is included below in figure 3.7. Before testing the alignment of the loading bars was verified to ensure no bending would occur during testing. The load bars used were also made from super-alloy materials and were manufactured to have a much larger diameter than the fatigue test specimen. The stress and strain data was logged using a National Instruments data logger connected to the load cell and high temperature extensometers (logging rate of 20 data points per second).

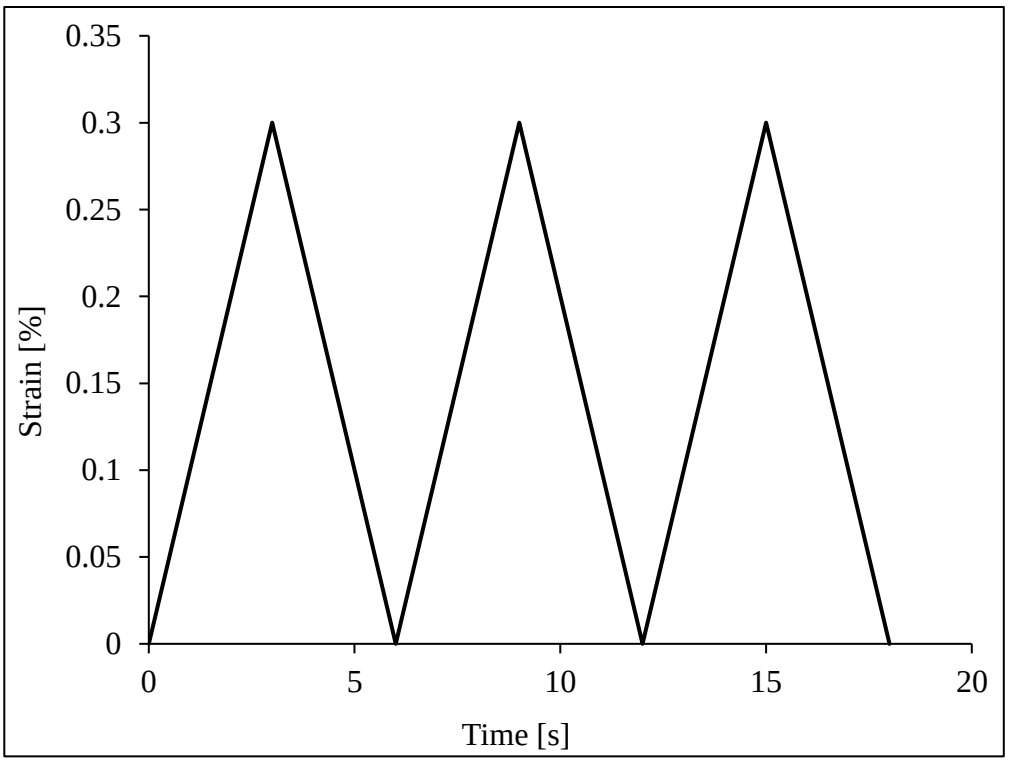

Figure 3.7: Loading sequence for 0.3 % strain fatigue test (test 1 – table 3.5).

3.4.4 Low Cycle Strain Controlled Creep-Fatigue Testing

Low cycle creep-fatigue interaction testing (table 3.6) has also been performed (uncoated and coated) using the same MAYES 250 kN machine. The same test specimens and strain controlled operation as the fatigue testing has been used. The only difference between this and pure fatigue in section 3.4.3 is that a dwell period was included at the peak tensile loading. This was more industrially relevant as it simulates a more typical power plant loading cycle (e.g. start up and shut down). An example loading sequence is included in figure 3.8 for one cycle. The main focus of this testing has been to investigate the effects of different dwell times (600, 1200 and 2400 seconds) at 0.3 % strain and 650 ^{o}C. Also the affect coating application has was also considered.

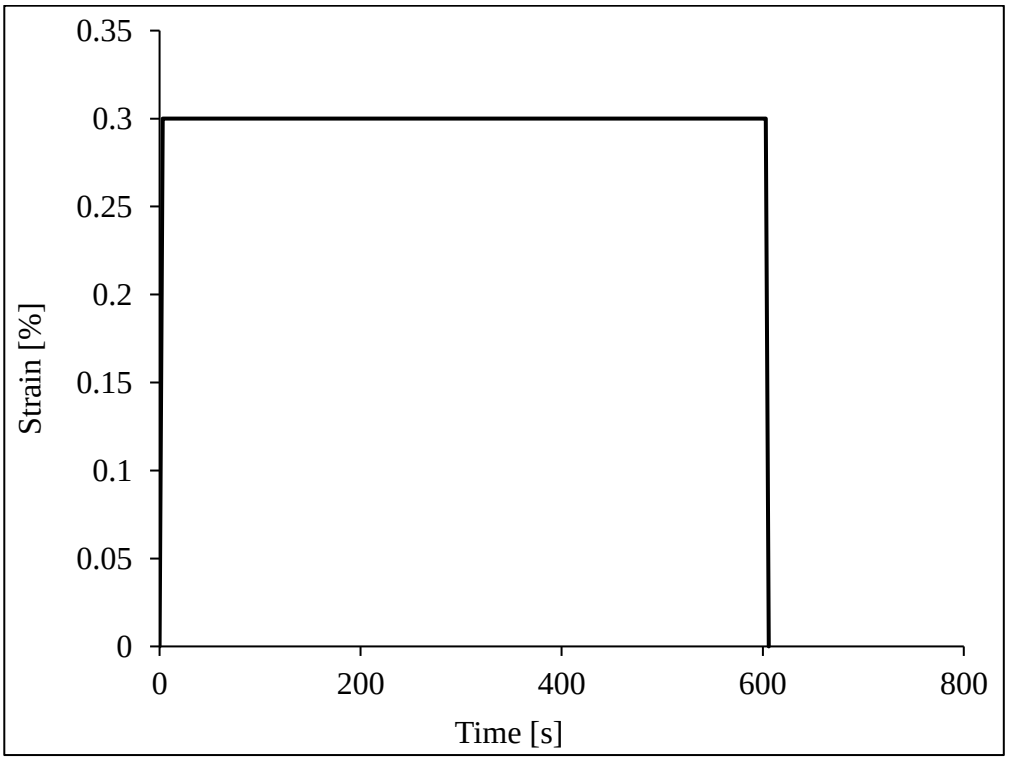

Figure 3.8: Loading sequence for 0.3 % strain creep - fatigue test with a 10 minute dwell time at peak tensile (test 1 – table 3.6).

Table 3.5: A summary of the uncoated and coated P92 fatigue testing conditions.

Test	Temp [°C]	Strain [%]	Cycle Time [s]	Strain Rate [%/s]	Uncoated	Coated
1	650	0.3	6	0.1	✓	✓
2	650	0.4	8	0.1	✓	
3	650	0.5	10	0.1	✓	

Table 3.6: A summary of the uncoated and coated P92 creep-fatigue testing conditions.

Test	Temp [°C]	Strain [%]	R_f	Cycle Time [s]	Strain Rate [%/s]	Dwell Time [s]	Uncoated	Coated
1	650	0.3	0	606	0.1	600	✓	✓
2	650	0.3	0	1206	0.1	1200	✓	✓
3	650	0.3	0	2406	0.1	2400	✓	

3.5 Microstructural Characterisation Methods

3.5.1 X-Ray Diffraction (XRD)

XRD is a standard technique for analysing phases present within materials. In this case it has been used to identify the phases within the coating material and the oxide formed on the coating. It is a powerful analytical technique that not only identifies the phases but when combined with SEM and EDX analysis can also give information about the spatial distribution of specific phases that are present. In an XRD, a beam of X-rays strike a crystal and constructively diffract according to Braggs Law:

$$n\lambda = 2d_{ps}\sin\theta \qquad \text{[Equation 3.1]}$$

In equation 3.1, n is an integer, λ is the incident wave wavelength, d_{ps} is the plane spacing and θ is the angle between the incident angle and the scattering angle. By analysing the angles and the intensities of the diffracted beams the crystal structure and therefore the phases within the material can be determined [Hussain, 2011; Callister and Rethwisch, 2007; Cullity and Stock, 2001].

The particular machine used for this work was a Siemens D500 diffractometer with monochromatic Cu-K_α radiation. Peak and phase identification was performed using the EVA diffraction software. This software works on the theory that a given phase will always produce a characteristic pattern which is unique to that phase. The software compares the 2θ positions and intensities obtained by the XRD diffractometer to the ICDD database of diffraction patterns for known phases [Hussain, 2011]. When XRD data is presented in the results chapters the specific ICDD entry used for identification of particular phases is referenced. Specific details of the published diffraction data are included in appendix A. X-ray penetration depth for the coating bulk and associated oxide phases is included in appendix B. The specific XRD scan conditions used for the Co-Cr-C free-standing coating samples and Co-Cr-C coated P92 samples are summarised in table 3.7.

3.5.2 Sample Preparation

The main aim of the microstructural examination was to assess the integrity of the coating samples following high temperature oxidation and mechanical testing. To begin with XRD and SEM imaging of the oxidised sample surfaces were performed. This testing required no sample preparation and the samples were examined in the oxidised state. It was important to perform this testing

first before any potential damage was caused to the oxidised surface. Carbon coating was required on oxidised samples to limit surface charging in the SEM. Cross-sectioned samples were also of interest to this study. For Co-Cr-C coated P92 coupons and Co-Cr-C free-standing coating samples, this meant the oxidised samples were cut in half to reveal a coating-oxide and coating-substrate cross-section. For the failed mechanical samples it was often desirable to cut circular cross-sections from along the gauge length of the failed samples (perpendicular to the applied stress direction). Care was taken to ensure that the position of samples from along the gauge length of the specimen was recorded so that any strain effects could be studied, as illustrated in figure 3.9. Generally cross-sections were taken on the gauge length as far away from the fracture surface as possible to minimise fracture surface effects. Cutting was performed using a diamond abrasive cut off wheel (Struers diamond cut-off wheel), cut at a speed of 0.005 mm/s and cooled with water/cooling fluid.

Table 3.7: XRD scan conditions for the samples studied in chapters 4 and 7.

Sample	**Range of Angles (2θ) [^{o}]**	**Step Size [^{o}]**	**Step Time [s]**
Co-Cr-C Free-standing Coating - **Oxide**	10 - 60	0.020	4
Co-Cr-C Free-standing Coating - **Bulk**	25 - 60	0.020	16
Co-Cr-C Coated P92 Coupon - **Oxide**	10 - 60	0.020	4
Co-Cr-C Coated P92 Coupon - **Bulk**	25 - 60	0.020	16
Failed Coated Creep Specimen - **Oxide**	10 - 60	0.020	4

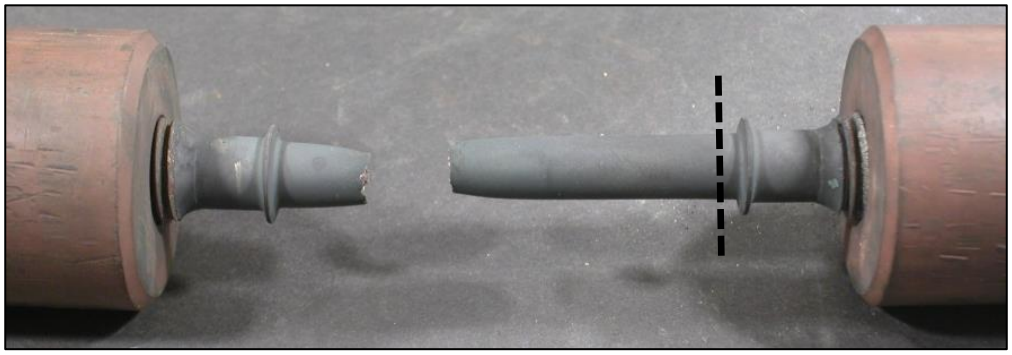

Figure 3.9: Schematic to show the position (dotted line) on the failed creep specimen where circular cross-sections were taken from.

It was necessary to protect the oxidised samples prior to cutting to prevent oxide damage. The technique used was to mount all of the exposed samples in a cold set epoxy resin before cutting. The resin needed to cover all oxidised faces of interest. This resin then protected the potentially delicate oxide layers during the cutting process. A cold set-resin was desirable as this minimises resin shrinkage during curing, which could further damage the oxide. In this particular case the epoxy resin was mixed with ballotini glass spheres in a 50:50 ratio, as the ballotini glass further reduces the potential for shrinkage during curing. Another method to protect the oxidised layer could have been to nickel plate the samples prior to cutting.

The resin mounted and cut samples could then be polished back using subsequently finer silicon carbide grit papers, from 240 (58.5 μm)-1200 (15.3 μm) grit. The surfaces were then polished using 6 and 1 μm diamond wheels until a mirror finish was obtained on the metal surface. When high resolution electron microscopy was required the samples were then given a final stage polish using 0.025 μm colloidal silica solution for ~ 30 minutes. Samples were

cleaned with distilled water and IMS between each polishing stage and prior to microscopy.

Chemical etchants could then be used, where appropriate, to further reveal the microstructure of the materials being examined. Etchants work by selectively dissolving certain parts of a sample surface (i.e. grain boundaries), this results in a change in the surface topography that can be observed using microscopy [Callister and Rethwisch, 2007]. For this work the P92 has been etched to observe the effects of inter-diffusion on the P92 substrate microstructure. An extensive range of etchants and conditions were considered until a suitable etchants was found [Chalk, 2015]. The P92 steel microstructure was best exposed for microscopy when etched using Vilella's reagent. This is a mixture of 1 g picric acid, 5 mL hydrochloric acid and 100 mL of ethanol. Exposures times varied from 10-60 seconds depending on the variation between etchant batches. Samples were cleaned with distilled water and IMS following etching. Etching showed no evidence of damaging the oxidised layers on samples.

For SEM imaging it was often desirable to carbon coat the mounted, polished and etched samples to reduce the effects of surface charging. This was particularly important when studying oxidised samples as the oxide was much less conductive than the coating and substrate bulk. If further sample grinding or polishing was required the carbon coating can be easily removed on the 1 µm diamond polishing wheel.

3.5.3 Optical Microscopy (OM)

Once samples had been mounted and etched, as described above, they could be examined using a Nikon Eclipse LV100ND optical microscope. This

microscope used a series of objective lenses, ranging for 5 x to 100 x, thus allowing small and relatively large features to be examined. OM was primarily used to observe the martensitic structure of P92 and any large features in the P92 or coating. The microscope was linked to a PC allowing digital images of the samples to be recorded [Clark, 2015].

3.5.4 Scanning Electron Microscopy (SEM)

The majority of SEM was performed using a Phillips FEI XL-30 W. The electron source was provided by a tungsten filament. This machine gave very high quality imaging and resolution which allowed features on the micron scale to be resolved. A small amount of work was performed on a Phillips FEI XL-30 ESEM. This machine was equipped with a FEG electron source.

An SEM works by accelerating an electron beam onto the surface of a sample in vacuum [Callister and Rethwisch, 2007; Reimer, 1998; Chescoe and Goodhew, 1990; Gabriel, 1985]. Electrons are created using either a tungsten filament or a FEG. The beam is then converged using a series of lenses and will be rastered across the surface of the sample. The electrons will interact with the surface of the material in a number of ways, the most useful of which is when the electrons penetrate the surface and travel into the surface layers of the sample. The interaction volume will balloon below the surface as the electrons interact with the sample. Different parts of the interaction volume will cause different types of emission. The most useful emissions for this work are: inelastically scattered electrons, elastically scattered electrons and x-rays. Three different detectors are used in a SEM to detect the three different emissions.

3.5.4.1 Secondary Electrons (SE)

The standard imaging mode in an SEM is SE imaging. The SE detector mainly picks up inelastically scattered electrons which interact with the surface; this means that SE mode is most useful for giving surface and topographical information. Differences in contrast will be due to differences in the height of the sample surface [Reimer, 1998].

Secondary electron imaging has predominantly been used to study etched samples of coated P92 as well as the topography of oxidised top surfaces. It is particularly useful for imaging porosity and cracking. Typically an accelerating voltage of 20 kV would be used along with a spot size of 4 and a working distance of 10 mm [Clark, 2015].

3.5.4.2 Backscattered Electrons (BSE)

The BSE detector is used to detect electrons that have interacted elastically with the sample; this means that most of the electrons are detected following interactions in the sub-surface of the material. The contrast in a BSE image is mainly a result of local atomic mass, but also the surface topography and other diffraction factors [Reimer, 1998]. Phases with a higher mean atomic number will appear brighter in BSE imaging mode.

BSE imaging has mainly been used to examine polished samples of coated P92 and Co-Cr-C free-standing coating to identify phases of different atomic number. It can be used to study the coating and substrate bulk as well as oxide features. Typically an accelerating voltage of 20 kV would be used along with a spot size of 4 and a working distance of 10 mm [Clark, 2015].

3.5.4.3 Energy Dispersive X-Ray Spectroscopy (EDX)

When an electron interacts with an atom often this can result in an electron being ejected from an orbital shell. When an electron is ejected from a lower energy orbital shell a higher level electron will drop down to fill the gap and restore equilibrium. When this happens an X-ray is emitted, with an energy equal to the difference in energy between the orbital shells. As such this X-ray is characteristic and unique to a particular element. Therefore if the energy of these X-rays is detected then this can be used to determine the local elemental composition of a sample. This is the principle of EDX which uses a detector to measure the energy of these X-rays and calculate elemental compositions for analysis [Clark, 2015; Gabriel, 1985].

EDX analysis is an incredibly useful tool and has been used extensively throughout this work. Primarily it has been used to measure elemental composition, in the P92, coated P92 and the Co-Cr-C free-standing coating material. Selected area analysis has been used for individual measurements with an area approximately 5 x 5 µm. This is more accurate that point analysis as it provides an average composition of the analysis area and limits effects of local variation.

Elemental profiles across coating-substrate interfaces were also measured using EDX selected area analysis with analysis areas chosen with dimensions ~ 50 x 2 µm, spaced at least 2 µm apart. For example, for a 50 µm wide coating-substrate region approximately 10-20 measurement areas would be performed. The analysis area in the coating would span the two phase carbide - matrix region. This was important to give accurate chromium values for the coating as a whole rather than just the matrix. For interface profiling measurements were

simplified to just cobalt, chromium and iron as minor additions could not be detected in sufficient quantities to observe diffusion.

When elemental compositions of phases or features are stated in the thesis they are taken from at least ten separate EDX measurements with a mean and standard deviation being calculated. Standard deviation can be useful to indicate the variability or consistency of certain phases. The mapping tool has also been a useful qualitative tool and has allowed for distinct layers in oxides or the IDZ to be identified. As mentioned previously, EDX can be used in combination with XRD to give more detail on the spatial distribution of phases within a system.

The main limitations of EDX are that at high accelerating voltages the resolution is limited because the interaction volume is large and therefore the ballooning below the surface is large. This means it is difficult to identify an accurate elemental profile for features much smaller than 5 μm. EDX also cannot accurately measure carbon content because of carbon contamination in the vacuum system and the small atomic number of carbon [Clark, 2015].

3.5.5 Micro-Hardness

To measure P92 micro-hardness a load was applied to a polished but un-etched P92 sample (1 μm polished finish) using a diamond indenter. The size of the indent could then be measured; if this information was combined with the load applied and the time of indentation the hardness of the particular material can then be calculated [Callister and Rethwisch, 2007]. For this work a Buehler MMT-7 digital micro-hardness tester was used. The Vickers indenter was used, with a 200 gf load and a 15 second dwell time for P92. In order to ensure

reliable results a number of repeats (at least 10 individual measurements) were performed for each material or region of a material, special care was taken to ensure that subsequent indents were spaced at least four indent diameters apart. This ensured that no local deformation caused by a previous indent affects subsequent measurements [Clark, 2015].

The Co-Cr-C free-standing coating was also tested to determine the micro-hardness of the bulk coating. The same testing procedure as described above was used, however this time it was important that the indent size used was large so a high load was used. Because the coating is a composite material made up of hard Cr_3C_2 particles (5-10 µm in diameter) within a relatively soft cobalt matrix it was important the indent size was much larger so that the bulk behaviour was measured and the effect of local variation of carbides and matrix was reduced. Therefore this time a load of 1000 gf was used with a 15 second dwell time. This gave an average indent diameter of 60 µm. Multiple indents (at least 10) were again taken and were spaced at least four indent diameters apart.

3.6 Summary

The experimental methods described in this section have been applied to the P92 substrate and the Co-Cr-C coating material described at the start of this chapter. The results are presented in chapters 4, 5, 6 and 7.

The mechanical testing allows for a detailed understanding of how coating deposition affects the mechanical performance of the substrate. The microstructural characterisation allows for a thorough understanding of the

microstructural and chemical evolution of the coating-substrate system during thermal and mechanical loading.

The Thermo-Calc CALPHAD modelling methodology has been presented in appendix C of this thesis. Primarily it was used to compliment the experimental testing.

CHAPTER 4

EFFECT OF HIGH TEMPERATURE OXIDATION ON THE CO-CR-C FREE-STANDING COATING

4.1 Introduction

The literature review presented in chapter 2 highlighted the need for an oxidation resistant coating to be applied to the inside surface of P92 pipework, to prevent steam oxidation damage at > 600 ºC. Chapter 2 suggested the electro-plated Co-Cr-C coating as a promising coating for investigation.

Therefore the aim of this chapter was to introduce the Co-Cr-C coating by studying samples of the Co-Cr-C free-standing coating. This chapter studied the oxidation behaviour and the microstructural evolution of the coating following high temperature oxidation in air.

This chapter contains two main sections. Firstly, section 4.2, presents the as-coated samples and phase equilibria. Secondly, section 4.3, presents the Co-Cr-C free-standing coating study following high temperature isothermal oxidation

in lab air at various temperatures. A discussion of the findings is included in section 4.4.

4.2 Co-Cr-C Phase Equilibria and Microstructure

4.2.1 As-Deposited Microstructure of the Free-Standing Coating

XRD analysis of the Co-Cr-C free-standing coating in the as-coated condition, shown in figure 4.1, identifies the chromium carbide phase as Cr_3C_2 and the matrix phase as FCC cobalt. Appendix B approximates the x-ray penetration depth in the coating as 1.02-2.35 μm.

Figure 4.2 shows an SEM micrograph of the as-coated Co-Cr-C free-standing coating. This shows there is a uniform distribution of Cr_3C_2 particles within the cobalt matrix, with particles typically 5-8 μm in size. There appears to be no evidence of cracking or porosity within the coating. The areas that appear black are probably areas of particle pull-out or carbide damage as a result of the polishing process. Two distinct phases can be seen, namely, the Cr_3C_2 phase (darker contrast particles) and the cobalt matrix phase (lighter contrast phase). Image analysis, using ImageJ software, shows that the coating has 37.6 ± 1.8 wt % Cr_3C_2 content when 10 separate SEM micrographs are analysed. The volume percentage was measured and then converted to weight percentage using the density of Cr_3C_2 and cobalt. When calculated using the stoichiometric composition of Cr_3C_2 the coating composition is 62.3 wt % Co, 32.6 wt % Cr and 5.0 wt % C and is summarised in table 4.1. The Vickers micro-hardness of the coating, with a 1000 gf load, is 466 ± 16 HV.

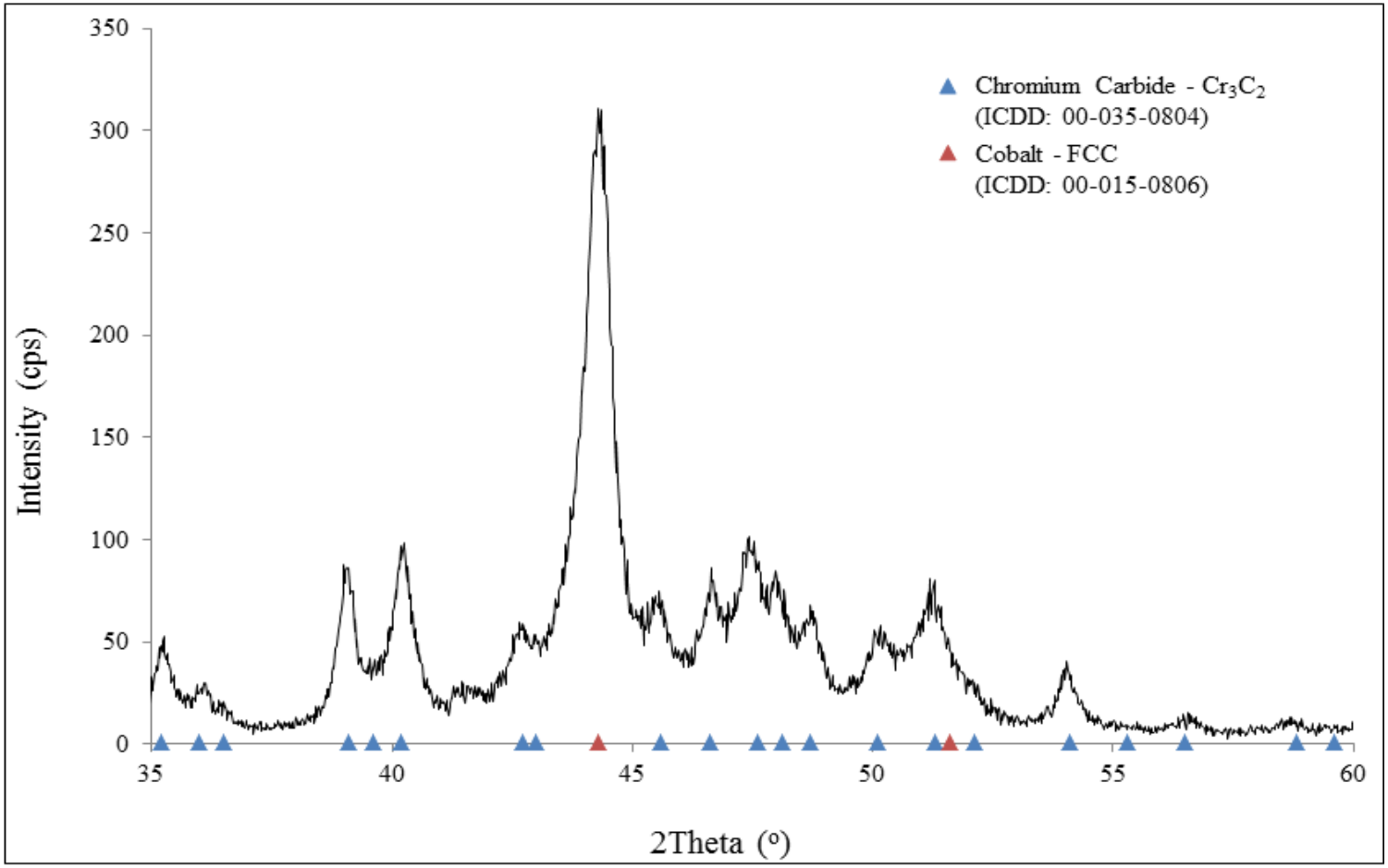

Figure 4.1: XRD pattern from the Co-Cr-C free-standing coating.

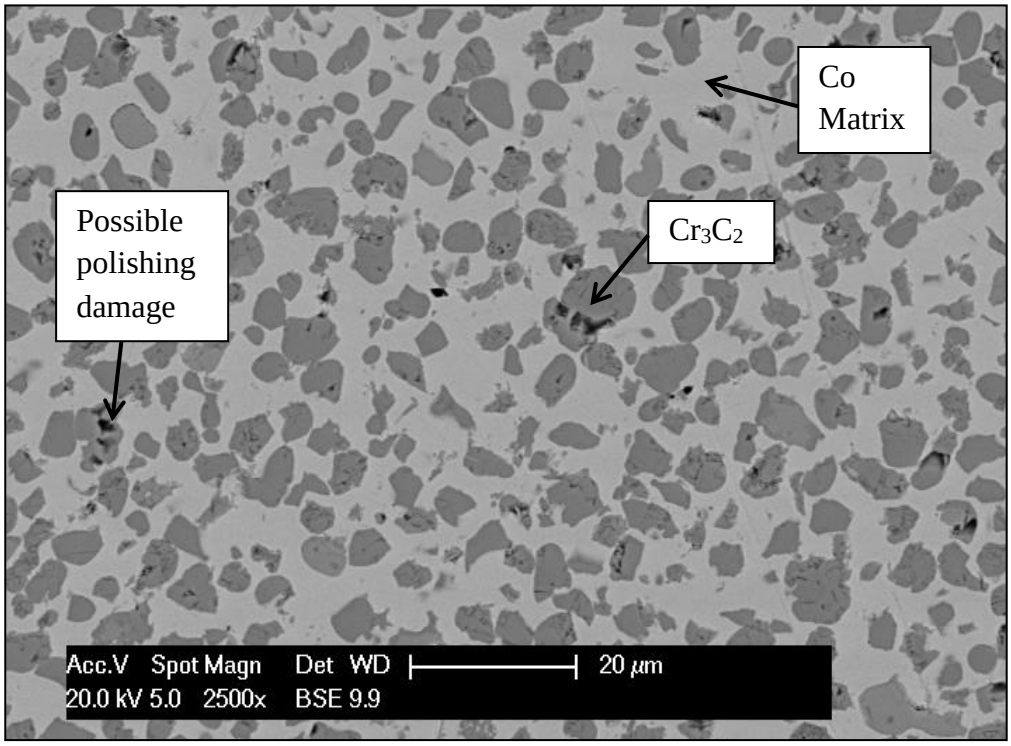

Figure 4.2: SEM micrograph of the Co-Cr-C free-standing coating.

4.2.2 Co-Cr-C Phase Equilibria

Table 4.1 shows the composition of the Co-Cr-C free-standing coating in mass percentage and mole fraction. These values were used in all the thermodynamic calculations. Figure 4.3 shows the ternary phase diagram for the Co-Cr-C system at 650 ^{o}C obtained using Thermo-Calc software and the SSOL5 database. The black symbol indicates the Co-Cr-C coating composition (table 4.1) on the diagram. This shows that the phases predicted to be present in the Co-Cr-C coating at 650 ^{o}C are: FCC-Co, M_3C_2 and M_7C_3. The M_3C_2 and M_7C_3 refer to the Cr_3C_2 and Cr_7C_3 based phases, whilst the FCC is the cubic form of cobalt. In fact the composition of the coating is shown to lie very close to the Co-M_3C_2 tie line and only a small proportion of M_7C_3 might be expected at equilibrium. If the carbon fraction is reduced then the lower carbon versions of

the chromium carbide start to become the dominant carbide phases (Cr_7C_3, $Cr_{23}C_6$).

A phase fraction versus temperature diagram was also calculated using the specific coating composition given in table 4.1. Figure 4.4 shows that under equilibrium conditions the phase fraction of M_3C_2 is gradually reducing between 500-735 ^oC whilst M_7C_3 is gradually increasing. Then after 735 ^oC the M_3C_2 experiences a transformation to M_7C_3 and graphite forms. Overall the coating phases of FCC-Co and Cr_3C_2 are predicted to be stable at around 600-700 ^oC, which is the likely future operation temperature.

Table 4.1: Co-Cr-C coating composition calculated from SEM image analysis.

Elemental	Mass-Percentage [%]	Mole-Fraction
Co	62.3	0.504
Cr	32.6	0.298
C	5.0	0.198

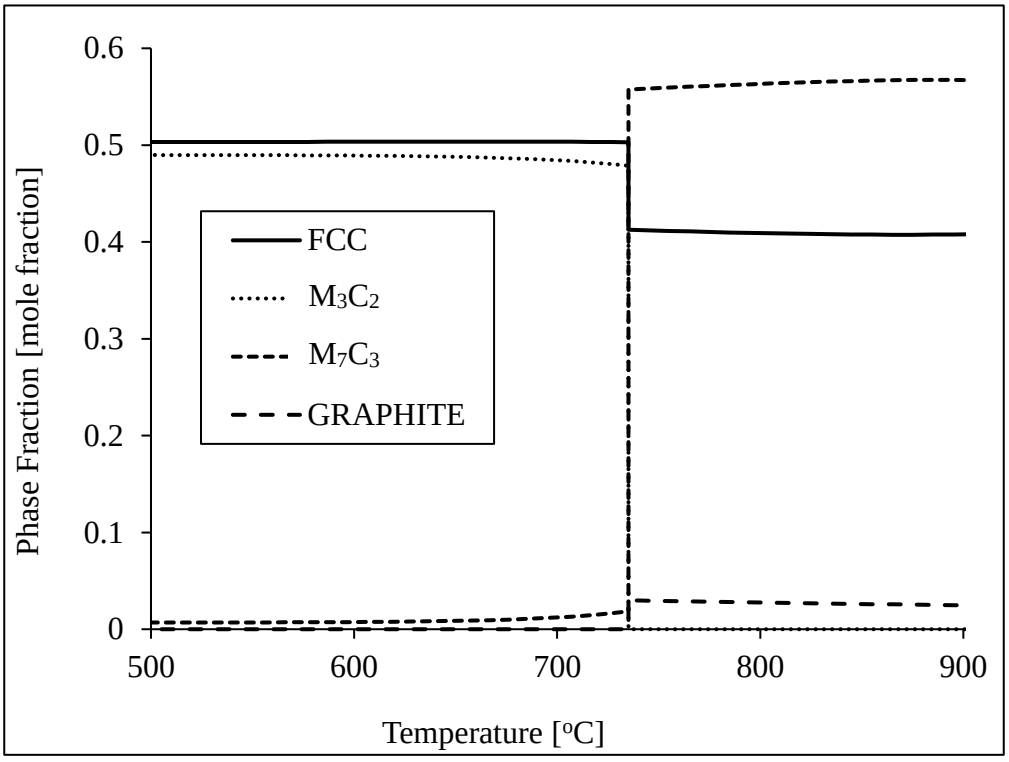

Figure 4.4: Phase mole fraction diagram for Co-Cr-C free-standing coating.

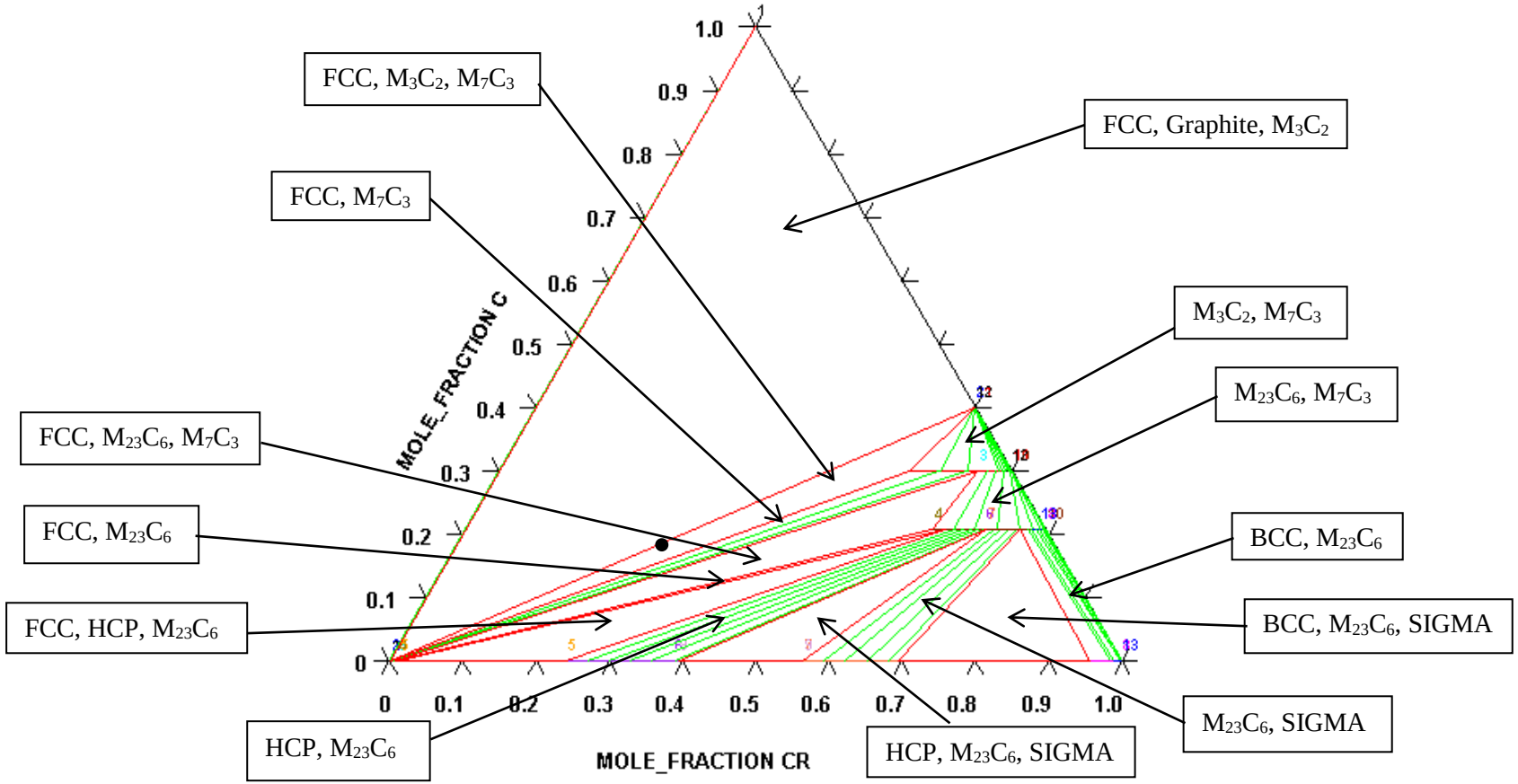

Figure 4.3: A ternary isothermal section, plotted in mole fraction, for the Co-Cr-C system at 650 ^{o}C. The black symbol indicates the Co-Cr-C free-standing coating composition (table 4.1) on the diagram.

4.3 Co-Cr-C Free-Standing Coating Study

This section of the chapter considers the experimental characterisation of the Co-Cr-C free-standing coating following isothermal high temperature oxidation in air.

4.3.1 Oxidation Kinetics

To evaluate the oxidation kinetics of the coating a series of isothermal oxidation experiments were performed in lab air. A list of the experiments is given in table 4.2, as from the experimental methods (table 3.2, chapter 3).

Table 4.2: A summary of the oxidation tests performed in air to study the oxidation kinetics of the Co-Cr-C free-standing coating.

Sample Number	Temperature [^{o}C]	Exposure Duration [h]
1	650	96
2	650	240
3	650	288
4	650	336
5	700	96
6	700	168
7	700	240
8	700	336
9	750	72
10	750	168
11	750	240
12	750	336

The Co-Cr-C coating reacted with the oxygen in air to form a thin external oxide scale on its surface. The samples gained weight as a result of this for a given oxidation time; weight gain per unit area versus time is presented in

figure 4.5. A parabolic rate law is used to fit to the oxidation kinetics of the Co-Cr-C coating. The oxidation of metals can be represented by the rate equation:

$$x_m{}^2 = k_p t + C_o \qquad \text{[Equation 4.1]}$$

In equation 4.1, k_p is the parabolic rate constant, x_m is the weight gain per unit area (g/cm^2), t is the time (s) and C_o is a constant (usually assumed to be zero) [Birks et al., 2006]. When plotted, as in figure 4.6, the gradient of the best fit line (table 4.3) provides the parabolic rate constant, k_p, which is a direct representation of the rate of oxidation for each temperature. The k_p values at 650-750 ^{o}C are given in table 4.4 in units of g^2.cm^{-4}.s^{-1}.

Table 4.3: Gradient ($\sqrt{k_p}$) and R^2 values for the fitting in figure 4.6.

Temperature [^{o}C]	Gradient [g.cm^{-2}.s$^{-1/2}$]	R^2
650	2.95 x 10^{-6}	0.990
700	4.31 x 10^{-6}	0.978
750	5.06 x 10^{-6}	0.991

Table 4.4: Parabolic rate constant, k_p, for the Co-Cr-C free-standing coating at 650, 700 and 750 ^{o}C, following isothermal oxidation in air.

Temperature [^{o}C]	Parabolic Rate Constant, k_p [g^2.cm^{-4}.s^{-1}]
650	8.70 x 10^{-12}
700	1.86 x 10^{-11}
750	2.56 x 10^{-11}

Table 4.4 shows that the oxidation rate at 650 ^{o}C has the lowest k_p value and the rate at 750 ^{o}C is the highest. The rate constant, k_p, is found to vary according to the Arrhenius type equation:

$$k_p = A_f \exp(-\frac{Q}{RT}) \quad \text{[Equation 4.2]}$$

In equation 4.2, A_f is the frequency factor constant, Q is the activation energy of the reaction, R is the gas constant and T is the temperature in Kelvin [Birks et al., 2006]. Taking the natural logarithms of both sides of equation 4.2:

$$lnk_p = lnA_f - (\frac{Q}{RT}) \quad \text{[Equation 4.3]}$$

When a graph of lnk_p against $1/RT$ is plotted the slope of the line will be equal to –Q, as shown in figure 4.7. Figure 4.7 shows that the activation energy of the Co-Cr-C coating oxidation is 85.3 kJ/mol and $R^2 = 0.9599$.

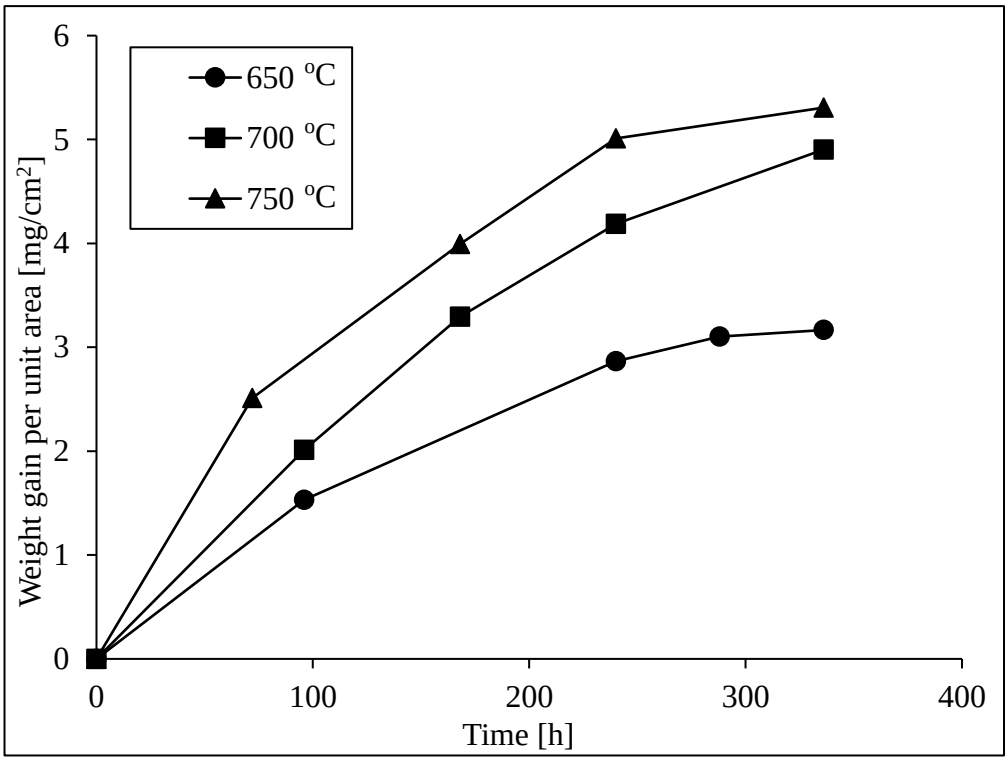

Figure 4.5: Weight gain per unit area versus time for the Co-Cr-C free-standing coating samples following oxidation in air at 650, 700 and 750 °C.

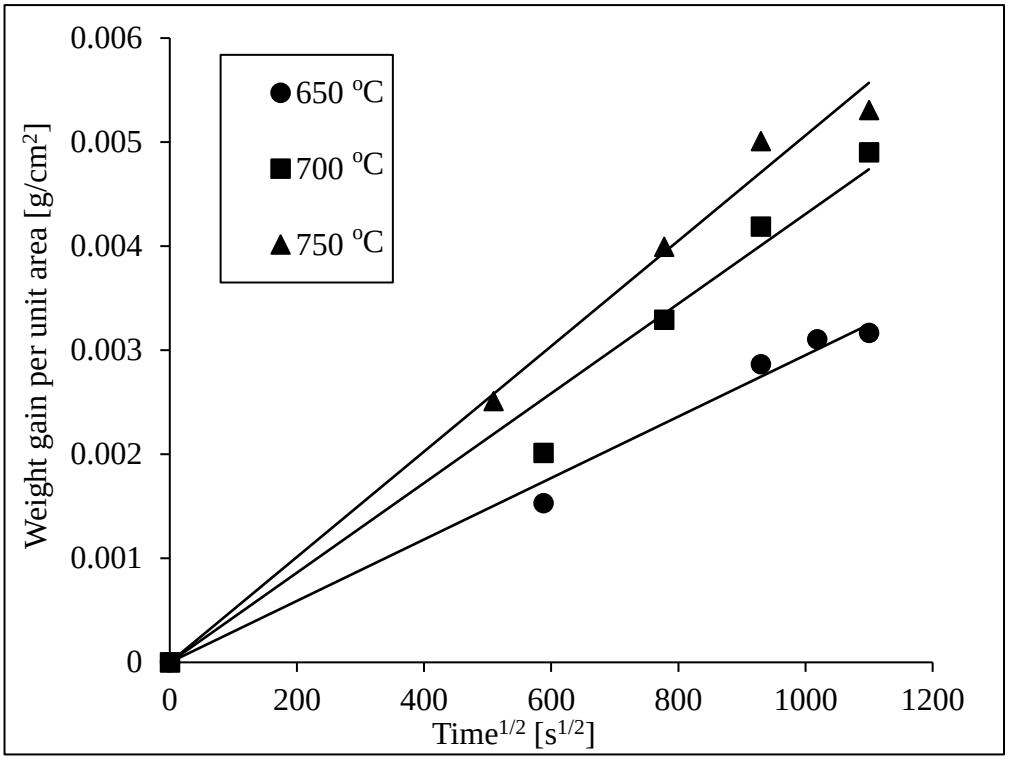

Figure 4.6: Weight gain per unit area versus square root time for the Co-Cr-C free-standing coating samples following oxidation in air at 650, 700 and 750 °C.

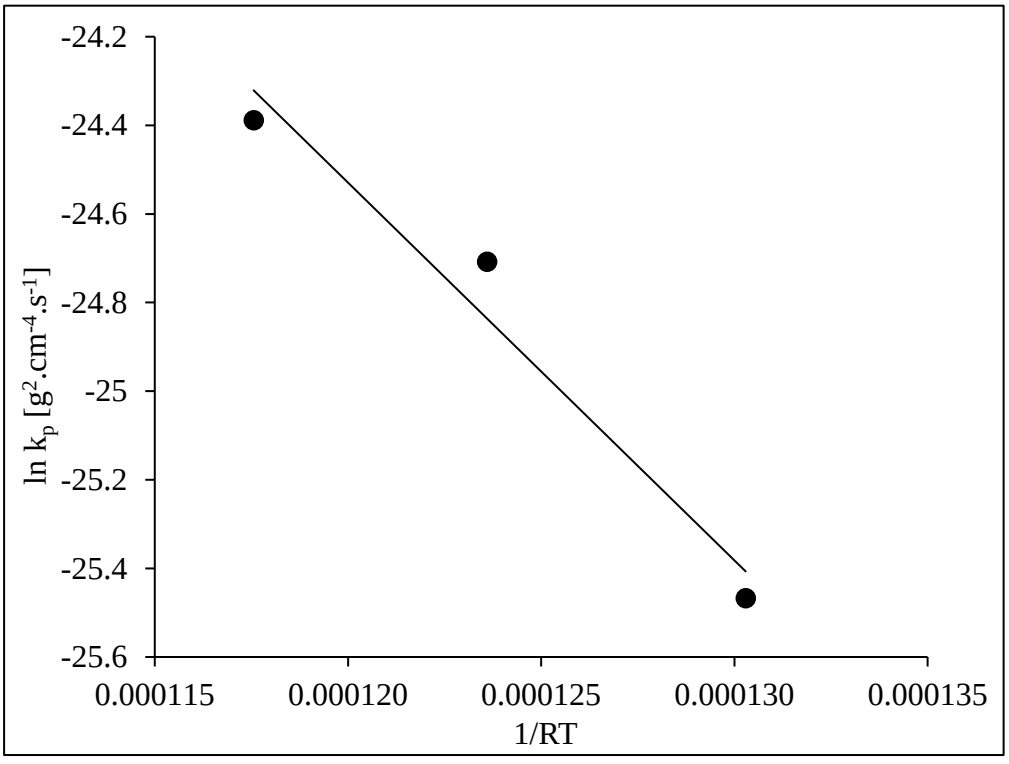

Figure 4.7: Arrhenius plot for oxidation of the Co-Cr-C free-standing coating.

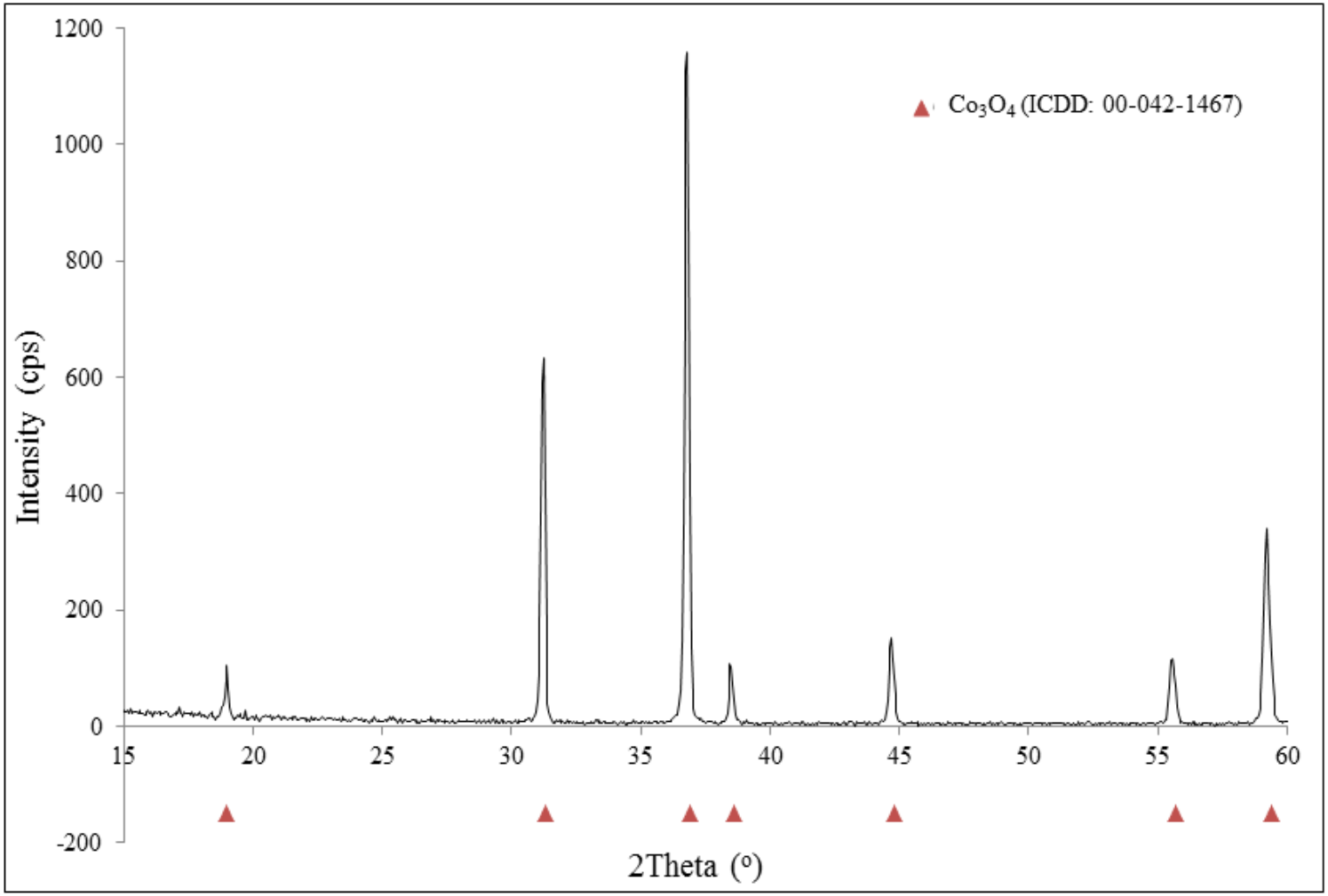

Figure 4.8: XRD pattern obtained from the top oxidised surface of the Co-Cr-C free-standing coating exposed for 288 hours at 650 ºC in air.

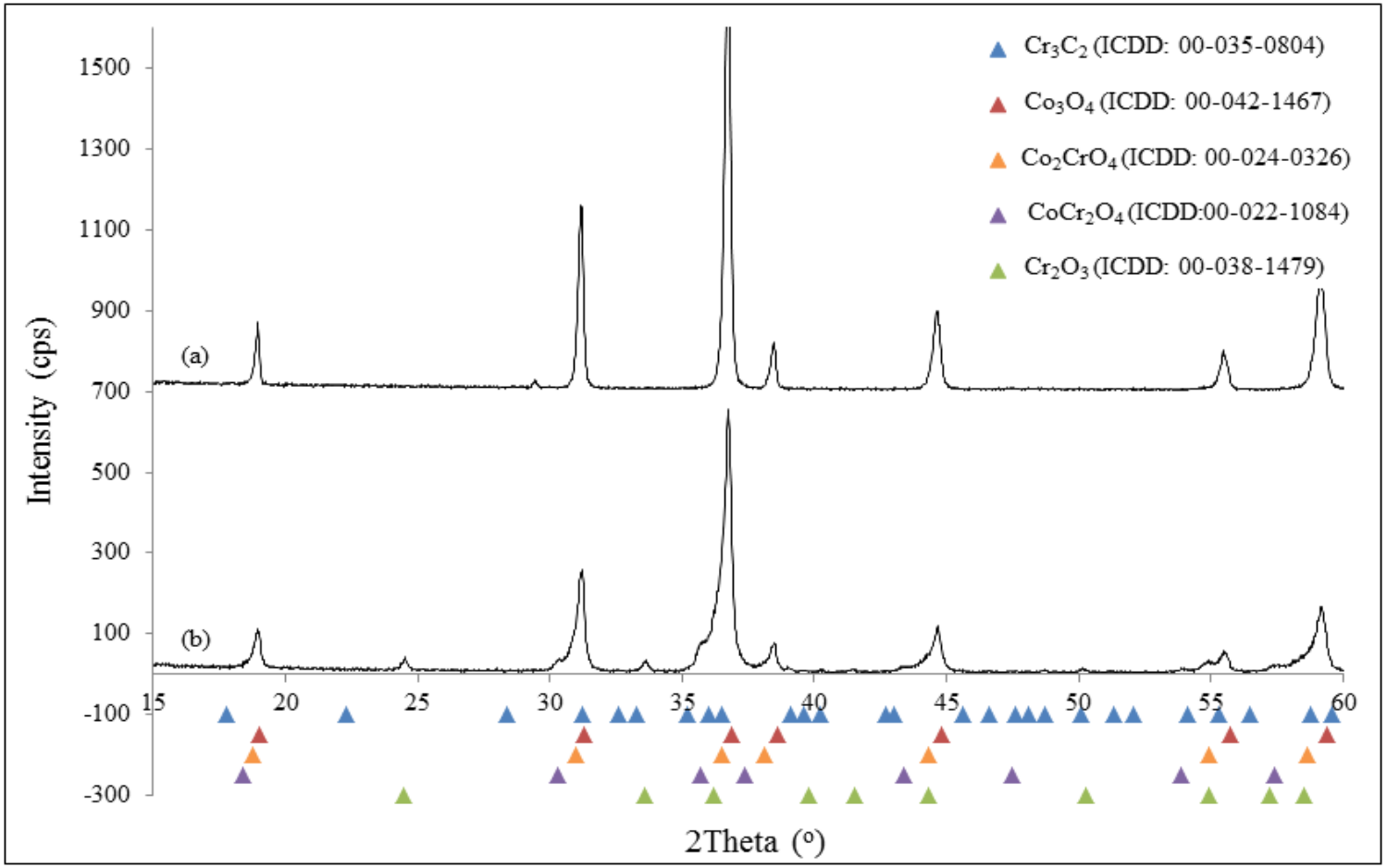

Figure 4.9: (a) XRD pattern obtained from the top oxidised surface of the Co-Cr-C free-standing coating exposed for 2691 hours at 650 ºC in air and (b) following partial grinding to remove approximately 10 µm of oxide to reveal the inner layers of the oxide.

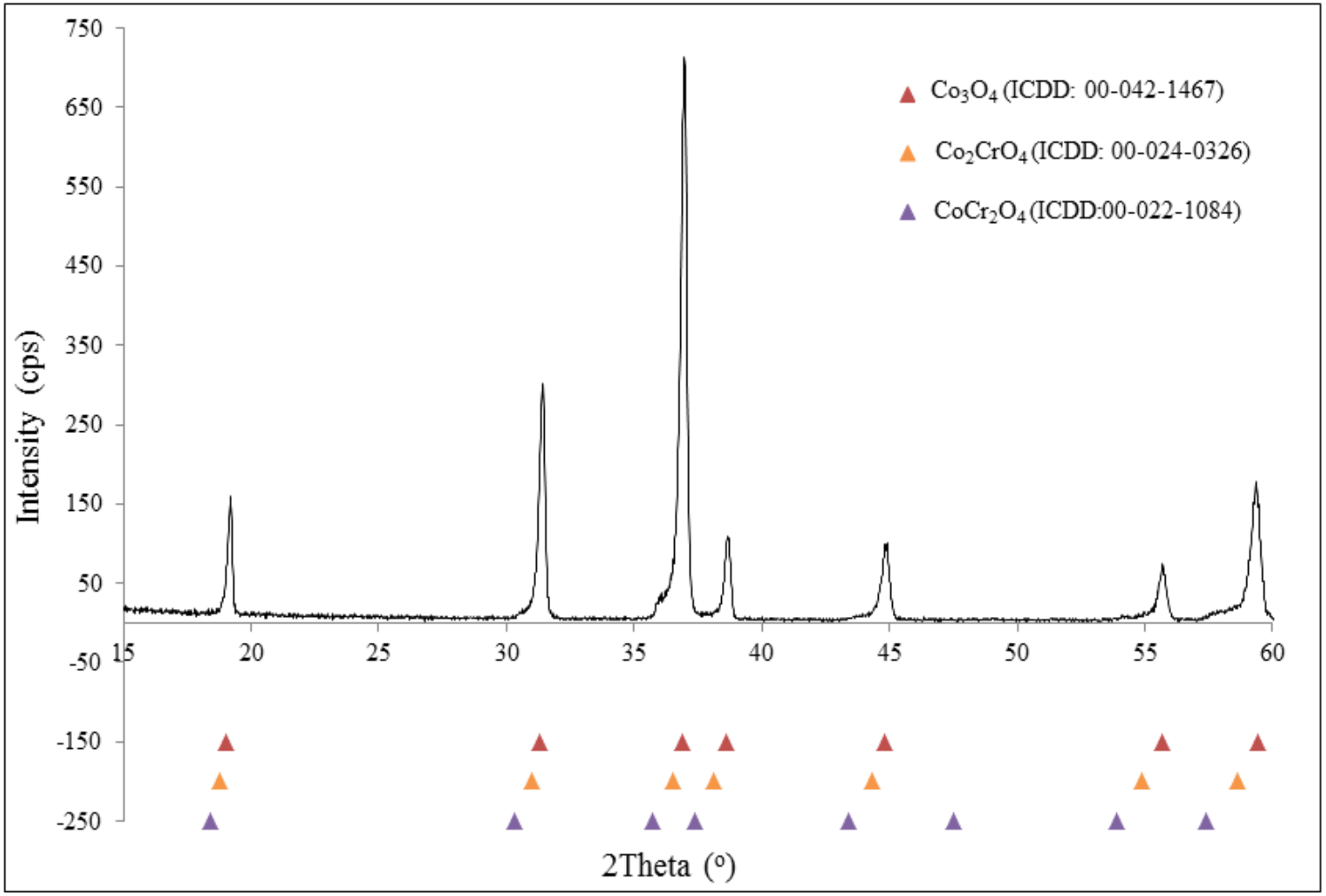

Figure 4.10: XRD pattern obtained from the top oxidised surface of the Co-Cr-C free-standing coating exposed for 3764 hours at 650 ºC in air.

4.3.2 Oxide Scale Characterisation

As well as the samples detailed in table 4.2 for the oxidation kinetics study (up to 336 hours), a series of longer term isothermal oxidation trials were also performed in air. These are summarised in table 4.5 (table 3.2, chapter 3) and are samples of the Co-Cr-C free-standing coating which were placed in the creep furnaces during coated P92 specimen creep testing (chapter 6), therefore the exposure times were dictated by creep failure times. Both sets of samples (tables 4.2 and 4.5) have been studied to characterise the oxide microstructure.

Table 4.5: A summary of the long term isothermal oxidation tests in air performed on the Co-Cr-C free-standing coating.

Sample Number	Temperature [^{o}C]	Exposure Duration [h]
1	650	2383
2	650	2691
3	650	3764
4	675	2659
5	700	1006

4.3.2.1 XRD Analysis of Oxide Top Surface

XRD patterns of the oxidised Co-Cr-C free-standing coating surface have been considered for this section, prior to any cutting or preparation of the oxidised samples. For all of the isothermal testing (tables 4.2 and 4.5) the XRD pattern identifies strong peaks for Co_3O_4 phase (figures 4.8-4.10). This suggests that this is the dominant outermost layer. Partial grinding of the oxide layer in figure 4.9b (~ 10 μm) and re-examination then identifies Cr_2O_3, $CoCr_2O_4$, Co_2CrO_4 and very small peaks for Cr_3C_2. Cr_2O_3, $CoCr_2O_4$ and Co_2CrO_4 are the inner layer oxide phases, whilst the Cr_3C_2 phase is likely to be embedded in the

inner oxide layer. These are not bulk coating carbides because no cobalt matrix phase is being identified. This need for partial grinding to identify inner layers shows that the outermost layer of Co_3O_4 is becoming so thick that the X-rays cannot penetrate through the oxide to the inner layers. This is illustrated in figure 4.9 for the 2691 hour at 650 ^oC sample. Appendix B shows that the X-rays penetrate the oxide phases between 0.78-7.93 µm, dependent on the specific oxide. This would therefore suggest that the outer Co_3O_4 oxide is at least 8 µm thick even for the shortest duration sample. Figure 4.9 shows that the Co_3O_4 oxide peaks at 31, 37, 45 and 60^o broaden after grinding and therefore reveal two new spinel oxide phases (Co_2CrO_4 and $CoCr_2O_4$). Figure 4.10 shows that for the longest term testing Co_3O_4 is still the dominant peak with very small peaks for the spinel phases, Co_2CrO_4 and $CoCr_2O_4$, being identified. This suggests that at longer exposure times the outer Co_3O_4 layer is becoming thinner allowing X-rays to penetrate the innermost layers.

At the higher temperatures of 675, 700 and 750 ^oC the same oxide phases are observed following removal of a thin layer, suggesting the same oxide evolution and composition.

4.3.2.2 SEM/EDX Analysis of Oxide Top Surface

SEM imaging has been performed plan view on the oxidised surface of the Co-Cr-C free-standing coating following high temperature oxidation in air, prior to any cutting or preparation of the oxidised samples. SE imaging (figure 4.11) shows the evolution of the top surface with time at 650 ^oC between 288 and 3764 hours of oxidation. In the first few hundred hours the oxide is shown to be composed of small crystals that are predominantly cobalt and oxygen rich

with only very small amounts of chromium present (figure 4.11a, table 4.6). Comparing the EDX to table 4.7 shows this is consistent with the stoichiometric composition of Co_3O_4. However, after nearly 3000 hours of exposure (figure 4.11b), the top surface looks more irregular with larger crystals present and clusters of oxide growth. The oxide is shown to be cobalt and oxygen rich (with slightly higher chromium levels than in figure 4.11a). This suggests that chromium richer phases are forming after the initially fast growing cobalt rich oxides on the top layer. Figure 4.11c shows the longest term 650 ^{o}C exposure following almost 4000 hours. The surface again looks more irregular with larger crystals and a more uneven surface. EDX analysis (table 4.6) shows that the oxide is again cobalt and oxygen rich with higher chromium values than in figure 4.11a. Overall the oxide in all cases appears to be Co_3O_4 and is adherent with no significant porosity.

At the higher temperatures of 675, 700 and 750 ^{o}C the same oxide evolution is observed; initially the fast growing cobalt oxides form and then the chromium richer phases begin to be identified. The oxide crystals become larger and the surface becomes more irregular with time. In all cases there is no evidence of significant porosity/cracking and no evidence of oxide spallation in the alumina crucible at any temperature.

Table 4.6: The elemental composition determined by EDX analysis of the top surface oxide for an average of 10 measurements (figure 4.11).

Image	Elemental Composition [at %]		
	Co	**Cr**	**O**
4.11(a) – Co_3O_4	49.6 ± 0.1	0.4 ± 0.1	50 ± 5.2
4.11(b) – Co_3O_4	33 ± 2.9	7 ± 1.5	60 ± 4.1
4.11(c) – Co_3O_4	41 ± 4.6	4 ± 0.6	55 ± 5.2

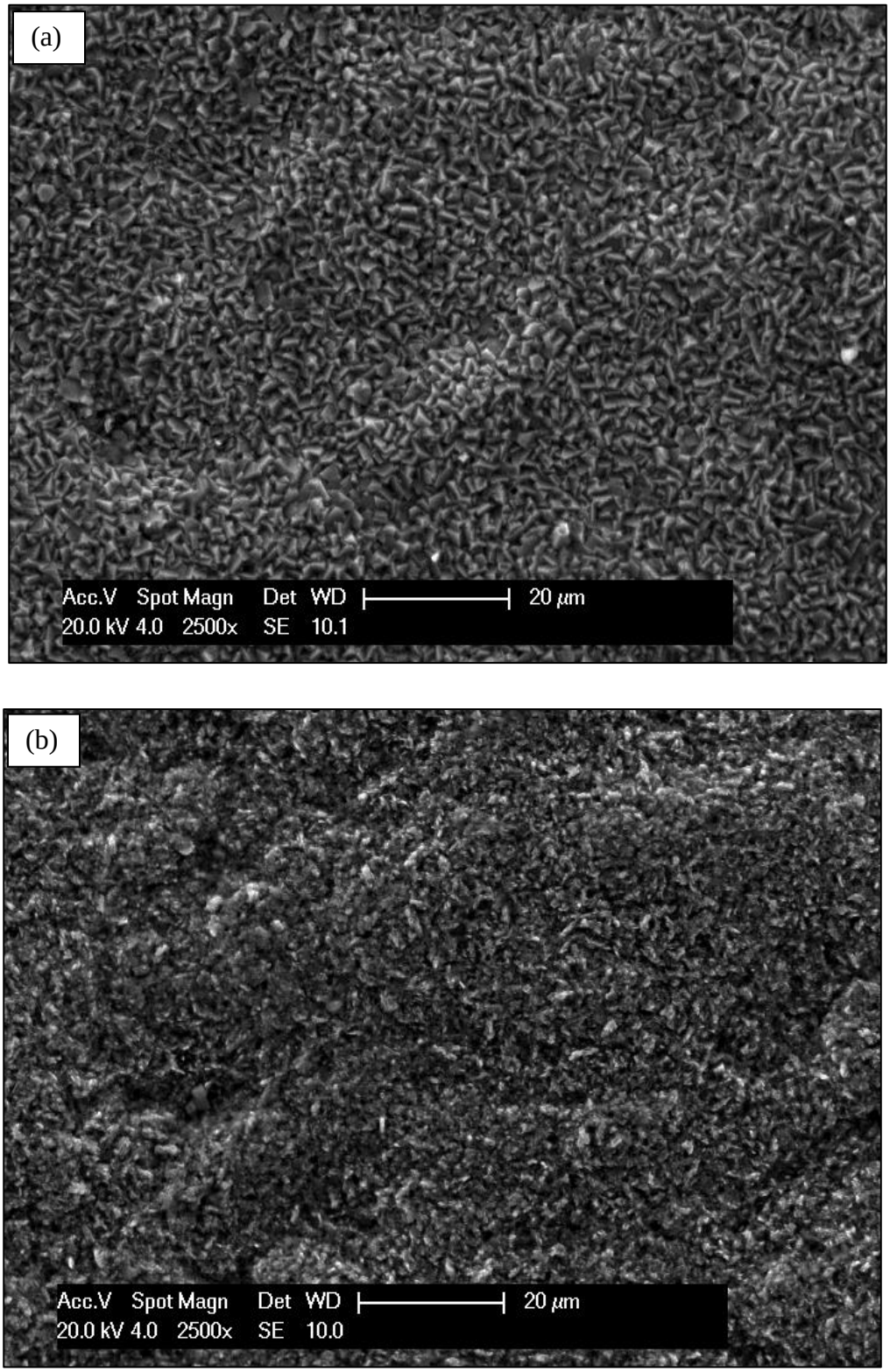

Figure 4.11: SEM micrographs of the Co-Cr-C coating top surface following oxidation in air for (a) 288 hours, (b) 2691 hours and (c) 3764 hours at 650 ºC.

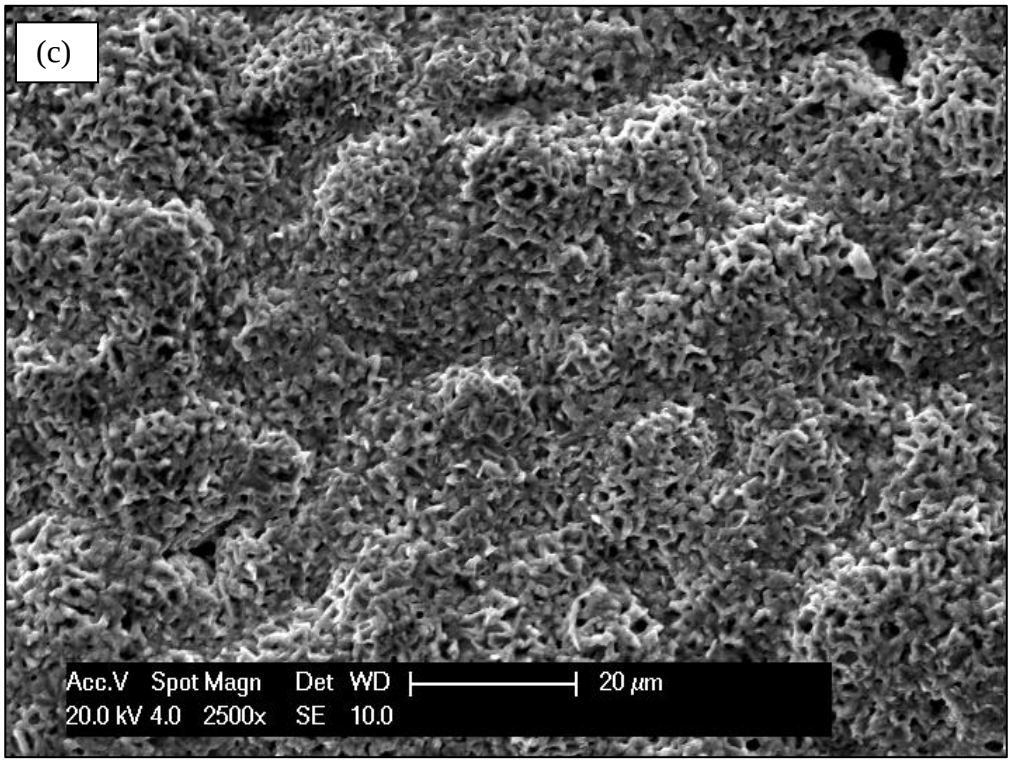

Figure 4.11: SEM micrographs of the Co-Cr-C coating top surface following oxidation in air for (a) 288 hours, (b) 2691 hours and (c) 3764 hours at 650 ^{o}C.

Table 4.7: Stoichiometric composition of the Co-Cr-C coating oxide phases in at %.

Phase	Elemental Composition [at %]		
	Co	**Cr**	**O**
Co_3O_4	43		57
Co_2CrO_4	29	14	57
$CoCr_2O_4$	14	29	57
Cr_2O_3		40	60

4.3.2.3 SEM/EDX Analysis of Oxide Cross-Section

Following the plan view oxide characterisation (SEM, XRD) the oxidised Co-Cr-C coating was cut and examined in cross-section in the SEM. Special care was taken during cutting to limit oxide damage (chapter 3). However some

damage of the oxide is likely to still occur during the abrasive grinding and polishing process. The samples exposed at 650 ^{o}C for between 96 and 3764 hours have been examined to establish how the oxide evolves with oxidation time (figure 4.12).

The overall thickness of the oxide is shown to increase with exposure time and approximately follows a similar parabolic relationship as seen in the oxidation kinetics study (section 4.3.1), although this cannot be conclusively proven because of higher standard deviation values for oxide thickness measurement. Average oxide thicknesses shown in figure 4.13 and table 4.8 are from 20 individual thickness measurements along the oxidised surface and standard deviations are included. The standard deviation values are reasonably small for oxide thickness suggesting a consistent oxide thickness across the specimens. The coating dimensions have been measured before and after oxidation testing and there is no observable evidence that coating bulk is being consumed during testing. There is also no evidence of any spallation of oxide or coating bulk in the test crucibles following testing.

From the SEM images in figure 4.12 there is clear evidence for inward and outward growth of the oxide. Within the inner oxide, there are several embedded Cr_3C_2 particles which act as markers to indicate approximately where the original coating bulk top surface would have been. This assumes that no Cr_3C_2 particles are being lost completely. This is a reasonable assumption as there is no evidence of the coating bulk being consumed during the test. There is an approximate ratio of 50:50 for inward and outward growth. The black contrast carbide shaped features in the oxide are probably areas of particle pull-

out during the polishing process; these too can be used as markers. Any smaller black contrast regions (less than 5 μm) are likely to be oxide porosity.

When the oxide itself is studied in more detail using EDX analysis (table 4.9) and compared to stoichiometric oxide phase compositions (table 4.7) a difference in composition can be seen between the inward and outward growth regions. The outward growing layer (labelled A) is shown to be mainly cobalt rich oxide with atomic % ratios suggesting Co_3O_4. The inward growth layer is shown to contain two different regions. Firstly, the darker contrast regions (labelled C) forming around the embedded carbides are shown to be chromium rich oxides with atomic % ratios suggesting Cr_2O_3. Secondly the areas (labelled B) between the Cr_2O_3 are shown to be a mixture of cobalt and chromium rich oxide, suggesting a mixed spinel type oxide. The atomic % ratios suggest approximately $CoCr_2O_4$ and Co_2CrO_4. Error in EDX measurement is introduced by beam spreading when trying to measure such small areas. The standard deviation values in region B are largest suggesting more variation.

As the exposure duration is increased at 650 ^oC and the oxides become thicker it becomes easier to identify the regions through the oxide as each area becomes thicker. As the time is increased Cr_2O_3 regions extend before finally starting to form an innermost distinct layer. Investigations at the higher temperatures of 675, 700 and 750 ^oC identify the same general oxide cross sections with inward and outward growth. At higher temperature the oxide is thicker for a given time. For example the 2691 hour at 650 ^oC sample has an average oxide thickness of 29 ± 2.7 μm, whilst the 2659 hour at 675 ^oC has an average oxide thickness of 37 ± 3.4 μm. This is also confirmed by the mass gain per unit area data given in the oxidation kinetics study (figure 4.5).

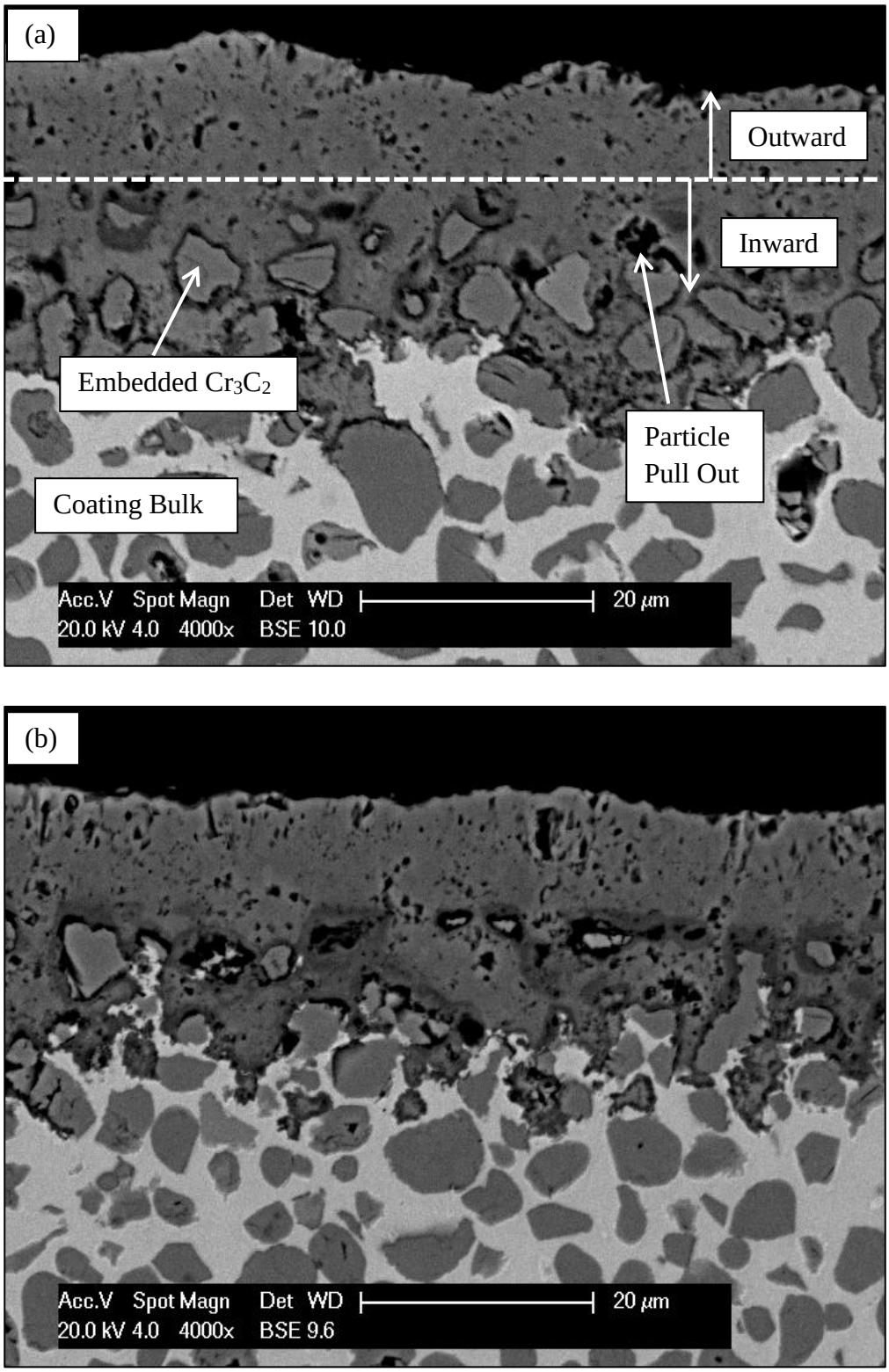

Figure 4.12: SEM micrographs to show the cross-section of the Co-Cr-C free-standing coating following oxidation in air for (a) 96 hours (b) 336 hours (c) 2383 hours (d) 2691 hours and (e) 3764 hours at 650 ^{o}C.

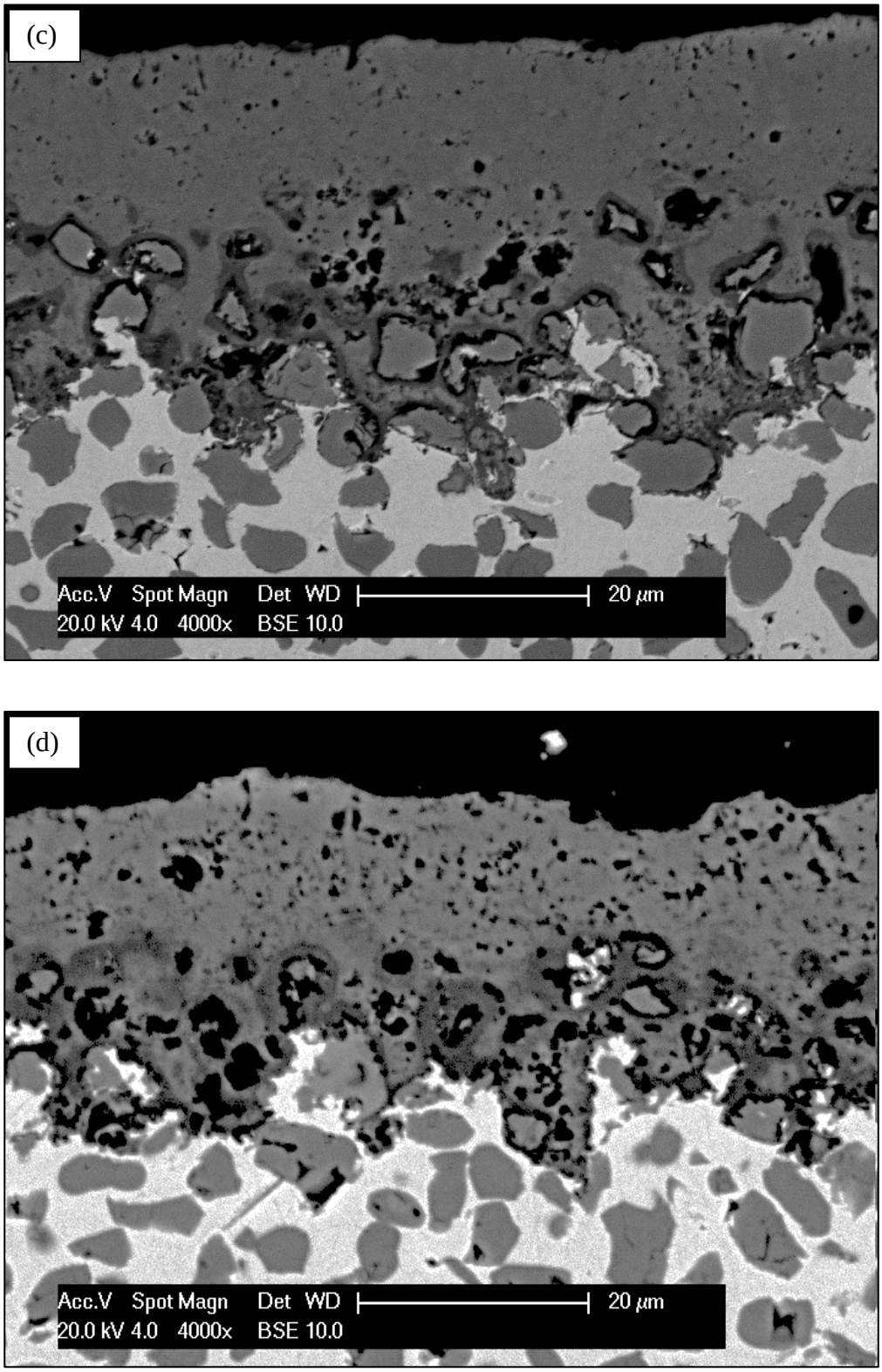

Figure 4.12: SEM micrographs to show the cross-section of the Co-Cr-C free-standing coating following oxidation in air for (a) 96 hours (b) 336 hours (c) 2383 hours (d) 2691 hours and (e) 3764 hours at 650 ^{o}C.

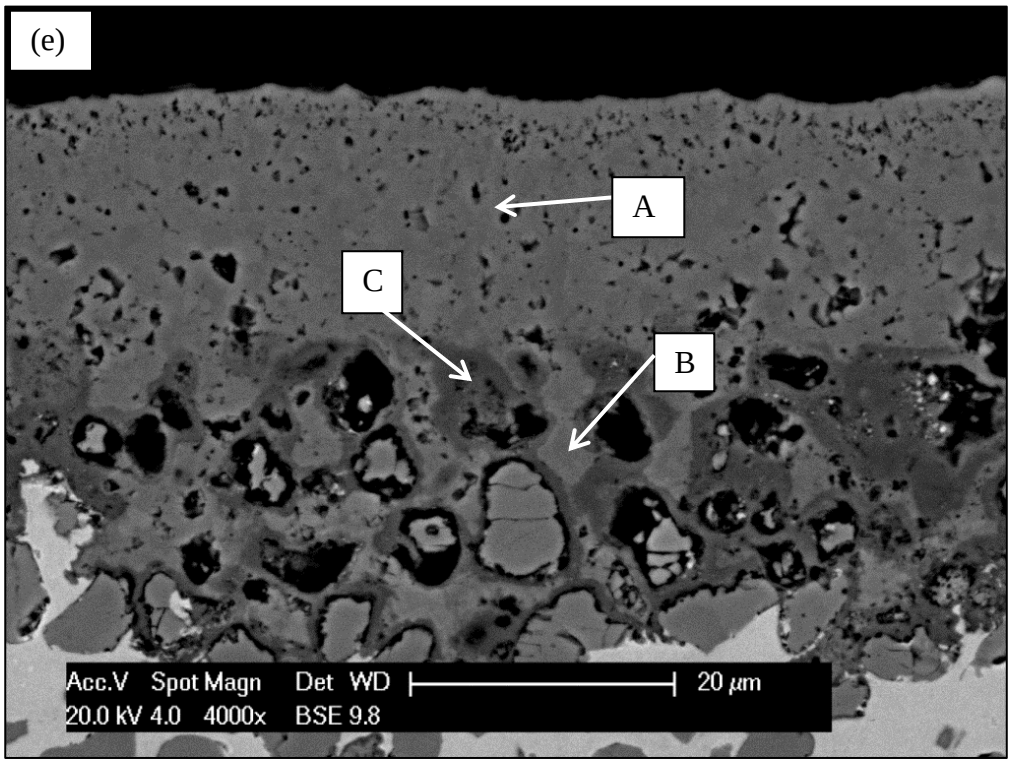

Figure 4.12: SEM micrographs to show the cross-section of the Co-Cr-C free-standing coating following oxidation in air for (a) 96 hours (b) 336 hours (c) 2383 hours (d) 2691 hours and (e) 3764 hours at 650 ºC.

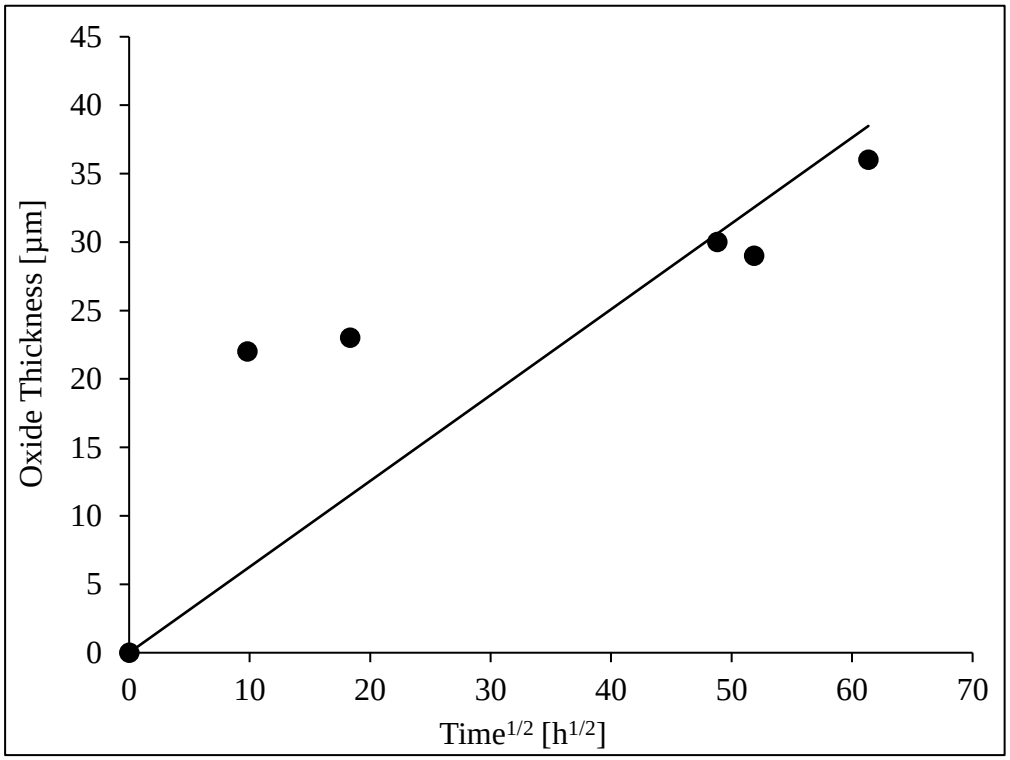

Figure 4.13: Average oxide thicknesses plotted against time for table 4.8.

Table 4.8: Average oxide thickness measurements for the Co-Cr-C free-standing coating following oxidation in air at 650 ^{o}C.

Exposure Time [h]	Exposure Time$^{1/2}$ [h$^{1/2}$]	Oxide Thickness [µm]
96	9.8	22 ± 2.7
336	18.3	23 ± 3.6
2383	48.8	30 ± 3.5
2691	51.9	29 ± 2.7
3764	61.4	36 ± 6.6

Table 4.9: The elemental composition determined by EDX analysis of the oxide cross-section for the measurement positions given in figure 4.12e.

Location	Elemental Composition [at %]		
	Co	Cr	O
A – Co_3O_4	43 ± 0.1	1 ± 0.4	56 ±0.5
B - $CoCr_2O_4$ and Co_2CrO_4	42 ± 7.1	24 ± 9.2	34 ± 10.1
C – Cr_2O_3	3 ± 0.3	35 ± 1.17	62 ± 0.9

4.3.3 Co-Cr-C Free-Standing Coating Evolution

Below the oxidised surface, the free-standing coating has experienced no obvious microstructural transformation. The Cr_3C_2 particles have retained their angular shape and there are no obvious features of microstructural evolution, as shown in figure 4.14, which presents the microstructure of the free-standing coating following exposure for 2691 hours at 650 ^{o}C (ground back at least 50 µm from the oxidised surface).

XRD was performed on the Co-Cr-C coating bulk (ground back at least 50 µm from the oxidised surface) following the high temperature oxidation. Figure 4.15 is an XRD scan of the bulk following 2691 hours at 650 ^{o}C, included as a representative example. This confirms that the only chromium carbide phase

present is Cr_3C_2 and there is no evidence of carbide transformation. This also shows that the FCC (electro-plated cobalt has an FCC structure which is metastable) to HCP transformation of the cobalt phase has occurred on cooling from high temperature.

Detailed examination of the samples reveals that this lack of microstructural evolution of the carbides and matrix HCP transformation is retained all the way up to the oxidised layer, as shown in figures 4.12. Examination of the 675 and 700 ^oC samples show the same microstructure has been retained even at higher temperature and longer duration. There is no XRD evidence to suggest that the Cr_3C_2 particles embedded in the inner oxide phase are transforming, although they appear smaller than the carbides in the bulk deposit below the oxide.

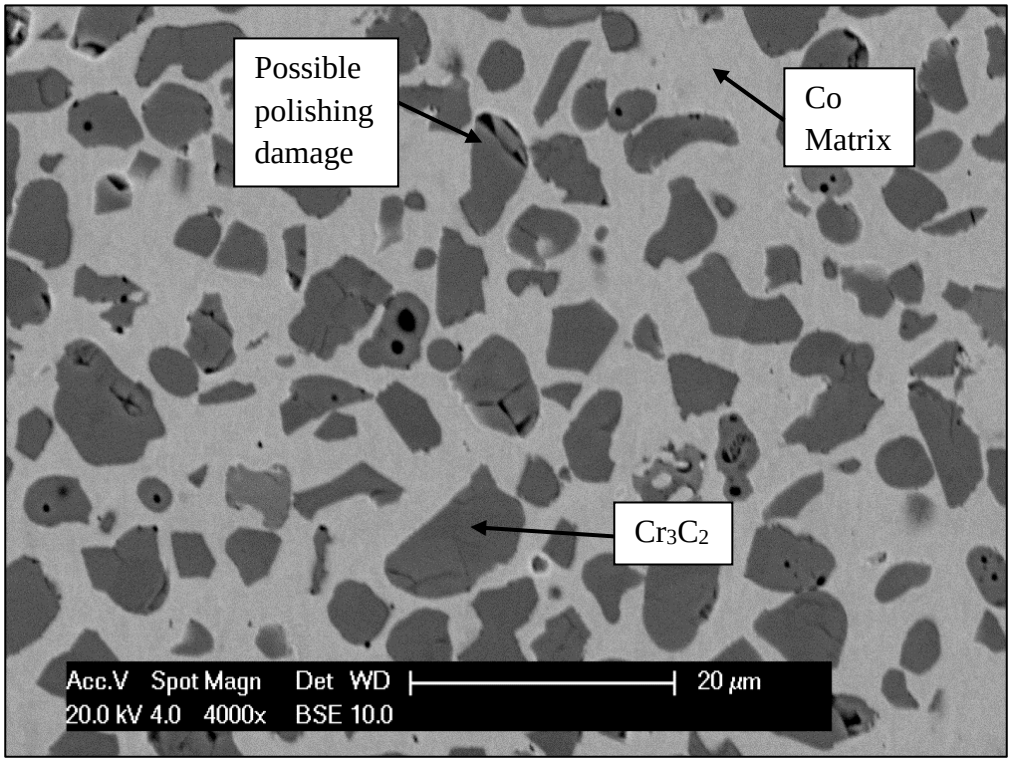

Figure 4.14: SEM micrograph to show the Co-Cr-C free-standing coating microstructure following high temperature oxidation in air at 650 ^oC for 2691 hours.

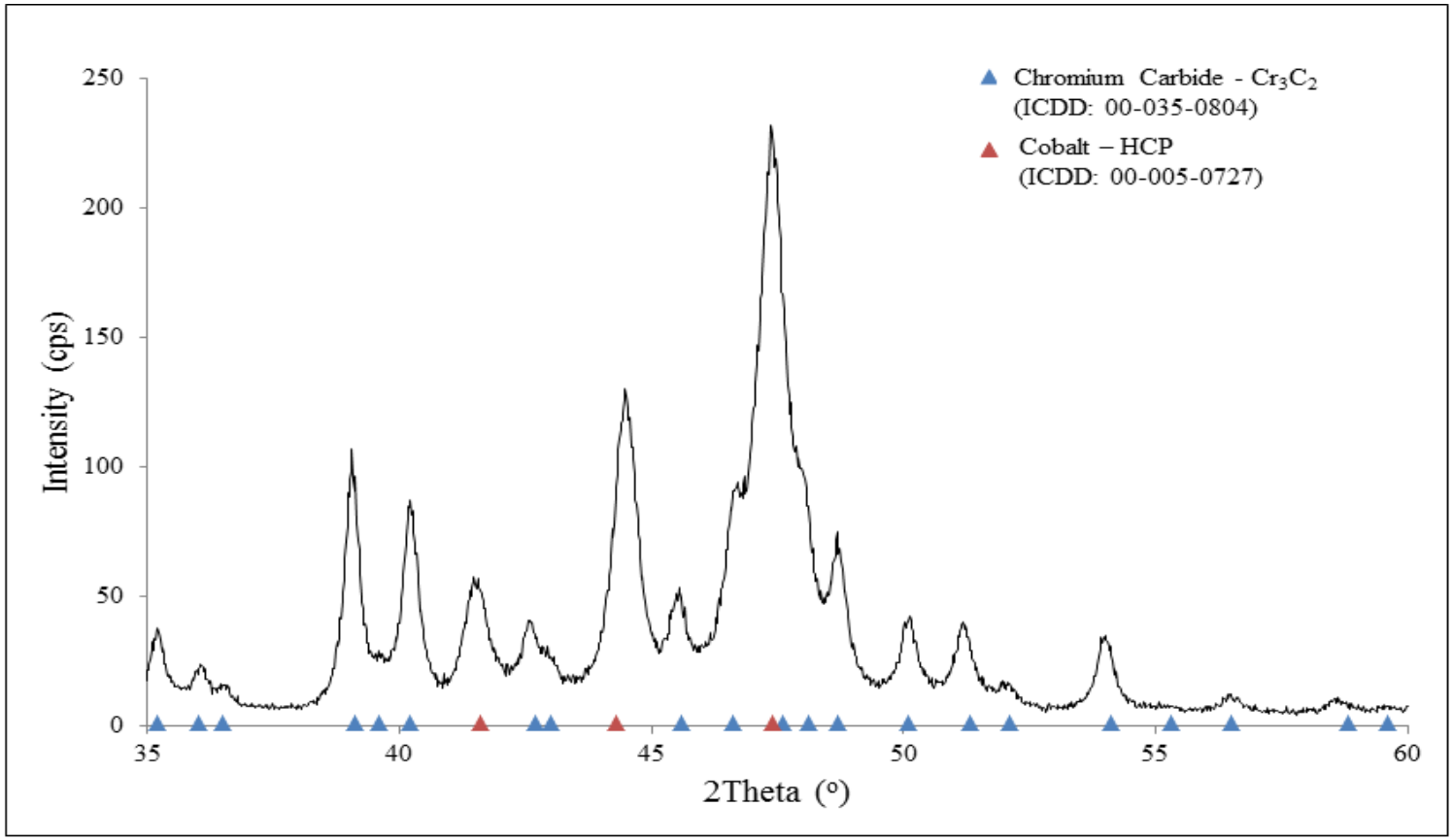

Figure 4.15: XRD pattern for the Co-Cr-C free-standing coating following high temperature oxidation for 2691 hours at 650 °C. Oxidised layers have been completely removed by grinding back ~ 50 µm.

4.4 Discussion

4.4.1 Oxidation Kinetics

The Co-Cr-C free-standing coating is shown to follow parabolic oxidation kinetics during isothermal oxidation for up to 336 hours. Initially the oxidation is rapid and after approximately 200-300 hours of exposure the oxidation rate begins to level out. The best way to interpret the parabolic oxidation kinetics is using the Wagner theory of oxidation presented in Birks et al. [2006]. This theory assumes that migration of ions or electrons across the oxide is the rate controlling step and that thermodynamic equilibrium is established at both the metal-oxide and oxide-gas (O_2) interfaces. Since thermodynamic equilibrium is assumed to be established at the metal-oxide and oxide-gas interfaces, it follows that activity gradients of metal (cobalt, chromium) and non-metal (oxygen) will be set up across the oxide. This means that metal ions and oxide ions will migrate across the oxide layer in opposite directions. At short times (< 200 hours), the oxide layer is thin and therefore provides little resistance to the transport of cobalt, chromium or oxygen ions, this causes the initial high oxidation rate. As the oxide layer starts to become thicker (> 200 hours) the cobalt, chromium and oxygen ions find it increasingly hard to penetrate through the oxide layer, this results in the reduction in the oxidation rate [Birks et al., 2006].

Desirable oxide phases such as Cr_2O_3 have good oxidation properties because they are very dense and adequately stoichiometric and therefore significantly limit the rate of cobalt, chromium and oxygen ion diffusion through them [Mandrino et al., 2008; Colson and Larpin, 1994]. Co_3O_4 oxides are less dense and therefore grow faster [Birks et al., 2006]. Cameron et al. [1979] and Foster

[2007] suggest that the oxidation rate of Co-Cr-C alloys will be lowest when a distinct layer of Cr_2O_3 has formed, therefore having the effect of 'sealing' the coating from further oxidation. This causes the oxidation rate to reduce with time. The oxidation rate will remain constant providing there is a sufficient supply of chromium to the oxidised surface to keep the Cr_2O_3 intact. Also providing there is no cracking or damage of the Cr_2O_3 during oxidation.

Detailed studies of the oxidation kinetics for Co-Cr-C type materials are very limited in the literature and it is therefore difficult to make meaningful comparisons. Of the oxidation kinetics work that has been conducted most is concerned with temperatures around 1000 ^oC. For example Durham et al. [1998a] oxidised a Co-Cr-C cast alloy (Co-25Cr-(0.5-1.0)C-0.05Si) in air at 1000 ^oC and reported k_p = 3.2 x 10^{-11} $g^2.cm^{-4}.s^{-1}$. This value is in good general agreement with the findings of this chapter at lower temperature and suggests the values obtained in this chapter are reasonable (table 4.4).

The activation energy for the Co-Cr-C free-standing coating, determined in this chapter, can be used to extrapolate the k_p values to higher and lower temperatures using equation 4.2. The oxide thickness/weight gain can then be estimated at these higher temperatures for a given time using equation 4.1. These extrapolated k_p values are presented in table 4.10 and compare well to the values determined by Durham et al. [1998a] for the higher temperature testing (k_p at 1000 ^oC = 3.2 x 10^{-11} $g^2.cm^{-4}.s^{-1}$). Foster [2007] has studied the specific Co-Cr-C free-standing coating used in this work and found that the oxidation rate reduces with increasing Cr_3C_2 content. This supports the theory of Cr_2O_3 being beneficial to oxidation rate. It also suggests that a greater Cr_3C_2 content allows the Cr_2O_3 to form more quickly per unit time. Foster [2007] also

shows that the application of a post-deposition heat treatment is beneficial and slows down the oxidation rate. When compared to Co-Cr alloys the Co-Cr-C free-standing coating in this thesis has an oxidation rate of ~25% of the rate for typical Co-Cr alloys [Foster, 2007].

Viswanathan et al. [2006] gives the P92 (8.9 % Cr) k_p value in steam, at 650 ^{o}C for up to 1000 hours, to be 9.04 x 10^{-12} $g^2.cm^{-4}.s^{-1}$. This means that the rate of oxidation in the early stages is fairly similar to the Co-Cr-C coating in air. However, as discussed in chapter 2, the adherence and the integrity of the P92 oxide is the major limitation. The adherence of Cr_2O_3 is expected to be much greater [Birks et al., 2006]. Indeed this is confirmed when examining oxidised cross-sections as shown in section 4.3.2.3.

Table 4.10: Extrapolated parabolic rate constants, k_p, for the Co-Cr-C free-standing coating.

Temperature [^{o}C]	**Extrapolated Parabolic Rate Constant, k_p [$g^2.cm^{-4}.s^{-1}$]**
550	2.40 x 10^{-12}
600	4.90 x 10^{-12}
800	4.37 x 10^{-11}
1000	1.96 x 10^{-10}

The k_p values calculated for the short duration oxidation kinetics study of the Co-Cr-C free-standing coating (table 4.4, section 4.3.1) can be used to approximate the oxide thicknesses expected at 650 ^{o}C for longer times and compared to the measured thicknesses (table 4.11). For simplicity the oxide formed was assumed to be made up entirely of Co_3O_4 with a density of 6.11 g/cm^3 [Birks et al., 2006]. Table 4.11 shows that the measured and

computational values have significant differences in oxide thickness values. This could suggest that the oxides begin to experience some spallation as the oxide becomes thicker. However as mentioned in the experimental results the coating bulk dimensions show no measurable signs of being reduced following testing and there was no evidence of spalled material in the alumina test crucibles. Therefore it seems most likely that if any oxide damage is occurring then it was caused post-test as a result of the sample preparation. Although reasonable precautions have been taken to protect the oxide during sample preparation (chapter 3) some damage will still be expected from the abrasive nature of grinding and polishing.

A more likely reason for the differences in table 4.11 is that the k_p values used for extrapolating oxide thicknesses have been calculated from short duration data (96-336 hours) and are being extrapolated to much longer durations (up to 3764 hours). Therefore it is likely to be less accurate at longer duration. Also the oxide is assumed to be entirely Co_3O_4, which does not take into account any differences in densities between the complex mixture of phases identified in section 4.3.2. For example the more protective Cr_2O_3 has a density of 5.22 g/cm^3. Birks et al. [2006] also shows that chromium and oxygen rich oxides (Cr_2O_3) are shown to form slower than cobalt and oxygen rich oxides (Co_3O_4). From experimental analysis it seems that these chromium richer oxides become more prevalent at longer times. This comparison suggests that extrapolations of k_p values should be used with caution and that in the future a longer term study of oxidation kinetics of the Co-Cr-C coating is needed to fully understand the long term kinetics.

Table 4.11: A comparison of the measured oxide thicknesses and the calculated values for the Co-Cr-C free-standing coating at 650 ºC, using k_p = 8.70 x 10^{-12} $g^2.cm^{-4}.s^{-1}$.

Temperature [ºC]	Time [h]	Experimentally Measured Oxide Thickness [µm]	Calculated Mass Gain per Unit Area [$g.cm^{-2}$]	Calculated Oxide Thickness [µm]
650	96	22 ± 2.7	1.73 x 10^{-3}	10.6
650	336	23 ± 3.6	3.24 x 10^{-3}	19.9
650	2383	30 ± 3.5	8.64 x 10^{-3}	53.2
650	2691	29 ± 2.7	9.18 x 10^{-3}	56.6
650	3764	36 ± 6.6	10 x 10^{-3}	61.6

4.4.2 Oxidation Mechanism

The work by Cameron et al. [1979] in air has studied an early version of the Co-Cr-C free-standing coating with varying carbide weight percentage and oxidation temperatures of ~ 1000 ºC in air. It shows that the Cr_3C_2 particles are unstable at high temperature and they dissolve into the matrix during alloying; this dissolution is particularly rapid at 1000 ºC. This agrees with Thermo-Calc simulations in section 4.2.2 which predicts significant Cr_3C_2 dissolution above 735 ºC. If the simulation temperature is extended the dissolution is greater at 1,000 ºC and the system has a final melting temperature of ~ 1200 ºC. Cameron et al. [1979] concludes that the oxide formed on the Co-Cr-C coating is similar to that of Co-Cr alloys, namely inner Cr_2O_3 and outer Co_3O_4, $CoCr_2O_4$ and Co_2CrO_4. Cameron et al. [1979] and Foster [2007] (conducted in air) show that when the Cr_2O_3 forms a distinct layer, it has the effect of 'sealing' the coating surface, meaning that the cobalt rich oxide formation rapidly reduces. Foster [2007] suggests this could possibly cause the cobalt

oxides to come away just leaving the adherent chromium based oxides. There is no clear evidence for spallation in this chapter. The temperatures being considered in this thesis are lower than those of Cameron et al. [1979] and Foster [2007], therefore the distinct layer of Cr_2O_3 has not yet fully formed. Future work will need to study the effect that the development of Cr_2O_3 has on the overall integrity of the coating-oxide system at high temperature.

Work by El Dahshan et al. [1975] in air (Co-(5-35)Cr-(0.5-1.0)C) and Durham et al. [1998a] in air (Co-25Cr-(0.5-1.0)C), considering homogenised cast Co-Cr-C alloy systems at ~ 1000 ^oC (with small $M_{23}C_6$, M_7C_3 and M_3C_2 particles which precipitate during casting), shows that the protective scale formed is Cr_2O_3 with a number of spinel oxides forming too (mainly Co_3O_4 and $CoCr_2O_4$). This work also found that higher proportions of chromium result in thicker and more adherent Cr_2O_3. They found that the chromium for the Cr_2O_3 phase is provided by the chromium carbide phase dissolving and releasing its chromium into the cobalt matrix. This chromium then diffused through the oxide to the reaction surface sustaining the growth of the Cr_2O_3. Because this dissolution process and the subsequent diffusion are not instantaneous this explains why the chromium oxide is slower to form than the cobalt rich oxide phases.

The oxidation mechanism of the Co-Cr-C coating studied in this chapter, for high temperature isothermal oxidation in air, broadly agrees with the literature presented above. The main differences are that the evolution of the oxide in this work is slower because it is being studied at lower temperatures (650-750 ^oC) than the previous work (1000 ^oC). This chapter shows that the oxide experiences both inward and outward growth. The outward growth layer is

composed of Co_3O_4 which is the fastest forming due to the ready availability of cobalt in the coating matrix. The inward growth layer contains embedded Cr_3C_2 around which halos of Cr_2O_3 form. The remainder of the inward growth layer is made of spinel type oxide, namely $CoCr_2O_4$ and Co_2CrO_4. The thickness of all of these oxide layers is shown to increase with temperature and time. The Cr_2O_3, Cr_2CoO_4 and $CrCo_2O_4$ form more slowly than the cobalt rich oxides because the chromium needed for their formation is contained within the Cr_3C_2 and must diffuse from these particles. As Cameron et al. [1979] and Foster [2007] show the Cr_2O_3 will eventually form a distinct layer, however this is not definitively observed in this study because the temperature is much lower and the times shorter. The Cr_2O_3 is the most desirable phase because it is slow growing and adherent [Mandrino et al., 2008; Birks et al., 2006; Nicholls, 2000; Colson and Larpin, 1994].

The cobalt matrix in the coating bulk is shown to be transforming from FCC to HCP as the sample has cooled from high temperature. HCP to FCC transformation occurs at ~ 417 ^oC, where FCC is the stable high temperature form of cobalt. The slow cooling from high temperature following testing allows FCC to transform back to HCP [Betteridge, 1982]. These experimental findings are in agreement with the Thermo-Calc equilibrium calculations which show that the FCC matrix phase is retained over the temperature range of interest (500-900 ^oC).

The Co-Cr-C coating is shown to retain the Cr_3C_2 phase following a series of high temperature isothermal oxidation exposures (650-750 ^oC) and there is no conclusive evidence of any carbide transformation (in either the coating bulk or the carbides embedded in the oxide). However Clark et al. [1986] and Kamal et

al. [2009] have shown that coarse Cr_3C_2 particles, in cermet type (Cr_3C_2-NiCr) coatings, oxidise which leads to decarburisation to form stable films of Cr_2O_3 around the carbide particles which then inhibits further oxidation. They also show that oxidation of Cr_3C_2 leads to transformation to Cr_7C_3 and $Cr_{23}C_6$ phase, occurring in halos around the Cr_3C_2. This transformation of Cr_3C_2 is very important for oxidation resistance as the release of chromium from the carbides into the cobalt matrix is vital for the formation of the desirable Cr_2O_3 oxide phase.

Thermo-Calc equilibrium calculations agree with the literature and show that between 500 and 735 ^oC the M_3C_2 phase fraction is reducing whilst M_7C_3 phase fraction is increasing. The Thermo-Calc phase fraction diagram shows that the transformation over this temperature range is occurring gradually and only small quantities of Cr_7C_3 will be present compared to Cr_3C_2 and the FCC cobalt phase. Then at 735 ^oC the M_3C_2 transforms to M_7C_3 and graphite phase is predicted to form. Thermo-Calc also suggests that the difference in carbon and chromium activity between the Cr_3C_2 particles and the predominantly cobalt matrix will result in carbon and chromium diffusing into the matrix. Some of this carbon will be retained in the Cr_7C_3 phase, however because this new carbide has lower carbon content compared to Cr_3C_2 Thermo-Calc predicts graphite phase will also be present. Work by Berthod [2013] for oxidation of nickel alloys which contain Cr_3C_2 show that when the Cr_3C_2 break down the carbon can also be lost at the surface of the sample in gaseous form. The behaviour of carbon diffusion is complex and in the future work more advanced microstructural characterisation will be used to fully understand its behaviour.

Therefore from the literature and Thermo-Calc modelling it seems likely that the $Cr_3C_2 \rightarrow Cr_7C_3$ carbide transformation is present in the Co-Cr-C free-standing coating in this study, especially for the carbides embedded in the inner oxide layers (they appear smaller suggesting carbide breakdown). The reason that Cr_7C_3 is missing from the experimental work is because of the sensitivity limits of XRD analysis when detecting small quantities of a phase [Cullity and Stock, 2001].

The oxidation mechanism of the Co-Cr-C free-standing coating at 650-750 ^oC is summarised in figure 4.16.

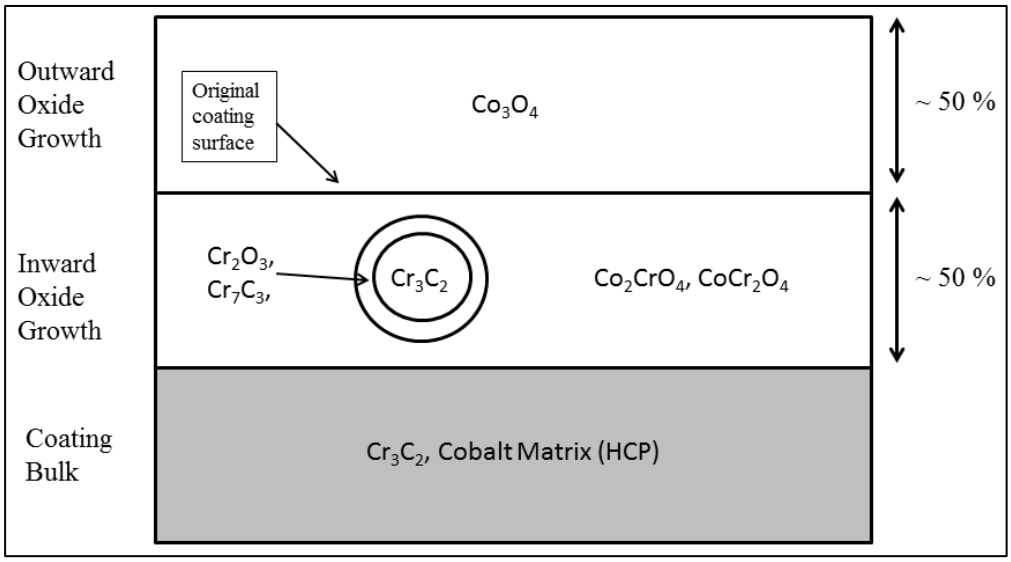

Figure 4.16: A schematic to summarise the multi-layered oxide formed on the Co-Cr-C free-standing coating following high temperature oxidation (650-750 ^oC) for up to 3764 hours.

4.4.3 Limitations

The high temperature oxidation study conducted in this chapter, and also in the majority of the literature, has mainly been performed in an air oxidation

environment, even though the final application of the coating will be in high temperature steam. This is mainly due to the limited availability of furnaces capable of performing very long term steam oxidation. Birks et al. [2006] has discussed in detail the differences between air and steam oxidation of metals and makes the following key points:

- The presence of water vapour in oxidising atmospheres has been shown to increase the observed reaction rate of steels and other metals; this is due to the influence of H_2O on the transport of oxygen across pores in the oxide. However it does not generally affect the actual phases forming.
- Water vapour can affect the plasticity of oxides which can mean the oxide is more likely to spall or can make it more adherent.
- Water vapour can adversely affect the selective oxidation of elements such as aluminium and chromium from metal base alloys. This can result in irregular and less adherent protective scales.
- One of the most serious effects of water vapour on the high temperature oxidation is the increased spalling tendencies of Cr_2O_3 scales [Birks et al., 2006].

Wood et al. [1970] has also studied air and steam environments by comparing the oxidation behaviour of Co-Cr alloys in air and steam at 1000 ^oC and showed that the oxidation is more severe per unit time in steam. However, the overall composition and structure of the oxide remains unchanged. This shows that although the rates of oxidation are different it is acceptable to make predictions about the composition of oxide phases in steam from work that has

been conducted in air. It is expected that the oxide damage of the Co-Cr-C coating will be more severe in steam. Steam oxidation testing of the Co-Cr-C free-standing coating is an essential area for future work. The oxidation kinetics in steam could be compared to the work in this chapter to quantify the differences between steam and air oxidation and allow for extrapolation of the air test data. Also a study of how steam conditions affect the long term integrity of Cr_2O_3 is vitally important.

The test conditions chosen in tables 4.2 and 4.5 have been conducted at industrially relevant temperatures (650-750 ^oC) which are well below the previous temperatures used to study this Co-Cr-C free-standing coating. The longest test durations have been determined by the duration of the coated creep tests in chapter 6. In reality 650-750 ^oC is probably slightly higher than the real in service temperatures for this coating. Initially it is anticipated that the coating would be used at closer to 600 ^oC, before gradually increasing the temperature in the future. Therefore the tests in this chapter can be considered to be slightly accelerated temperatures. It is possible to calculate the amount of exposure time at 600 ^oC that would give the same amount of oxidation (thickness or mass gain per unit area) for a shorter duration, higher temperature test, assuming that the oxidation mechanism does not change with temperature. Equation 4.1 and the Co-Cr-C free-standing coating k_p values (table 4.4) at both temperatures are used and the equations solved. As an example the 3764 hour at 650 ^oC is equivalent to 6683 hours at 600 ^oC. This shows that because the k_p values vary only very slightly between 550 and 1,000 ^oC (table 4.10) it is very difficult to perform accelerated oxidation tests (short durations at high

temperature) that are anywhere near to real power plant exposures. The only way would be to vastly increase the oxidation temperature, however this then limits the industrial relevance of the test as oxidation mechanism long term will likely vary at very high temperatures [Birks et al., 2006]. Therefore the only way in the future work to achieve real power plant levels of oxidation will be to perform very long duration testing (in the order of years of exposure). Alternatively placing some coating samples in situ in power plants would be very beneficial. It would also be desirable to study how the oxide behaves under thermal cycling conditions which are typical of real power plant operation. This is especially important because power plant are increasingly being required to operate more flexibly to accommodate renewables on the grid [DECC, 2014; Lefton and Besuner, 2006; Bugge et al., 2006].

4.5 Summary

The aim of chapter 4 was to characterise the Co-Cr-C free-standing coating prior to studying the coated P92 system in chapters 6 and 7. The motivation for this first stage of testing was to identify any desirable characteristics of the Co-Cr-C coating that may make it suitable for application to P92 substrate. Experimental investigations as well as thermodynamic modelling have been used to achieve this. In summary of this chapter, the following key results have been obtained:

- Oxidation of Co-Cr-C free-standing coating in air at 650, 700 and 750 ^{o}C shows parabolic oxidation kinetics with an activation energy of Q = 85.3 kJ/mol. Spallation of the oxide does not appear to be occurring during

isothermal oxidation testing. Oxidation kinetics of the Co-Cr-C coating are comparable to Co-Cr-C alloys studied in the literature and superior to Co-Cr alloys. The oxidation kinetics values are shown to be similar to those for P92 steel, however the oxide for the Co-Cr-C is much more adherent and less prone to spallation.

- The oxide on the Co-Cr-C free-standing coating following high temperature isothermal oxidation in air contains inward and outward growth. The outward growth is formed of Co_3O_4 and is the fastest growing and thickest oxide. The inward growth contains embedded Cr_3C_2 with Cr_2O_3 oxide forming in halos around them, which will eventually extend to a distinct layer. The rest of the inward growth is made up of the spinel oxide, $CoCr_2O_4$ and Co_2CrO_4. The chromium containing oxides are shown to become more prevalent with time as they are dependent on the release of chromium from the Cr_3C_2 phase. Cr_2O_3 is the most desirable oxide as it is very slow growing and very adherent, once a distinctive layer exists the oxidation properties will be significantly improved. Overall the entire oxide-coating system appears adherent and free from major defects.
- Thermo-Calc modelling and the literature suggests that the Cr_3C_2 particles in the Co-Cr-C coating (especially the carbides embedded in the innermost layer of oxide) are transforming to Cr_7C_3 as they release their chromium and carbon into the matrix to form Cr_2O_3. Carbide transformation has not been observed experimentally due to the limitations of the sensitivity of XRD. The cobalt matrix retains its FCC crystal structure at high temperature which reverts to the low temperature HCP version on slow cooling.

- Air oxidation testing can be used as a representation of oxidation mechanisms that will be expected in high temperature steam. The oxide structure is expected to be reasonably consistent in air/steam, however the oxidation rate is increased in steam. Steam is also expected to affect the integrity of Cr_2O_3.
- Accelerated oxidation testing is limited in application for the Co-Cr-C coating because the oxidation rate constant varies only slightly as temperature increases. Therefore the only way to get truly industrially relevant oxidation tests is to perform long duration exposures.
- Overall the oxidation of the Co-Cr-C free-standing coating shows very promising oxidation properties and good integrity under service relevant temperatures (650-750 ^{o}C). Therefore it is viable to investigate the Co-Cr-C coated P92 system, both mechanically and microstructurally. This free-standing coating study can be used as the basis for interpreting future results.

CHAPTER 5

MICROSTRUCTURAL AND MECHANICAL CHARACTERISATION OF P92 STEEL

5.1 Introduction

The literature review in chapter 2 presented the well documented research on microstructure, oxidation behaviour and mechanical properties of P92 steel. It highlighted a lack of mechanical testing at higher temperatures, particularly between 650-760 ^{o}C, a temperature range that is likely to become much more important as energy generators move towards USC operation. Chapter 2 also showed that in order to understand the effect of coating application on the mechanical properties of the substrate, it is vital to characterise the uncoated DB P92 being used in this study.

Therefore the overall aim of the work reported in this chapter was to characterise the microstructure and mechanical properties of the DB P92. A focus was put on higher temperature testing than has previously been considered in the literature. By the end of this chapter a detailed series of

baseline data had been determined to allow comparison to coated P92 mechanical testing in chapter 6.

This chapter contains two main sections. Section 5.2 presents the DB P92 microstructural characterisation with CALPHAD analysis, with a discussion of the findings in section 5.3. Sections 5.4-5.8 presents the mechanical properties of DB P92 at high temperature, with a discussion of the findings in section 5.9.

5.2 P92 Phase Equilibria and Microstructure

5.2.1 P92 Phase Fraction Diagrams

Table 5.1: Maximum and minimum P92 composition [Richardot et al., 2000], along with the composition of the DB P92 material studied in this thesis.

Element	Min [wt %]	Max [wt %]	DB P92 [wt %]
C	0.070	0.130	0.10
Mn	0.030	0.600	0.46
P	-	0.020	0.013
S	-	0.010	<0.002
Si	-	0.500	0.19
Cr	8.500	9.500	8.72
W	1.500	2.000	1.70
Mo	0.300	0.600	0.51
V	0.150	0.250	0.18
Nb	0.040	0.090	0.05
N	0.030	0.070	0.051
B	0.001	0.006	0.003
Al	-	0.040	<0.02
Ni	-	0.400	0.14
Cu	-	-	0.17
Fe	Balance	Balance	Balance

Table 5.1 presents the measured compositions of the DB P92 used for this thesis compared to the long established ASME standards for P92 presented in the literature [Richardot et al., 2000]. The chromium content is towards the

lower limit for P92, as is nickel, niobium, aluminium, vanadium and tungsten. However molybdenum is shown to be towards the upper limit for P92. Vyrostkova et al. [2008] and Masuyama [2001] show that molybdenum is included as it is an extremely effective solid solution strengthener.

The equilibrium phases expected in P92 were calculated using Thermo-Calc and the TCFE7 database (see appendix C for detailed modelling methods). The following phases, identified from the literature as being present in ~ 9 % Cr steels [Hald, 2008; Vyrostkova et al., 2008; Hattestrand and Andren, 2001], were included in the calculation:

- BCC (α-Fe/ferrite)
- FCC (γ-Fe/austenite)
- Laves Phase - $(Fe, Cr)_2(Mo, W)$
- MX Phase (M = V or Nb, X = C or N)
- $M_{23}C_6$ (M = Cr, Mo, Fe, W)

Figure 5.1 shows the phase fraction diagram for DB P92 plotted between 500 and 950 ºC. The transformation of the main matrix phase from α-ferrite to γ-austenite; the point at which this transformation begins is defined as the Ae_1 temperature and is calculated for DB P92 to be 819 ºC [Chalk et al., 2011]. The tempered martensite (non-equilibrium) is not predicted because Thermo-Calc is equilibrium modelling software. Figure 5.1 also shows that MX, $M_{23}C_6$ and Laves Phase precipitates are all present in the DB P92 in small concentrations at equilibrium.

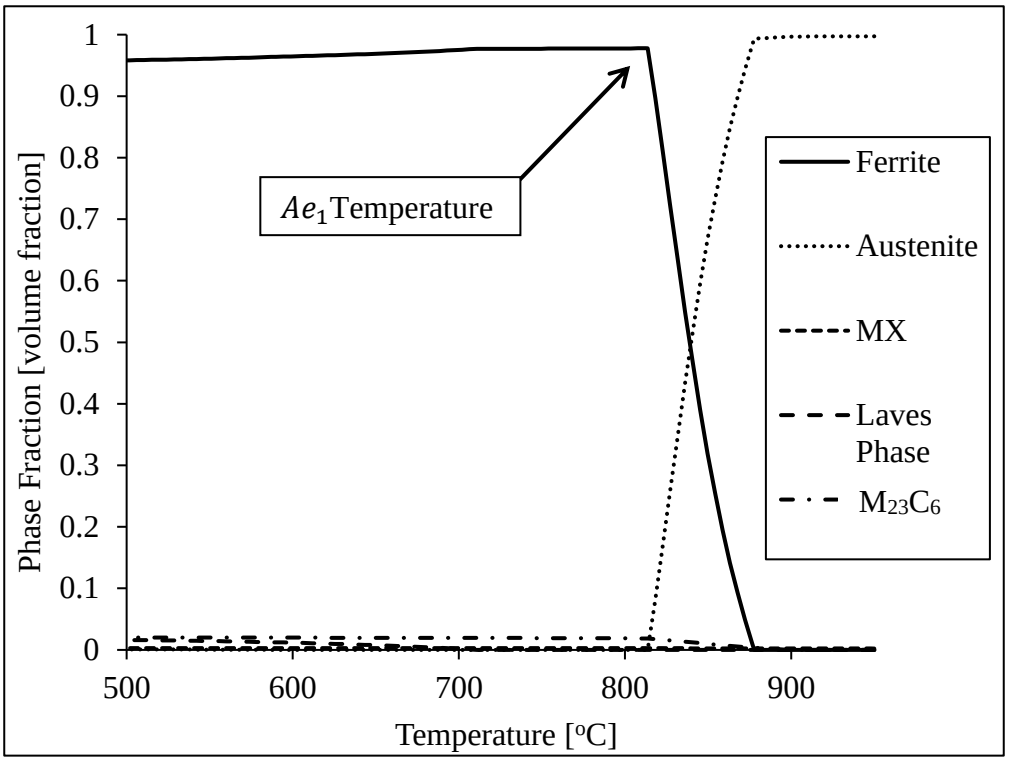

Figure 5.1: Predicted equilibrium phase fraction diagram for DB P92 steel from 500-950 °C.

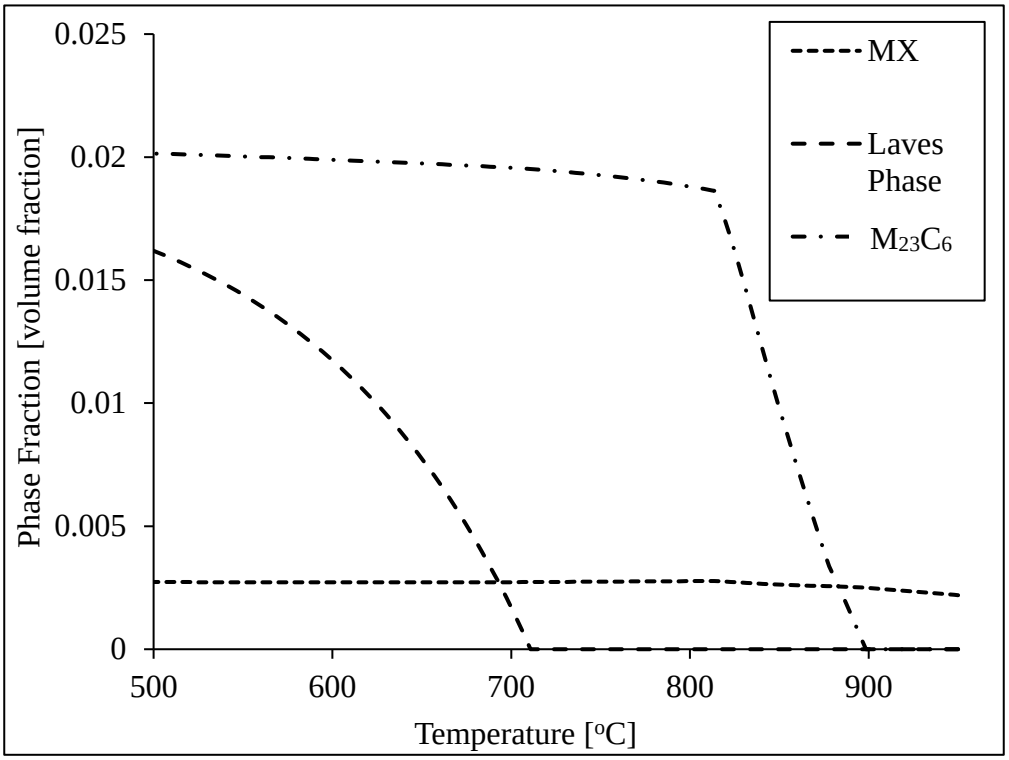

Figure 5.2: Predicted equilibrium phase fraction diagram for the precipitate phases for the DB P92 steel from 500-950 °C.

Figure 5.2 is an enlarged plot of the phase fraction diagram for the DB P92 between 500-950 ^{o}C (the same as in figure 5.1); however this time only the precipitate phases have been considered. This identifies three main precipitate phases: MX, Laves Phase and $M_{23}C_6$. Figure 5.2 shows that the volume fraction of MX and $M_{23}C_6$ phases remains constant between 500 and 800 ^{o}C. However Laves phase experiences significant reduction in volume fraction, suggesting dissolution of the phase is occurring at higher temperature.

5.2.2 Composition of the Precipitate Phases in P92

Thermo-Calc has been further used to predict the composition of the MX, $M_{23}C_6$ and Laves phases at equilibrium for the DB P92. Figures 5.3, 5.4 and 5.5 show how the composition of these precipitates is expected to vary with temperature. Figure 5.3 shows that MX phase is expected to be of the form (V,Nb)(N,C), with VN being the most likely version. Figure 5.4 shows that $M_{23}C_6$ is expected to be of the form $(Cr, Fe, Mo, W)_{23}C_6$, where $Cr_{23}C_6$ is the dominant carbide phase. Figure 5.5 shows that Laves phase is tungsten and iron rich and is expected to be $(Fe, Cr)_2(Mo, W)$.

The elemental composition of the MX, $M_{23}C_6$ and Laves phase are all shown to be reasonably insensitive to temperature, especially over the operation temperature regime for DB P92 (600-700 ^{o}C). This suggests that there is unlikely to be any significant precipitate transformation over this temperature range. Of the three precipitates considered the $M_{23}C_6$ shows the largest potential composition change with temperature.

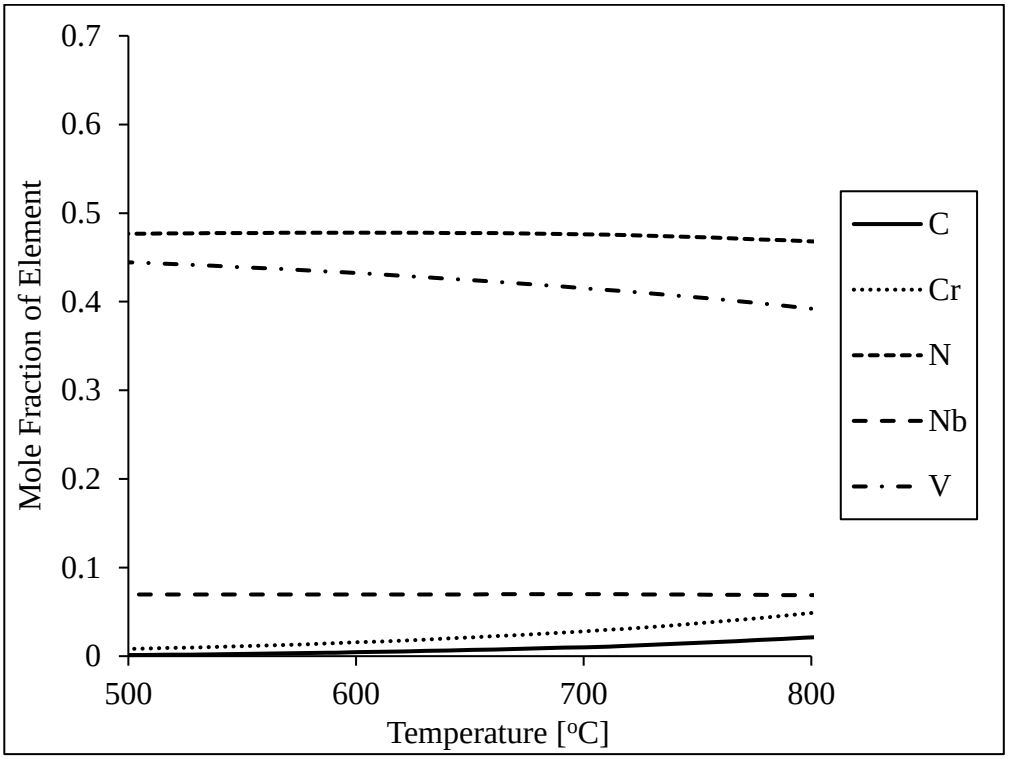

Figure 5.3: Predicted composition of the MX phase in the DB P92.

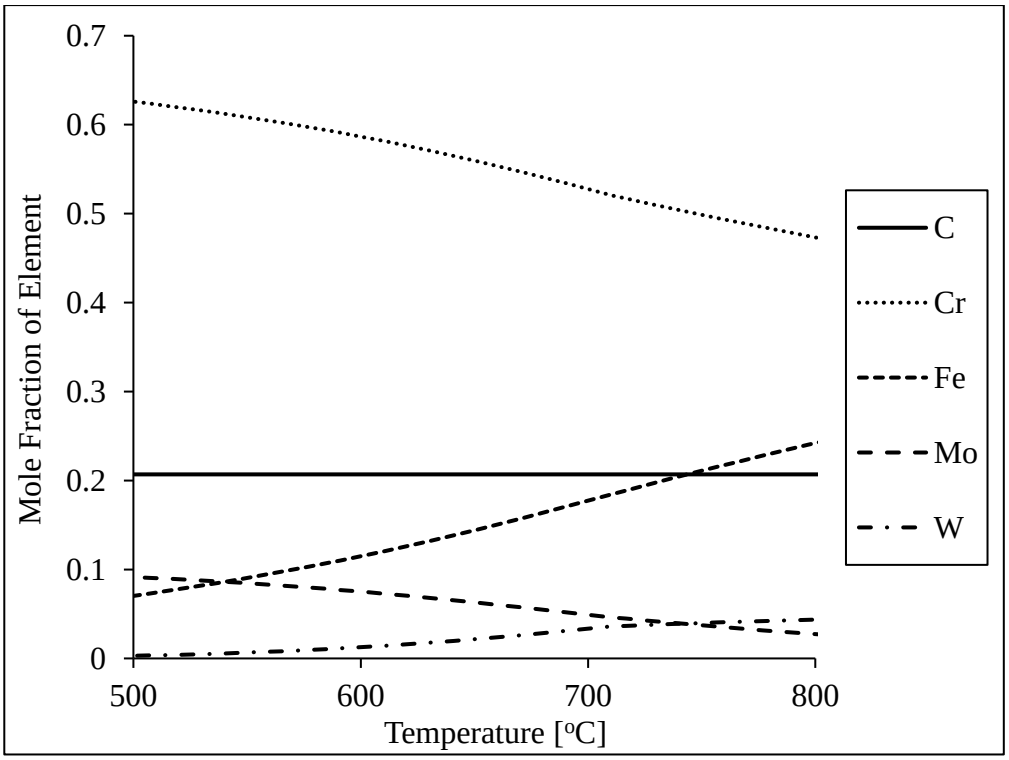

Figure 5.4: Predicted composition of the $M_{23}C_6$ phase in the DB P92.

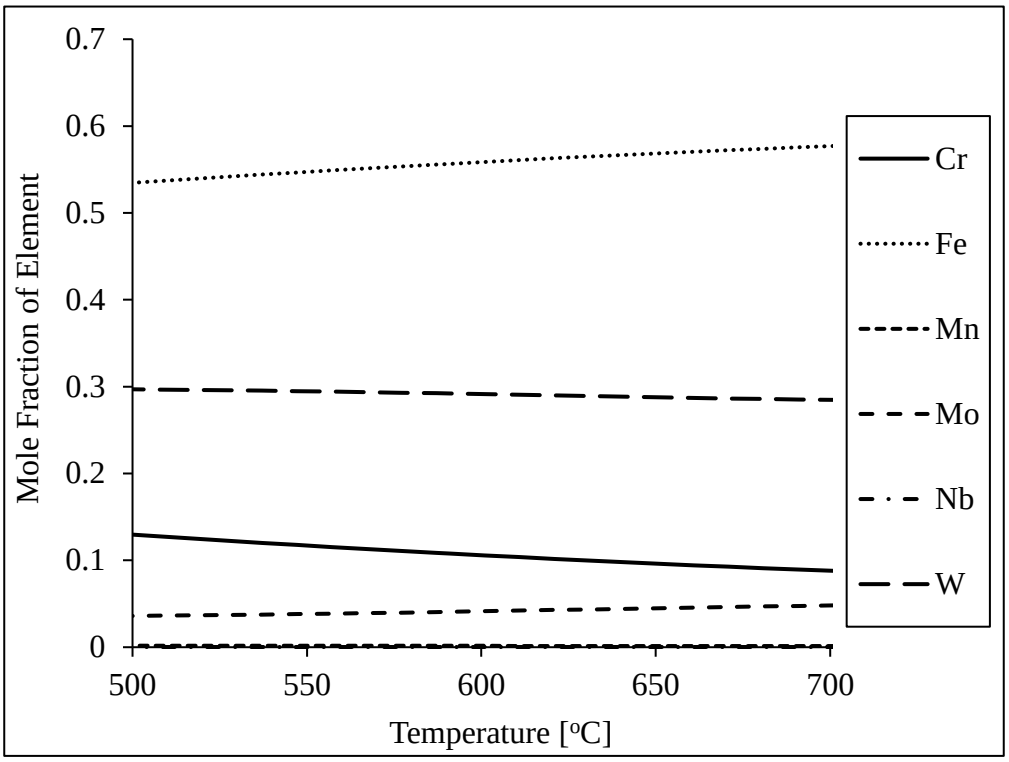

Figure 5.5: Predicted composition of the Laves Phase in the DB P92.

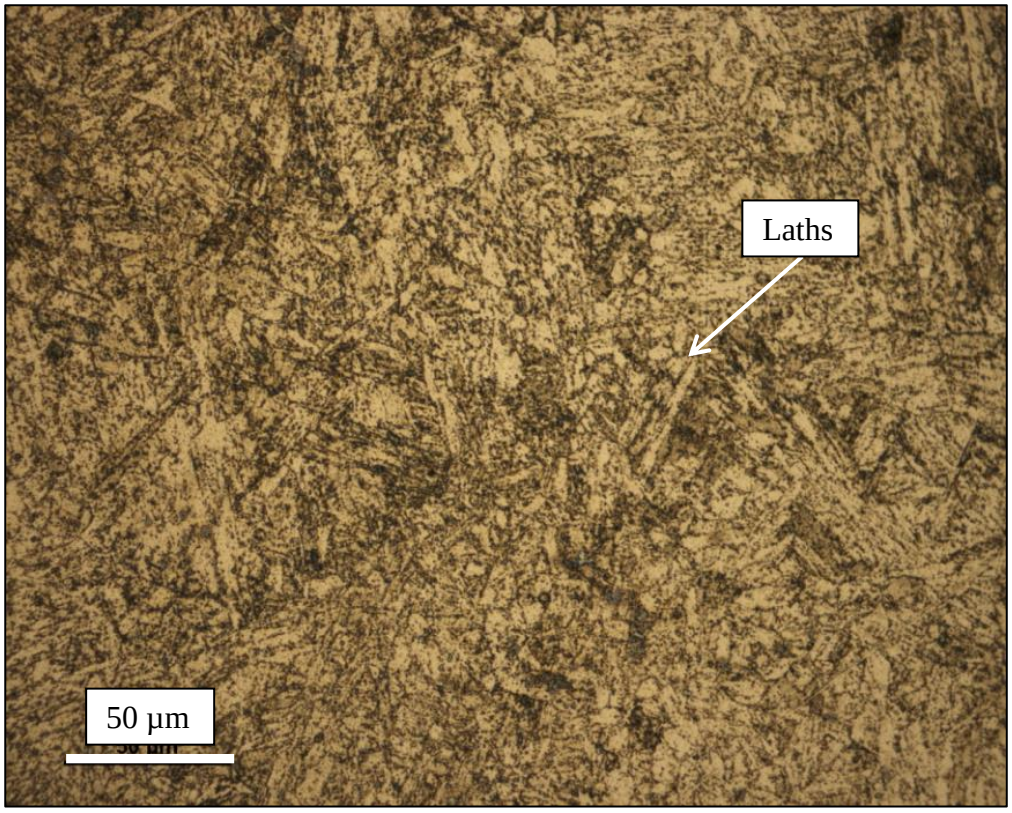

Figure 5.6: Optical micrograph of the microstructure of DB P92, showing the tempered martensitic lath structure.

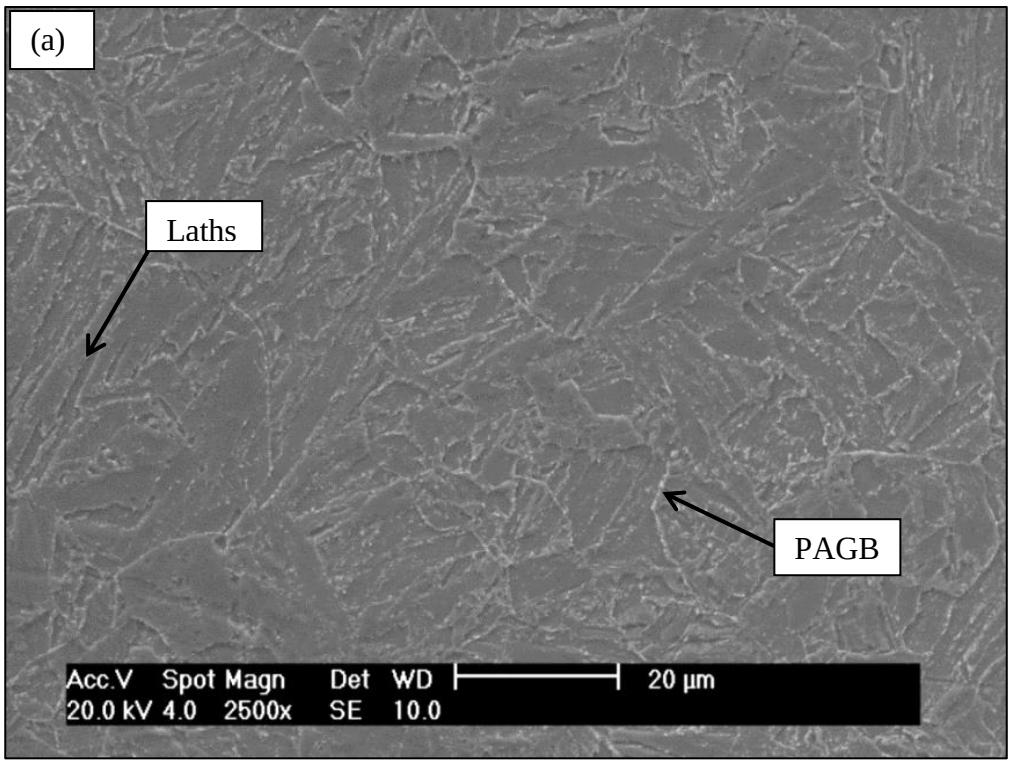

Figure 5.7 (a): SEM micrograph of DB P92 showing the PAGBs and tempered martensitic lath boundaries.

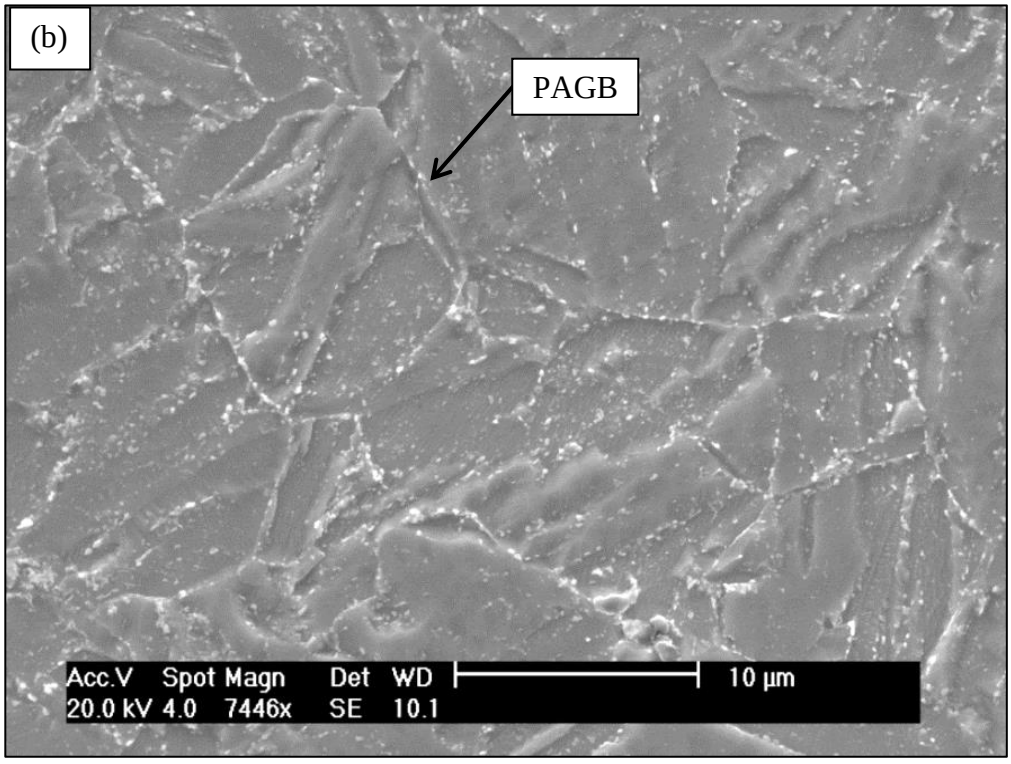

Figure 5.7 (b): SEM micrograph of DB P92 showing a number of submicron precipitates located at PAGBs.

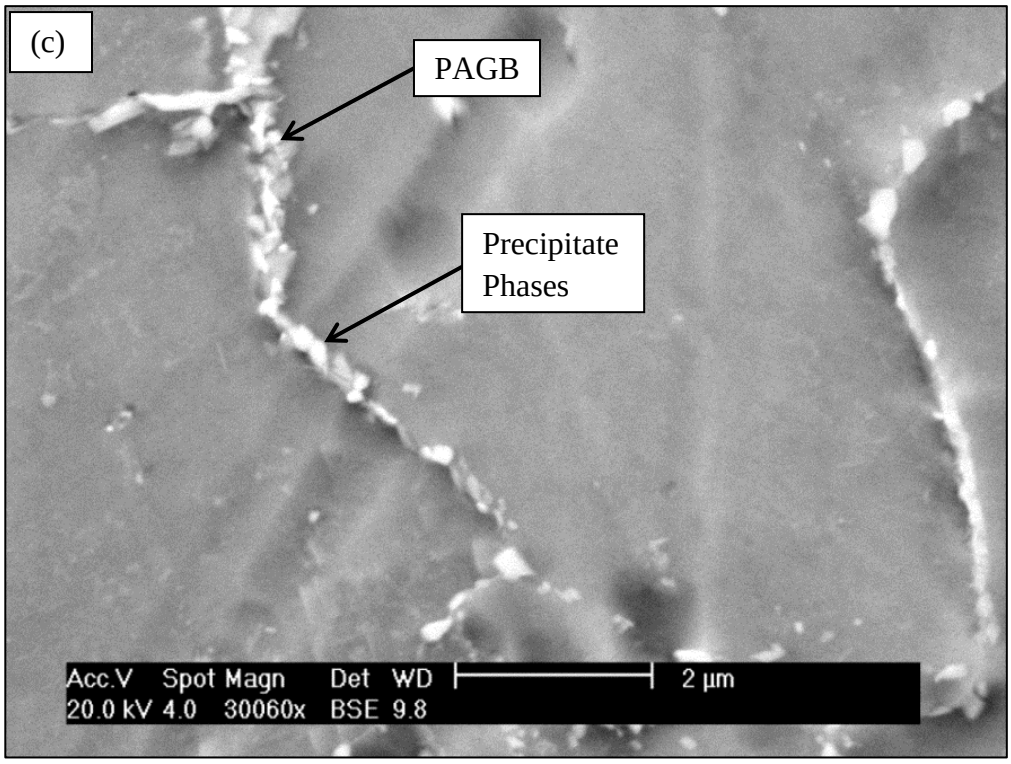

Figure 5.7 (c): High magnification SEM micrograph of DB P92 showing a number of submicron precipitates located on PAGBs.

5.2.3 P92 Microstructural Characterisation

OM, SEM and micro-hardness testing have all been used to characterise the as-received DB P92. Figures 5.6 and 5.7 show a series of OM and SEM images of DB P92 following etching with Vilella's reagent. Figure 5.6 is an optical micrograph showing the tempered martensitic lath structure. Figure 5.7 shows a series of SEM images of increasing magnification that were taken to characterise the precipitate phases in the as-received DB P92. Figure 5.7a again shows the tempered martensitic lath structure. In figure 5.7b the PAGBs are decorated by precipitates and they have a grain size of between 10-20 µm. Precipitates are also seen at lath boundaries. On PAGBs the larger particles in figure 5.7c were found by EDX analysis to be chromium rich and probably

therefore $M_{23}C_6$, with a diameter of around 50-100 nm [Zielinska-Lipiec and Czyrska-Filemonowicz, 2007]. The remaining precipitate species were too small to be analysed conclusively by SEM but from the literature in chapter 2 they are most likely to be MX phase [Czyrska-Filemonowicz et al., 2006; Gustafson and Hattestrand, 2002]. Zielinska-Lipiec and Czyrka-Filemonowicz [2007] show MX phase have a diameter of 10-20 nm.

The average micro-hardness of the as-received DB P92 was measured using a Vickers hardness indenter and a 200 gf load. 10 measurements were performed and an average calculated. The average hardness was calculated to be 234 HV, with a standard deviation of ± 7 HV. Chalk [2013] shows that the hardness values for DB P92 are slightly lower than typical values in the literature (250-300 HV).

5.3 Discussion of P92 Microstructure and Modelling

Phase fraction diagrams for DB P92 identify the Ae_1 temperature, the point at which ferrite starts to transform to austenite [Chalk, 2013; Srinivas Prasad et al., 2012; Chalk et al., 2011]. For DB P92 this is identified as being 819 ^{o}C, this is slightly higher than the Ae_1 temperatures calculated using Thermo-Calc for several typical P92 steels by Chalk [2013]. This work found that P92 had Ae_1 values of between 758 and 771 ^{o}C. This slight difference is likely due to small differences in the amount of minor alloying elements in the DB P92. For example chapter 2 showed that some minor additions like nickel, manganese and carbon are shown to be austenite stabilisers, therefore lowering the Ae_1 temperature. As shown the DB P92 composition does not have particularly high concentrations of any of these austenite stabilisers. It is important that

accelerated testing temperatures (isothermal ageing and creep) conducted throughout the rest of the thesis for DB P92 remain well below this predicted Ae_1 temperature because after this point the mechanical and microstructural properties of the P92 would be significantly altered [Ennis et al., 2000]. Likewise when considering coating technologies for DB P92 it is important that the coating deposition or any subsequent heat treatment does not exceed the Ae_1 temperature.

The precipitate phase fraction diagram for the DB P92 shows that the MX phase remains relatively stable, especially between 500 and 800 ^{o}C. This would suggest that MX phase is the most useful precipitate for pinning and preventing the movement of dislocations. $M_{23}C_6$ shows a slight reduction in phase fraction as temperature is increased, although it appears fairly stable between 500 and 800 ^{o}C. After 800 ^{o}C though significant reduction in the $M_{23}C_6$ phase is seen. Laves phase shows the most significant result for future high temperature operation as between 500 and 700 ^{o}C the phase fraction of Laves phases almost completely reduces as temperature is increased. By 700 ^{o}C the Laves phase has completely dissolved, this agrees with the work of Falat et al. [2009], Vyrostkova et al. [2008] and Dimmler et al. [2003] which all study Laves phase stability. The literature generally agrees that MX and $M_{23}C_6$ have a beneficial effect on the mechanical properties mainly by precipitation strengthening and the pinning of dislocation motion [Abe at al., 2007]. However the effect of Laves phase on the mechanical properties (especially long term creep) has been widely debated in the literature. When Laves phase composition is plotted it is clear that the precipitation of Laves phase will promote the depletion of tungsten and molybdenum, meaning they are not

available for solid solution strengthening. Typically it has always been thought that Laves phase precipitation is detrimental to creep strength because of the associated reduction in the solid solution strengthening [Chalk, 2013; Hosoi et al., 1986]. However more recently it has been suggested that the precipitation of fine Laves phase could be beneficial to P92 creep as it contributes to the precipitate strengthening [Chalk, 2013; Hald, 1996]. The study of precipitate phase fractions again highlights the importance of keeping coating deposition temperatures low to prevent adverse effects for the precipitate phases.

The MX phase in DB P92 is predominantly expected to be of the form (V, Nb)(N,C) when the composition is compared to the known compositions of the MX phase [Chalk, 2013; Sourmail, 2001]. The MX phase is shown to contain mainly vanadium with smaller amounts of niobium as the non-metal, and mainly nitrogen with small amounts of carbon as the non-metal (V, N). This VN form is the most prevalent version of MX that is observed and is desirable because its fine size and distribution can prevent the movement of dislocations [Sawada et al., 2003; Sourmail, 2001]. This is the most dominant type rather than the niobium rich version, (Nb(N,C)), because in DB P92 the niobium content is relatively low. Over the range of temperatures from 500-800 ^{o}C the composition of the precipitate appears to be stable with very little variation. This is very encouraging for the high temperature integrity of the steel following long exposures as this would suggest that the MX phase remains stable even at high temperature. MX phase is shown to be one of the most desirable phases for high temperature creep resistance (chapter 2) by pinning and preventing dislocation movement [Ennis et al., 1997].

The $M_{23}C_6$ in DB P92 is found to be chromium rich and is most likely of the form $Cr_{23}C_6$ with an FCC crystal structure [Hald, 1996]. The general form of the $M_{23}C_6$, considering the minor elements in the composition, would be (Cr, Fe, Mo, W)$_{23}C_6$. In other words the $M_{23}C_6$ is mainly $Cr_{23}C_6$ but iron, molybdenum and tungsten can partially substitute for the chromium. Again over the range of temperatures from 500-800 ^oC the composition of the precipitate appears to be stable. However, Thermo-Calc does predict that the composition will vary with temperature [Hald and Korcakova, 2003]. The iron and tungsten levels increase with temperature whilst the chromium and molybdenum are shown to decrease. This would suggest that iron and tungsten rich $M_{23}C_6$ begin to form at the expense of chromium rich $M_{23}C_6$.

The intermetallic Laves phase in DB P92 is tungsten and iron rich. Once again over the range of temperatures from 500-800 ^oC the composition of the precipitate phase is stable. The extensive work conducted by Hald [2008] would suggest that the Laves phase is of the form; (Fe, Cr)$_2$(Mo, W) following creep tests at below 720 ^oC.

Overall the microstructural characterisation and thermodynamic modelling of DB P92 in this chapter suggest that the P92 is more than capable of operating at temperatures of 600-700 ^oC without major microstructural transformation. Also there is no evidence of precipitate dissolution, of the most important precipitates for creep resistance (MX, $M_{23}C_6$), until > 700 ^oC. However as shown in the literature in chapter 2 the major limiting factor for P92 operation temperature is the enhanced oxidation damage that occurs. Oxidation resistant coatings are a solution for higher temperature operation.

5.4 P92 Tensile Properties

Tensile testing of DB P92 has been performed at room temperature (20 ^{o}C), 650 ^{o}C and 675 ^{o}C. The primary aim is to determine the yield stress, ultimate tensile stress and Young's modulus of the DB P92 steel at these temperatures. This not only allows comparison of the behaviour of DB P92 to the typical P92 in the literature but it also allows the test conditions for creep and fatigue testing of the material to be determined. Table 5.2 summarises the tensile testing that is presented in figures 5.8-5.10. The general trend shows that when the temperature is increased the yield stress, ultimate tensile strength and Young's modulus of the DB P92 all decrease. The elongation to failure is shown to increase with increasing temperature suggesting the material is becoming more ductile at higher temperatures. Examination of all of the failed samples shows a failure mechanism dominated by ductile failure at all three temperatures. The shape of the curves in figures 5.8-5.10 also suggests a classically ductile tensile test. Extension is measured using the high temperature extensometers and the position is measured from the crosshead movement of the test machines (less accurate than extensometers).

Table 5.2: Tensile Properties of DB P92.

Temperature [^{o}C]	**Yield Stress [MPa]**	**Ultimate Tensile Stress [MPa]**	**Modulus [GPa]**	**Elongation to Failure [%]**
20	450	700	207	20.0
650	150	290	172	26.5
675	125	250	132	28.0

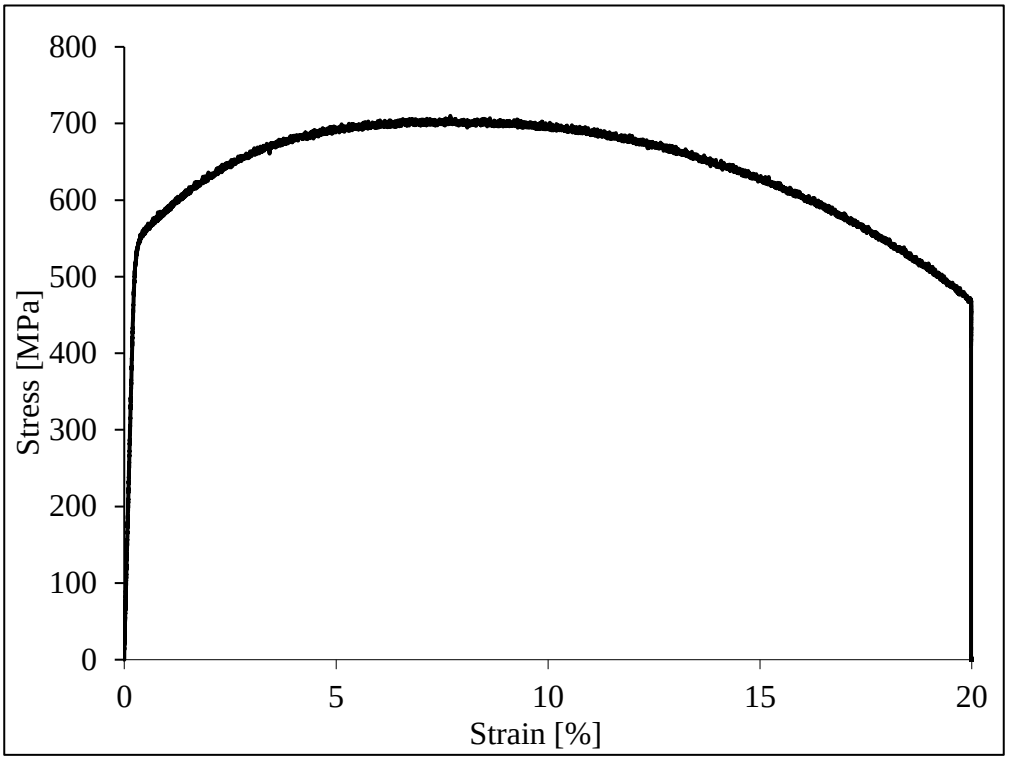

Figure 5.8: Tensile test for DB P92 at room temperature (20 ºC).

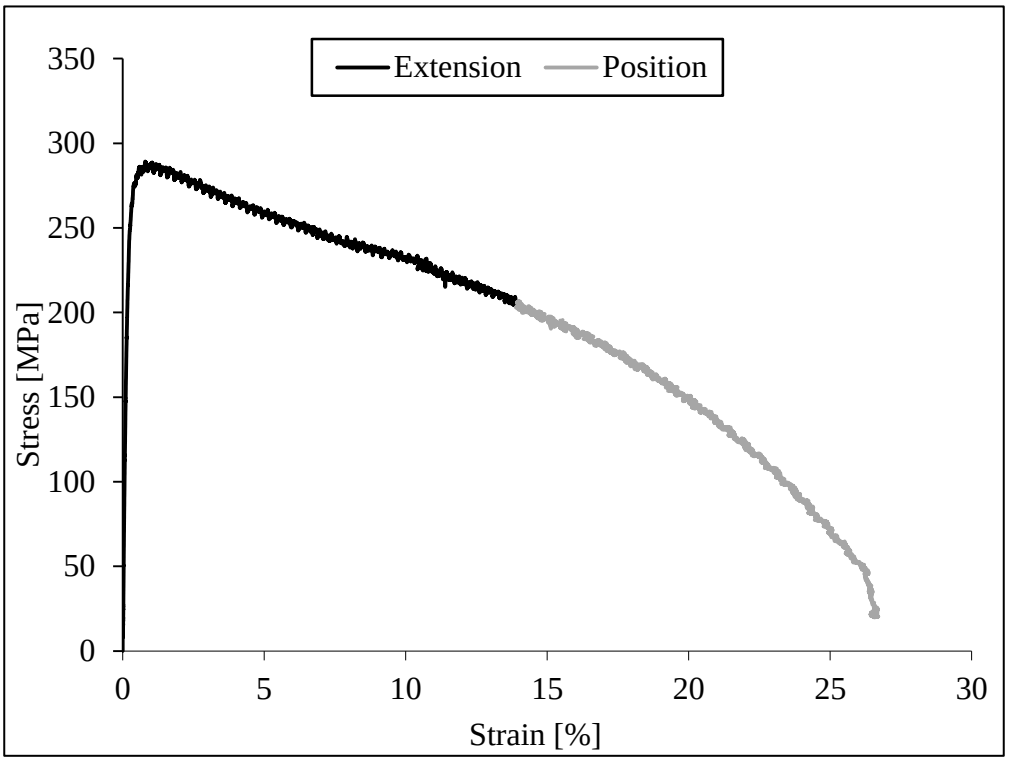

Figure 5.9: Tensile test for DB P92 at 650 ºC.

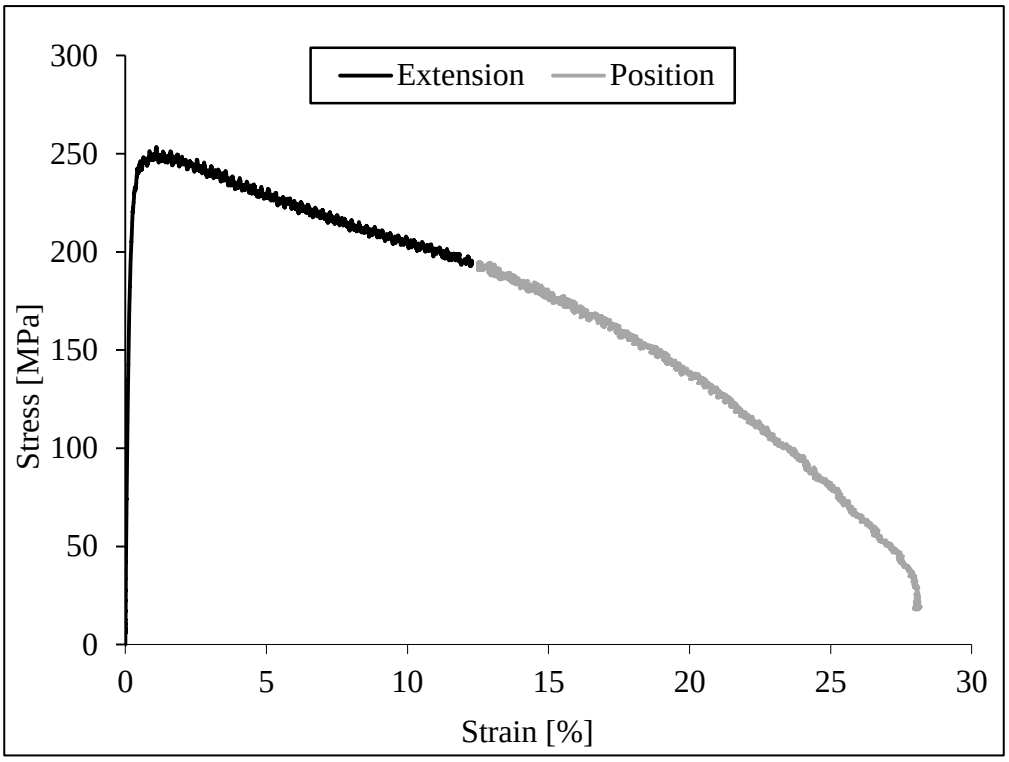

Figure 5.10: Tensile test for DB P92 at 675 ºC.

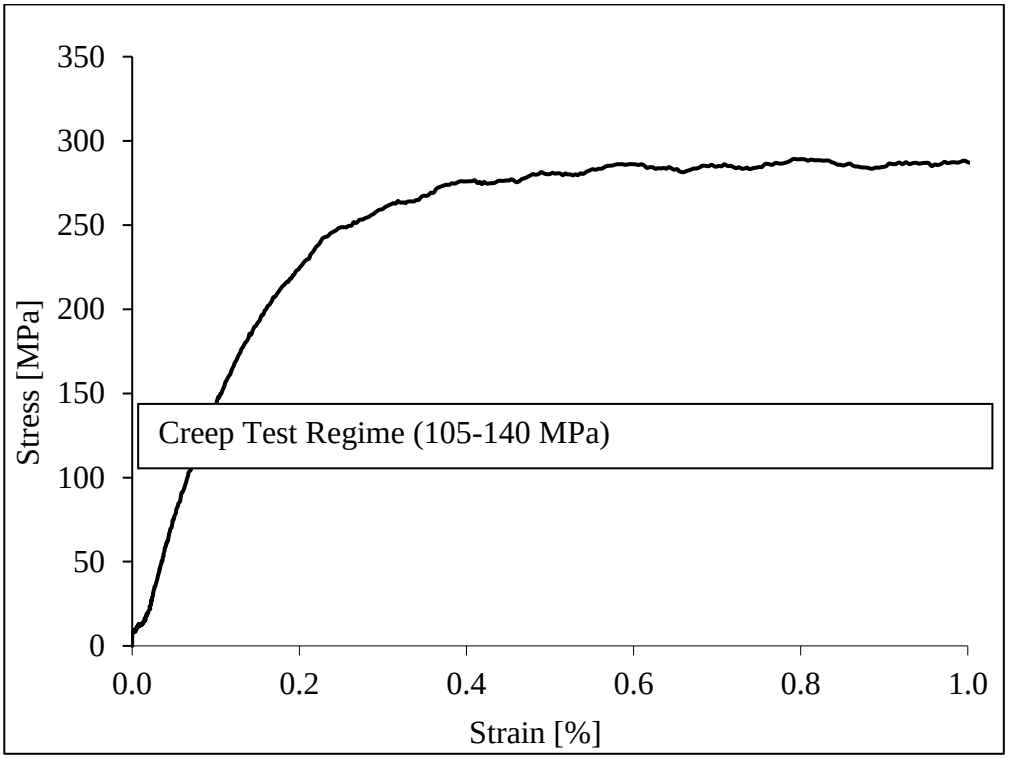

Figure 5.11: Tensile test for DB P92 material at 650 ºC (figure 5.9), with the creep testing regime for this temperature labelled.

5.5 P92 Creep Properties

Figure 5.11 shows that the creep test regime at 650 ^{o}C is chosen to be below the yield point and the ultimate tensile strength of the material. This is consistent with the 675 and 700 ^{o}C testing. Figures 5.12-5.14 present the creep curves (strain versus time) for the uncoated P92 testing performed at 650, 675 and 700 ^{o}C, respectively. The first observation to make is that in all cases a reduction in the test stress results in an increase in the failure life and a decrease in the minimum creep strain rate (figure 5.15). Table 5.3 also generally indicates that the failure strains decrease with decreasing stress. This illustrates that as the stress is reduced the failure mechanism will become more creep brittle in nature. At the highest stresses the failure strains are large suggesting a more ductile failure. Figure 5.15 also suggests that there is a difference in the creep failure mechanism from ductile (140, 130 MPa) to more brittle (105-120 MPa). Temperature also influences creep behaviour, for example consider the 80 MPa test at 675 and 700 ^{o}C. There is a ~ 10 fold reduction in the creep life when increasing the creep test temperature from 675 to 700 ^{o}C.

Figure 5.16 shows the 650 ^{o}C creep tests plotted against the ECCC mean data for P92 [ECCC, 2005], taken from chapter 2 (equation 2.1). From figure 5.16 the DB P92 at high stress (ductile failure) is below the ECCC mean values suggesting that DB P92 has a shorter creep life than the P92 average. At lower stress (brittle failure) the DB P92 matches the ECCC mean data much more closely. This is most likely explained because the ECCC mean data has mainly been determined from low stress brittle creep tests and is therefore unlikely to

account for the change in failure mechanism at high stress. This suggests that for coated creep tests the lower stress conditions should be used.

The creep tests performed for DB P92 have been conducted at accelerated conditions. This means that a higher test stress and temperature have been used, compared to conditions that would actually be seen in service. This is to ensure that total creep test time is within the constraints of the research project. One of the principle extrapolation techniques is the Larson-Miller relationship [Callister and Rethwisch, 2007]. This allows for the results of higher temperature accelerated creep tests to be extrapolated down to more realistic industrial temperatures. This theory is derived based on the Arrhenius equation but it is also found to hold empirically. The Larson-Miller equation is given by equation 5.1:

$$P_{LM}(\sigma) = T(C_{LM} + log_{10}t_f) \qquad \text{[Equation 5.1]}$$

In equation 5.1, P_{LM} is the Larson-Miller parameter for a given material and stress level, T is the absolute temperature in kelvin, C_{LM} is a constant (typically around 20 [Callister and Rethwisch, 2007]), t_f is the time in hours to failure (or to reach a given value of creep strain) and σ is the stress in MPa. The time to failure of a given material, at a specific stress, will vary with temperature such that the Larson-Miller parameter remains constant [Callister and Rethwisch, 2007]. Assuming a C_{LM} value of 20, figure 5.17 shows the Larson Miller constant plotted against the stress for all three temperatures of the DB P92 tests. For example the 105 MPa creep test in air at 650 ºC failed at 3647 hours. When extrapolated down to 600 ºC (105 MPa), the failure time is 81,489 hours.

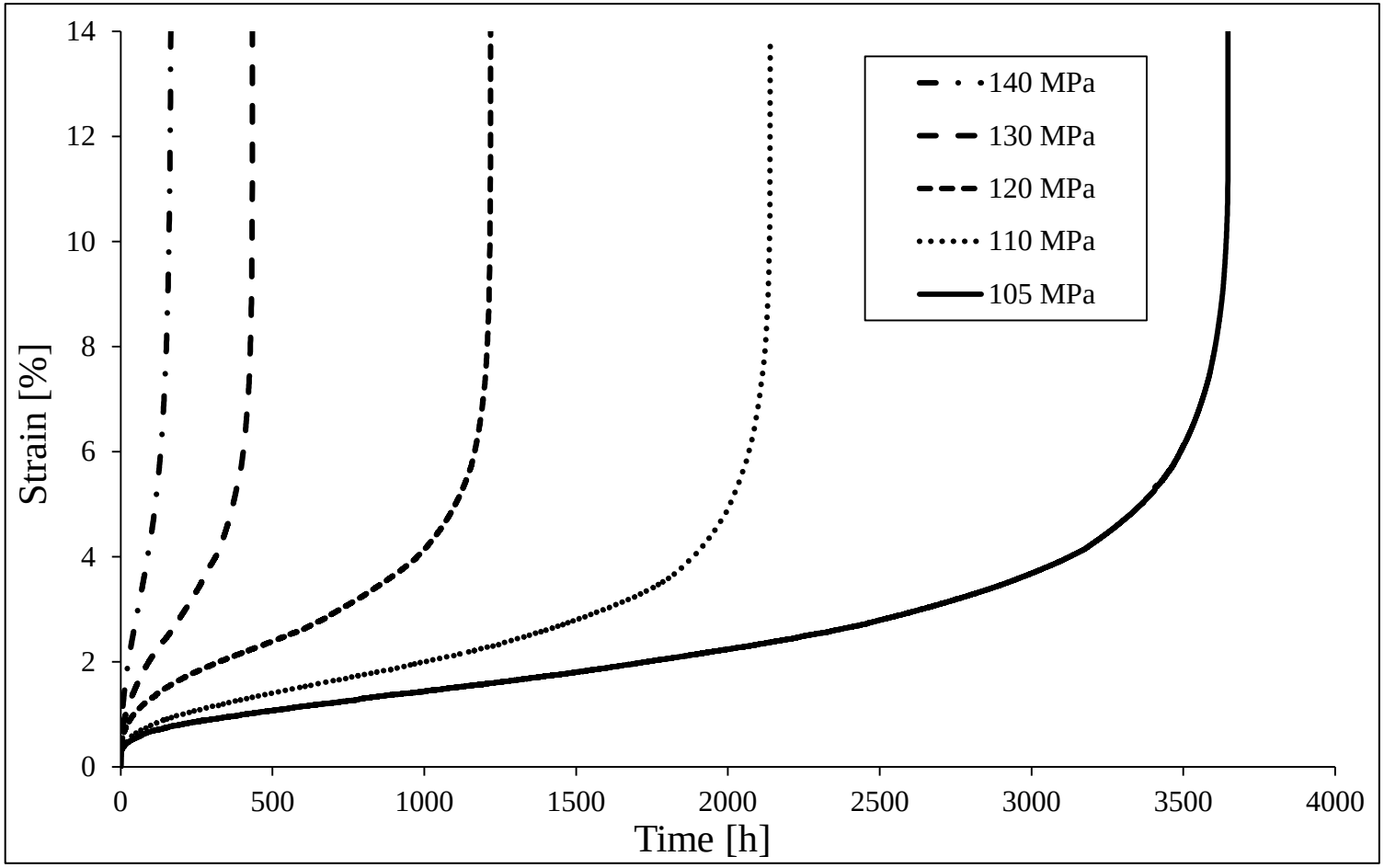

Figure 5.12: Strain-time curves for uniaxial creep testing of DB P92 at 650 ºC and stresses from 105-140 MPa.

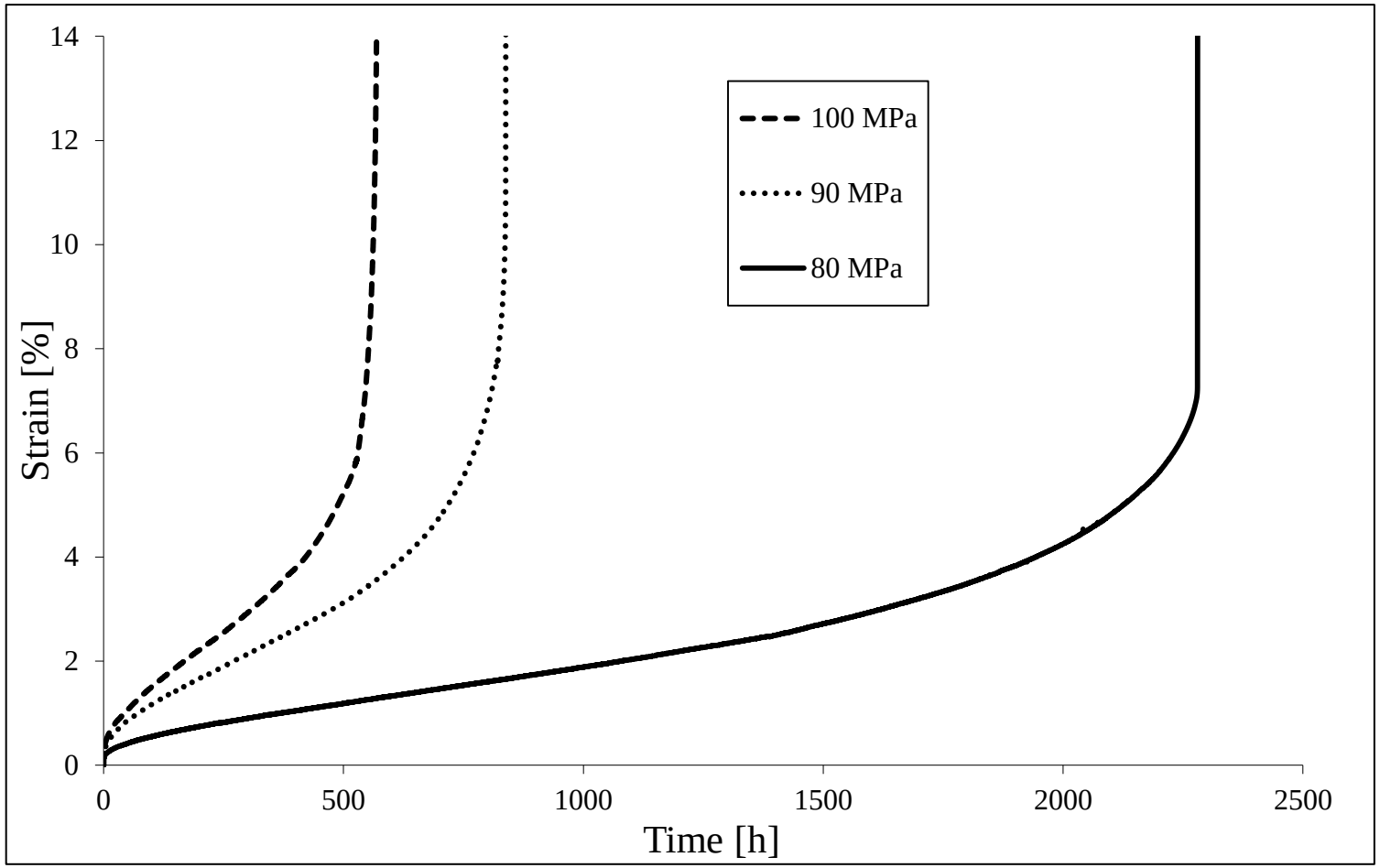

Figure 5.13: Strain-time curves for uniaxial creep testing of DB P92 at 675 ºC and stresses from 80-100 MPa.

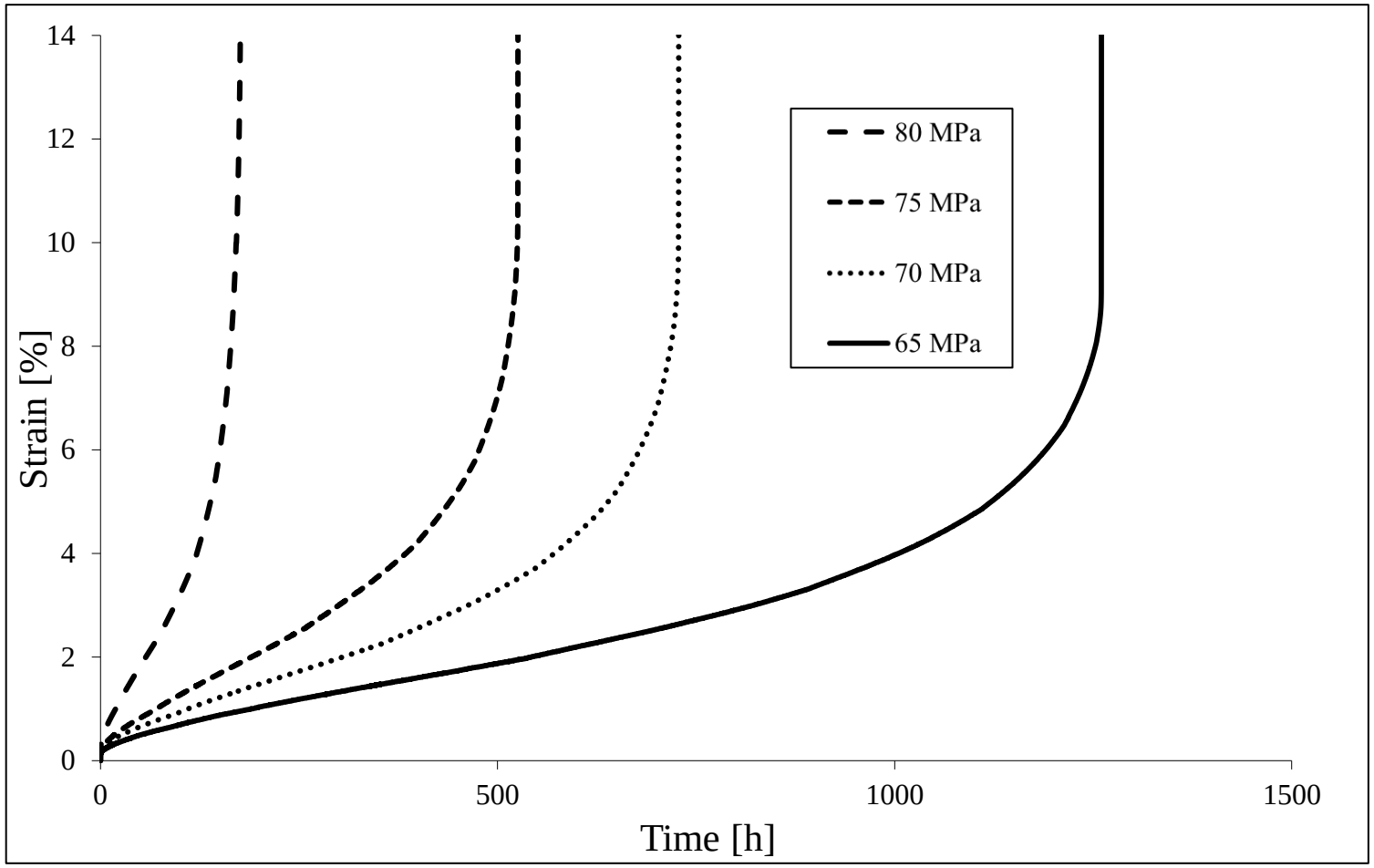

Figure 5.14: Strain-time curves for uniaxial creep testing of DB P92 at 700 ºC and stresses from 65-80 MPa.

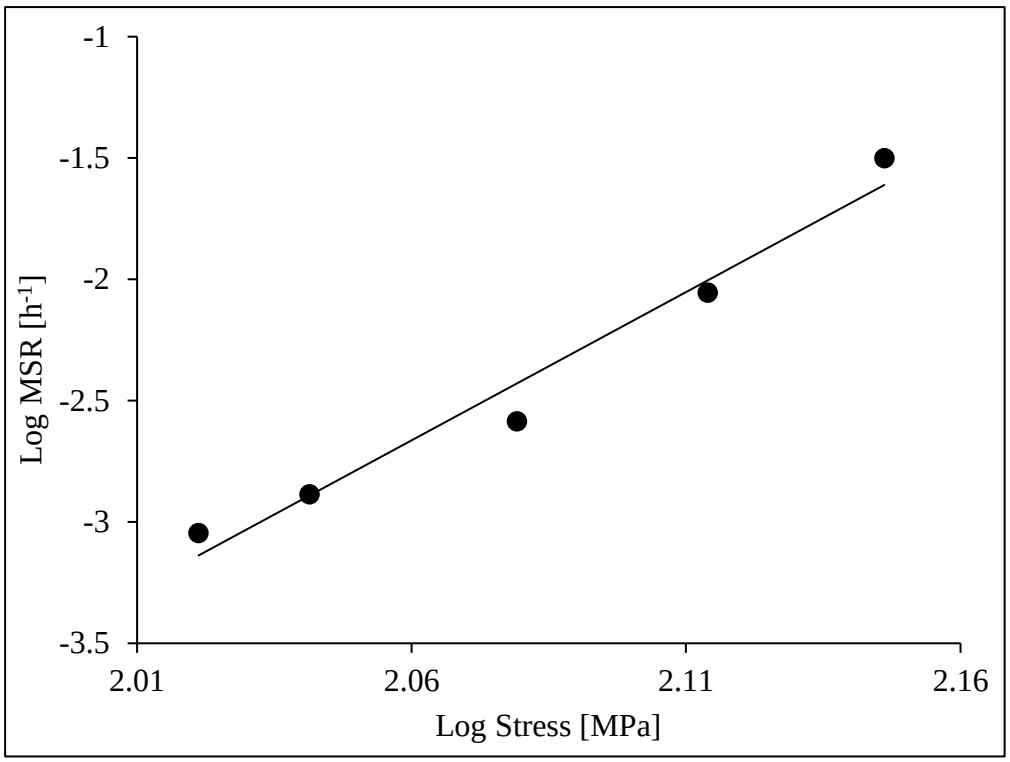

Figure 5.15: Log-log plot of minimum creep strain rate against stress for DB P92 650 ^{o}C creep testing performed at stresses of 105-140 MPa.

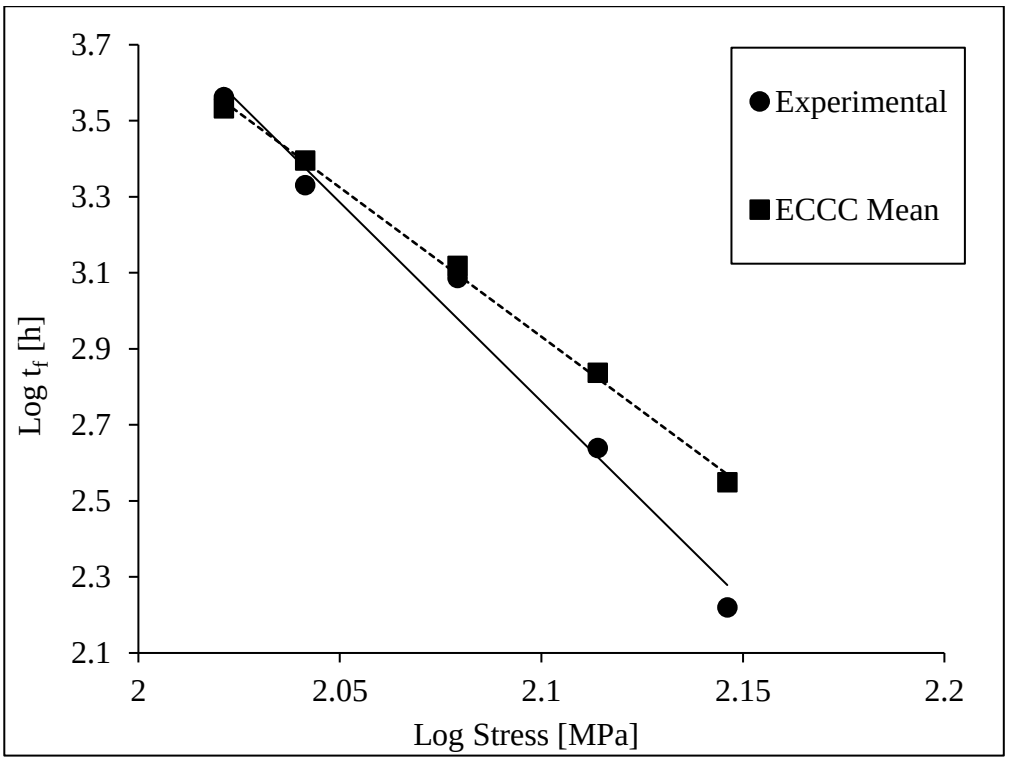

Figure 5.16: Log-log plot of time to failure against stress for DB P92 650 ^{o}C creep testing plotted with ECCC mean data for comparison [ECCC, 2005].

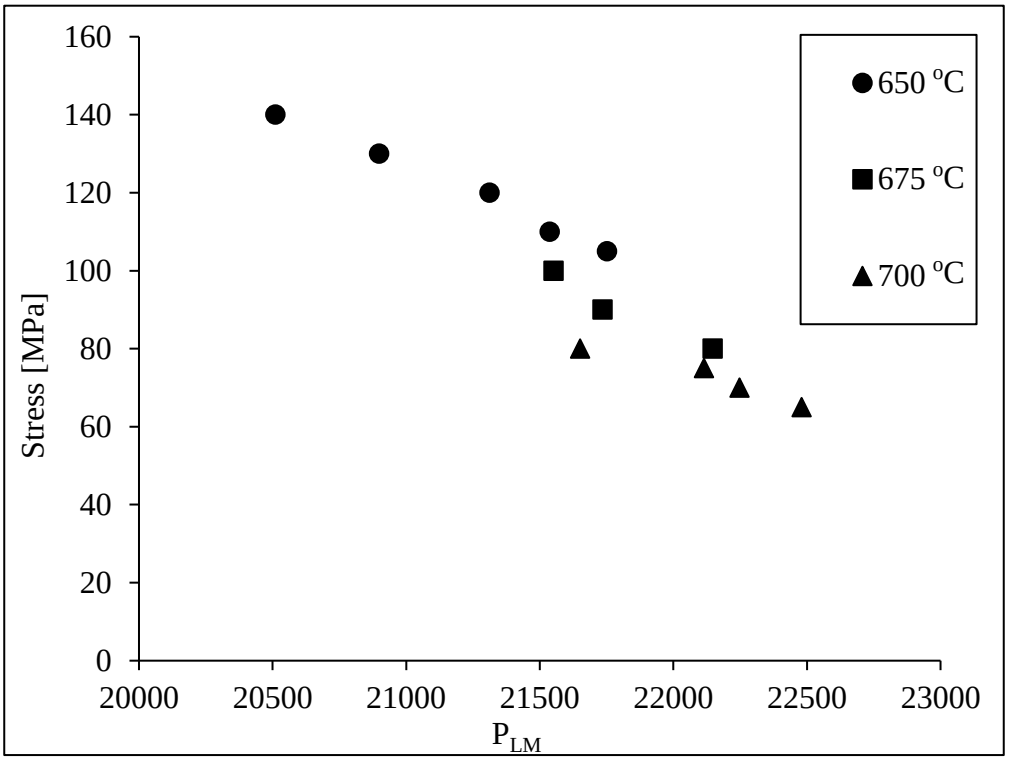

Figure 5.17: The applied stress for DB P92 plotted against the Larson-Miller parameter, P_{LM}, for creep testing at 650-700 °C.

Table 5.3: Summary of DB P92 Creep Test Results.

Temperature [°C]	**Stress [MPa]**	**Rupture Time [h]**	**Approximate Failure Strain [%]**
650	105	3647	9.9
650	110	2139	5.3
650	120	1219	6.8
650	130	435	7.7
650	140	165	9.0
675	80	2280	6.9
675	90	838	8.0
675	100	538	9.0
700	65	1260	8.6
700	70	728	9.4
700	75	530	11.4
700	80	177	14.0

5.6 P92 Low Cycle Fatigue Properties

Although creep is the main concern for power plant steels, cyclic testing is also becoming increasingly important to simulate the typical start up/shut down behaviour of a power plant. Strain values of 0.3, 0.4 and 0.5 % have been chosen. Figure 5.18 shows that the stresses being used for LCF testing are considerably higher than those used for creep testing. A summary of the three tests conducted is included in table 5.4. A comparison of the peak stress reduction is included in figure 5.19 to show the stress evolution during the strain controlled LCF tests. This shows that as the strain percentage is reduced the cycles to failure increases. The 0.4 and 0.5 % tests are similar partly because the corresponding stress at these test strains is similar (figure 5.18). Figure 5.20 shows the LCF tests follow an approximately linear trend.

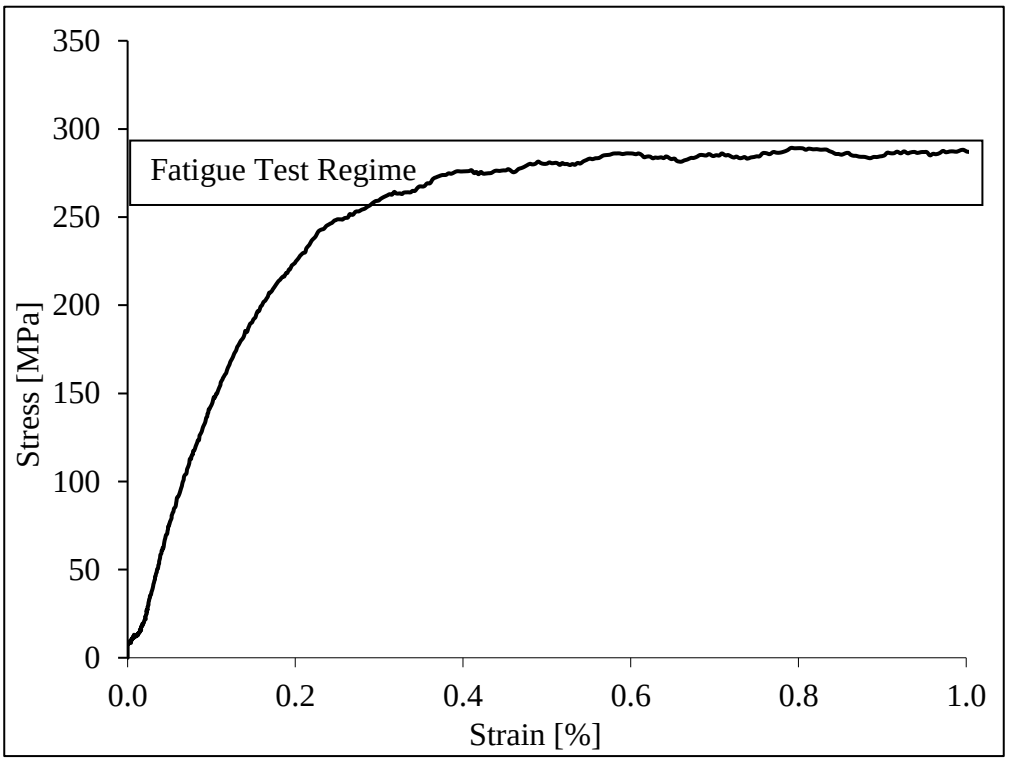

Figure 5.18: Tensile test for DB P92 material at 650 ºC (figure 5.9), with the low cycle fatigue testing regime for this chapter labelled (0.3-0.5 % strain).

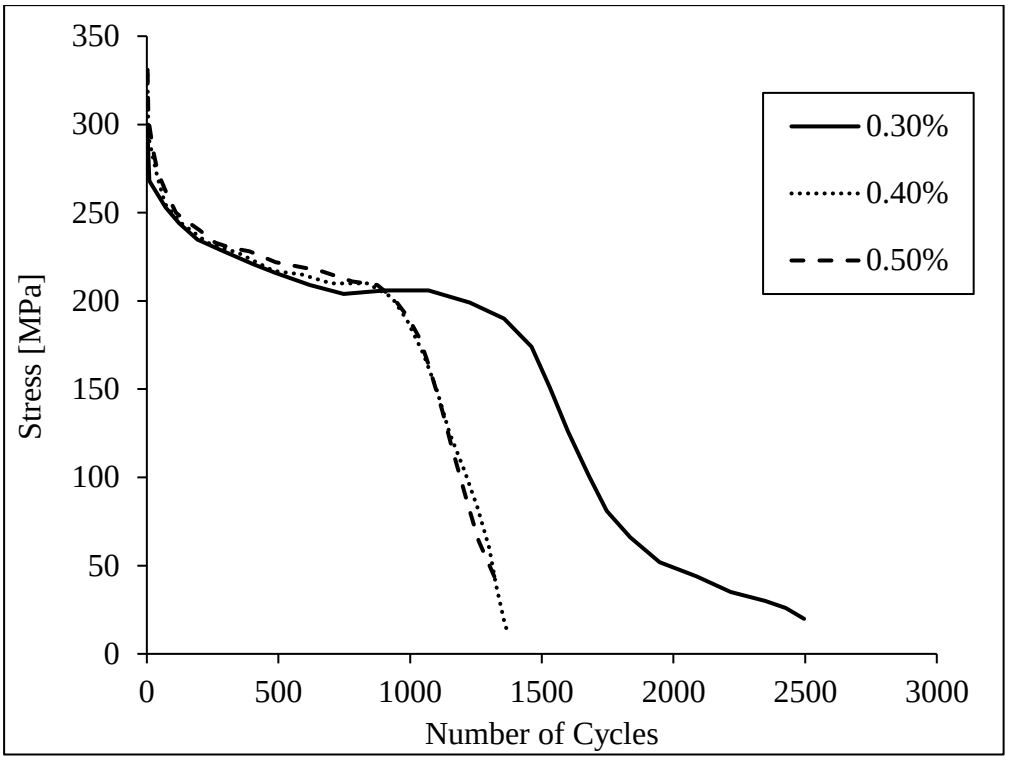

Figure 5.19: Peak stress plotted against number of cycles for the 650 ºC strain controlled LCF tests for DB P92 at 0.3, 0.4 and 0.5 % strain.

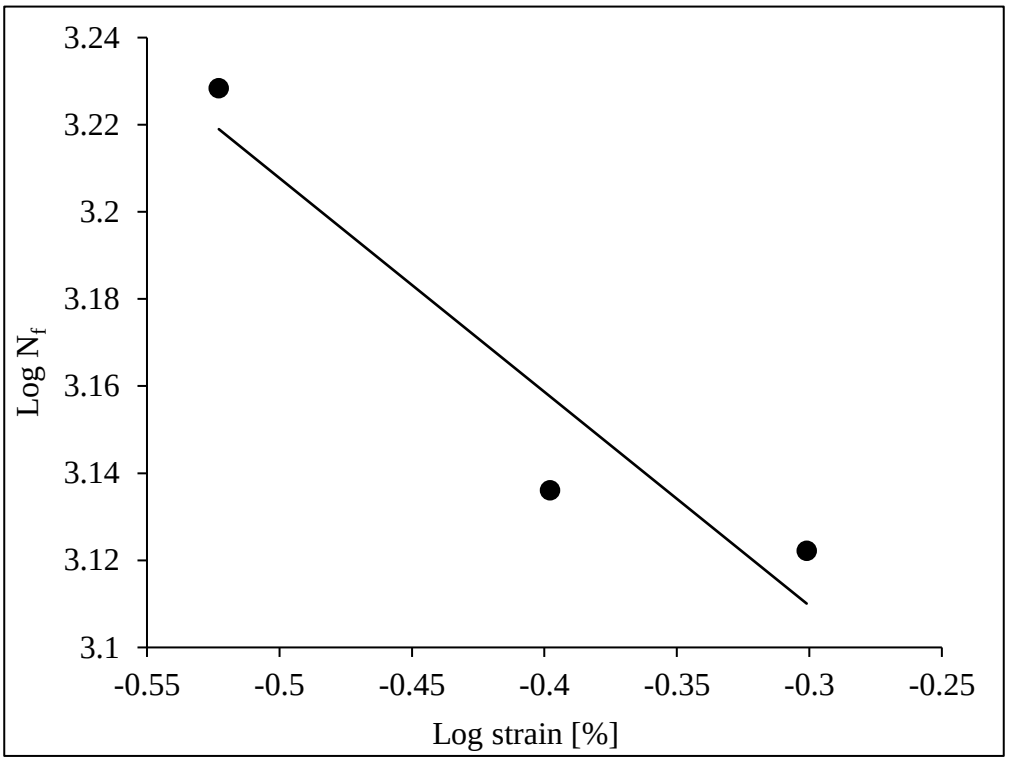

Figure 5.20: Log-log plot to show number of cycles to failure plotted against strain percentage for the LCF tests of DB P92

Table 5.4: Uncoated DB P92 LCF tests.

Temp [ºC]	Strain [%]	Speed [%/s]	Cycle Time [s]	Cycles to Failure	Total Test Time [h]
650	0.3	0.1	6	2496	4.2
650	0.4	0.1	8	1368	3.0
650	0.5	0.1	10	1325	3.7

5.7 P92 Low Cycle Creep-Fatigue Properties

Although LCF testing is very useful for simulating start up and shut down, in reality a power plant would never experience such a defined fatigue loading form. In reality the power station would be operated at full capacity with an occasional shut down cycle. Therefore it is much more relevant to test a waveform that is predominantly creep loading with an occasional cyclic load. Table 5.5 summarises the exact test conditions of the creep-fatigue tests.

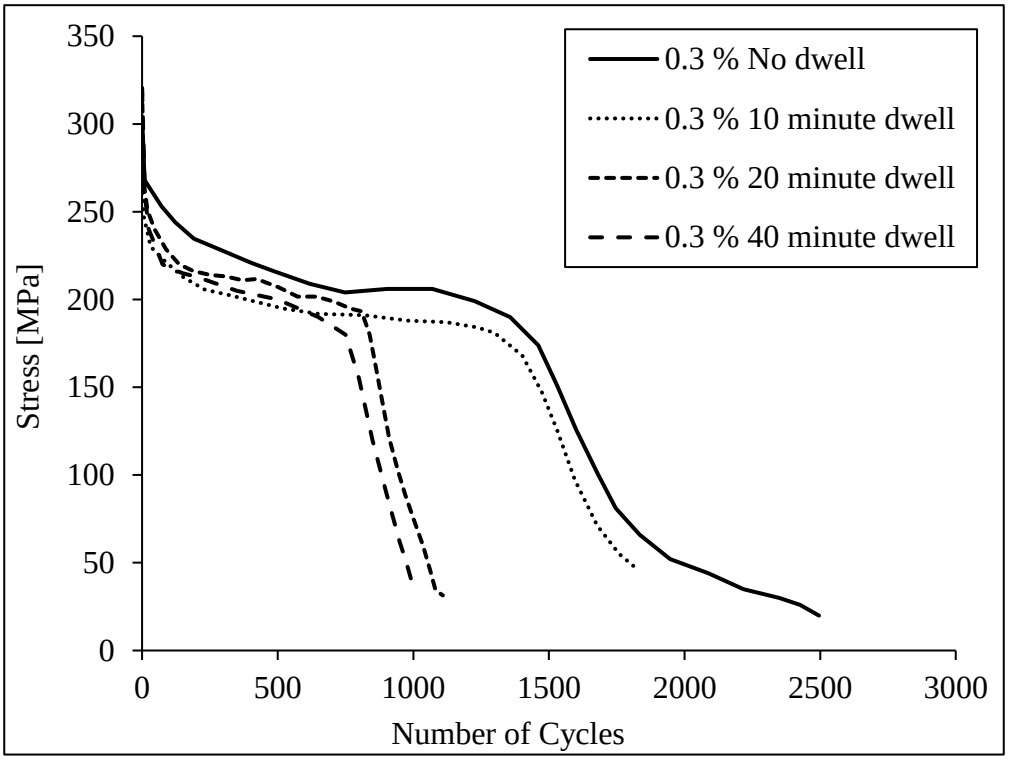

Figure 5.21: Peak stress plotted against number of cycles for the 0.3 % strain creep-fatigue tests at 650 ºC with tensile dwells of 10, 20 and 40 minutes.

Table 5.5: Uncoated DB P92 creep-fatigue tests.

Temp [ºC]	Strain [%]	Speed [%/s]	Dwell Time [s]	Cycle Time [s]	Cycles to Failure	Total Test Time [h]
650	0.3	0.1	600	606	1811	304
650	0.3	0.1	1200	1206	1109	372
650	0.3	0.1	2400	2406	1002	670

Figure 5.21 shows the peak stress evolution with cycle number for the creep-fatigue tests compared to the corresponding pure fatigue test performed at 0.3 % strain. Increasing the dwell time is shown to increase the overall time of the cyclic test but is shown to reduce the cycles to failure. This is likely because the specimen experiences increased creep loading during the longer dwell time.

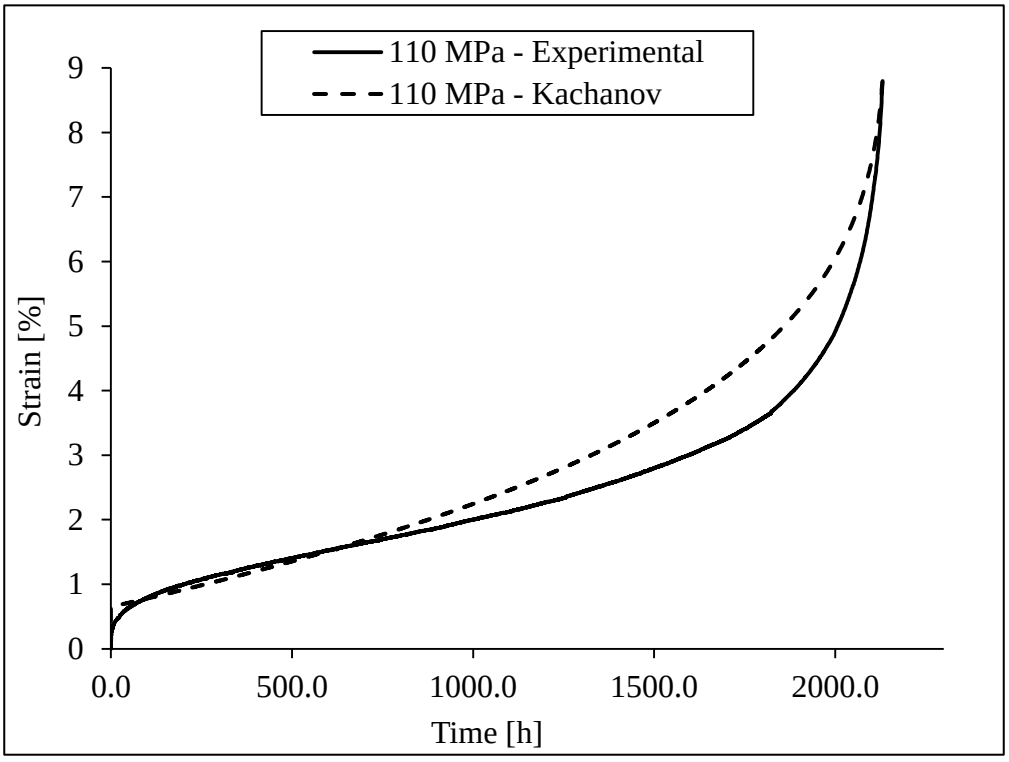

Figure 5.22: Calculated creep strain curves (Kachanov model) fitted to experimental creep strain curves, for DB P92 at 650 ºC and 110 MPa (see page 159).

5.8 Creep Modelling

5.8.1 Creep Models

Some of the most common creep models are Norton, Kachanov and Liu and Murakami. For the purposes of this work Kachanov will be used because of its relative simplicity [Hyde et al., 2006; Liu and Murakami, 1998; Kowalewski et al., 1994].

5.8.1.1 Norton Creep Model

Norton's law is one of the most commonly used models because of its simplicity. Only secondary creep, known as steady state creep, is modelled using the minimum creep strain rate. Norton's creep law is given in equation 5.2:

$$\dot{\varepsilon}_{min} = A\sigma^{n} \qquad \text{[Equation 5.2]}$$

In equation 5.2, $\dot{\varepsilon}_{min}$ is the minimum creep strain rate, A is the creep intercept, n is the creep exponent and σ is the stress [Saber et al., 2011].

5.8.1.2 Kachanov Damage Model

Kachanov's model is based on Norton's power law creep model (equation 5.2); however it also takes into account the material cavitation during creep. This means that the model can extend to the tertiary creep region. This versatile use means it is frequently used for life prediction in industrial applications. The

uniaxial creep strain of the Kachanov model, developed for P92 steel, is given by Saber et al. [2011] and Saber [2011] as:

$$\varepsilon^c = \frac{A\sigma^{(n-\chi)}}{B(n-\phi-1)} \left([1 - B(1+\phi)\sigma^{\chi} t]^{\frac{\phi+1-n}{\phi+1}} - 1\right) \quad \text{[Equation 5.3]}$$

In equation 5.3, A, n, χ, B and ϕ are all constants to be determined from experimental data. The stress, σ, and time, t, are the only variables to be input. The constants hold for each temperature at which the tests are performed. Although caution should be exercised when using these constants beyond the stress range within which they were originally calculated [Saber et al., 2011].

5.8.2 Determination of Material Constants for Damage Model

Experimental creep rupture tests have been used to obtain the DB P92 material constants for the Kachanov damage model. Since the constants are temperature dependent a separate set of constants (A, n, χ, B and ϕ) has been determined for each temperature of interest (650, 675 and 700 ^{o}C). Determination of the 650 ^{o}C constants have been included below as an example.

5.8.2.1 A and n

To determine the values of A and n take the Log function of the equation 5.2 to give equation 5.4:

$$Log\ (\dot{\varepsilon}_{min}) = \text{Log (A)} + n\ Log(\sigma) \quad \text{[Equation 5.4]}$$

Using equation 5.4, $Log\ (\dot{\varepsilon}_{min})$ can be plotted against $Log(\sigma)$ for all stresses. The line of best fit can then be plotted where the slope is n and the intercept is $Log(A)$. Figure 5.15 shows $Log\ (\dot{\varepsilon}_{min})$ plotted against $Log(\sigma)$ for the DB P92 tested at 650 ^{o}C and stress levels of 105-140 MPa.

5.8.2.2 χ and M

Uniaxial failure time, t_f, is given by the equation 5.5. The log of equation 5.5 can then be taken to give equation 5.6.

$$t_f = \frac{1}{M\sigma^{\chi}} \quad \text{[Equation 5.5]}$$

$$Log\left(t_f\right) = -Log(M) - \chi Log(\sigma) \quad \text{[Equation 5.6]}$$

Therefore when $Log\left(t_f\right)$ is plotted against $Log(\sigma)$ the slope of the line of best fit is $-\chi$ and the intercept is $-Log(M)$. Figure 5.16 shows $Log\left(t_f\right)$ plotted against $Log(\sigma)$ for the DB P92 tested at 650 ^{o}C and stress levels of 105-140 MPa.

5.8.2.3 B and ϕ

Considering again the Kachanov equation given in equation 5.3 the material constants of B and ϕ are limited by:

$$M = B(1+\phi) \quad \text{[Equation 5.7]}$$

B and ϕ are obtained by curve fitting to experimental data using the condition given in equation 5.7. An example of this fitting for the 650 ºC tests is shown in figure 5.22 for the 110 MPa uniaxial creep test, showing a reasonably good fit.

5.8.2.4 Summary of P92 Constants

Table 5.6: A summary of creep damage constants for DB P92 at 650, 675 and 700 ºC (for stress in MPa and time in hours).

Constant	Temperature [ºC]		
	650	**675**	**700**
A	1.6 x 10^{-31}	2.2 x 10^{-17}	2.1 x 10^{-21}
n	12.7	7.3	10.0
χ	10.3	6.5	8.9
B	2.6 x 10^{-26}	2.2 x 10^{-17}	3.6 x 10^{-21}
ϕ	16.0	8.0	14.0

5.9 Discussion of P92 Mechanical Testing

5.9.1 Tensile and Creep Behaviour

Tensile testing has been conducted for the DB P92. Ennis et al. [2000] and Giroux et al. [2010] investigated the tensile properties of P92 following a series of different heat treatments. For the heat treatment closest to that of DB P92 (austenitising = ~ 1070 ºC, tempering = ~ 775 ºC) the ultimate tensile stress (285 MPa) and the elongation to failure (38.9 %) at 650 ºC are comparable, suggesting that DB P92 is typical for these heat treatment conditions. Richardot et al. [2000] has shown that at room temperature the minimum yield strength of P92 is 440 MPa and the minimum value for tensile strength is 620 MPa. The DB P92 tested in this project satisfies these minimum requirements.

To understand how the DB P92 creep behaviour compares to typical P92 the DB P92 data was plotted against the data obtained from the ECCC master curves for P92 [ECCC, 2005]. At 650 and 675 ºC the creep failure times for DB P92 are slightly below the ECCC mean data. As mentioned before this difference is greater at higher stresses and is explained because the mean data is calculated for relatively low stress tests. This is important to remember when extrapolating results and trying to draw broad conclusions on the performance of P92 steel from this work. It is important to note that this does not mean the P92 being studied is creep weak, it simply means the creep life is lower than the ECCC mean but is still within the standard deviation.

Experimental data shows that there is scatter for P92 creep testing which can come from a number of different sources including [Wasmer et al., 2006]:

- Temperature variation of the test specimen or the laboratory.
- Variation of specimen dimension and the machining tolerances.
- Accuracy of the load applied by the Denison machine.
- Differences between the various Denison creep testing rigs that were used.
- Differences and imperfections in the material (typical of material used in service).
- Differences in the heating time before the load is applied.

Wasmer et al. [2006] reports that the scatter (time to failure) in a creep-rupture test for P92 at high temperature has been statistically found to be anything up to ± 8 % in the worst cases. It is important to consider this value when considering the effect that coating application has on the creep rupture life. To

assess the scatter for the testing in this chapter the 110 and 120 MPa tests at 650 ^{o}C were repeated under the same conditions, using the same machines. This found the scatter was 10 % and 14 % respectively (1 repeat each). Therefore slightly higher than the figures quoted by Wasmer et al. [2006]. As the test schedule did not allow for multiple repeats of uncoated creep tests, other data which has been conducted in the University of Nottingham high temperature creep lab was also scrutinised (considering many different types of steel) and the scatter was shown to never be higher than 15 %.

The lowest stress creep tests that have been conducted will be the most industrially relevant as they are more typical of the loads that would actually be experienced by these power plant components in service. Richardot et al. [2000] shows that the maximum allowable stress for in service P92 pipework at 650 ^{o}C is 48 MPa. Tanner et al. [2014] suggests that the mean diameter hoop stress for P92 can be between 60-80 MPa at 675 ^{o}C. In both cases this is lower than the creep test stresses performed in this chapter. Also as shown previously the temperatures being used are also accelerated compared to the current power plant operation temperatures. The higher temperatures were chosen to provide accelerated testing but also to widen the scope of the work, especially as USC operation is considered more seriously in the future. When comparing coated mechanical tests in chapter 6 the lower temperature, lower stress tests will be considered as these will be currently most industrially relevant.

Examination of the failed creep specimens show that the high stress tests show ductile failure with large amounts of cross-section reduction. Plastic deformation is the dominant failure mechanism. However the lower stress tests show more brittle failure with less cross-section reduction. Fracture surface

examination of low stress tests shows that the failure is dominated by creep cavity formation and linkage [Gu et al., 2014; Callister and Rethwisch, 2007; Kassner and Hayes, 2003; Evans and Wilshire, 1993; Evans and Wilshire, 1985]. This can also be confirmed when studying SEM images; the amount of cavitation is shown to increase closer to the fracture surface [Gu et al., 2014]. The longer duration creep tests (lower stress) also show the greater oxidation damage. In the highest temperature and the longest duration cases this oxide is the thickest and spalls away during the creep test. Therefore these highest temperature and longest duration tests are expected to be the most suitable to see any beneficial effect of the oxidation resistant coating in chapter 6.

The creep data has been used to create a mathematical model of the DB P92 creep behaviour using the Kachanov model. This method has been presented by a number of authors including Hyde et al. [2013]. At 675 ^{o}C if we compare the constants to those determined by Saber et al. [2011] for the Kachanov model we can see that they are comparable and give similar values. Obviously there will be some variation as the P92 used by Saber et al. [2011] is different in composition to the DB P92 used in this project. This model will be used in chapter 6 when developing a cross section reduction model.

5.9.2 Fatigue / Creep-Fatigue Behaviour

Strain controlled LCF testing has been conducted to assess the high stress cyclic response of DB P92 steel. When peak stress is plotted against cycle number the peak stress reduction follows the expected shape [Saber, 2011]. An initial sharp decrease in the peak stress, followed by a steady state region (of almost constant stress reduction) and finally a rapid decrease in the stress as

failure occurs (associated with cracking and failure) [Saber, 2011]. The reason that stress reduces throughout the test is because the material experiences cyclic softening and in the later stages fatigue crack initiation and growth will occur [Junak and Ciesla, 2011; Giroux et al., 2010].

The next stage of cyclic testing was to introduce a dwell at the peak tensile. From an industry point of view this is much more relevant as this simulates much better the periodic start up and shut down of a fossil fuel power plant. The cyclic conditions are the same as the pure fatigue testing but a 10, 20 and 40 minute peak tensile dwell has been added. The increase in dwell time has been shown to increase the overall time of the test but decrease the number of cycles to failure; this is likely because creep damage is occurring during the tensile dwell period [Junak and Ciesla, 2011; Giroux et al., 2010]. In all fatigue/creep-fatigue cases the fracture surfaces of the failed specimens show that the samples fail by crack initiation, propagation and finally failure. There is no obvious change in failure mechanism with strain %. The longer overall time of test is shown to result in more oxidation damage and spallation of the specimen surface. Thus fatigue crack initiation is easier. Therefore it is these longer duration tests that will be most suitable for coated testing comparison in chapter 6, to see the effects of oxidation resistant coatings.

Both pure fatigue testing and creep-fatigue testing have been conducted at stress values in excess of the creep test regime to accelerate the overall test time. LCF testing was chosen to be representative of the slow ramp up and ramp down times of fossil fuel power plant. The overall cyclic test time was however limited by machine availability and reliability of equipment for very long duration testing, a problem experienced at many other research

institutions wishing to perform long duration cyclic testing. In the future LCF testing of DB P92 will be conducted with much longer tensile dwell times (up to 1 week). Not only will this be mechanically more relevant but will also allow for an investigation of the effect of oxidation damage (something that is very important when considering coated cyclic testing).

Overall DB P92 has been characterised mechanically at 650-700 ^{o}C and would appear to show good mechanical properties even at higher temperature. This suggests that increasing the operation temperature of DB P92 is a viable future development for increased efficiency. Preliminary examination of the failed specimens also shows increased oxidation damage as temperature is increased and therefore an oxidation resistant coating seems a logical solution; this is consistent with chapter 2. A reliable set of baseline mechanical data has been produced for uncoated DB P92 to enable comparison to coated testing in chapter 6.

5.10 Summary

Chapter 5 aimed to fully characterise the DB P92 steel, both microstructurally and mechanically, so that reliable baseline data could be determined for DB P92. This baseline data would be very important when comparing to coated mechanical testing later in the thesis (chapter 6). In summary of this chapter, the following key results have been found:

- As-received DB P92 has been characterised computationally and experimentally and has been found to be composed of a martensitic

structure which is mainly BCC ferrite phase and a number of precipitate phases of the following composition. MX phase which is specifically (V, Nb)(N, C). $M_{23}C_6$ which is specifically (Cr, Fe, Mo, W)$_{23}C_6$, where $Cr_{23}C_6$ is the dominant form. Laves Phase, of the form (Fe, Cr)$_2$(Mo, W), which will form following isothermal ageing and high temperature creep exposure. The most important precipitates for creep properties (MX, $M_{23}C_6$) are stable until ~ 700 ^{o}C. This suggests that accelerated testing or coating deposition temperature should not exceed this limit in order to retain the precipitate structure and preserve mechanical properties.

- The Ae_1 temperature for DB P92 was calculated to be ~819 ^{o}C, after this temperature significant microstructural transformation occurs as ferrite begins transforming to austenite. It is important that accelerated testing or coating deposition temperatures do not exceed the Ae_1 limit.
- Mechanical testing shows that the DB P92 being studied in this project compares very well to typical P92 presented in the literature. The creep life is slightly below that of the ECCC mean for P92, especially for high stress testing.
- Tensile testing shows that the yield stress, ultimate tensile strength and Young's modulus all decrease as the temperature is increased. The elongation to failure is shown to increase with increasing temperature. P92 shows ductile failure between 20-675 ^{o}C.
- Creep testing shows that a reduction in the test stress, at a given temperature, gives a longer time to creep failure (and more brittle creep failure, dominated by creep cavitation). An increase in the temperature, at a given stress, is shown to give a decrease in the time to creep failure.

Oxidation damage is increased as the temperature is increased and the stress is reduced. Scatter in creep testing is seen to not exceed 15 %. Kachanov damage modelling can be used to mathematically model the creep behaviour and extrapolate to different stress regimes.

- The most industrially relevant creep testing will be the low stress, low temperature testing as this is most typical of real power plant operation.
- The highest temperature, low stress creep testing will be most suitable to identify effects of oxidation resistant coatings as the oxidation damage will be greatest.
- Fatigue testing has shown that DB P92 experiences cyclic softening during strain controlled pure fatigue testing. An increase in the strain value decreases the number of cycles to fatigue failure. Oxidation damage is increased as cycle number (and total time) is increased. Fatigue failure occurs by crack initiation at the surface of the sample and slow crack propagation.
- Creep-fatigue testing has shown that the introduction of a peak tensile dwell increases the overall test duration but decreases the number of cycles to failure. Creep-fatigue testing with long total durations is most suitable to compare to coated tests.
- Mechanical testing and microstructural examination has shown that DB P92 is more than capable of operating at 650-700 ^{o}C and that the mechanical properties are not significantly affected by this temperature increase. However, as discussed, the main limiting factor for higher temperature operation is the increased oxidation damage. Therefore oxidation resistant coatings appear to be a viable solution.

CHAPTER 6

MECHANICAL CHARACTERISATION OF COATED P92

6.1 Introduction

Chapter 6 brings together the work of chapters 4 and 5 to determine how the Co-Cr-C coated P92 behaves under mechanical loading, in the form of creep and fatigue. Chapter 2 showed that for previous P92 coatings (aluminides) the negative effect of coating deposition on the P92 substrate mechanical properties has been a major limitation to their future development.

The overall aim of this chapter was to determine how the Co-Cr-C coating applied to DB P92 affects the mechanical performance of the DB P92 substrate and what this could mean for industrial application. Comparisons are made with the previous coated P92 work in the literature.

Section 6.2 presents the coated creep testing and analysis of the results. Section 6.3 and 6.4 presents the coated fatigue and creep-fatigue testing. Discussion of the findings is included in section 6.5.

6.2 Coated P92 Creep Behaviour

6.2.1 Creep Test Results at 650, 675 and 700 ºC

Figures 6.1-6.3 present the creep curves for the uncoated and coated DB P92 (batches 1 and 2) testing performed at temperatures of 650, 675 and 700 ºC respectively. These are shown as plots of strain percentage versus time. The uncoated and coated specimens have the same dimension P92 substrate. The only difference is that the coated specimen has the 34-37 µm coating applied around the gauge circumference (chapter 3). Uncoated and coated tests have been performed at the same test conditions so that comparisons can be made to show the effect of Co-Cr-C coating application. The main difference observed between the uncoated and coated creep tests is that the time to failure is increased by the application of the coating to the DB P92 specimen. Table 6.1 shows that the coated specimens always have a longer time to failure than the corresponding uncoated specimens at the same temperature and stress. Table 6.2 shows that this can be anything from a 3-47 % increase in the life. Both the uncoated and coated specimens again show that a reduction in the test stress results in an increase in the failure life and a decrease in the creep strain rate.

Figures 6.4 and 6.5 present the minimum creep strain rate against stress and the time to failure against stress, respectively for the 675 ºC coated and uncoated creep tests. These figures show that the application of a coating has a beneficial effect on the substrate mechanical properties and that this beneficial effect is often greater at longer times. It also shows that there are no obvious differences between the batch 1 and the batch 2 coated creep specimens (same coating thickness). This suggests that the inclusion of alumina grit at the coating-substrate interface in batch 1 does not affect the creep properties of the coated

system. The 675 ^{o}C figures presented are representative of all three temperatures studied.

Table 6.1: Uncoated and coated DB P92 creep test results.

Temp [^{o}C]	Stress [MPa]	Uncoated		Coated – Batch 1		Coated – Batch 2	
		Rupture Time [h]	Failure Strain [%]	Rupture Time [h]	Failure Strain [%]	Rupture Time [h]	Failure Strain [%]
650	105	3647	9.9	3764	9.5		
650	110	2139	5.3	2382	9.1	2691	7.2
650	120	1219	6.8	1377	10.0		
650	130	435	7.7				
650	140	165	9.0				
675	80	2280	6.9	2918	5.7	2659	6.6
675	90	838	8.0	1231	9.9		
675	100	538	9.0	582	13.9		
700	65	1260	8.6	1403	11.3		
700	70	728	9.4	1006	9.8		
700	75	530	11.4				
700	80	177	14.0				

Table 6.2: Uncoated and coated DB P92 creep test results to show the effect of Co-Cr-C coating application on creep failure time.

Temp [^{o}C]	Stress [MPa]	Time to Rupture [h]		Coated Specimen Time to Rupture Increase [%]
		Uncoated	Coated	
650	105 – Batch 1	3647	3764	3
650	110 – Batch 1	2139	2382	11
650	110 – Batch 2	2139	2691	26
650	120 – Batch 1	1219	1377	13
675	80 – Batch 1	2280	2918	28
675	80 – Batch 2	2280	2659	16
675	90 – Batch 1	838	1231	47
675	100 – Batch 1	538	582	8
700	65 – Batch 1	1260	1403	11
700	70 – Batch 1	728	1006	38

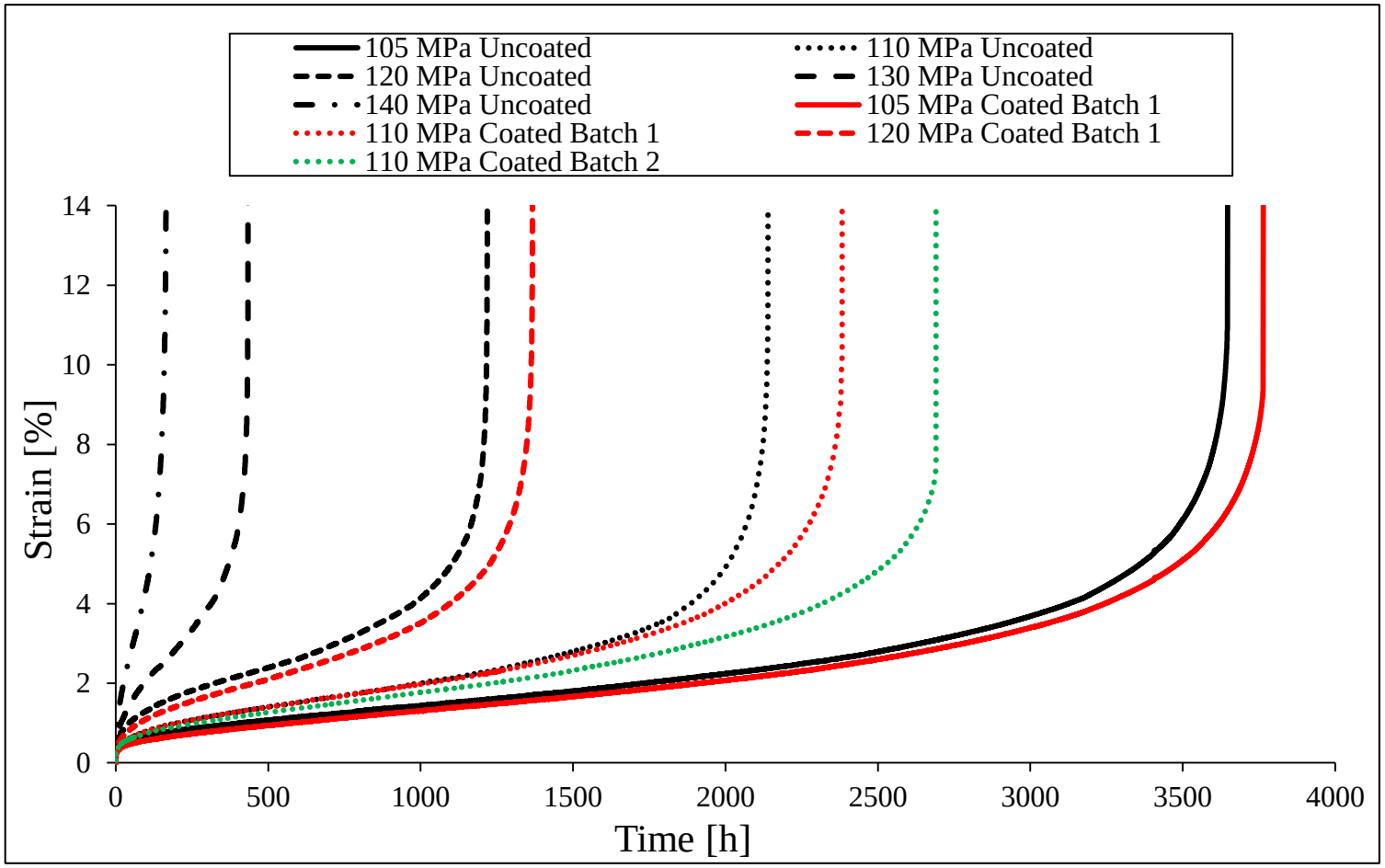

Figure 6.1: Strain-time curves for creep testing of uncoated and coated DB P92 at 650 ºC and stresses from 105-140 MPa.

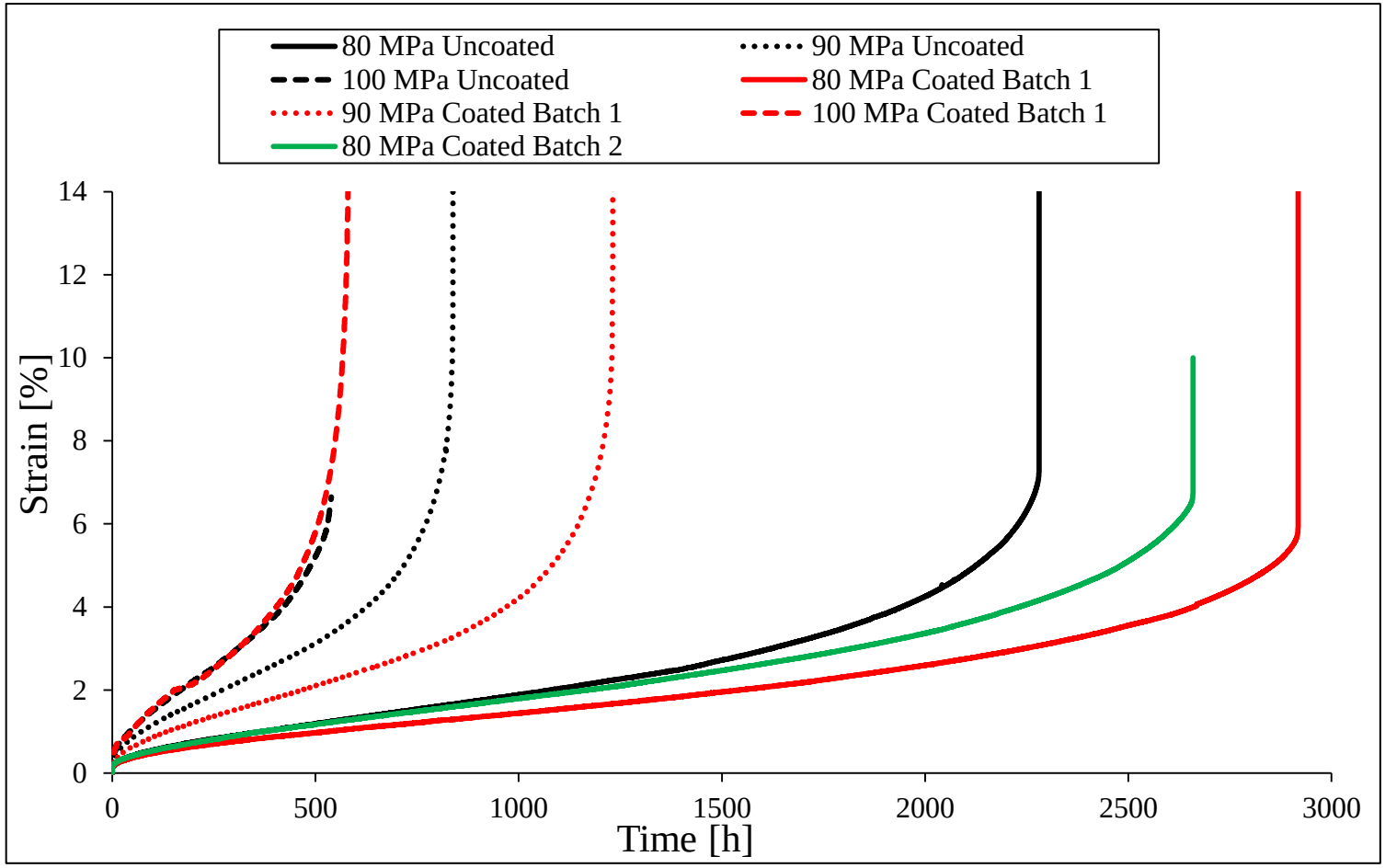

Figure 6.2: Strain-time curves for creep testing of uncoated and coated DB P92 at 675 ºC and stresses from 80-100 MPa.

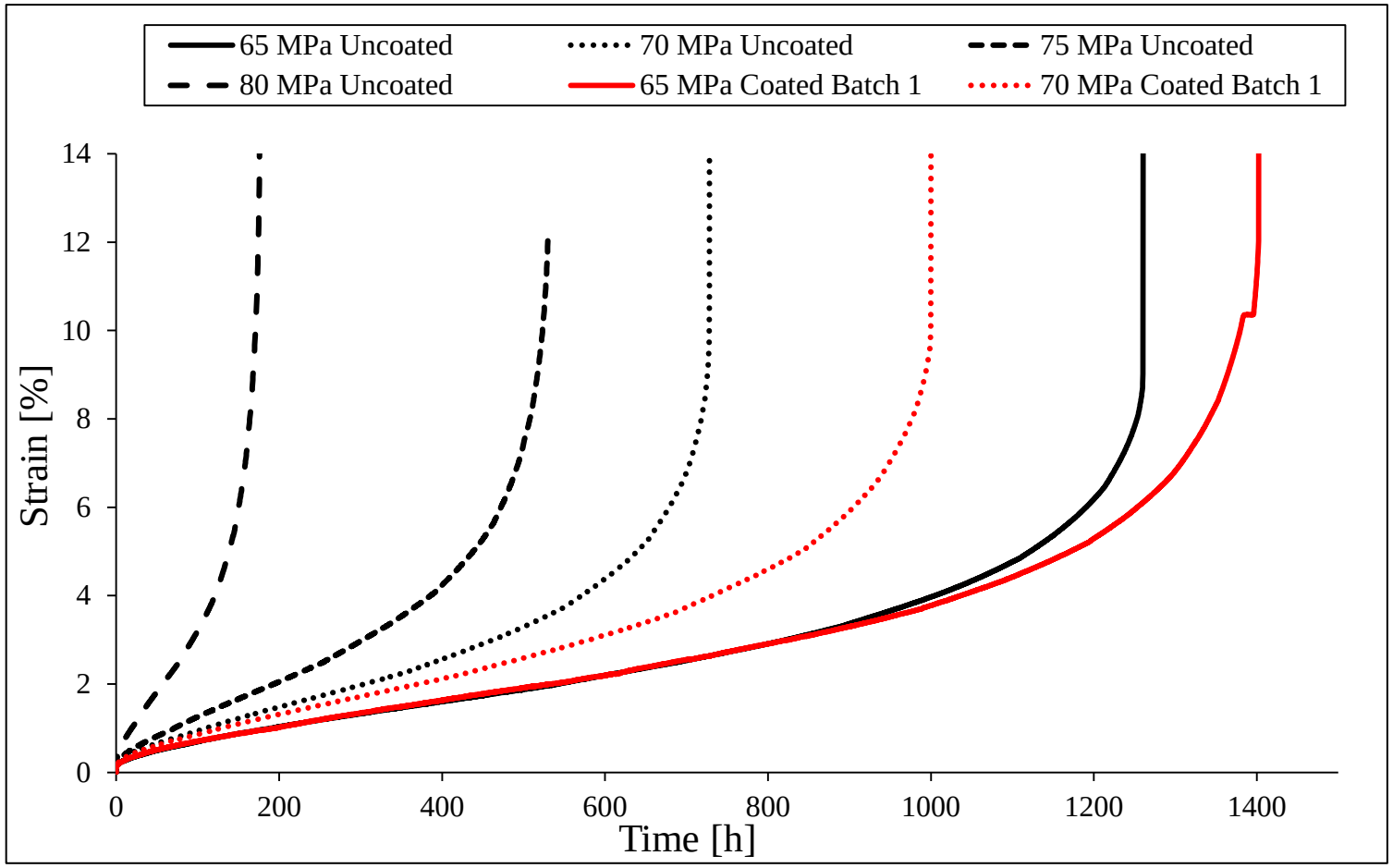

Figure 6.3: Strain-time curves for creep testing of uncoated and coated DB P92 at 700 ^{o}C and stresses from 65-80 MPa.

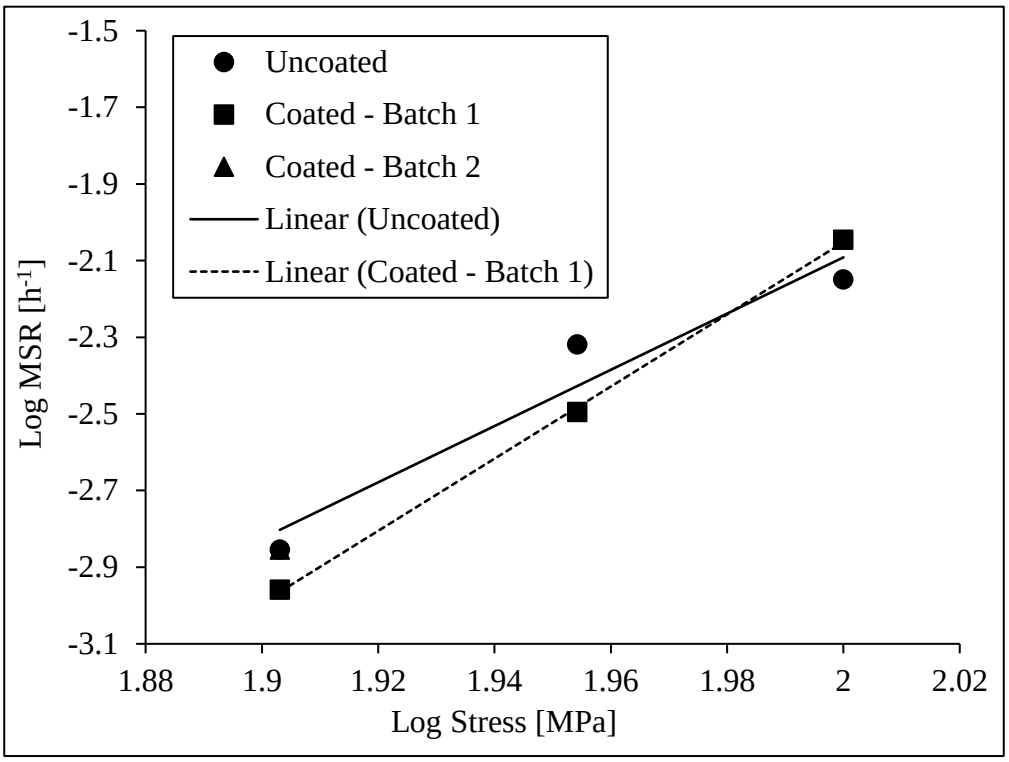

Figure 6.4: Log-log plot of minimum creep strain rate against stress for the uncoated and coated DB P92 675 ^{o}C creep testing.

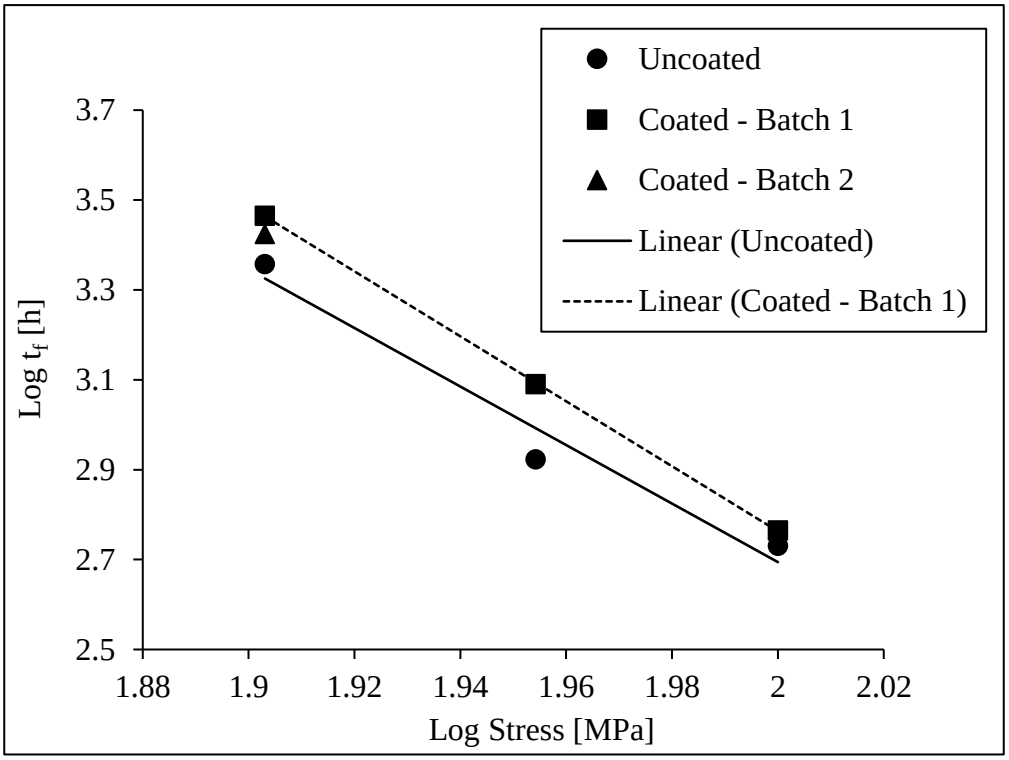

Figure 6.5: Log-log plot of time to failure against stress for the uncoated and coated DB P92 675 ^{o}C creep testing.

The Larson-Miller parameter can again be calculated for the coated DB P92 creep tests using equation 5.1. Figure 6.6 shows the coated creep tests again fit the linear relationship.

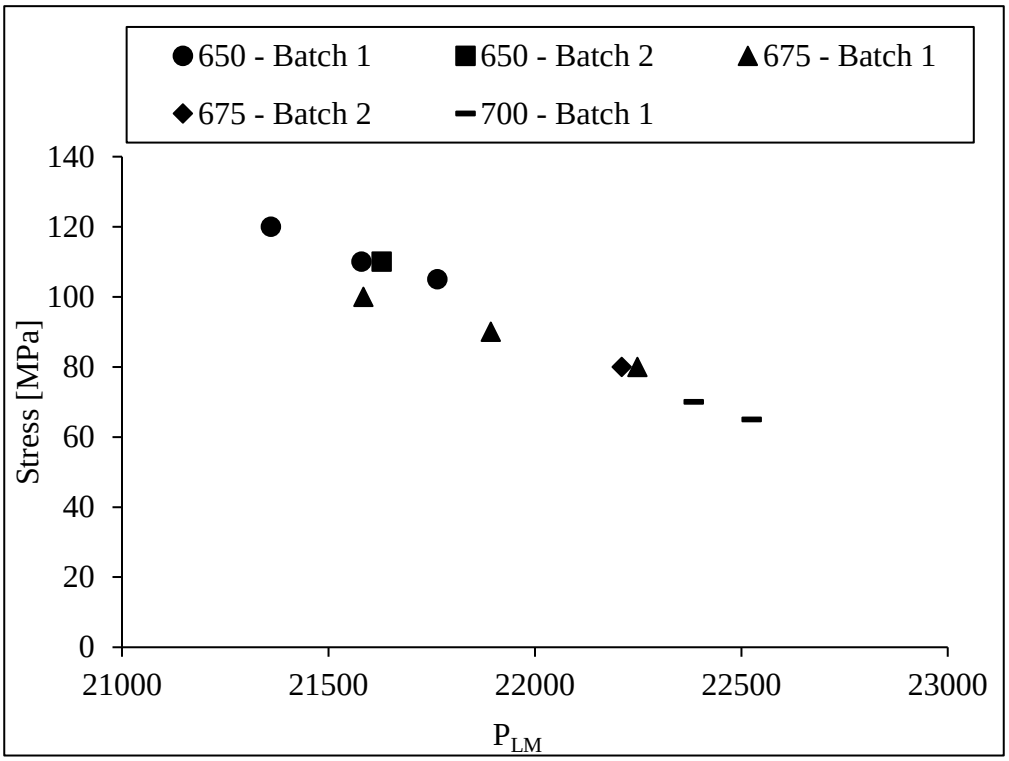

Figure 6.6: The applied stress for coated DB P92 plotted against the Larson-Miller parameter, P_{LM}, for coated creep testing at 650-700 ºC.

6.2.2 Creep Cross-Section Reduction Model

As shown previously there is an apparent positive effect on the DB P92 creep behaviour of applying the 34-37 µm Co-Cr-C coating to the creep specimen. This beneficial effect is seen because the coated samples are oxidation resistant which means oxidation damage of the DB P92 at high temperature will be prevented. This means that in the coated case the P92 substrate gauge diameter of 10 mm will not be reduced due to oxidation damage. Whereas on the uncoated specimen significant oxide damage will occur and cross section will be lost. This means the stress in the uncoated specimen will increase during the

test causing it to prematurely fail. This could be proven by performing uncoated and coated creep tests in an inert environment (argon). However due to the limited availability of this facility the cross section reduction will be treated mathematically instead. The difference between the oxidation damage on the coated and uncoated specimens is illustrated in figure 6.7.

To understand this cross section reduction, creep modelling techniques will be used to take into account the effect of oxidation damage on the uncoated creep specimens and adjust the creep curves accordingly. To do this we will incorporate an oxidation term (which allows the cross-section loss to be approximated)) into the Kachanov equation for uniaxial creep that was studied in chapter 5 (equation 5.3).

A number of assumptions have been made to simplify this model meaning it only relates to oxidation damage. These assumptions are:

- The coating thickness of 34-37 μm is not considered load bearing, therefore the coated and uncoated specimen both have a diameter of 10 mm at the start of the simulation.
- The coating deposition is low temperature (~ 45 ^{o}C) meaning that the coating deposition does not have a significant effect on the microstructure of the substrate P92. Therefore both the uncoated P92 and the coated P92 substrate will have the same mechanical properties.
- No damage occurs to the coating during testing and the 10 mm diameter of the coated sample is retained throughout the test. It is assumed that no other cross section reduction occurs. As brittle, low stress, tests are the focus this is a reasonable assumption.

- There are no significant diffusion processes occurring during the creep test to cause microstructural changes. This includes detrimental inter-diffusion effects that may be caused by the application of a coating.

These series of assumptions means that the coated creep test in air should be analogous to performing an uncoated test in an un-oxidising environment.

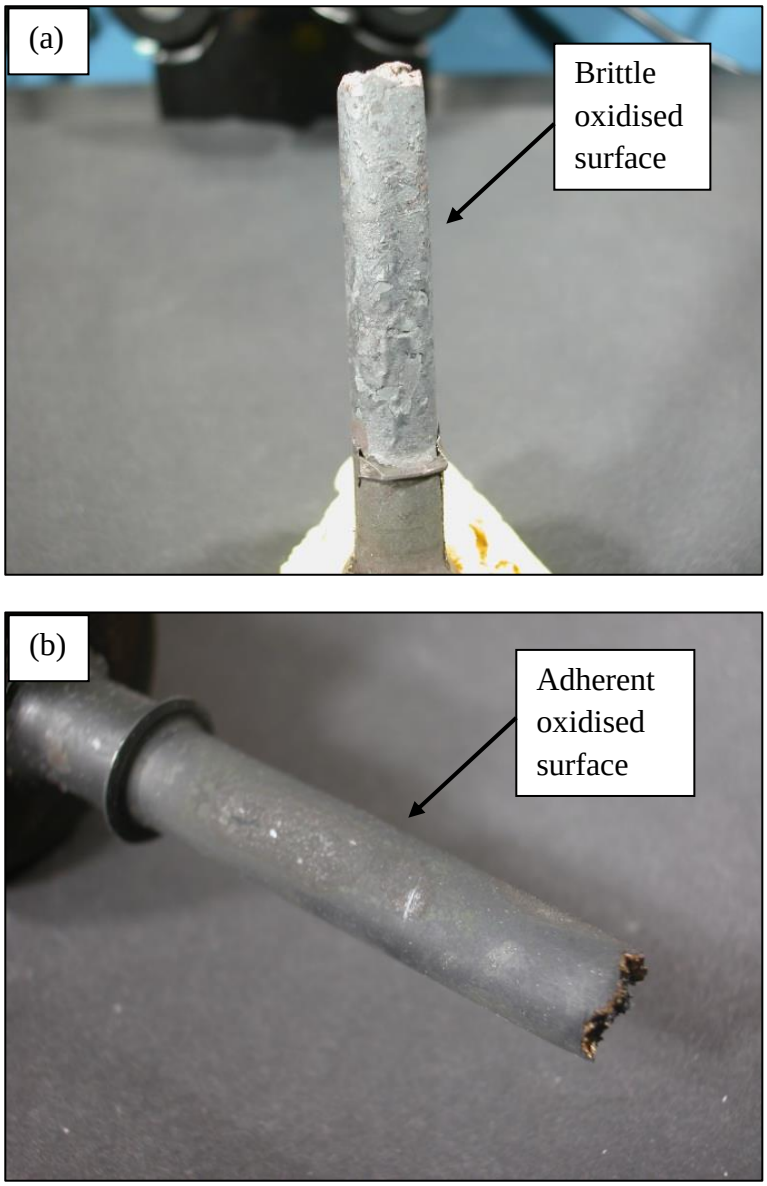

Figure 6.7: Photograph of the (a) uncoated – 2139 hours and (b) coated – 2382 hours failed creep specimens for 110 MPa at 650 ^{o}C.

Using the Kachanov equation included previously in chapter 5:

$$\varepsilon^c = \frac{A\sigma^{(n-\chi)}}{B(n-\phi-1)}\left([1-B(1+\phi)\sigma^{\chi}t]^{\frac{\phi+1-n}{\phi+1}}-1\right) \quad \text{[Equation 5.3]}$$

The Kachanov constants have been determined for both the coated and uncoated creep tests as shown in table 6.3.

As can be seen from equation 5.3 the stress is included as a constant value for the traditional Kachanov model. However for this simulation an expression is included that allows the stress to vary with cross-sectional area reduction as a result of oxidation damage. In order to do this the oxidation kinetics equation for P92 steel is used to approximate the amount of oxide damage and therefore the loss of cross section. A number of authors [Birks et al., 2006] show that the equation for oxide growth on ferritic steels is:

$$d_o{}^2 = k_p t + C_o \quad \text{[Equation 6.1]}$$

In equation 6.1, d_o is the total thickness of the oxide scale, t is the oxidation time, k_p is a constant which is a function of time and C_o is also a constant (assumed to be zero in this case):

$$k_p = A_f \exp(-\frac{Q}{RT}) \quad \text{[Equation 6.2]}$$

In equation 6.2, A_f is the frequency factor constant, Q is the activation energy, R is the gas constant and T is the absolute temperature in Kelvin. The k_p value

for P92 in air is taken from the literature [Laverde et al., 2004]. Stress variation with oxidation damage is given by equation 6.3 where, σ is the stress, F is the load, r is the radius of the creep specimen gauge and A is cross sectional area:

$$\sigma = \frac{F}{A} = \frac{F}{\pi r^2} = \frac{F}{\pi(r-d_o)^2} \quad \text{[Equation 6.3]}$$

Equation 6.1 can then be substituted into equation 6.3 to give:

$$\sigma = \frac{F}{\pi(r-(\sqrt{k_p t}))^2} \quad \text{[Equation 6.4]}$$

Equation 6.4 can then be substituted into equation 5.3 to give the modified form of the Kachanov equation (equation 6.5). A factor of 0.5 is also included to show that P92 has an approximately 50:50 ratio of inward to outward growth [Aguero et al., 2005].

$$\varepsilon^c = \frac{A\sigma^{(n-\chi)}}{B(n-\phi-1)}\left(\left[1-B(1+\phi)\left(\frac{F}{\pi\left(r-\left(0.5(\sqrt{k_p t})\right)\right)^2}\right)^{\chi} t\right]^{\frac{\phi+1-n}{\phi+1}} - 1\right) \quad \text{[Equation 6.5]}$$

The model presented in equation 6.5 can now be plotted alongside the real experimental data, both coated and uncoated, to verify the accuracy of the model. Examples of the modelling at 650 ^{o}C are included in figures 6.8-6.9.

Figures 6.8 and 6.9 show the coated and uncoated creep data determined experimentally. The traditional Kachanov fitting for the coated test data is also included (equation 5.3). In both cases this shows a good fitting between

experimental and modelled data. Then finally the Kachanov fitting for the coated test is included with the cross section reduction term included (equation 6.5). If oxidation damage is the only factor causing the difference between coated and uncoated tests, then the Kachanov fitting with cross section reduction term (equation 6.5) for the coated test should be shifted to approximately the uncoated experimental data position. This would confirm that oxidation damage and loss of gauge cross section is the only difference between the tests.

Figures 6.8 and 6.9 shows that for the 110 and 120 MPa uncoated and coated creep tests at 650 ^{o}C the cross section reduction model fits well. These figures are representative of all coated creep testing performed. In all creep cases the cross section reduction model accounts for almost all of the increase in the creep life when the coating is applied. Modelling at 650 ^{o}C suggests that gauge cross section reduction can be responsible for up to a 15 % difference in the creep failure times for uncoated and coated specimens. The remainder of the increase is likely to be as a result of normal creep scatter and any diffusion effects that affect the creep properties of the substrate P92. These diffusion effects would need to be studied in more detail in future work.

Table 6.3: A summary of the creep damage constants for uncoated and coated DB P92 at 650 ^{o}C (for stress in MPa and time in hours).

Constant	Uncoated	Coated
A	1.6 x 10^{-31}	1.451 x 10^{-29}
n	12.7	12
χ	10.3	6.3
B	2.6 x 10^{-26}	3.4 x 10^{-18}
Φ	16.0	16.0

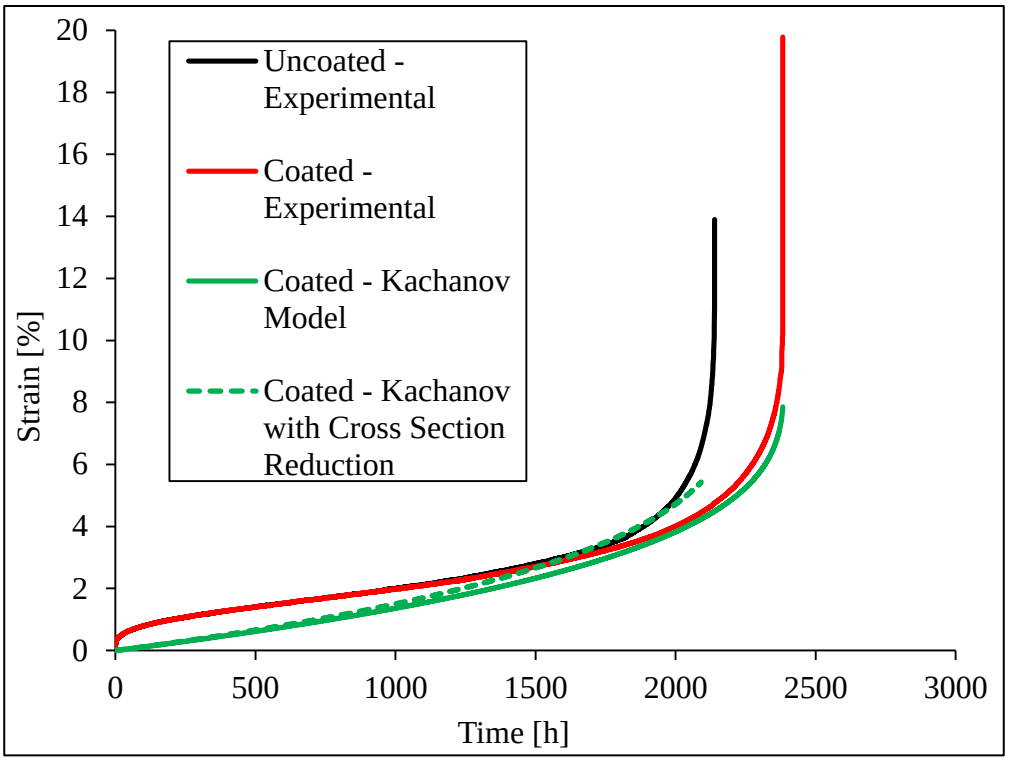

Figure 6.8: The experimental creep data plotted alongside the creep cross section reduction model for 110 MPa creep test performed at 650 ºC (batch 1).

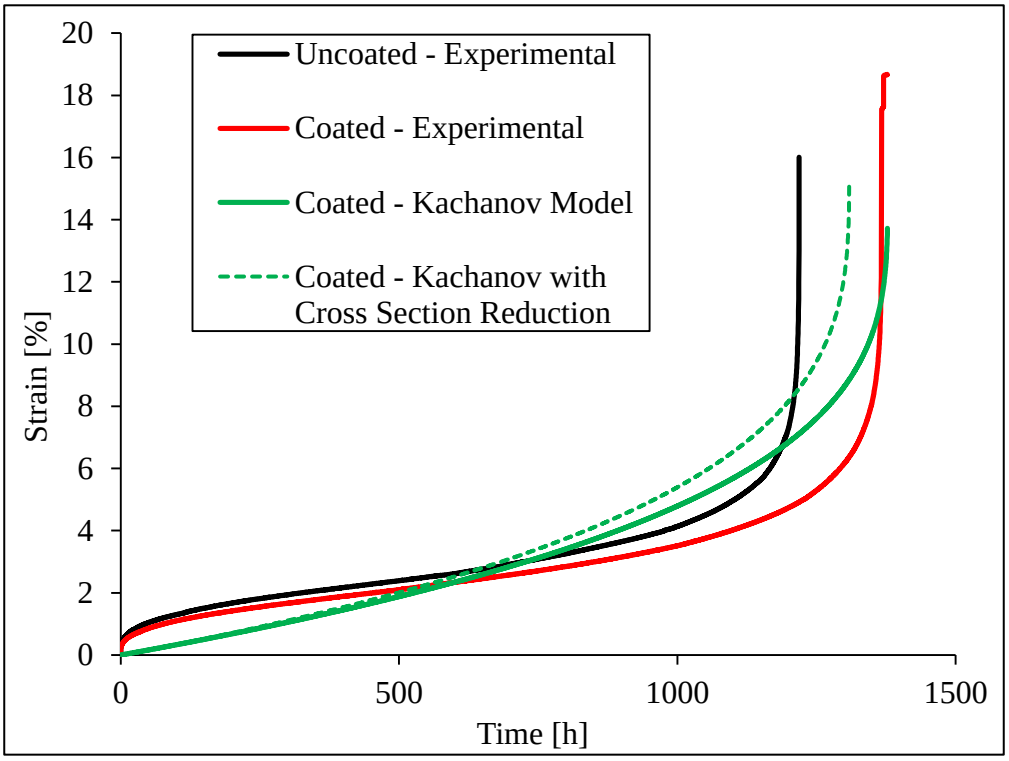

Figure 6.9: The experimental creep data plotted alongside the creep cross section reduction model for 120 MPa creep test performed at 650 ºC (batch 1).

6.3 Coated P92 Low Cycle Fatigue Properties

As detailed in chapter 5 LCF testing of uncoated DB P92 has been performed. This section compares the coated fatigue testing and establishes the effect that coating application has on the LCF properties of the substrate P92. Figure 6.10 and table 6.4 compare the uncoated and coated pure fatigue tests conducted at 0.3 % strain and 650 ^{o}C when the peak stress is plotted against cycle number. Figure 6.10 suggests that the coated specimen shows a reduction in the fatigue cycles to failure of 13 %. This is expected to be within the fatigue test scatter for short tests; therefore the application of the coating has no observable effects on the fatigue cycles to failure at these very short exposures of between 3 and 4 hours. The stress reduction curves and fracture surfaces are also very similar suggesting that both samples are failing in a similar way (crack initiation, crack propagation and failure).

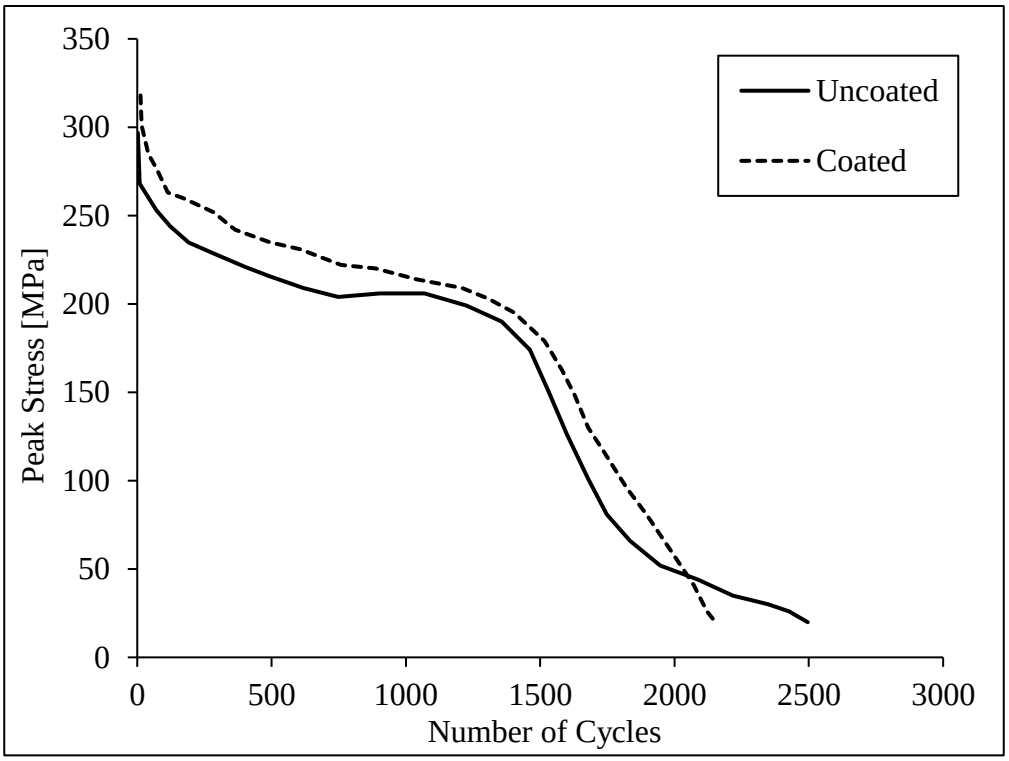

Figure 6.10: Peak stress plotted against cycles for LCF tests conducted at 650 ^{o}C on coated and uncoated DB P92 steel at 0.3 % strain.

Table 6.4: Summary of the uncoated and coated DB P92 LCF tests.

Temp [ºC]	Strain [%]	Speed [%/s]	Cycle Time [s]	Uncoated		Coated		
				Cycles to Failure	Total Time [h]	Cycles to Failure	Total Time [h]	Δ Total Time [%]
650	0.3	0.1	6	2496	4.2	2153	3.6	- 13%
650	0.4	0.1	8	1368	3.0			
650	0.5	0.1	10	1325	3.7			

6.4 Coated P92 Low Cycle Creep-Fatigue Properties

Creep-fatigue testing has also been conducted for uncoated DB P92 as presented in chapter 5. Creep-fatigue is considered to be more industrially relevant as the load form is closer to real power plant operation. This section presents the coated creep-fatigue substrate and establishes the effect that coating application has on the creep-fatigue properties of the DB P92.

Figures 6.11-6.12 and table 6.5 present comparisons of the coated and uncoated creep-fatigue tests of P92 at 650 ºC and 0.3 % strain with peak dwell times of 10 and 20 minutes respectively. At 10 minute dwell (324 hour total coated test time) no effect of the coating application is observed. As the dwell time is increased to 20 minute dwell (483 hour total coated test time) the coating is shown to have a small positive 30% increase in the creep-fatigue cycles to failure. These results indicate that as the total test time is increased, and therefore the oxidation damage is increased, this allows for a more noticeable effect of the oxidation resistant coating application to be seen. Observed in all the samples, the stress reduction is shown to be similar for both the uncoated and coated samples but then when the stress drops below 150 MPa the coated

specimen seems to slow down in stress reduction. This could suggest that the oxidation protection is slowing down the crack propagation in the P92.

Figures 6.13 and 6.14 compare the uncoated and coated P92 failed specimens with a 20 minute dwell. The fracture surface imaging shows that both specimens fail in the conventional way with crack initiation, propagation and finally failure. The oxidised surface imaging of both samples shows that the uncoated specimen has a brittle oxidised surface even following 372 hours at 650 ^{o}C. In contrast the coated surface is much less damaged with evidence of a smooth, adherent oxide forming with very little spallation. There is no evidence of any coating damage (except for very close to the fracture surface) and it remains intact along the specimen gauge length for all tests. This is encouraging because as shown in figure 5.18 the stress level is far beyond what this coated system would experience in service.

Table 6.5: Summary of the uncoated and coated DB P92 creep-fatigue tests.

Temp [^{o}C]	**Strain [%]**	**Dwell Time [s]**	**Cycle Time [s]**	**Uncoated**		**Coated**		
				Cycles to Failure	**Total Time [h]**	**Cycles to Failure**	**Total Time [h]**	**Δ Total Time [%]**
650	0.3	600	606	1811	305	1923	324	+ 6
650	0.3	1200	1206	1109	372	1443	483	+ 30
650	0.3	2400	2406	1002	670			

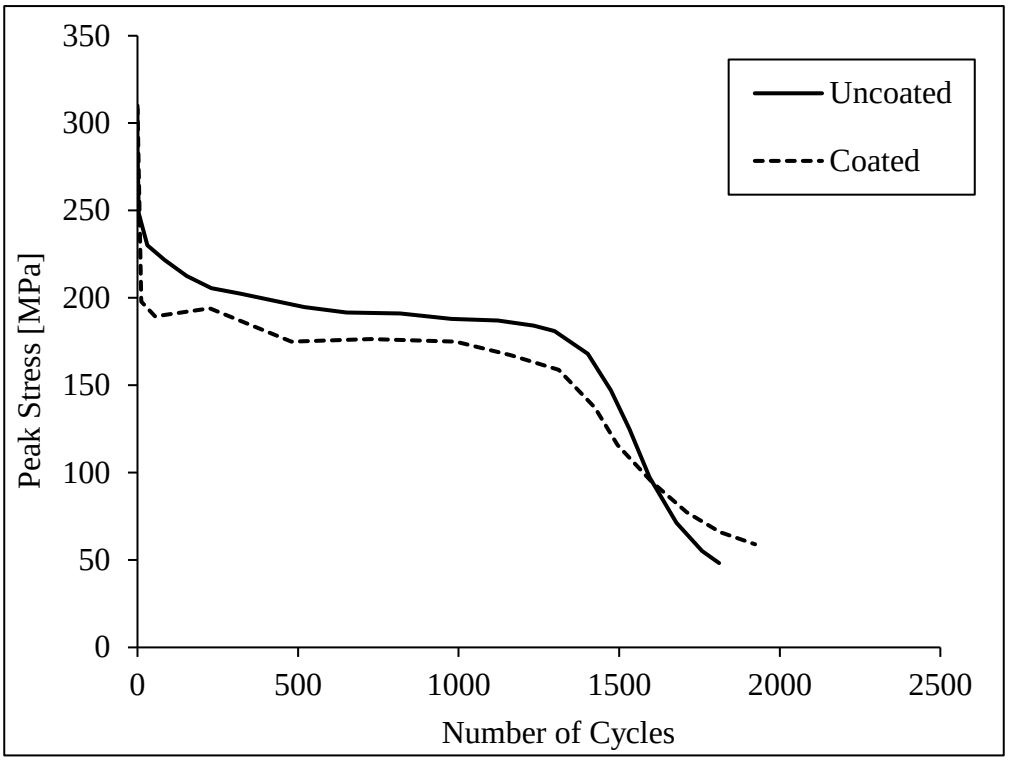

Figure 6.11: Peak stress against cycles for uncoated/coated creep-fatigue tests at 650 ºC, conducted at 0.3% strain and 600 second dwell at peak tensile.

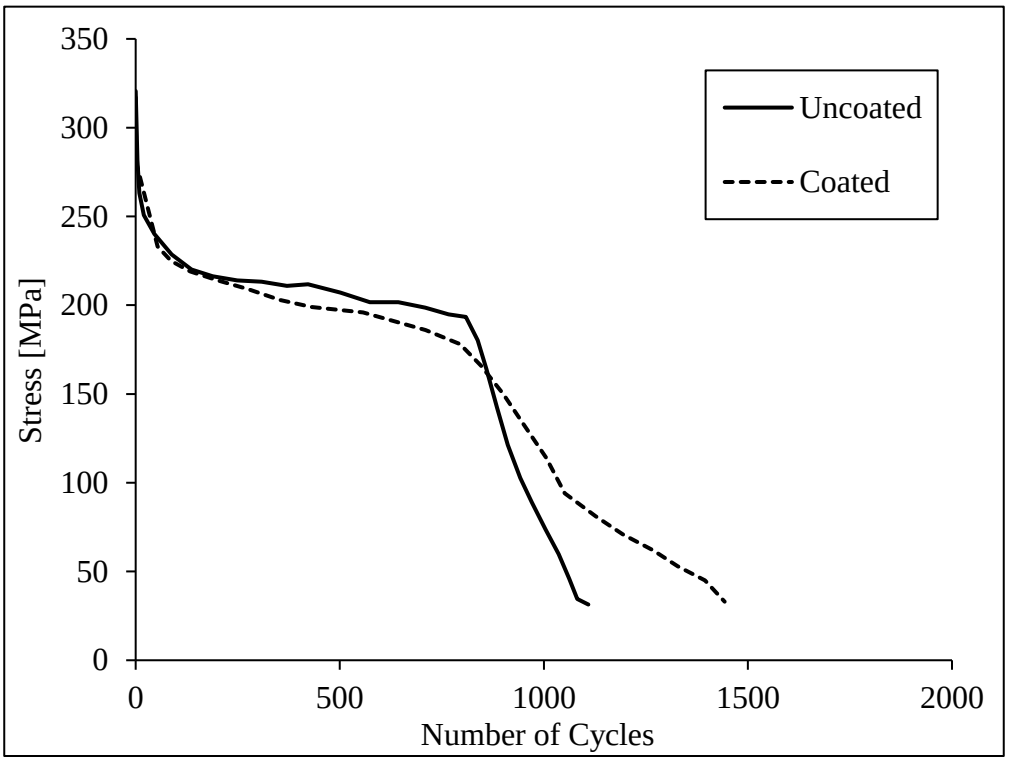

Figure 6.12: Peak stress against cycles for uncoated/coated creep-fatigue tests at 650 ºC, conducted at 0.3% strain and 1200 second dwell at peak tensile.

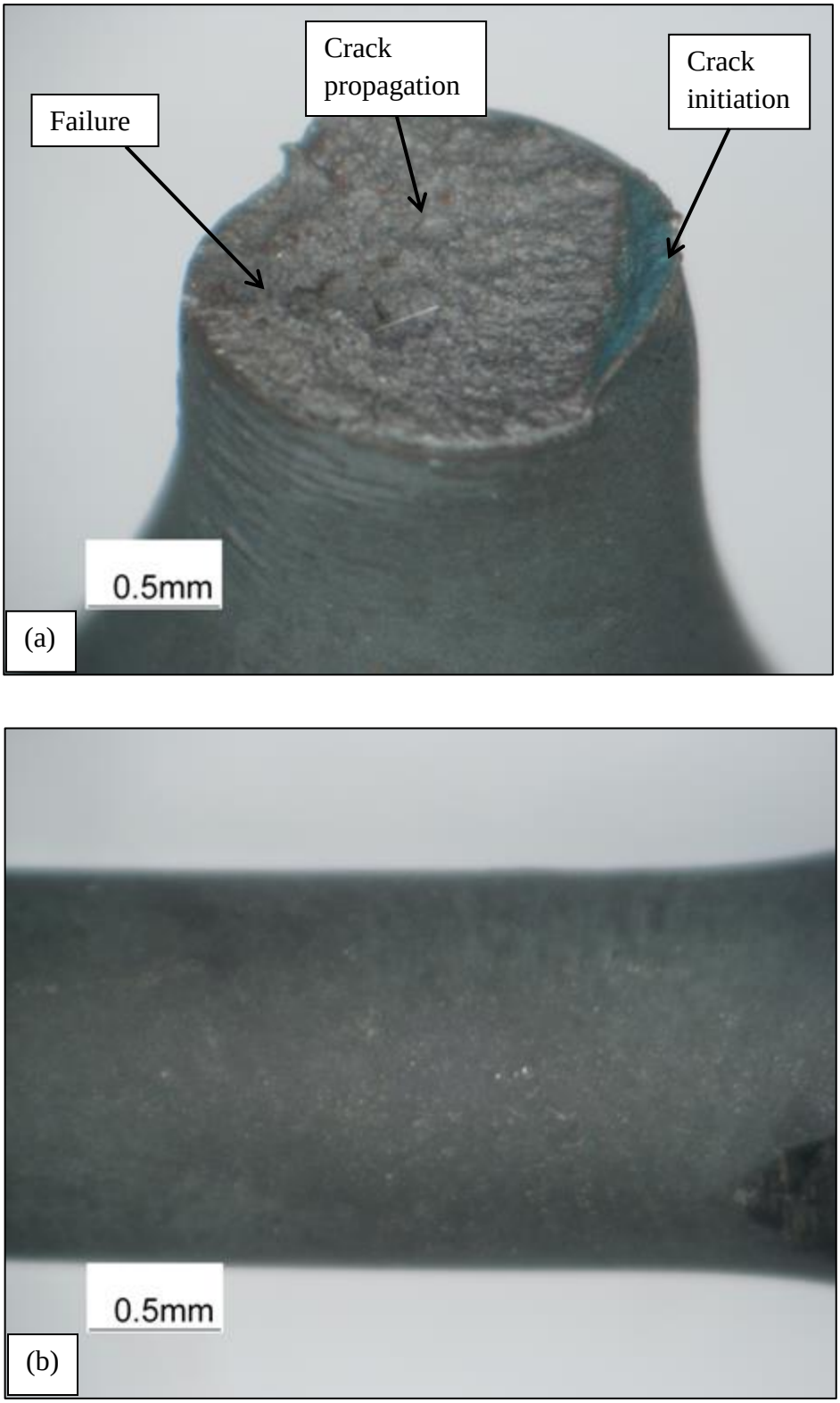

Figure 6.13: Photography to show (a) the fracture surface and (b) the oxidised specimen surface of the coated creep-fatigue test at 650 ^{o}C, conducted at 0.3 % strain and 1200 second dwell at peak tensile.

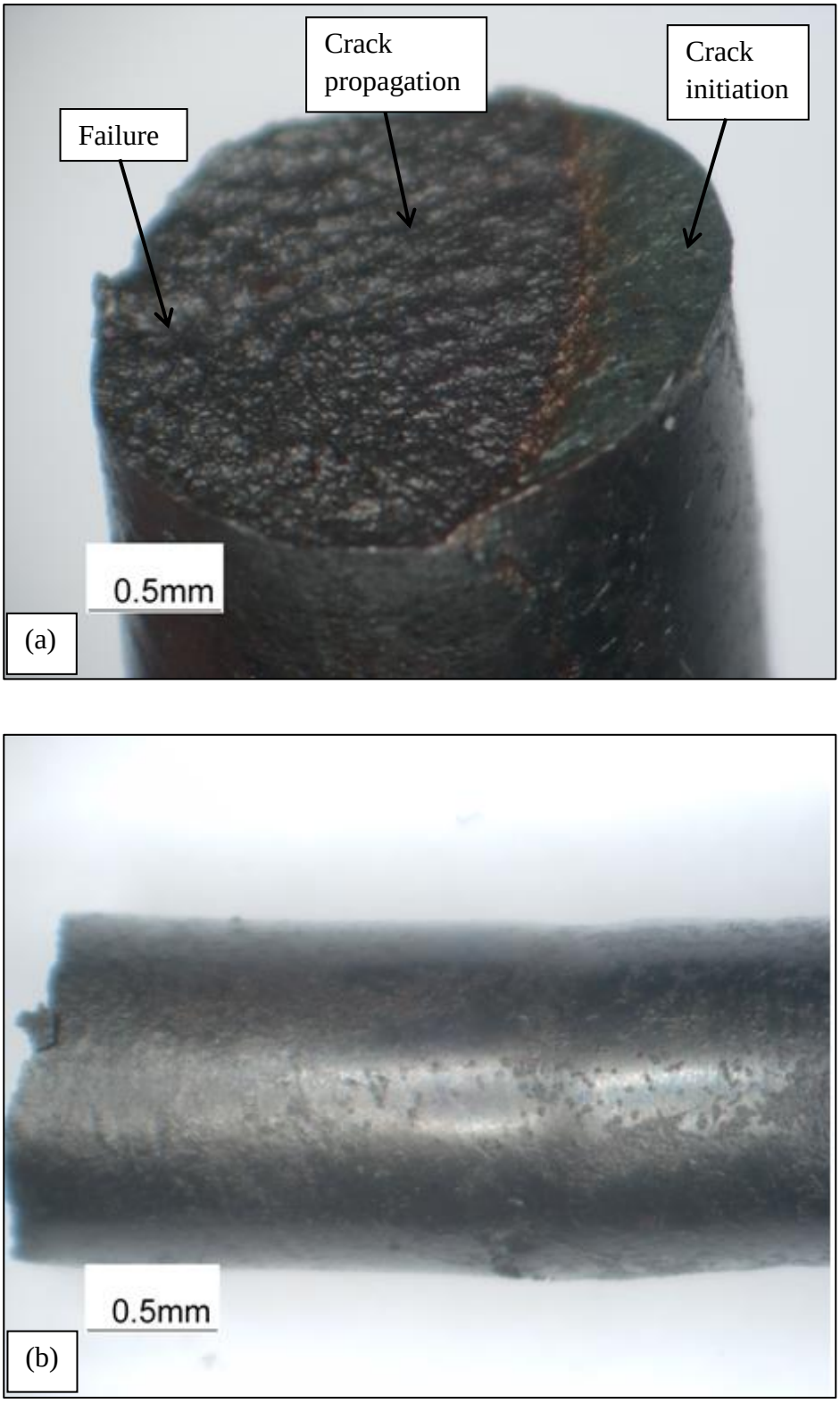

Figure 6.14: Photography to show (a) the fracture surface and (b) the oxidised specimen surface of the uncoated creep-fatigue test at 650 ^{o}C, conducted at 0.3 % strain and 1200 second dwell at peak tensile.

6.5 Discussion

6.5.1 Coated Creep Behaviour

The experimental creep results show that in all cases the application of the coating appears to have a positive effect on the creep properties of the DB P92 substrate; this can be anything from a 3-47 % increase in the creep life. There are no observable differences between the batch 1 and the batch 2 specimens, showing that the presence of alumina grit at the coating-substrate interface does not affect the creep behaviour. Wasmer et al. [2006] shows that the creep scatter of P92 high temperature creep tests can be anything up to ± 8 %. This scatter is mainly caused by material variation or procedural error. As mentioned in chapter 5 the scatter for creep testing at the University of Nottingham is shown to be no greater than 15 %. This suggests that in almost all cases the positive effect of the coating on the creep life must be caused by something other than the scatter of creep testing.

The deposition method of the Co-Cr-C coating is low temperature (~ 45 ^{o}C), therefore the experimental observations and the literature suggest that the P92 will suffer no significant microstructural transformations at 45 ^{o}C [Hald, 2008]. This means the mechanical properties of the substrate P92 should remain unchanged following deposition. Creep rupture strain levels are also similar for the uncoated and coated specimens suggesting that the deposition process does not affect the ductility of the DB P92. The coating is also thin (34-37 μm) compared to the specimen diameter (10 mm) so it is not considered load bearing. This therefore suggests that the oxidation resistance of the coating is responsible for the beneficial effect of the coating.

The cross-section reduction model confirms that a major contributor to the positive effect of coating application is that the coating prevents cross-section reduction of the P92 substrate as a result of oxidation damage. The level of oxidation of P92 at 650-700 ^{o}C is enough to cause a significant decrease in the creep specimen gauge diameter at long exposures. The positive effect of oxidation resistant coating on the creep properties of P92 is likely to be reduced as real P92 wall thicknesses are considered. David et al. [2013] shows that P92 in service will typically have a wall thickness of 34 mm (greater than the 10 mm creep specimen gauge diameter). However caution must be exercised when making assumptions about P92 pipework as the stress and steam environment are different to the conditions used for this creep testing of uniaxial bars in air. It is also important to note that the stresses being used in this study are higher than would actually be seen in service in P92 pipework. For example Richardot et al. [2000] states that the maximum allowable stress for P92 at 650 ^{o}C is 48 MPa. This is far below the 105-140 MPa used for the creep tests conducted in this work at 650 ^{o}C. In the future an extensive study of the coated P92 pipework will be needed to examine how the coating affects the creep properties of real P92 power plant components.

The most interesting previous work to compare these creep findings to is the aluminide coated P92 work, as presented extensively in chapter 2. Most aluminide work has been conducted using the same method as this thesis (chapter 3), coated and uncoated specimens are compared with a coating thickness that is non-load bearing. Most aluminide authors only perform creep testing for 100-300 hours at ~ 650 ^{o}C. Very little work is performed for longer than 500 hours or at temperatures greater than 650 ^{o}C. This was identified as

being a limitation of the previous aluminide work because as shown in chapters 5 and 6 longer term testing is more industrially relevant and allows for more oxidation damage to be seen. Therefore for the work in this thesis longer duration testing was also performed. Also higher temperatures (675 and 700 ^{o}C) were considered to increase the scope of this work as USC generation becomes more widespread.

Aguero et al. [2007] shows a 10 % drop in the time to creep failure as a result of aluminide slurry deposition (deposited at 700 ^{o}C). The reduction in creep life is greater following longer creep testing. Aguero et al. [2007] concludes that the reduction in life is caused by the high temperature coating process altering the microstructure (4-7 % reduction in creep life) as well as a diffusion zone that forms which is considered to have no creep strength. Aguero et al. [2007] mentions that the negative effects of diffusion are often only limited to small diameters and that at more representative wall thicknesses the negative effect can be neglected. Bates et al. [2014] has performed similar work with an aluminide coating deposited by the pack deposition process. This work found that the higher the deposition temperature (650-1000 ^{o}C) the greater the negative effect on the creep life. The microstructural change of the P92 during coating is seen to have the biggest effect on the overall creep performance of the coated system.

The Co-Cr-C coating considered in this thesis has superior creep properties to the previous aluminide type coatings detailed above. The main advantage of the Co-Cr-C coating is the low temperature deposition process (~ 45 ^{o}C) compared to aluminide coatings (650 ^{o}C +). Low temperature deposition means no detrimental effect of coating on the creep resistant P92 microstructure.

6.5.2 Coated Fatigue / Creep-Fatigue Behaviour

Low cycle cyclic testing (pure fatigue and creep-fatigue) of coated P92 has also been performed and shows no obvious effects of coating application. However for longer duration testing, with long tensile dwells, and increased oxidation, this allowed for a small positive effect of coating application to be seen. This small positive effect is observed for the total cycles to failure and is not seen until a greater than 50 % stress drop. This suggests that the coated samples perform slightly better when cracking becomes dominant. Fatigue scatter has again been studied for fatigue testing performed in the high temperature testing laboratory at University of Nottingham and is found to have a scatter of no greater than 15 %. This is consistent with the creep scatter discussed earlier.

The literature shows that for a fatigue failure caused by surface initiation of a crack, followed by crack propagation, the coating and the adherent oxide will prevent surface damage, therefore making it more difficult for surface cracks to initiate and increasing the number of cycles to failure [Meyers and Chawla, 2009; Connolley et al., 2000; Gell and Leverant, 1973]. As shown in chapter 4 the longer the duration of isothermal exposure the more adherent the oxide is that is produced (distinct layers of Cr_2O_3). This possibly explains why the beneficial effect is not seen immediately for short durations. The amount of oxidation damage at longer durations will also be greater meaning that beneficial effects of the coating are more likely to be seen. As with creep testing there will be some positive effect of coating application because of the preservation of cross section but this effect will be limited because the duration of the fatigue tests is significantly less than corresponding creep tests and also the cyclic tests are being performed in strain controlled mode.

Jiang et al. [2015] shows that oxidation damage causes the crack propagation in steels to advance more quickly. The final drop in maximum stress is associated with the crack growth regime and is seen in this chapter to be slightly more gradual for coated samples compared to uncoated. This suggests that the crack growth is being slowed down or impeded. Aguero et al. [2007] has observed the same behaviour for aluminide coated alloy 122 (representative of P92) subjected to TMF testing and showed that in their case it was the coating-substrate interface that was retarding the crack growth. In this case coating application has been shown to be responsible for up to a 50 % increase in the number of cycles to failure. Although not completely understood Aguero et al. [2007] suggests that this is due to the change in alloy chemistry (and fracture toughness) in the IDZ. Chapter 7 shows that the Co-Cr-C coated DB P92 system forms an IDZ so it seems likely that this will have some effect on the fatigue behaviour at longer exposures.

Caution must be exercised when drawing conclusions on beneficial fatigue properties based on a small number of specimens without a detailed microstructural study. In the future Co-Cr-C coated P92 work, longer term and more industrially relevant fatigue conditions are needed. At this stage of preliminary fatigue testing it is more appropriate to conclude that the Co-Cr-C coating has no observable effect on the fatigue properties of the substrate P92 at these conditions. This is still encouraging for industry sponsors as it shows no negative effect caused by this coating. A minimal negative effect on creep and fatigue life was always the main criteria for industry sponsors when considering potential coated systems.

Overall the Co-Cr-C coating appears to have a number of promising effects on the mechanical properties and appears to have a number of advantages over the aluminide coatings considered previously. This work has highlighted a number of future research areas of interest. For example; longer duration coated creep testing in steam and longer duration and more detailed fatigue testing. This encouraging series of results also suggests the Co-Cr-C coating has a promising future for application to P92. The next stage is to consider the coated P92 system in more detail by considering the oxidation, microstructural evolution and inter-diffusion behaviour.

6.6 Summary

Chapter 6 aimed to characterise the coated DB P92 steel mechanically, by performing creep and fatigue testing, to determine what effect coating application had on the bulk mechanical properties of the substrate steel. A number of promising properties were identified. In summary of this chapter, the following key results have been found:

- Application of a 34-37 μm Co-Cr-C coating to a DB P92 creep specimen has been shown to have a positive effect on the creep life compared to uncoated P92. The time to failure was increased and the minimum creep strain rate was reduced. This positive effect was caused by preservation of the coating cross-section by the oxidation resistant coating preventing oxidation damage. It is expected that at representative wall thicknesses this positive effect will be reduced. Inter-diffusion effects are also expected to

influence the creep properties, however this effect will again be limited at real wall thicknesses.

- The Co-Cr-C coated P92 has been shown to have superior creep properties compared to aluminide coated P92. The main benefit of the Co-Cr-C coating compared to other technologies is the low temperature deposition temperature (~ 45 ^{o}C) which has no effect on the ductility or microstructure of the P92 substrate. This deposition temperature is far below the transformation temperatures identified in chapter 5.
- Application of a 34-37 µm Co-Cr-C coating to a DB P92 fatigue specimen has been shown to have no effect on fatigue/creep-fatigue life for short duration testing. For longer duration testing the coating appears to have a small positive effect on the fatigue/creep-fatigue life of the P92, when the total test time is long enough to allow sufficient oxidation. One possible explanation is that the Co-Cr-C coating preserves the specimen surface and the coating-substrate interface preventing crack initiation and propagation. In addition to this preliminary study a much more detailed microstructural study would be required to conclusively prove this. However crucially coating application does not negatively affect fatigue life. The coating is shown to survive fatigue loading and shows no signs of coating damage.

CHAPTER 7

OXIDATION AND MICROSTRUCTURAL STUDY OF COATED P92

7.1 Introduction

Chapter 4 has reported the high temperature oxidation of the Co-Cr-C free-standing coating and chapters 5 and 6 have reported the effect of Co-Cr-C coating application on the mechanical properties of the substrate P92. These chapters show that the Co-Cr-C coating has a number of promising oxidation and mechanical properties. To be confident that this coating would be suitable for long term service an oxidation and microstructural study of coated P92 was performed. This was conducted in close collaboration with Doosan Babcock and Praxair Surface Technologies.

The aim of this chapter was to microstructurally characterise the Co-Cr-C coated P92 system following industrially relevant high temperature oxidation and mechanical testing. Industrial collaborators have contributed significantly to determine typical power plant conditions for this testing. Coated P92 coupons and failed coated creep specimens (from chapter 6) have been studied

for this section (both with 34-37 µm coating). Oxidation, microstructural evolution and inter-diffusion zone development have all been studied.

Section 7.2 presents the coated coupon oxidation study following high temperature oxidation. Section 7.3 presents analysis of the failed coated creep specimens. Section 7.4 presents the inter-diffusion and coating evolution study of coated P92. Section 7.5 presents discussion of the coated P92 case study.

7.2 Oxide Scale Characterisation of Coupons

To initially understand the oxidation behaviour of Co-Cr-C coated P92 a series of coated coupons have been studied at industrially relevant conditions, as shown in table 7.1 (table 3.3, chapter 3). These are coated P92 coupons (batch 1) which have been placed in the creep furnaces during coated creep testing in chapter 6. Hence the exposure times were dictated by the creep failure times. The coating is deposited to ~ 34-37 µm (in service thickness).

Table 7.1: Oxidation conditions for Co-Cr-C coated P92 coupons in air.

Sample Number	Temperature [ºC]	Exposure Duration [h]
1	650	1377
2	650	1993
3	650	2383
4	650	2691
5	650	3764
6	675	2659
7	700	1006
8	700	1403

7.2.1 XRD Analysis of Oxide Top Surface

The oxidised top surface of the coated coupons following high temperature oxidation in air were all examined using XRD (figure 7.1). Figure 7.1 shows the main oxides being identified in all cases are: Co_3O_4, Co_2CrO_4, $CoCr_2O_4$ and Cr_2O_3. Comparing the XRD scans in figure 7.1 and table 7.2 there is significant variation between the patterns with different peak intensities for the oxides being seen. This suggests the oxide is irregular on the surface of the coating as there are no obvious trends relating to either time or temperature. The main broad peak positions at ~ 31, 37, 45 and 60^o are shown to be a mixture of all the spinel type phases: Co_3O_4, Co_2CrO_4 and $CoCr_2O_4$. In all coated P92 samples there is no evidence of Cr_3C_2 phase. Appendix B shows that the XRD penetration depth in oxide is ~ 0.78-7.93 µm, dependent on the specific oxide. This shows that the oxide must be at least ~ 8 µm thick as no coating bulk phases are identified by XRD. If the oxide on the coated coupons is the same as on the Co-Cr-C free-standing coating (chapter 4) then the outer layer must be thinner as all of the expected oxide phases are observed without the need for grinding. This suggests the oxide is influenced by the presence of a substrate.

Table 7.2: Summary of the relative XRD peak intensities in figure 7.1.

Temp [^{o}C]	Time [h]	Peak Intensity [Strong, Medium, Weak]			
		Co_3O_4	Co_2CrO_4	$CoCr_2O_4$	Cr_2O_3
650	1377	weak	strong	strong	weak
650	1993	weak	strong	medium	weak
650	2383	weak	medium	strong	weak
650	2691	weak	weak	strong	medium
650	3764	strong	weak	medium	medium
675	2659	weak	strong	strong	weak
700	1006	weak	medium	strong	weak
700	1403	weak	strong	medium	weak

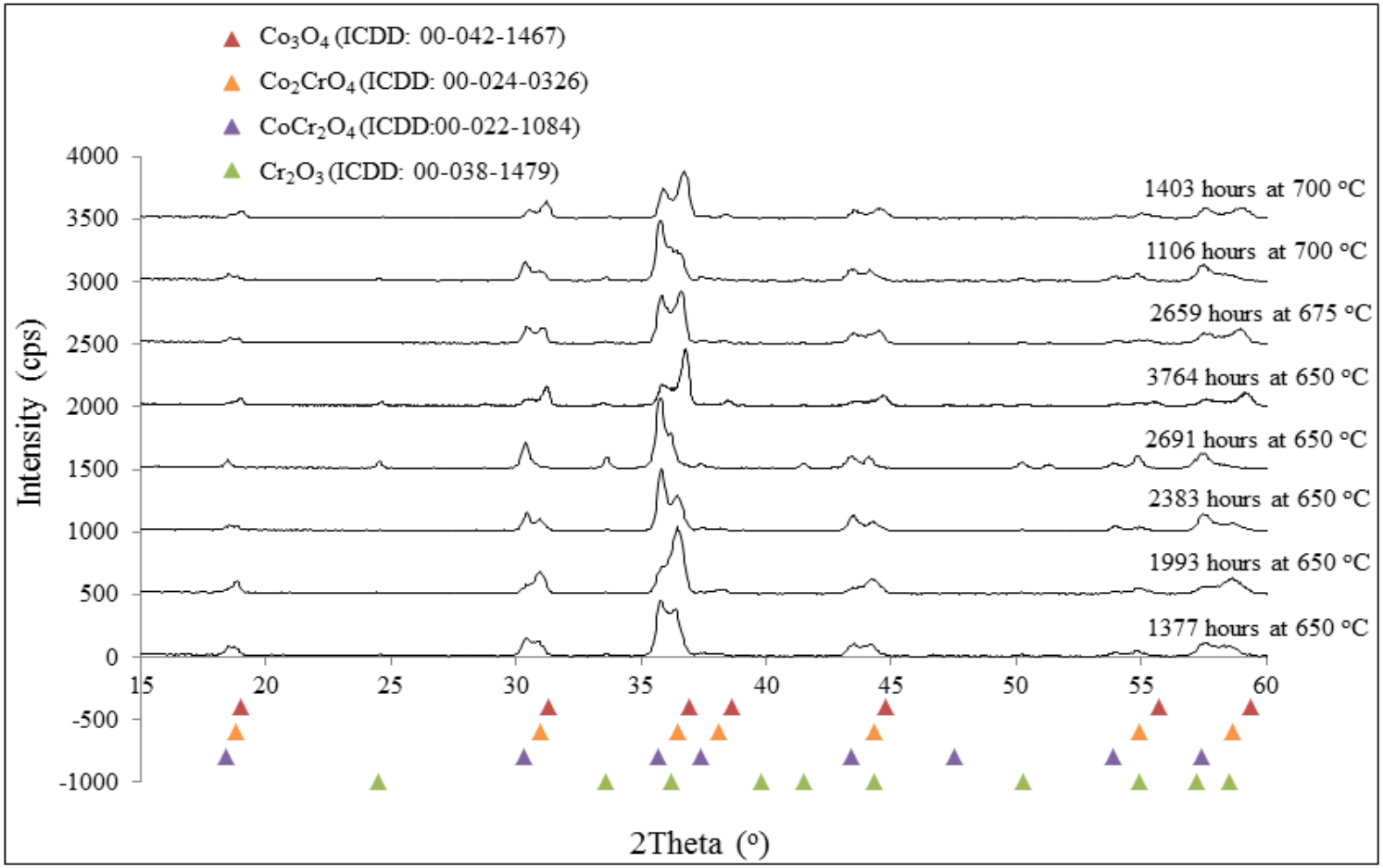

Figure 7.1: XRD patterns obtained from the top oxidised surface of coated coupons following isothermal oxidation in air at 650, 675 and 700 ºC.

7.2.2 SEM/EDX Analysis of Oxide Top Surface

SEM imaging has also been performed plan view on the oxidised top surface of the coated coupons following high temperature oxidation in air. SE imaging of the 2691 hour at 650 ^{o}C sample (figure 7.2) shows that the oxidised surface appears irregular with pores and small cracks being present, there are also clusters of oxide growth across the surface rather than a uniform growth. All of which were not present on the free-standing coating samples in chapter 4. This suggests that the oxide is more irregular than the free-standing case and that the oxide may be less distinctly layered.

EDX analysis (table 7.3) has been performed at ten points across the oxidised surface with an average composition calculated, along with a standard deviation value. This elemental analysis confirms that the oxide on the top surface is composed entirely of an oxide rich in chromium, cobalt and oxygen. Comparing the EDX measurements to the stoichiometric atomic percentages of the oxide phases (table 4.7), it identifies Co_2CrO_4 and $CoCr_2O_4$ as being the most probable phases. Although Co_3O_4 and Cr_2O_3 cannot be ruled out completely due to error in the EDX interaction volume and the limited number of measurement points. All of the 650 ^{o}C samples (1993-3764 hours) show the same oxidised surface; no identifiable evolution is observed and the top surface appears to be an irregular mixture of Co_2CrO_4 and $CoCr_2O_4$. This is different to the free-standing coating in chapter 4 which only identified the Co_3O_4 phase. At the higher temperatures of 675 and 700 ^{o}C the same irregular oxide structure on coated P92 coupons is observed; there appears to be no additional porosity or cracking at higher temperature. EDX analysis also confirms the same outermost oxide phases (Co_2CrO_4 and $CoCr_2O_4$).

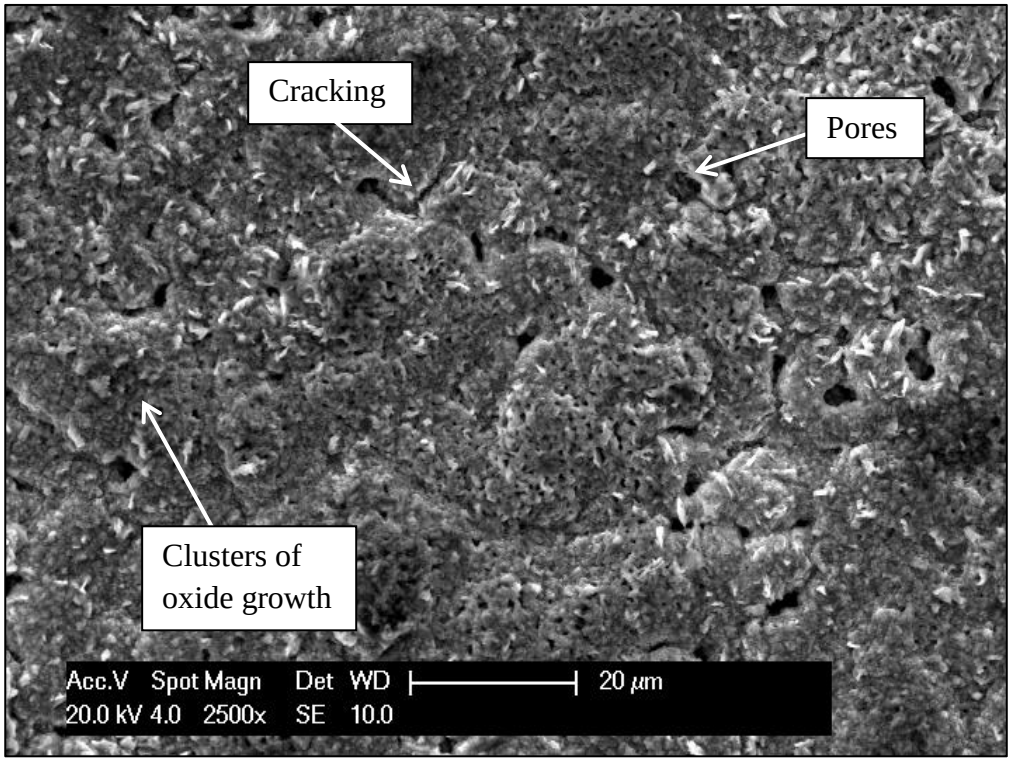

Figure 7.2: SEM micrograph of the coated coupon top oxidised surface following oxidation in air for 2691 hours at 650 ^{o}C.

Table 7.3: The elemental composition determined by EDX analysis of the top surface oxide for an average of 10 measurements (figure 7.2).

Image	Elemental Composition [at %]		
	Co	Cr	O
7.2 - $CoCr_2O_4$ and Co_2CrO_4	24 ± 3.6	20 ± 4.8	56 ± 6.3

7.2.3 SEM/EDX Analysis of Oxide Cross-Section

Following plan view oxide characterisation (SEM, XRD), the oxidised coated coupons were cut and examined in cross-section in the SEM. Special care was taken during cutting to limit oxide damage (chapter 3). However some damage of the oxide is likely to still occur during the grinding and polishing process due to its abrasive nature.

Measurement of the coating thickness in the as-coated condition (before any oxidation occurs) is ~ 34-37 µm (figure 7.3). Figures 7.4-7.6 show that the overall coating thickness following oxidation is now ~ 25 µm. For this measurement the coating surface is approximated from the location of the embedded carbides. This reduction suggests that the coating bulk is being consumed during the oxidation test. The overall thickness from coating-substrate interface to oxide top surface is ~ 27-30 µm. Free-standing coating samples (chapter 4) showed no evidence of coating consumption.

The overall thickness of the oxide on coated coupons is shown to be a function of temperature and time and suggests approximately parabolic oxidation kinetics, as shown in table 7.4 and figure 7.7. Although this is not conclusive because of large standard deviation values in table 7.4. The overall thickness of the oxide is thinner than the free-standing coating (chapter 4).

Figures 7.4-7.6 show the SEM imaging for the 650, 675 and 700 ^{o}C oxidised coupons respectively. Inward and outward oxide growth is observed from SEM imaging (embedded Cr_3C_2 indicate the original top surface); however the inward growth appears to advance much less significantly into the coating bulk than on free-standing coating samples. The ratio of outward to inward growth is approximately 70:30. Cr_3C_2 is seen to be partially embedded within this inward layer, however there are less particles embedded as the oxide advances less significantly. The black contrast carbide shaped features in the oxide are probably particle pull-out during polishing.

EDX analysis (table 7.5) was used to investigate the difference in composition throughout the oxide. The outward growing layer is shown to be a mixture of cobalt, chromium and oxygen rich. The atomic % ratios in table 7.5 suggest

this refers to a mixture of Co_3O_4, $CoCr_2O_4$ and Co_2CrO_4, when compared to the stoichiometric compositions given in table 4.7. There is no obvious evidence for a distinct outermost layer of Co_3O_4, as seen on the free-standing coating (chapter 4). The small inward growth region contains mainly a chromium and oxygen rich phase with an atomic ratio (table 7.5) suggesting it is Cr_2O_3 when compared to table 4.7. This phase seems to exist as a more distinct innermost layer rather than halos forming around the Cr_3C_2, as seen for the free-standing coating. Considering figure 7.4 the Cr_2O_3 phase (darker contrast inner layer) is shown to be slightly thicker and appears more distinct as the oxidation time is increased. This suggests that the integrity of the beneficial oxide (Cr_2O_3) increases with time. When comparing figure 7.4a and figure 7.6b the Cr_2O_3 is also shown to be slightly thicker and more distinct as the oxidation temperature is increased. This suggests that Cr_2O_3 is forming quicker at higher temperature.

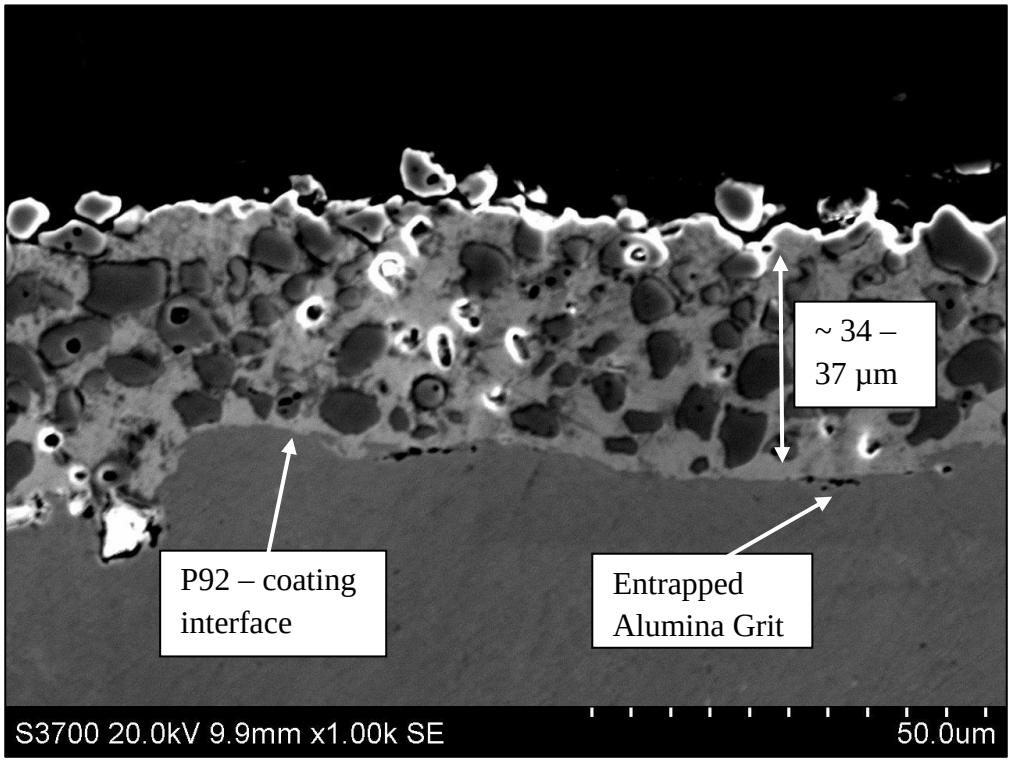

Figure 7.3: SEM micrographs of as-coated P92 coupon cross-section [Chi and Barnard, 2012; Foster, 2007].

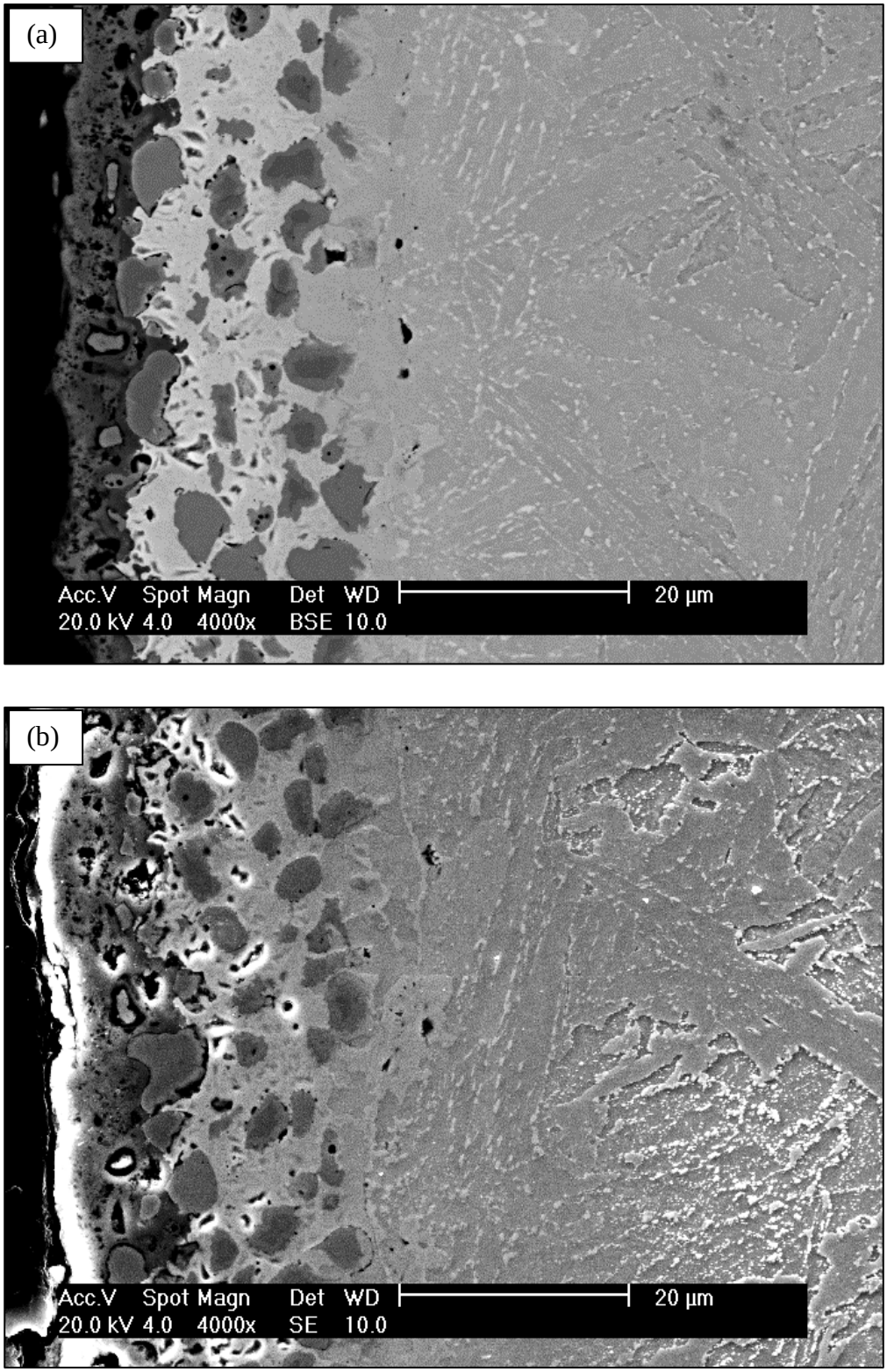

Figure 7.4: SEM micrographs of coated coupons oxidised at 650 ^{o}C for (a) 1377 hours (b) 1993 hours (c) 2383 hours (d) 2691 hours and (e) 3764 hours.

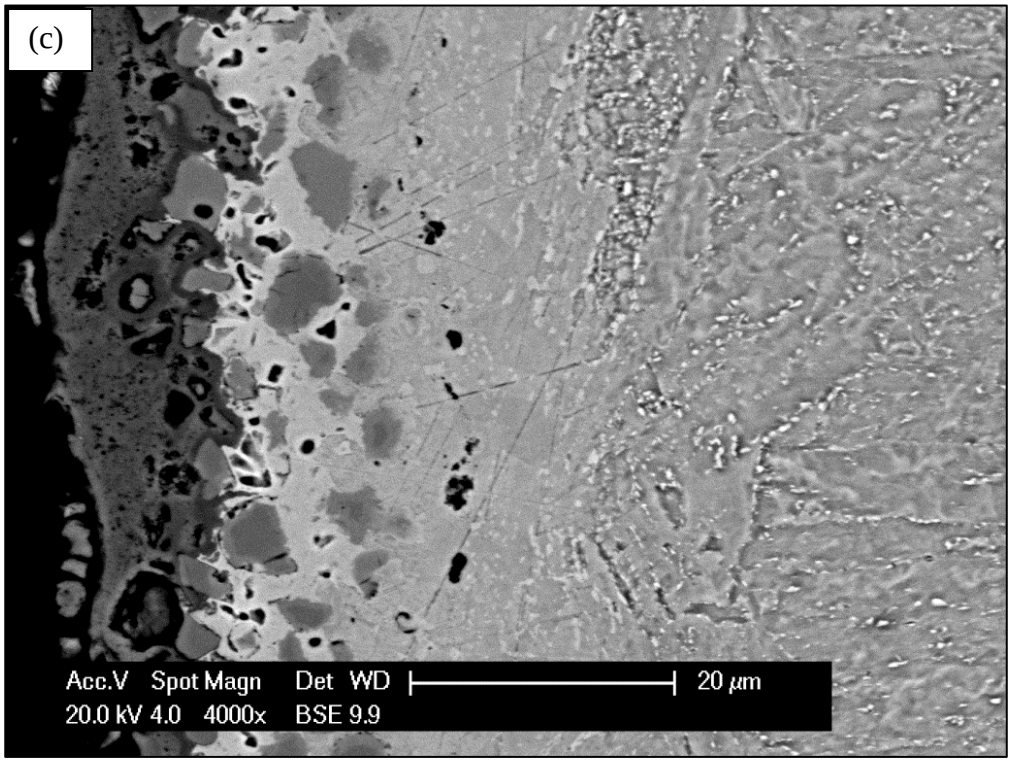

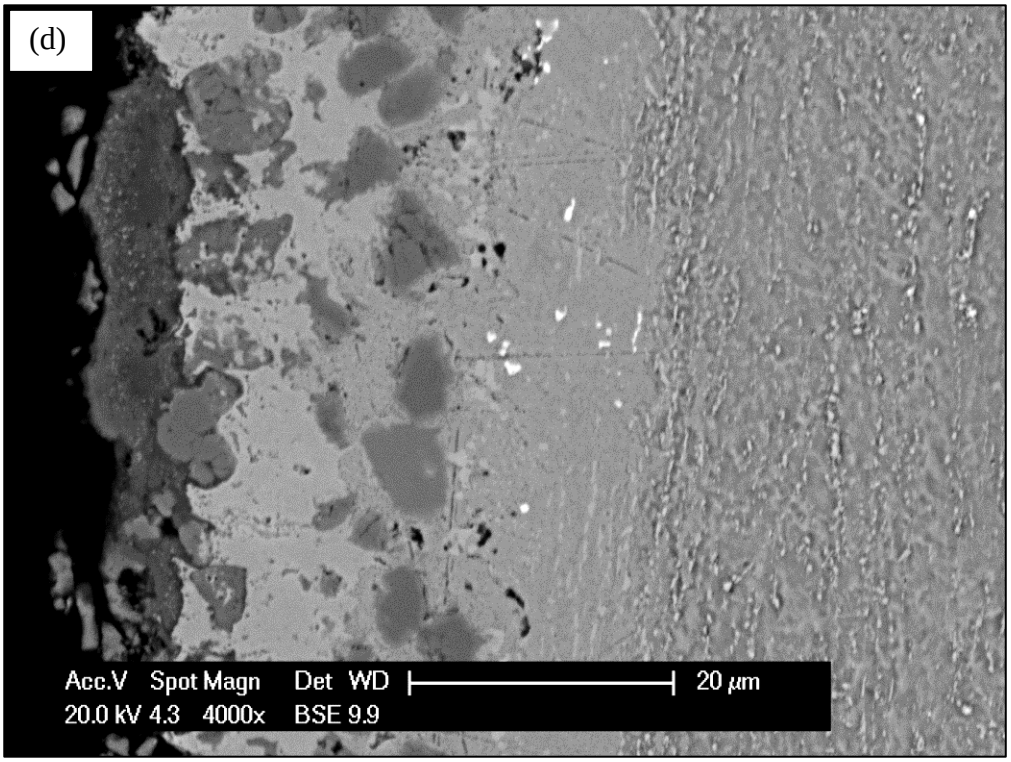

Figure 7.4: SEM micrographs of coated coupons oxidised at 650 ^{o}C for (a) 1377 hours (b) 1993 hours (c) 2383 hours (d) 2691 hours and (e) 3764 hours.

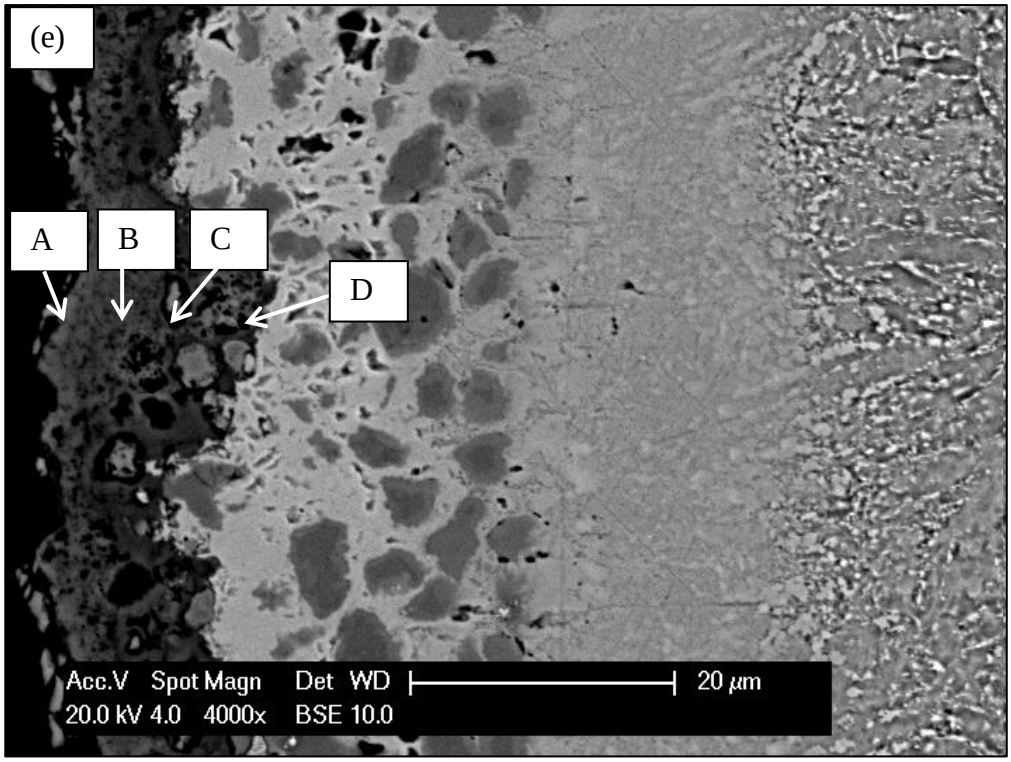

Figure 7.4: SEM micrographs of coated coupons oxidised at 650 ^{o}C for (a) 1377 hours (b) 1993 hours (c) 2383 hours (d) 2691 hours and (e) 3764 hours.

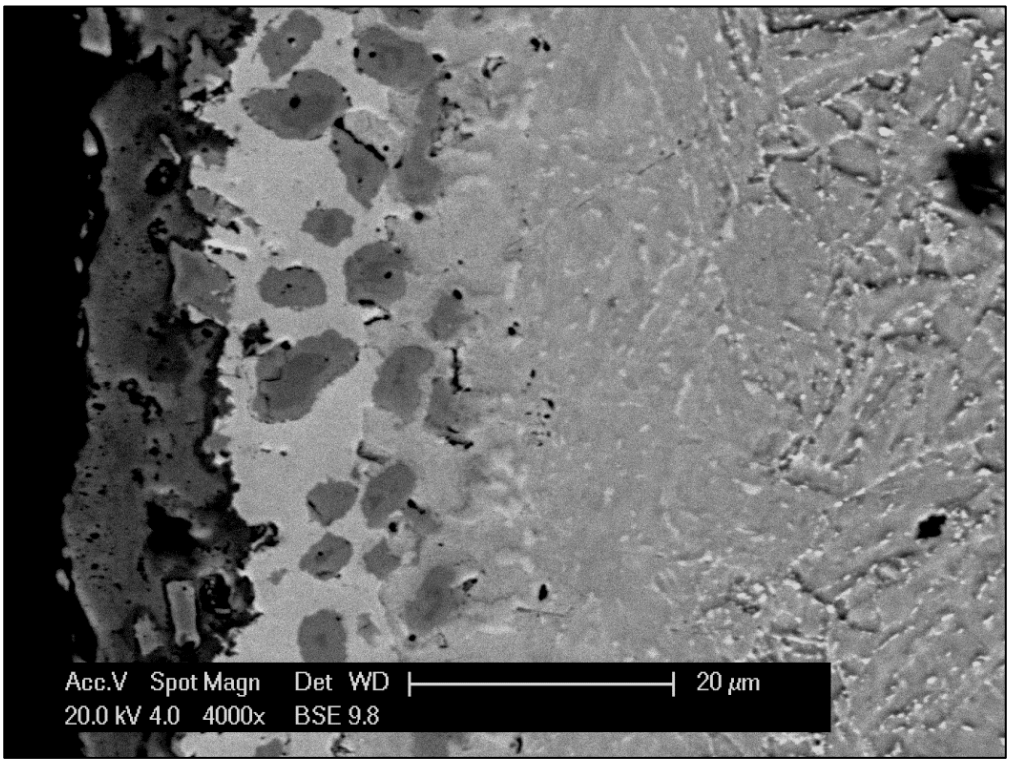

Figure 7.5: SEM micrograph of coated coupons oxidised at 675 ^{o}C for 2659 hours.

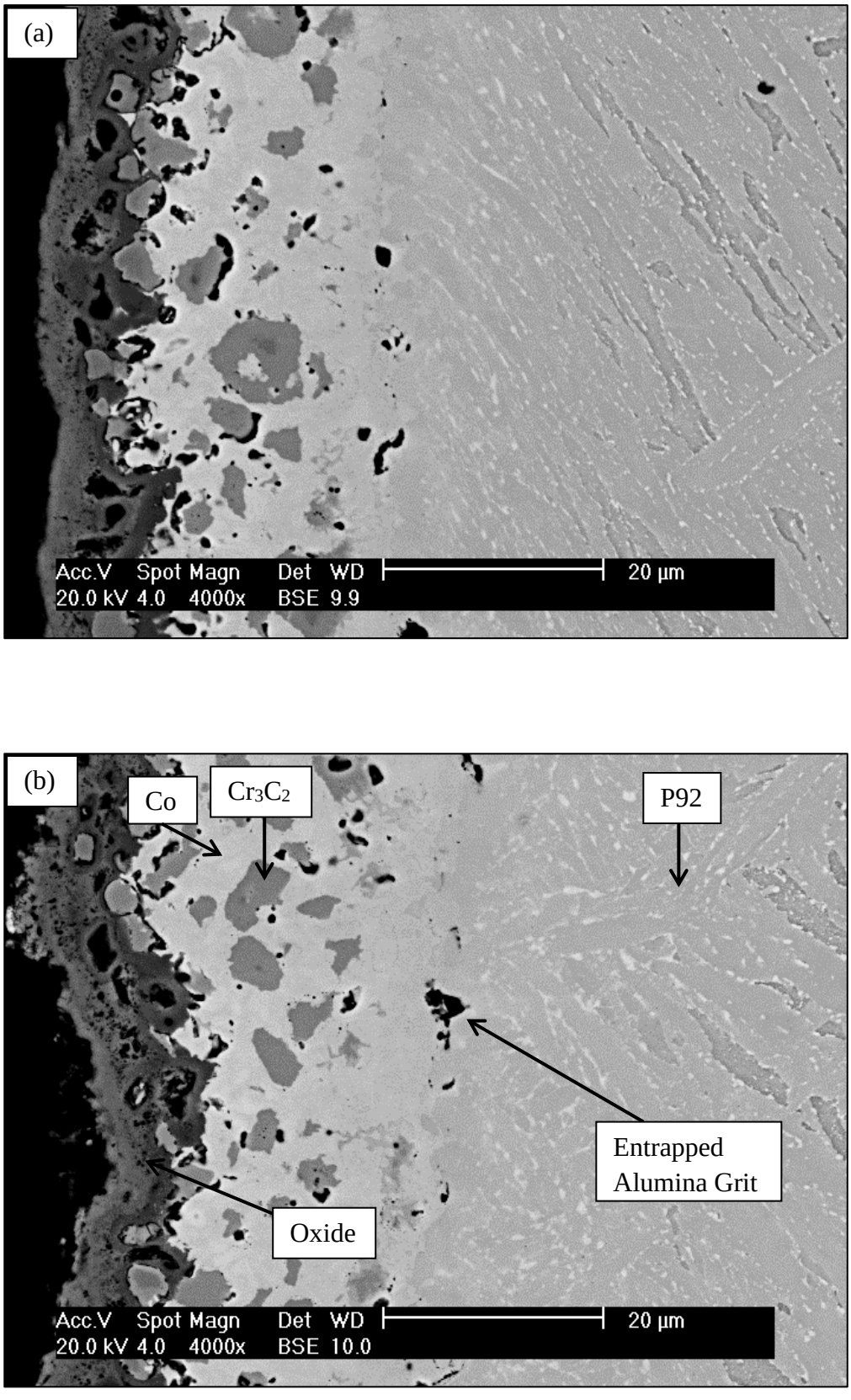

Figure 7.6: SEM micrographs of coated coupons oxidised at 700 ^{o}C for (a) 1006 hours (b) 1403 hours.

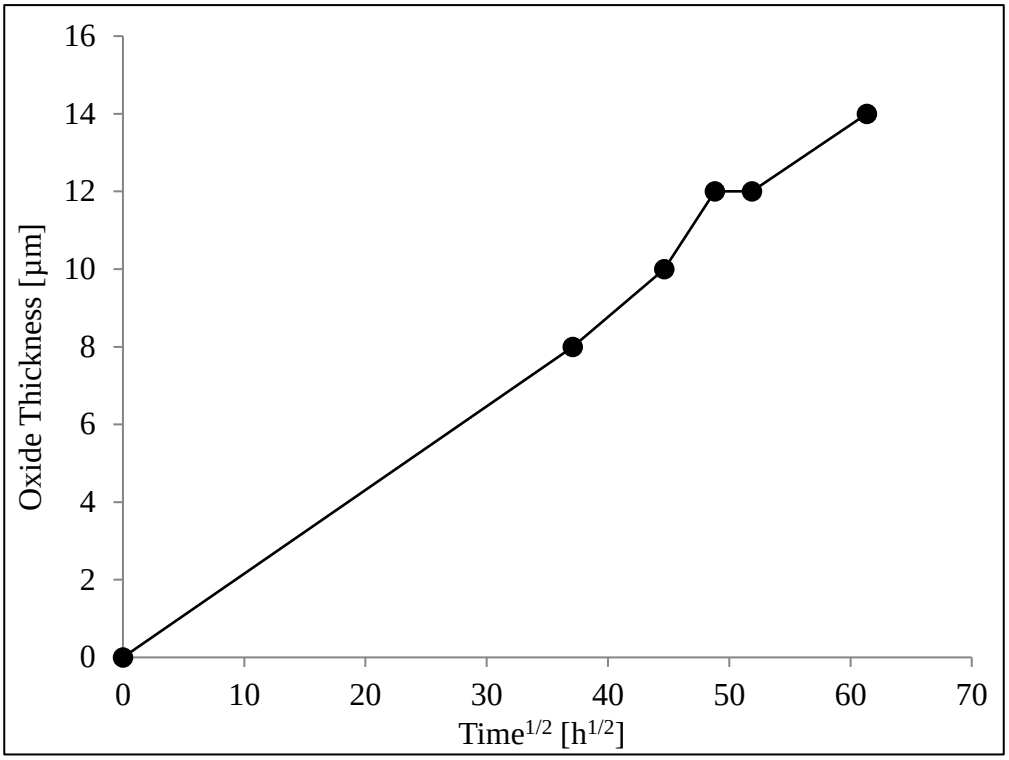

Figure 7.7: Oxide thicknesses plotted against time for coated P92 coupons following oxidation in air at 650 ºC (table 7.4).

Table 7.4: Average oxide thickness measurements for coated P92 coupons following oxidation in air at 650, 675 and 700 ºC.

650 ºC		**675 ºC**		**700 ºC**	
Time [h]	**Oxide Thickness [µm]**	**Time [h]**	**Oxide Thickness [µm]**	**Time [h]**	**Oxide Thickness [µm]**
1377	8 ± 0.9	2659	12 ± 2.5	1006	9 ± 2.1
1993	10 ± 0.7			1403	10 ± 1.3
2383	12 ± 0.9				
2691	12 ± 1.9				
3764	14 ± 1.7				

Table 7.5: The elemental composition determined by EDX analysis of the oxide cross-section for the measurement position given in figure 7.4e.

Location	Elemental Composition [at %]		
	Co	Cr	O
A - Co_3O_4	34 ± 7.7	4 ± 6.1	62 ± 2.5
B - $CoCr_2O_4$ and Co_2CrO_4	26 ± 6.3	13 ± 7.0	61 ± 1.9
C - $CoCr_2O_4$ and Co_2CrO_4	23 ± 5.0	17 ± 4.8	60 ± 1.1
D - Cr_2O_3	3 ± 3.4	42 ± 3.1	55 ± 1.3

7.3 Oxide Scale Characterisation of Creep Specimens

The next area of investigation highlighted as important by industry was the effect that stress, especially creep, has on the coating system during high temperature oxidation. To evaluate the effect of stress on the oxidation behaviour of the coated P92 system, the failed creep specimens were examined (table 6.1). Both batch 1 and 2 samples were considered for this section to understand if entrapped alumina grit in batch 1 has any effect on the coating or oxide integrity. Industry are also interested in the reliability of coating onto curved surfaces.

7.3.1 XRD Analysis of Oxide Top Surface

XRD patterns of the oxidised top surface of the failed creep specimens have been considered for this section, as shown for the representative example in figure 7.8. The patterns show that the main phases being identified in all cases are: Co_3O_4, Co_2CrO_4, $CoCr_2O_4$ and Cr_2O_3. This is consistent with the coated coupons in section 7.2 and once again no grinding is required to reveal the inner oxide layers, suggesting overall a thin oxide is present compared to the

free-standing coating samples in chapter 4. The XRD patterns suggest that there is variation between samples in the ratios of these phases; this again suggests that an irregular oxide is present on the creep specimens. There is again no evidence for embedded Cr_3C_2 in the oxide layer. As shown in section 7.2.1 and appendix B the X-ray penetration depth in the oxide is calculated to be ~ 0.78-7.93 μm, dependent on the specific oxide.

A common feature with all the creep specimen XRD patterns, as illustrated by figure 7.8, is that the peaks for Cr_2O_3 are slightly more dominant than they were in section 7.2 for corresponding coated coupons. This would suggest that Cr_2O_3 is more dominant in the outermost layers of the creep specimen, compared to the coated coupons in section 7.2. This could suggest cracking or damage of the outermost oxide layer exposing the chromium richer layers.

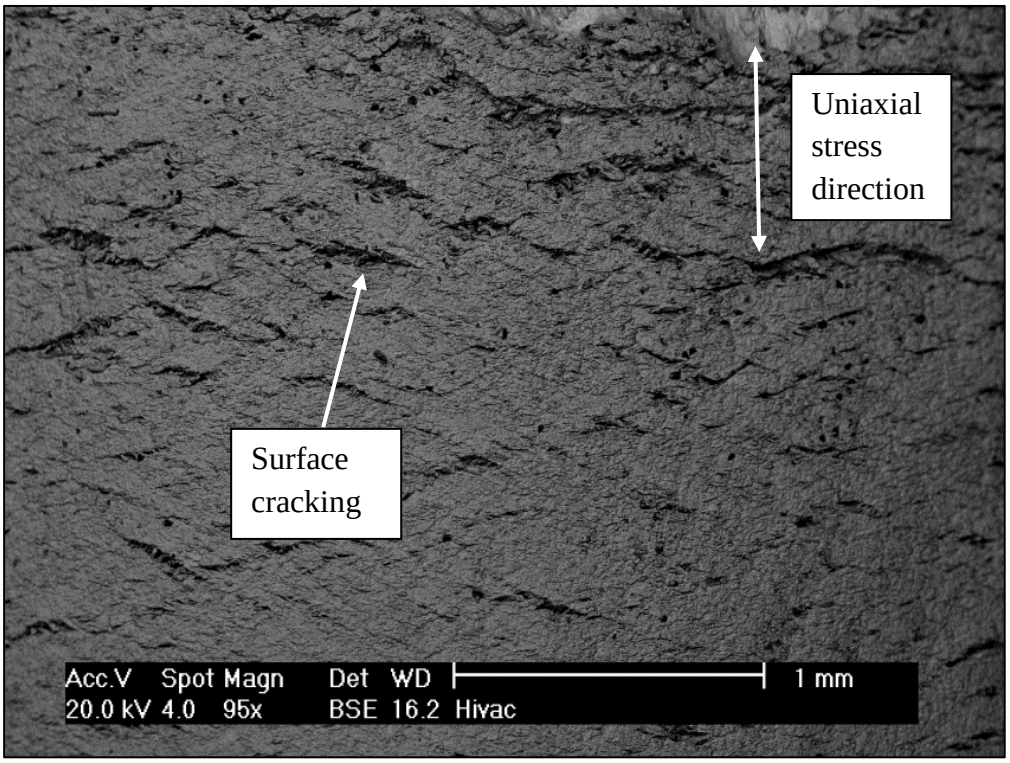

Figure 7.9: SEM micrograph to show cracking on the surface of the 110 MPa coated creep test (batch 1) at 650 ºC – 2383 hours.

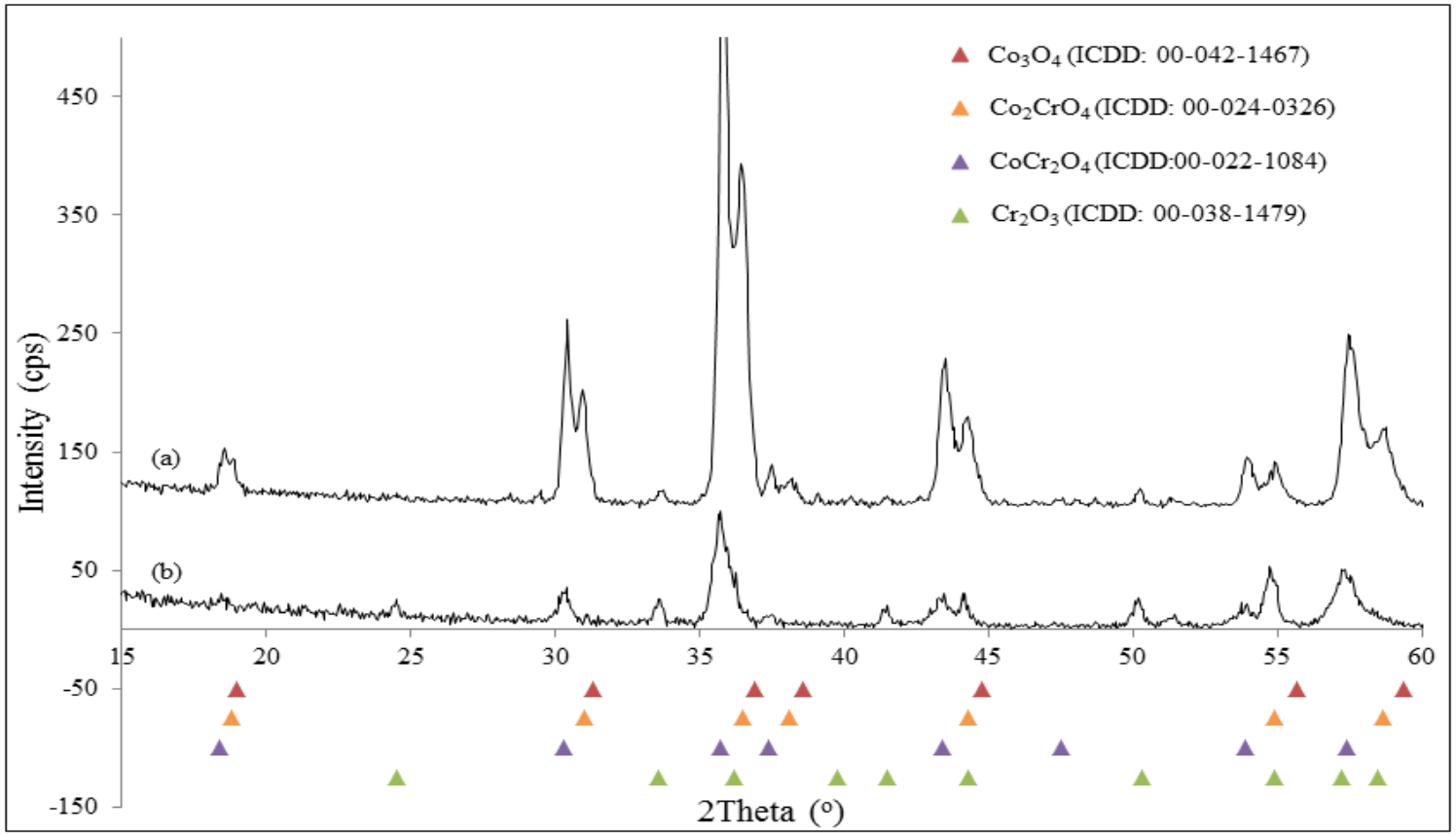

Figure 7.8: Comparison of the XRD pattern of the oxide top surface for (a) the coated P92 coupon and (b) the failed creep specimen (110 MPa), both following oxidation for 2383 hours at 650 °C.

7.3.2 SEM/EDX Analysis of Oxide Top Surface

SEM imaging has been performed plan view on the oxidised surface of the failed creep specimens. For all specimens, summarised in table 6.1, cracking was observed on the outer surface, as illustrated for the 110 MPa 650 ^{o}C creep test in figure 7.9. Cracks would appear to be propagating perpendicular to the applied stress direction in all cases, with slightly more evidence at higher stress. The cracking is also increased when imaging closer to the fracture surface but is present along the entire gauge length. Figure 7.9 is taken at the mid-point along the specimen gauge length. EDX analysis (table 7.6) identifies that the outer oxide is a mixture of chromium, cobalt and oxygen rich, similar to stress free samples (section 7.2). Comparison to table 4.7 suggests that the oxide is primarily Co_2CrO_4 and $CoCr_2O_4$. Examination of the higher temperature samples shows the same irregular oxide and there does not appear to be more evidence for cracking or porosity.

Table 7.6: The elemental composition determined by EDX analysis of the top surface oxide for an average of 10 measurements (figure 7.9).

Image	Elemental Composition [at %]		
	Co	Cr	O
7.9	26 ± 7.6	15 ± 9.2	59 ± 7.5

7.3.3 SEM/EDX Analysis of Oxide Cross-Section

Following plan view oxide characterisation (XRD, SEM) the failed creep specimens were cut and examined in cross-section in the SEM. Once again special care was taken during cutting to limit oxide damage (chapter 3). The position was chosen along the gauge length as far away from the fracture

surface as possible (chapter 3). This was to minimise the effects of proximity to the fracture surface.

Figures 7.10-7.12 present SEM micrographs of selected cross-sections. The first observation from figures 7.10-7.12 is that at all stresses (65-120 MPa) the coating remains intact and shows no signs of failure. This is encouraging as it shows that even at high stresses and temperatures the coating-substrate interface retains its integrity. The coating is also retaining its integrity when applied to a curved substrate.

The overall oxide thickness on the coated creep specimens is shown to be comparable to the corresponding coated P92 coupons presented in section 7.2. For example the stress free 3764 hour sample at 650 ^{o}C is ~10 μm and following creep testing the oxide is ~ 10 μm. There are no measurable differences in oxide thickness (within standard error). The oxide on the creep specimens is again shown to follow approximately parabolic kinetics (table 7.7, figure 7.13).

Table 7.7 and figure 7.13 also compare the coating oxide thicknesses for the failed batch 1 coated creep specimens to the oxide thickness on uncoated specimens. Standard deviation values for oxide thickness are included in table 7.7. The oxide thickness is significantly reduced by coating application, especially at the highest temperatures and longest times. The standard deviation is also significantly reduced for coated specimens suggesting a more stable and regular oxide. The coating bulk also shows some signs of being consumed by the oxidation process. For example the as-coated thickness is 34-37 μm. Figures 7.10-7.11 show that after creep this is reduced to ~ 25 μm. This is consistent with coated coupons in section 7.2.

Figure 7.10 presents a representative cross-section SEM image for the 105 MPa batch 1 creep specimen at 650 ºC (3764 hours). Figure 7.11 presents a cross-section SEM image for the 110 MPa batch 2 creep specimen at 650 ºC (2691 hours). Once again inward and outward oxide growth is observed with an outward to inward growth ratio of ~ 70:30. Cr_3C_2 phase can be seen partially embedded within the inner layer. Black contrast, carbide shaped areas can be seen in the oxide which are as a result of pull out during the polishing process. The creep stress has introduced more cracking and voiding in the outermost layer of the oxide. In the majority of cases the damage is not seen to propagate through to the innermost layer of the oxide or through to the coating. EDX analysis (table 7.8) shows that the cracked outermost oxide layer is a mixture of cobalt and chromium rich oxides. The atomic % ratios (table 4.7) suggest that this refers to the Co_3O_4, Co_2CrO_4 and $CoCr_2O_4$. The small inward growth region contains mainly an inner layer of Cr_2O_3, which remains intact and shows no signs of damage. The oxide structure is consistent with section 7.2.

Table 7.7: Average oxide thickness measurements for the failed creep specimens, both uncoated (U) and coated-batch 1 (C).

650 ºC			**675 ºC**			**700 ºC**		
Stress [MPa]	Average Oxide Thickness [µm]		Stress [MPa]	Average Oxide Thickness [µm]		Stress [MPa]	Average Oxide Thickness [µm]	
	U	C		U	C		U	C
110	8.7 ± 7.1	6.7 ± 1.0	80	48.2 ± 34.5	9.7 ± 1.8	65	38.6 ± 56.7	6.0 ± 3.6
120	6.0 ± 2.2	5.2 ± 1.4	90	28.2 ± 5.7	8.3 ± 2.4	70	39.7 ± 110.2	6.0 ± 1.0
			100	24.8 ± 10.3	7.3 ± 1.9			

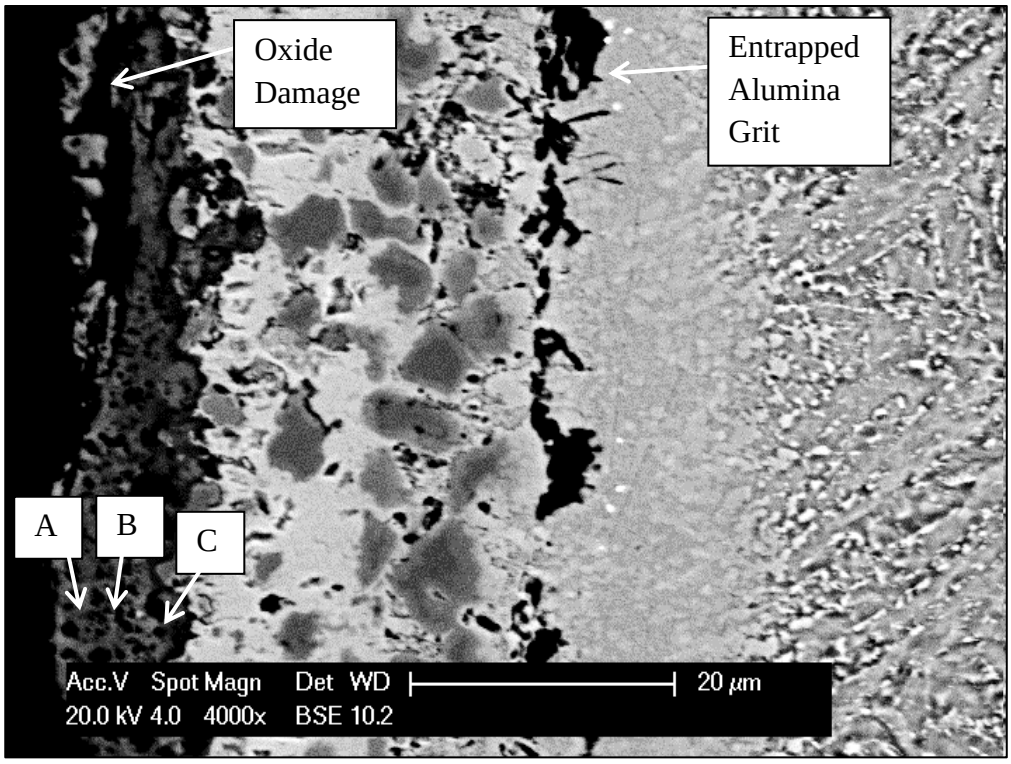

Figure 7.10: SEM micrograph of coated P92 specimen following creep testing at 650 ^{o}C and 105 MPa for 3764 hours (batch 1).

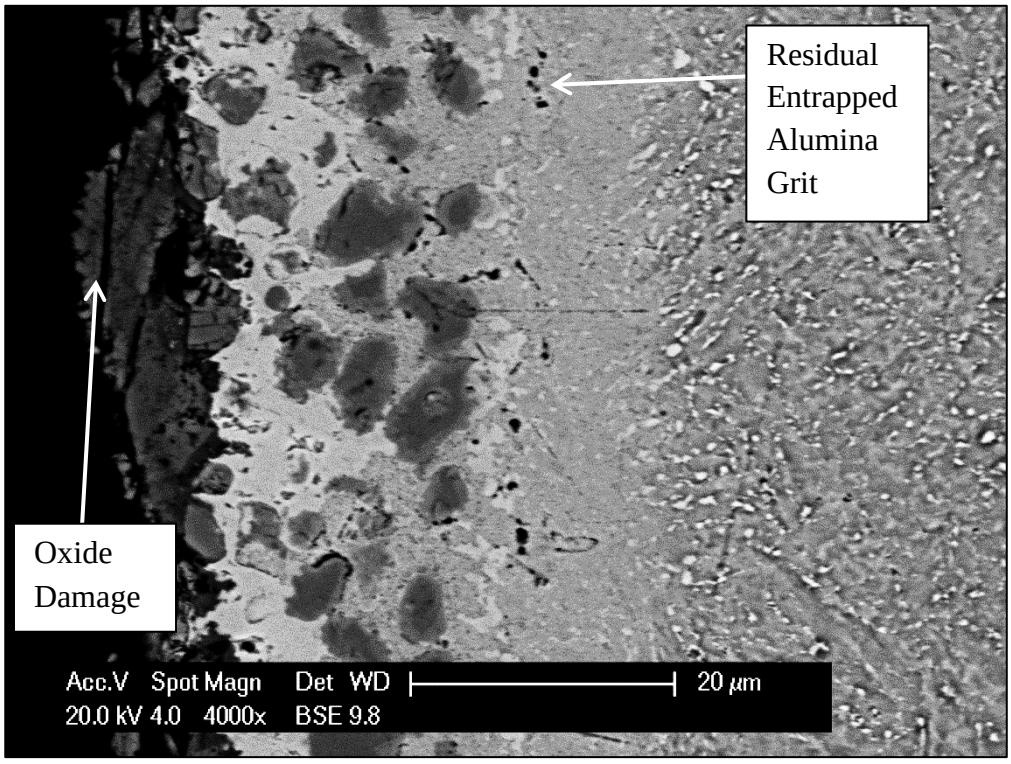

Figure 7.11: SEM micrograph of coated P92 specimen following creep testing at 650 ^{o}C and 110 MPa for 2691 hours (batch 2).

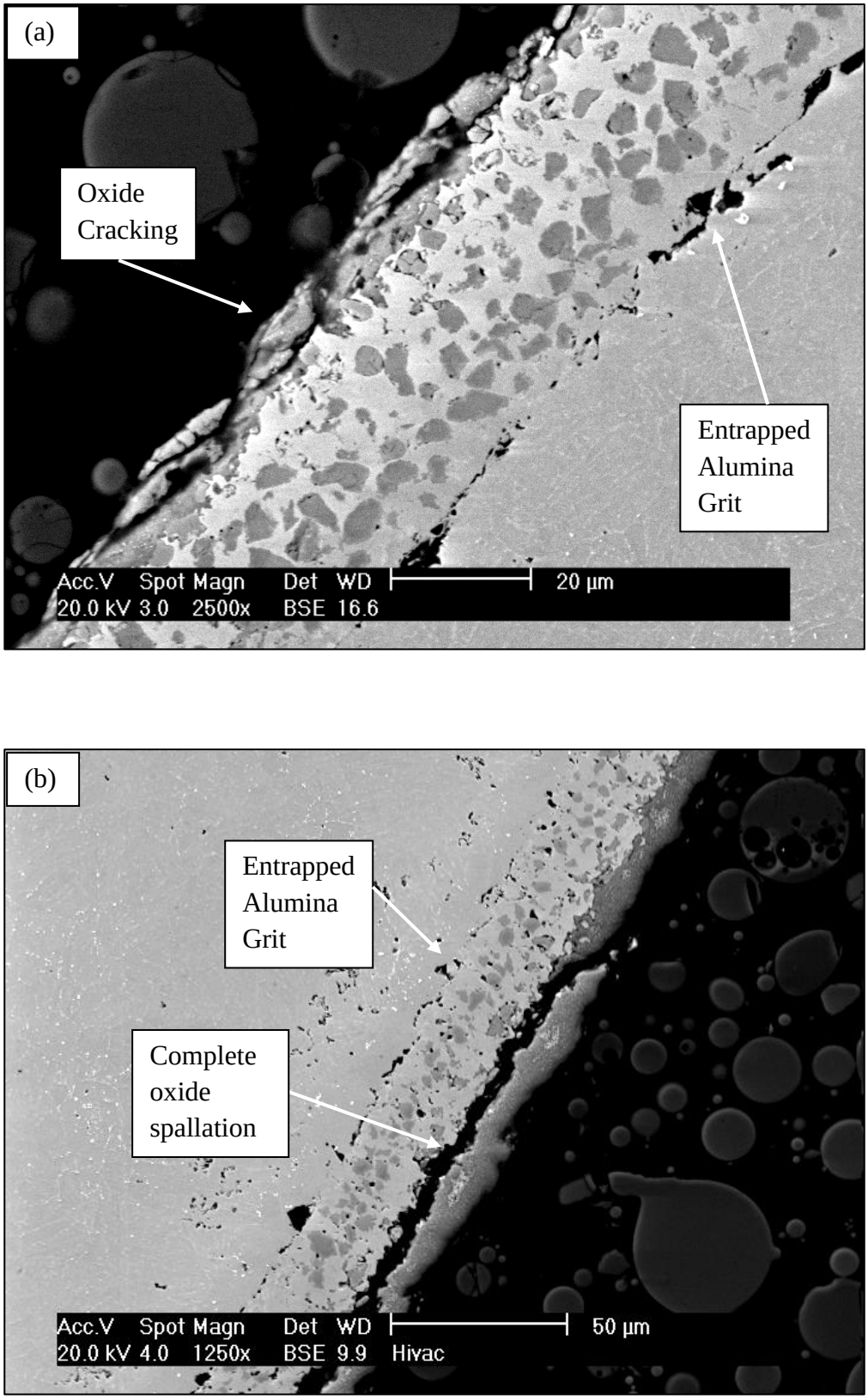

Figure 7.12: SEM micrographs of more severe oxide damage on the failed creep specimens (batch 1) for (a) 110 MPa at 650 ºC and (b) 80 MPa at 675 ºC.

Table 7.8: The elemental composition determined by EDX analysis of the oxide cross-section for the measurement position given in figure 7.10.

Location	Elemental Composition [at %]		
	Co	Cr	O
A - $CoCr_2O_4$, Co_2CrO_4 and Co_3O_4	34 ± 5.0	8 ± 6.1	58 ± 2.5
B - $CoCr_2O_4$ and Co_2CrO_4	26 ± 3.4	13 ± 7.0	61 ± 1.9
C - Cr_2O_3	5 ± 1.2	41 ± 1.7	54 ± 2.2

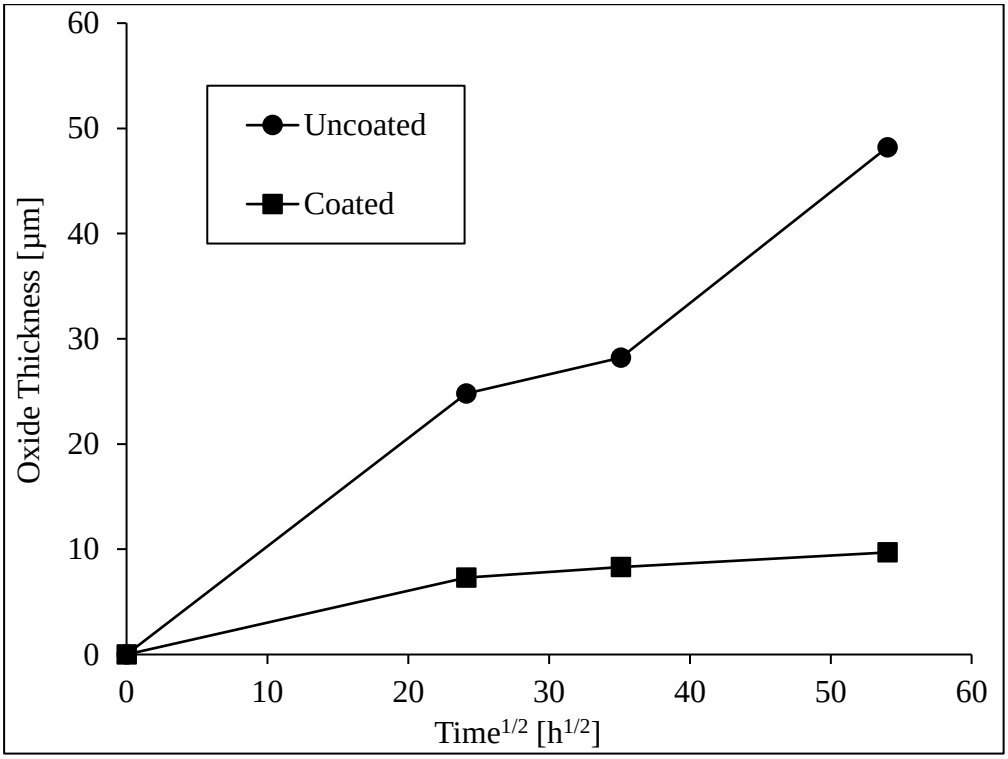

Figure 7.13: Average oxide thicknesses plotted against time for the 675 ºC failed uncoated and coated creep specimens in table 7.7.

As mentioned cracking is evident on the outermost surface of the oxide for most failed coated creep specimens. In places on the specimens this damage can propagate through to the inner layers and cause complete spallation of the

oxide layer. This would be particularly detrimental in service as it could cause excessive consumption of the coating and ultimately coating failure. This is shown clearly on figure 7.12. This effect is only observed in a few places on each specimen and is usually occurring when the oxide is becoming unusually thick.

7.4 Coating-Substrate Characterisation of Coupons / Creep Specimens

7.4.1 Coating Evolution

As mentioned previously the coating bulk material in both the coated coupons and coated creep specimens appears to show signs of being consumed during oxidation testing. The Cr_3C_2 particles within the coating bulk also appear to be evolving as shown in figures 7.4-7.6 and figures 7.10-7.11. The Cr_3C_2 particles appear to have a dark inner region and a lighter outer halo. In even the longest term cases (figure 7.4e) the Cr_3C_2 particles remain present and complete dissolution has not occurred. XRD has been performed on the coating bulk once the oxidised surface had been fully ground away (~ 15 µm), as shown in figure 7.14. Appendix B shows the X-ray penetration depth is 1.02-2.35 µm.

Figure 7.14 shows that the coating bulk carbide phase is now composed of Cr_3C_2 (strong peaks) and Cr_7C_3 (weak peaks) suggesting a transformation from Cr_3C_2 to Cr_7C_3. Cr_7C_3 will have a higher mean atomic number than Cr_3C_2 and will appear brighter in BSE mode. Therefore the dark centre of the carbide particle refers to Cr_3C_2 and the lighter halo refers to Cr_7C_3. This level of transformation was not observed for the free-standing coating in chapter 4.

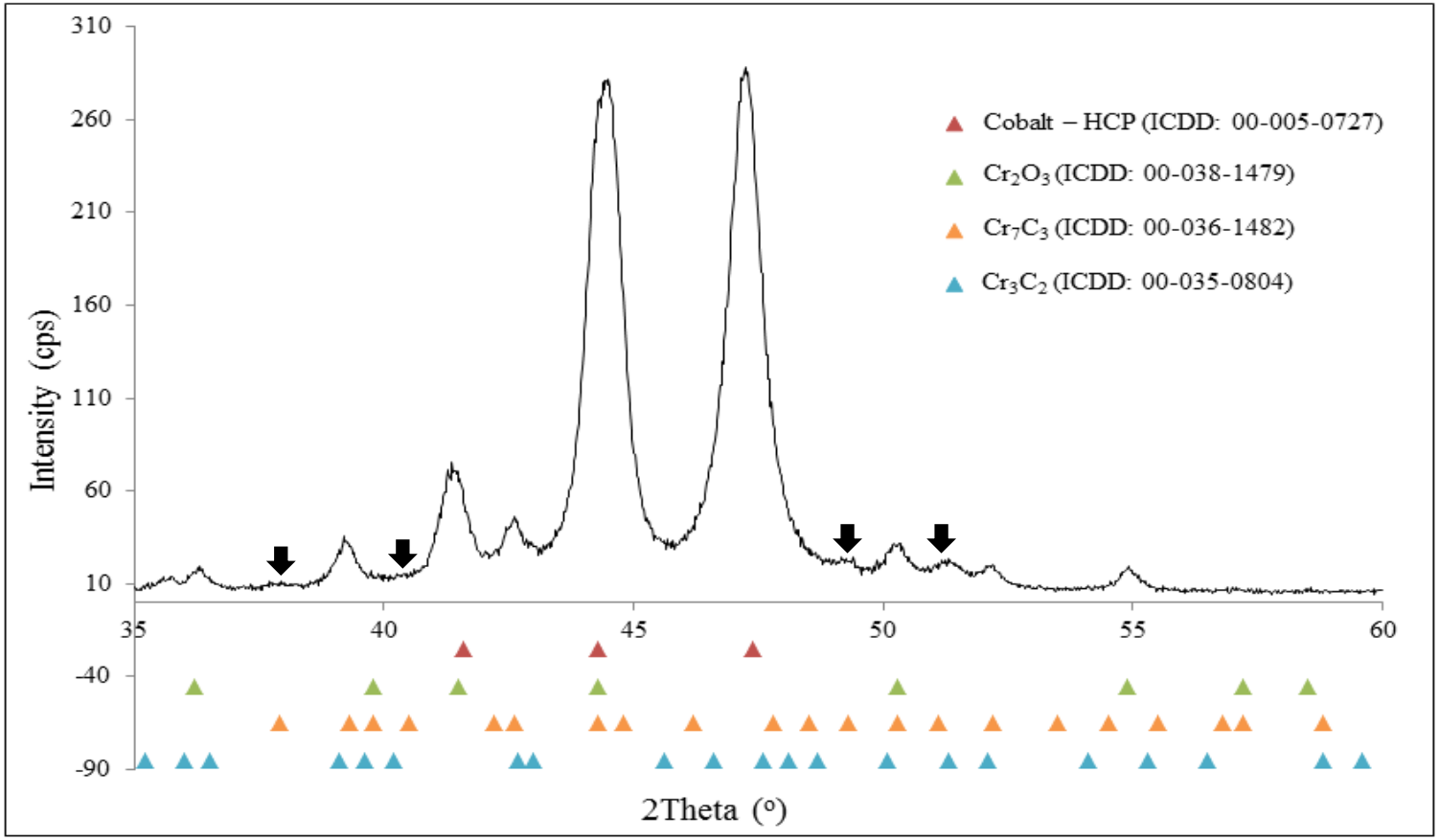

Figure 7.14: XRD pattern of the Co-Cr-C coating bulk, once the oxidised surface had been completely removed, for the coated P92 coupon following oxidation in air for 1377 hours at 650 °C. Characteristic Cr_7C_3 peaks marked with black arrows.

7.4.2 Inter-Diffusion Zone Formation

The coated P92 coupons (section 7.2) and coated creep specimens (section 7.3) have been further studied in cross-section to understand the diffusion of elemental species across the coating-substrate interface and to characterise the IDZ. Industry is especially interested in diffusion properties and what effect this could have on the coating integrity or the substrate material. The main diffusion species of interest will be carbon, chromium, cobalt and iron. Batch 1 coated coupons and coated creep specimens have primarily been used to study the diffusion because the entrapped alumina grit at the coating-substrate interface act as inert markers to indicate the original coating-substrate interface following diffusion. Inert alumina markers will not have any effect on the diffusion processes.

Figures 7.4-7.6 and 7.10-7.11, presented previously, show evidence of microstructural change in the P92 steel close to the coating-substrate interface following high temperature oxidation (samples polished to a high standard and etched with Vilella's reagent). This area of microstructural change is defined as the IDZ and is found to be present in all samples detailed in table 7.1 and table 6.1. This IDZ is summarised in the schematic in figure 7.15. Table 7.9 show that this IDZ in coated coupons increases in size with time and temperature. EDX mapping of the coating-substrate interface shows that cobalt diffuses from the coating into the steel and iron diffuses from the steel into the coating. The IDZ size can be estimated from the diffusion distance of cobalt. The presence of an IDZ appears to have no effect on the coating-substrate adherence at these exposure conditions. There is also no evidence of porosity

or damage around the IDZ at these test conditions, even for the failed creep specimens.

For a more detailed consideration of the diffusion between the coating and the substrate, EDX elemental profiling across the interface has been used to investigate the coated coupons; specifically the diffusion of iron, cobalt and chromium. To reduce complexity only these three elements have been analysed at this stage. The line profiles have been presented in figures 7.16-7.18 for 650 ^{o}C samples at increasing exposure times. Before diffusion P92 contains ~ 91 % iron, ~ 9 % chromium and 0 % cobalt. Before diffusion the Co-Cr-C coating contains ~ 70 % cobalt, ~ 30 % chromium and 0 % iron. Carbon cannot be measured accurately due to the limitations of EDX so will be characterised computationally later in this chapter. In the P92 side the EDX values have an average standard deviation of ± 0.3 wt %. In the coating side the standard deviation is on average ± 5.4 wt %. The increase in error in the coating side is due to the analysis area spanning the multi-phase region of carbides and matrix (see chapter 3).

Figures 7.16-7.18 show that the cobalt is diffusing from the coating into the substrate and the iron is diffusing from the substrate into the coating. This is expected and elements are diffusing along the concentration profile. However, chromium appears to be diffusing from the steel into the coating; this is against the concentration profile. Cobalt, iron and chromium diffuse to similar distances and the diffusion distances are shown to increase with temperature and time.

Reconsidering figures 7.4-7.6 and figures 7.10-7.11 the IDZ appears to have the same microstructure as the rest of the P92 but the contrast of the matrix is

different. For example the bright precipitate phases (typically $M_{23}C_6$) still appear to be present however the matrix appears darker. It seems likely that the diffusion processes taking place are altering the composition of the P92 matrix in the IDZ and therefore causing the contrast to be different when BSE SEM is performed.

There is no evidence of any interface damage or detrimental effects of the inter-diffusion, even when stress is applied (creep specimens). There is also no evidence of new precipitates forming in the P92 substrate that could be detrimental to mechanical properties. Figure 7.10 and 7.11 also show that the inclusion of alumina grit in the batch 1 creep specimens does not have a detrimental effect. The large dark contrast features at the interface in figure 7.10 are leftover alumina grit from the slurry grit blast pre-deposition treatment for batch 1 samples. Figure 7.11 is batch 2 and only contains some very fine residual grit as it has been prepared by a chemical etch process rather than slurry grit blasting. The grit is not seen to be having a detrimental effect on the system and crucially is not acting as stress concentrators.

Table 7.9: Estimated IDZ size in the coated coupons from SEM micrographs and EDX mapping of cobalt.

Sample Number	Temperature [ºC]	Exposure Time [h]	Estimated IDZ Size [µm]
1	650	1377	11 ± 1
2	650	1993	13 ± 1
3	650	2383	14 ± 1
4	650	2691	14 ± 1
5	650	3764	18 ± 1
6	675	2659	21 ± 1
7	700	1006	15 ± 1
8	700	1403	16 ± 1

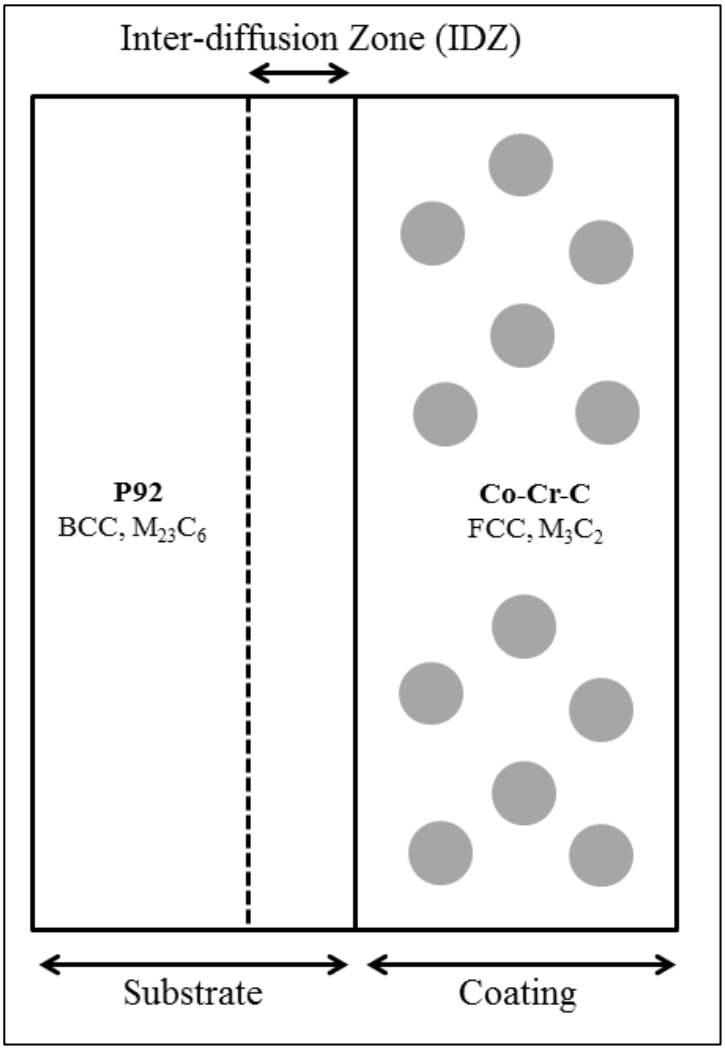

Figure 7.15: Schematic cross-section of the IDZ development between the DB P92 substrate and the Co-Cr-C coating.

Table 7.10: Activities of the elements in the Co-Cr-C coating and the DB P92 ferritic steel substrate material at 650 ^{o}C, calculated using Thermo-Calc.

Element	DB P92 Activity [TCFE7]	Co-Cr-C Coating Activity [SSOL5]	Activity Difference
C	5.10×10^{-4}	1.54×10^{-1}	0.15349
Cr	4.76×10^{-3}	5.39×10^{-4}	4.221×10^{-3}
Co	0	5.81×10^{-3}	5.81×10^{-3}
Fe	6.90×10^{-3}	0	6.90×10^{-3}

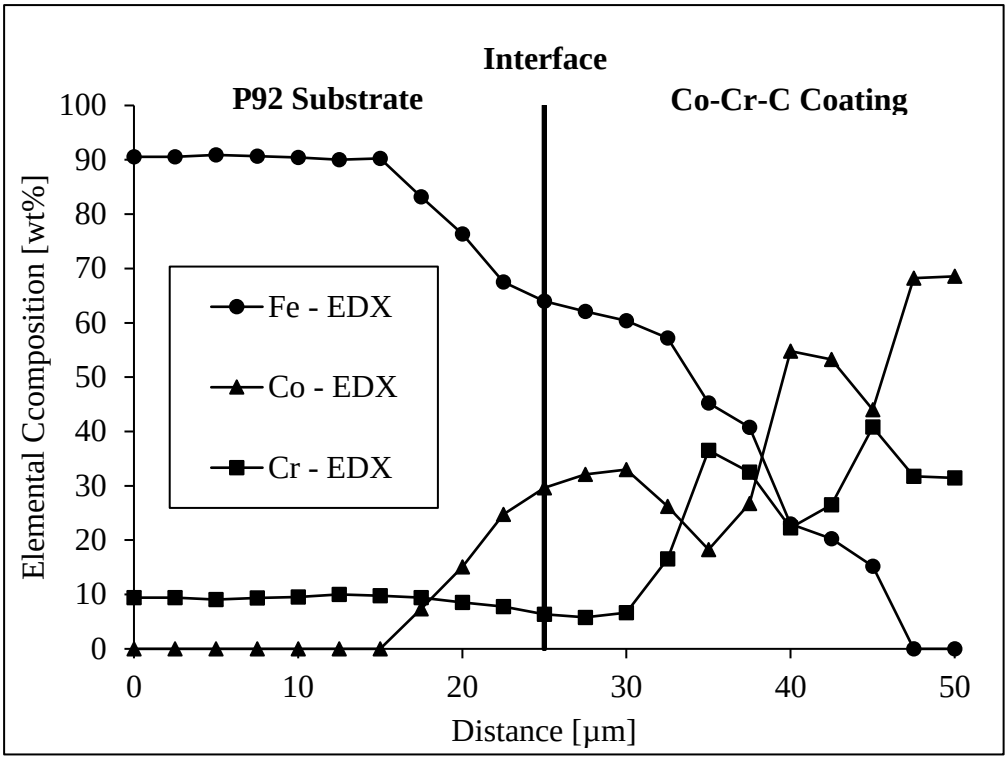

Figure 7.16: EDX measured composition across the coating-substrate interface following high temperature oxidation for 1993 hours at 650 ºC (coupon).

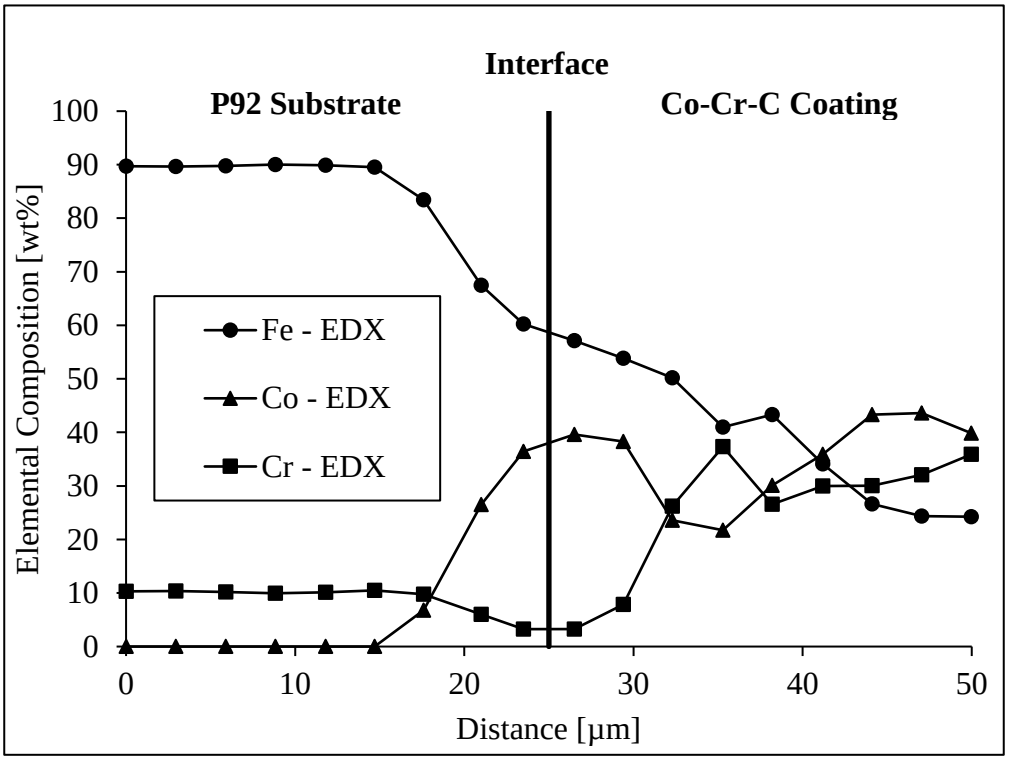

Figure 7.17: EDX measured composition across the coating substrate interface following high temperature oxidation for 2691 hours at 650 ºC (coupon).

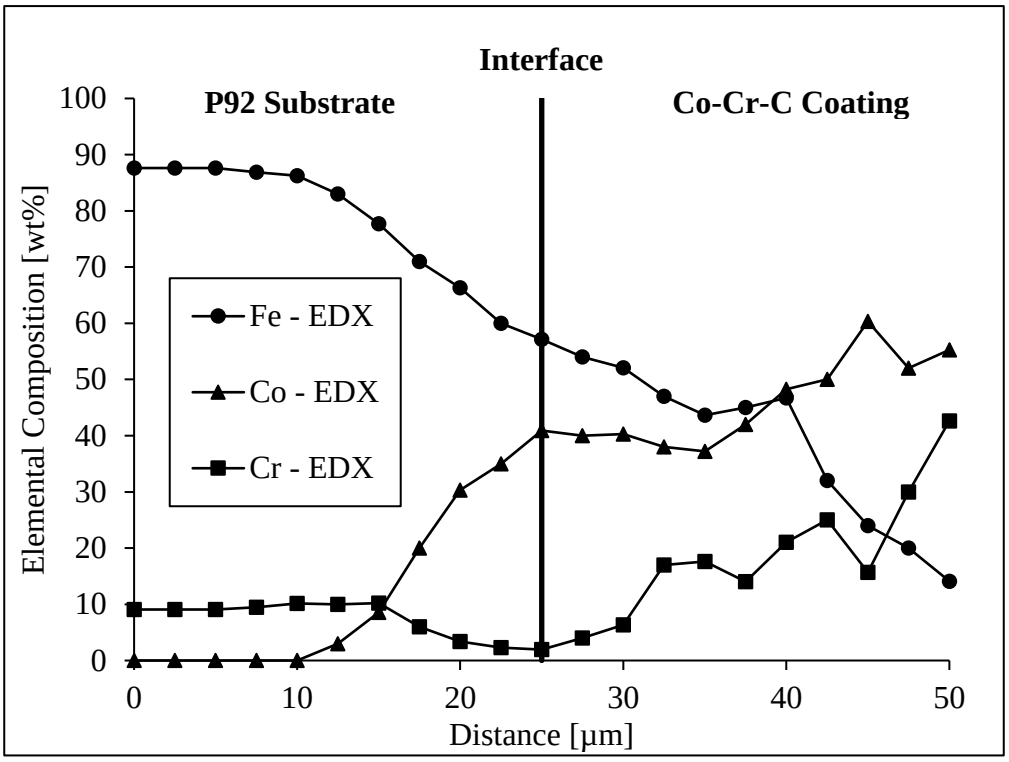

Figure 7.18: EDX measured composition across the coating-substrate interface following high temperature oxidation for 3764 hours at 650 ^{o}C (coupon).

The direction of elemental diffusion is always driven by the chemical potential, which can be best represented by Henry's law:

$$\mu_{cp} = RT\ lna \qquad \text{[Equation 7.1]}$$

In equation 7.1, μ_{cp} is the chemical potential, R is the gas constant, T is the absolute temperature in Kelvin and a is the activity [Clark, 2015; Ding, 2009; Saunders and Miodownik, 1998]. Equation 7.1 shows that the activity is a vital part of the diffusion process. The activities of the elemental species in DB P92 steel and in the Co-Cr-C coating can be calculated using Thermo-Calc thermodynamic software. The P92 elemental composition and the Co-Cr-C coating composition are simplified and details are included in appendix C. DB

P92 is modelled using the TCFE7 steels database whilst the Co-Cr-C coating is modelled using the SSOL5 alloys database. Table 7.10 presents the carbon, chromium, cobalt and iron activities in both the DB P92 and the Co-Cr-C coating material at 650 ^{o}C. Diffusion will occur from areas of high activity to areas of low activity. Cobalt is shown to diffuse from the coating into the substrate and iron from the substrate into the coating. This is in agreement with the experimental characterisation and occurs along the concentration gradient. The chromium is confirmed to be diffusing from the substrate into the coating. This diffusion occurs along the chemical potential gradient and is against the concentration gradient. Carbon is shown to be diffusing from the coating into the steel, following the concentration and activity gradient. The difference in activity values between the coating and the substrate will indicate the speed and distance of diffusion across the interface. Chromium, cobalt and iron are shown to diffuse at a similar speed whilst carbon will be diffusing faster and further.

7.5 Discussion

7.5.1 Coated Coupon Oxidation

Chapter 4 presented the oxidation mechanism for the Co-Cr-C free-standing coating at 650-750 ^{o}C and showed that it broadly agreed with the limited published literature at higher temperature (1000 ^{o}C). Section 7.2 shows that the coated coupons form the same oxide phases as the free-standing coating samples (Co_3O_4, Co_2CrO_4, $CoCr_2O_4$ and Cr_2O_3) and that this once again broadly agrees with the literature [Chi and Barnard, 2012; Foster, 2007; Durham et al., 1998a; Cameron et al., 1979; El Dahshan, 1975].

However section 7.2 also shows that there are a number of differences between the coated coupons and the free-standing coating samples, when exposed to exactly the same high temperature oxidation conditions. Firstly, the overall thickness of the oxide on coated P92 is shown to be ~ 25 % of the oxide formed on free-standing samples and is shown in figure 7.19 and table 7.11.

Table 7.11: Comparison of oxide thicknesses of free-standing coating and coated coupons for oxidation testing at 650 ^{o}C in air.

Exposure Time [h]	Free-standing Coating Oxide Thickness [µm]	Coated P92 Coupon Oxide Thickness [µm]
2383	30 ± 3.5	12 ± 0.9
2691	29 ± 2.7	12 ± 1.9
3764	36 ± 6.6	14 ± 1.7

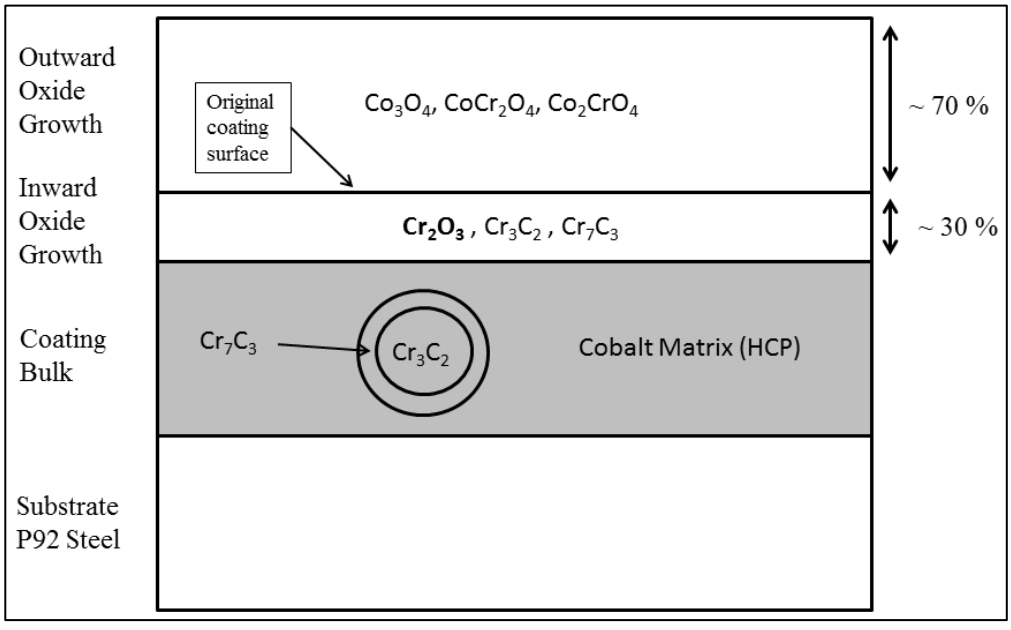

Figure 7.20: Schematic to summarise the oxidation and microstructural evolution of the coated P92 coupons following high temperature oxidation (650-700 ^{o}C).

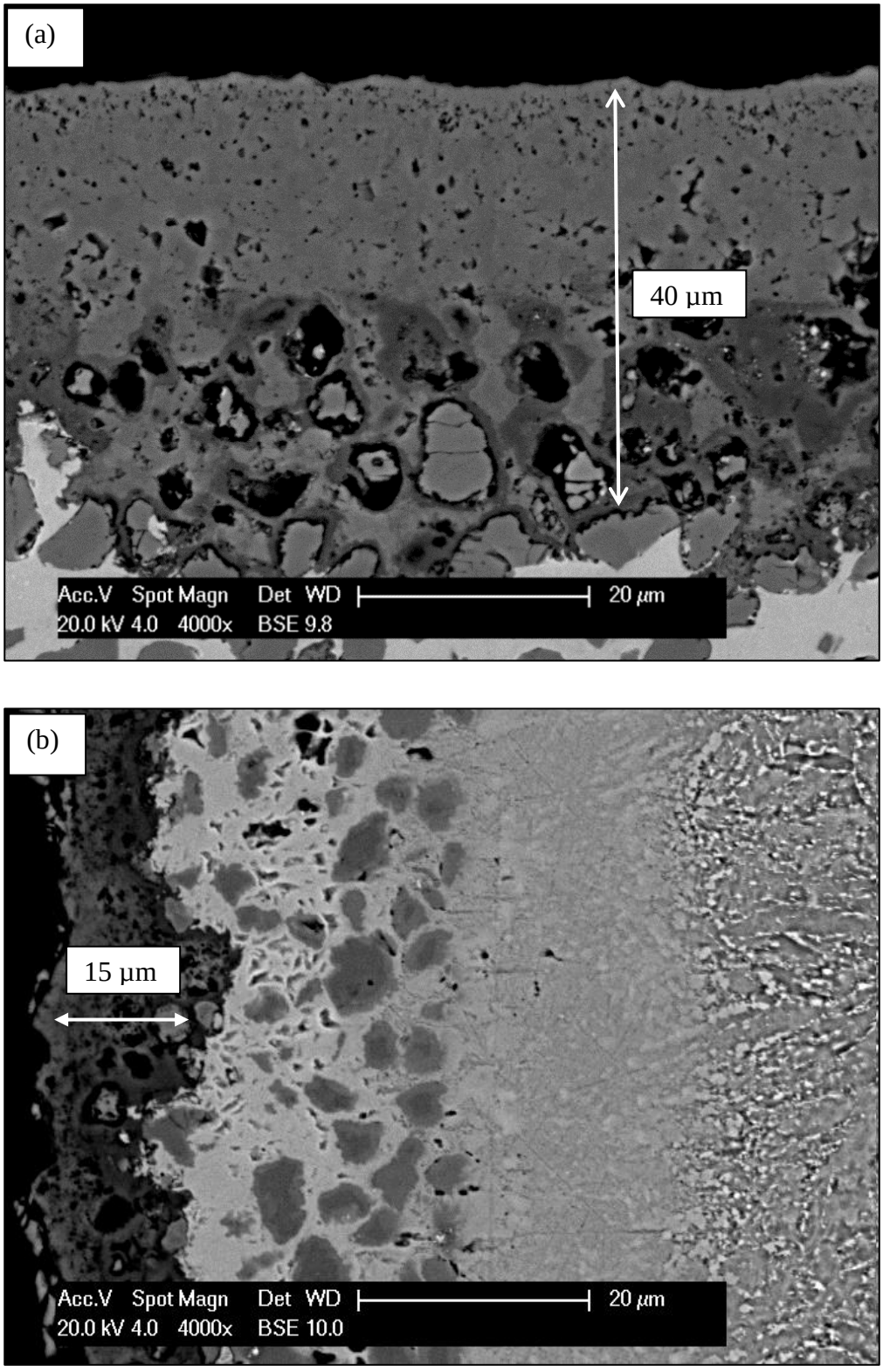

Figure 7.19: Cross section SEM micrographs of oxidised Co-Cr-C coating for 3764 hours at 650 ºC for (a) free-standing coating and (b) coated coupons.

The structure of the oxide on coated coupons is also different to the free-standing coating samples, although all of the same phases are identified. On the isothermally oxidised coated coupons inward and outward oxide growth is again present. However there is less inward growth and the clear inward and outward growth seen on the free-standing coating is not present. The outward growth is composed of a mixture of spinel type oxides: Co_3O_4, $CoCr_2O_4$, and Co_2CrO_4, rather than just Co_3O_4 as seen on the free-standing coating. The coated coupon oxide appears more irregular with less distinct layering compared to the free-standing samples. There is also evidence of porosity and cracking on the top surface. The small inward growth region is composed of a Cr_2O_3 which seems to be present as more of a distinct layer rather than halos around embedded particles. This suggests that Cr_2O_3 is forming more quickly per unit time when P92 substrate is present.

In the coated coupon, the cobalt matrix is again seen to be HCP, the low temperature form of cobalt which forms on slow cooling. FCC is the high temperature form of cobalt. Also Cr_3C_2 appears to be transforming from Cr_3C_2 to Cr_7C_3, however there is now experimental evidence unlike for free-standing coating samples. This suggests that the amount of Cr_7C_3 is now greater meaning that it exceeds the XRD sensitivity limit [Cullity and Stock, 2001; Clark et al., 1986; Kamal et al., 2009]. This again suggests that the presence of the P92 substrate is accelerating the transformation. The oxidation mechanism for coated P92 coupons at 650-700 ^oC is summarised in figure 7.20.

Industry is therefore very keen to understand the differences between the free-standing coating and coated P92 coupons presented above.

Both the Co-Cr-C free-standing coating and the coated coupon cross-sections have been produced using the same sample preparation techniques to preserve the oxide (chapter 3). Etching has been performed on the coated coupons and is shown to have no detrimental effect on the oxide. Therefore there is no reason to think the grinding and polishing damage would be any more severe on the coated coupons. Certainly this cannot explain the very large differences between the free-standing and coated coupon oxides. Examination of the coated coupon coating bulk thickness also shows a reduction following the oxidation testing which would suggest the coating bulk is being consumed. This could suggest oxide spallation is occurring. Examination of the oxide top surface (XRD, SEM), before any sample preparation takes place, also shows a more irregular surface with cracking and porosity. This is further evidence that the oxide structure difference is occurring during the test as a result of the presence of a P92 substrate, rather than any external factors during sample preparation.

Review of the literature suggests that the difference in the oxidation behaviour between the free-standing coating and the coated coupon can be explained by a number of different possible theories.

Firstly the thickness of the coating on P92 coupons is only ~ 34-37 µm compared to the 1mm thickness for the free-standing coating. Therefore there is a finite reservoir of cobalt and chromium which can have an effect on the oxidation rate and therefore the final phases formed [Birks et al., 2006].

Secondly the oxide growth and phase transformations appear to be occurring more quickly with the presence of the substrate. For example Cr_7C_3 is forming

more quickly and Cr_2O_3 phase appears to be forming in greater quantities compared to the free-standing coating material. The transformation and diffusion processes will be accelerated by the presence of a diffusion sink (i.e. P92 substrate) which will allow the cobalt and carbon to diffuse into the substrate, rather than being retained in the coating bulk [Callister and Rethwisch, 2007; Birks et al., 2006]. The effect of the sink is to increase the concentration gradient between the coating and substrate meaning the diffusion processes can occur more quickly. This acceleration of transformation will therefore liberate chromium quicker, therefore allowing Cr_2O_3 to form more quickly and Cr_3C_2 to transform to Cr_7C_3 more readily. It is possible that the oxide (especially Co_3O_4) is becoming thicker on the coated P92 sample per unit time and is therefore more likely to spall. Therefore leaving behind a significantly thinner oxide that is richer in chromium. Foster [2012], Foster [2007] and Cameron et al. [1979] show that the Co-Cr-C coating was originally designed as a wear resistant coating when applied to a super-alloy substrate. Therefore these outer cobalt rich outer layers were designed to spall on contact and form an adherent glaze. It is possible that this process is beginning to occur under flowing air as the oxide becomes thicker.

Finally the inter-diffusion of elements out of the coating and into the substrate has an effect on the oxidation rate and the oxides formed. Inter-diffusion with the substrate can deplete the scale forming elements and introduce other elements into the coating [Birks et al., 2006; Nicholls, 2000]. The diffusion of cobalt from the coating bulk into the substrate steel and the diffusion of iron into the coating results in a depletion with time of the cobalt available for oxidation. This could explain why the coated P92 has less distinct cobalt rich

phases (Co_3O_4). Also chromium is retained in the coating bulk for longer (in the form of carbides) and chromium is diffusing into the coating which may explain why the chromium rich oxide phases appear to be more prevalent. Vialas and Monceau [2006] and He et al. [2009] show that for diffusion coatings and TBCs on super-alloy substrates, the substrate has a significant effect on the oxide properties because of inter-diffusion and new phases precipitating in the oxide and coating.

Overall it seems likely that the differences in the oxide between coated coupons and free-standing coating is due to a combination of the reasons suggested above. The evidence suggests that the differences are real rather than simply sample preparation effects. Because the system is very complex it is difficult to identify a definitive reason for this difference without significant further work. This area will be subject to future work and much longer duration testing by industry partners. Section 4.4.3 in chapter 4 discusses the limitations of this testing, in terms of the oxidising environment and the exposure conditions (temperature and time) which were selected. The same discussion applies to the testing in this chapter.

7.5.2 Creep Specimen Oxidation

Industrial sponsors have also expressed an interest in the influence of stress on the oxidation and integrity of the coated P92 system; in particular creep loading. For this section the failed creep samples were examined and compared to the corresponding coated coupon tests discussed in section 7.5.1.

The coating is shown to remain intact even following the highest stress coated creep testing (120 MPa). This suggests that the coating has good ductility and

is not brittle at high temperature, otherwise spallation would be observed [Aguero et al., 2001; Nicholls, 2000]. As discussed in chapter 6 the maximum allowable stress for P92 pipework in service is 48 MPa at 650 ^{o}C, therefore the coating is shown to be capable of surviving uniaxial creep loads far in excess of the maximum service load [Richardot et al., 2000].

Oxidation of the coating during creep testing is consistent with the coated coupons discussed in section 7.5.1 with the same inward and outward growth. The oxide is again shown to have a consistent thickness and appears adherent following all creep tests. The coating evolution is also shown to be comparable to coated coupons.

SEM examination suggests some slight oxide cracking is seen on the outer layer of the oxide. This cracking is transverse to the stress direction in the sample. This would suggest that the coating oxide is more brittle than the coating bulk and under loading cracking occurs. SEM of the oxide cross-section shows that this cracking and subsequent damage is confined to the outer oxide layers (Co_3O_4, $CoCr_2O_4$, Co_2CrO_4) and that normally the cracking does not propagate through to the inner layers of the oxide (Cr_2O_3) or the coating bulk. XRD shows that the Cr_2O_3 is more prevalent and identified on a series of peaks in higher quantities than the corresponding stress free samples. This suggests that increased spallation of the outer layers is occurring due to the stress.

The original function of the coating was for wear resistance, therefore the outer oxides were designed to come away on contact and form a glaze for wear protection [Foster, 2012a; Foster, 2007; Cameron et al., 1979]. Therefore it is not surprising that during mechanical testing these outer oxides come away.

The Cr_2O_3 and inner chromium rich phases are always present for all samples which is very encouraging as these are the most crucial phases for oxidation resistance. In some rare incidents complete spallation of the oxide is observed, however this is only observed to occur in a few isolated locations.

Industry is keen to understand the impact of this potential Co-Cr-C coating oxide spallation. To put the extent of this spallation into context we can consider figure 7.21. This compares the oxidised surfaces of an uncoated P92 coupon face and a coated P92 coupon face following oxidation for 3764 hours at 650 ^oC, which shows no signs of oxide spallation from either surface. Figure 7.21 shows that the overall oxide thickness in this case for uncoated P92 is up to 10 times thicker than the coated case. For uncoated P92 this entire oxide has the potential to spall away [Osgerby, 2000]. Thus repeatedly exposing the material beneath to further oxidation and damage and meaning that spallation will occur throughout the lifetime of the component [Viswanathan et al., 2006]. The Co-Cr-C coating oxide is much thinner and this means there is physically less oxide to spall away. Cr_2O_3 is also more adherent and slow growing than the $(Fe, Cr)_3O_4$ oxide formed on uncoated P92 [Birks et al., 2006; Viswanathan et al., 2006]. Also the experimental work presented shows no clear evidence for severe spallation of the oxide from coated P92. Industry indicate that spallation from the coated P92 compared to uncoated P92 will be negligible.

7.5.3 Inter-Diffusion Zone

7.5.3.1 Inter-Diffusion Mechanism

The as-coated P92 system has a definite elemental interface with limited diffusion between the coating and substrate. This is due to the deposition

temperature of ~ 45 ^{o}C being insufficient to cause substantial diffusion of elements. When high temperature oxidation testing (650-700 ^{o}C) was performed diffusion occurred across the coating-substrate interface and also between the Cr_3C_2 particles and the cobalt matrix phase.

The main elements that were diffusing between the coating and the substrate were: cobalt, iron, chromium and carbon. Carbon was shown to diffuse the furthest into the P92 steel because of its small atomic size and ability to interstitially diffuse [Callister and Rethwisch, 2007]. Carbon will also be lost from the system at the oxide surface in the form of CO_2. Cobalt was shown to diffuse from the coating into the steel whilst iron diffused from the steel into the coating. Chromium was also shown to be diffusing from the steel into the coating (following the chemical potential gradient rather than concentration gradient). Cobalt, chromium and iron all diffuse to similar distances because of their similar atomic sizes and substitutional diffusion [Callister and Rethwisch, 2007]. Cobalt, chromium and iron are primarily responsible for the IDZ in the P92. Temperature and time are both shown to increase the diffusion distances of the elemental species. The direction of elemental diffusion is driven primarily by the gradient from high to low concentration (or more accurately chemical potential) and also the drive for chromium and cobalt to combine with oxygen atoms at the coating surface to form oxide phases (and for carbon to be lost from the oxide surface) [Callister and Rethwisch, 2007; Birks et al., 2006]. Clark et al. [1986] and Kamal et al. [2009] show that the diffusion of carbon and chromium from the Cr_3C_2 particles causes Cr_2O_3 to form and the Cr_3C_2 to begin transforming to its lower carbon version, Cr_7C_3. Carbon and

chromium are shown to diffuse out of the Cr_3C_2 particles into the cobalt matrix when activities are taken from Thermo-Calc modelling of diffusion distance.

All of the coated coupons in table 7.1 and the creep specimens in table 6.1 have been examined experimentally and there seems to be no sign of any detrimental effects (i.e. voiding) of inter-diffusion. There appears to be no signs of porosity or cracking either along interfaces or within the bulk materials. Micro-hardness testing and XRD cannot be used to examine the IDZ because of its small size at the interface. Future work could investigate nano-indentation hardness testing, EBSD and TEM to give a more detailed understanding of the interface.

The IDZ is shown to have a maximum size of around 20 μm, even for the longest duration and highest temperature exposures in this thesis. Even if this region is assumed to be completely creep weak for real component wall thicknesses (P92 pipe ~ 34 mm [David et al., 2013]) the effect of this IDZ on the creep properties of real components will be negligible. Industry sponsors are not concerned by this IDZ as uncoated P92 steel would suffer surface decarburisation to a similar extent so components are already designed to take this into account [Parker, 2013]. Carbon however is predicted to diffuse much further into the P92 and therefore could realistically have an effect on the P92 substrate. This could cause carbon rich precipitates or other detrimental phases to form [Llewellyn and Hudd, 1998], although no such phases have been observed for these test conditions. A more detailed understanding of the effect of carbon diffusion will be needed in the future, possibly utilising DICTRA diffusion modelling software.

A schematic of the inter-diffusion with the coated P92 system is included in figure 7.22.

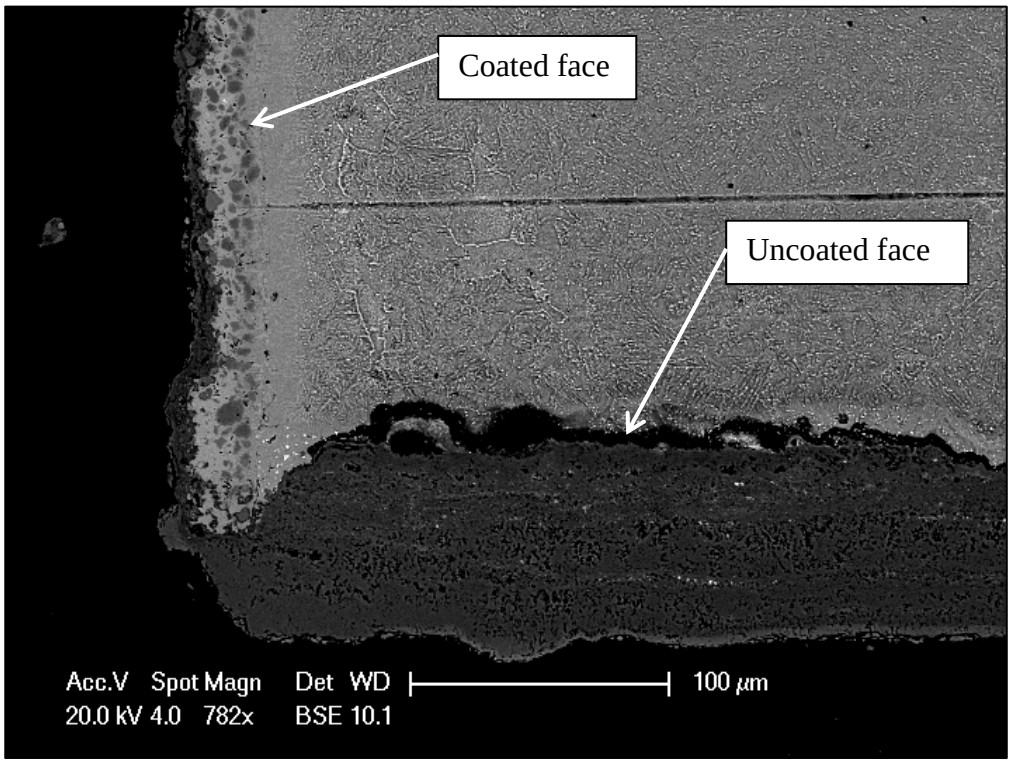

Figure 7.21: A comparison of the oxidised surface of uncoated and coated P92 coupons following isothermal oxidation for 3764 hours at 650 ºC.

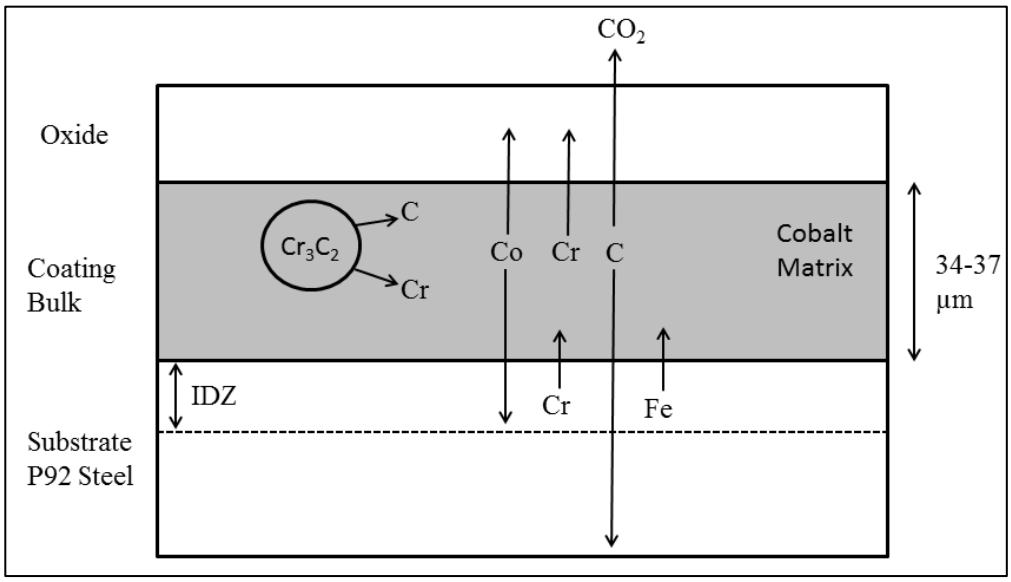

Figure 7.22: Schematic of the inter-diffusion occurring in Co-Cr-C coated P92 at 650-700 ºC for up to 3764 hours.

7.5.3.2 Comparison to Aluminide Coated P92

The most relevant literature to compare these inter-diffusion findings to is the previous work on aluminide coated P92. Aguero et al. [2007] found Kirkendall porosity was present beneath aluminide coatings on P92 following exposure in steam for 40,000 hours at 650 ^{o}C. This is a significant limitation for aluminide coatings as it causes cracking and potential spallation of the coating. It is caused by the mismatch in diffusion speeds of the iron and the aluminium, caused primarily by the difference in atomic size [Aguero et al., 2007; Callister and Rethwisch, 2007]. The chromium, iron and cobalt in the Co-Cr-C coating all have a similar atomic size; therefore the experimental work shows the diffusion speeds/distances will be similar for all three elements. This results in less potential for Kirkendall porosity [Hoglund and Agren, 2001]. Overall the Co-Cr-C coated P92 coupons in this work appear to have performed much better than aluminide type coatings with no signs of degradation effects due to inter-diffusion.

Although unable to run isothermal oxidation testing for 40,000 hours at 650 ^{o}C on the Co-Cr-C-P92 system a series of accelerated isothermal oxidation tests were conducted at higher temperatures of 675 and 700 ^{o}C for shorter times. This allowed for the diffusion process to be accelerated and in theory any microstructural evolution (formation of detrimental phases) as a result of inter-diffusion to also be accelerated. The Hollomon-Jaffe parameter, HP (derived from the Arrhenius equation and similar to the Larson-Miller parameter in chapters 5 and 6), can be used to calculate approximate lower temperature equivalent ageing times and is given by equation 7.2 [Callister and Rethwisch, 2007]. This can be used to assess the industrial relevance of accelerated testing.

$$HP = \frac{T(C_{HP}+Log\ t)}{1000} \qquad \text{[Equation 7.2]}$$

In equation 7.2, HP is the Hollomon-Jaffe parameter, T is the temperature in Kelvin, C_{HP} is a constant and t is the time in hours of the isothermal heat treatment. Janjusevic et al. [2009] show that C_{HP} is a constant specific to a type of material and Nawrocki et al. [2001] states that C_{HP} values as high as 30 have been used for 9 % Cr steels. Therefore a C_{HP} value of 30 will be assumed for this investigation. By calculating HP_1 for T_1 and t_1, equation 7.2 can then be re-arranged to find the equivalent time, $t_{eqv,}$ at a different temperature of T_2, as shown in figure 7.3:

$$t_{eqv} = 10^{(\frac{(HP_1 x\ 1000)}{T_2} - 30)} \qquad \text{[Equation 7.3]}$$

Equivalent times at 650 ^{o}C for the accelerated 675 and 700 ^{o}C tests are included in table 7.12. Table 7.12 shows that the accelerated isothermal ageing of coated P92 at 675 and 700 ^{o}C are equivalent to longer term testing at 650 ^{o}C. Therefore these samples have similar exposure times to those of Aguero et al. [2007].

Viswanathan and Bakker [2001] state that coal fired power plant are designed for a life of no less than 25 years (~ 220,000 hours), with minimal modification needed during this time. The fact that coated P92 performs very well following equivalent exposures of almost 90,000 hours at 650 ^{o}C suggests that the coating will survive very well long term (table 7.12). Future work will study longer term aged samples and also in service test pieces. The Holloman-Jaffe

parameter also suggests that accelerated testing is better at simulating long term inter-diffusion processes rather than long term oxidation (chapter 4). This means elemental diffusion is more dependent on a temperature change from 650-700 ^{o}C than the oxidation properties.

Table 7.12: The Hollomon-Jaffe conversion of accelerated test conditions to equivalent lower temperature conditions.

Accelerated Test Conditions		**Equivalent Conditions**	
Temp [^{o}C]	**Time [h]**	**Temp [^{o}C]**	**Time [h]**
675	2659	650	21,374
700	1006	650	61,673
700	1403	650	87,575

7.5.4 Industrial Considerations

Having investigated the Co-Cr-C coated P92 system in this chapter and reviewed the literature it is now possible to make a series of suggestions as to how the coating composition could potentially be improved for future coating composition development. This would require further R&D by the coating manufacturer. These include:

- Lower carbon versions of chromium carbides (Cr_7C_3 and $Cr_{23}C_6$) could be used instead of Cr_3C_2. This could be advantageous because the amount of carbon in the coating system would be reduced whilst the chromium would be increased. This means more chromium for production of Cr_2O_3 and less carbon diffusing into the substrate and potentially causing mechanical problems. This will however increase cost and economic viability of any

coating modifications would need to be considered. There would also need to be a full investigation of the rate of carbide evolution.

- A post-deposition heat treatment (conditions TBD) could be beneficial to induce the formation of protective oxide scales before exposure to service conditions. This would be beneficial to protect the potentially vulnerable as-coated surface from initial service conditions. This would also allow alloying to begin between the carbides and matrix to make chromium available for scale formation. It would also be beneficial to ensure that the coating is well adhered to the substrate P92. Once again the cost and economic viability of the process would need to be considered. Also consideration should be given to other standard power plant processes (e.g. acid cleaning) and what affect this may have on the coating.
- The coating thickness on P92 could be increased (conditions TBD) to make available more chromium for oxidation and ensure the long term integrity of the coating. However this would still need to comply with standard P92 pipework dimensions to ensure that fluid flow is not affected by a very thick coating. The ratio of Cr_3C_2 to matrix has already been investigated by Foster [2007] and Walton [1990]. Foster [2007] showed that increasing the carbide ratio is beneficial to oxidation properties, however Walton [2007] showed that increasing too much beyond the current 34 wt % Cr_3C_2 makes the coating more brittle meaning it is more likely to spall from the P92 when under stress (i.e. creep or fatigue). Therefore the carbide to matrix ratios should be retained for any future coating development.

7.6 Summary

Chapter 7 characterised the Co-Cr-C coating when applied to P92 substrate material, considering an oxidation and microstructural study. These feasibility investigations have provided the basis for more detailed in-house work at industrial sponsors. In summary of this chapter, the following key results have been obtained:

- The oxide on coated P92 coupons is shown to consist of an innermost layer of Cr_2O_3 and an outer region that is predominantly a mixture of the spinel type oxides: $CoCr_2O_4$, Co_2CrO_4 and Co_3O_4 (parabolic growth kinetics). There is no distinct outer Co_3O_4 layer present and the oxide appears more irregular than free-standing coating samples. Overall the oxide is thinner when compared to free-standing coating samples for a given unit of time and there appears to be more evidence of a Cr_2O_3 distinct innermost layer. This difference is caused primarily by the influence of the substrate and because the coating material is much thinner than in chapter 4. The transformation of $Cr_3C_2 \rightarrow Cr_7C_3$ is accelerated compared to free-standing coating samples as a result of the substrate and thin coating. Oxide spallation is possibly occurring during testing and also consumption of the coating bulk.
- The difference in the oxidation behaviour and microstructural evolution can be explained by: (a) the presence of a diffusion sink (P92 substrate) accelerating the transformation processes, (b) the thin coating only containing a finite reservoir of active elements compared to the free-standing samples and (c) inter-diffusion influencing the oxidation

behaviour and enhancing the coating bulk evolution. In reality this complex oxidation behaviour is likely to be a combination of all of the above reasons.

- Mechanical loading causes cracking in the outer oxidised layer which causes the outer layer spinel type oxide to spall away in places. For all loading conditions (far above real power plant conditions) the innermost Cr_2O_3 oxide is usually always retained. This is most important for integrity of the coating and long term performance of the system. The volume of possible spallation is shown to be significantly less than for the uncoated P92 case. The Cr_2O_3 formed on the coating is also much more adherent than the oxides formed on uncoated P92.
- Carbon is diffusing the furthest from the coating into the substrate due to its small atomic size and ability to interstitially diffuse. This result can potentially affect the P92 substrate for real component thicknesses. Cobalt is also diffusing from the coating into the steel. Iron and chromium are diffusing from the steel into the coating. Temperature and time are both shown to increase the diffusion distances of carbon, chromium, cobalt and iron. Cobalt, chromium and iron are shown to diffuse to similar degrees because of their similar atomic sizes and substitutional diffusion.
- Inter-diffusion of the cobalt, chromium and iron causes a distinct IDZ to be formed in the P92 substrate steel. This area is depleted in chromium and iron and enriched in cobalt. The general P92 microstructure is retained within this area although the contrast in SEM imaging is affected by the different elemental composition of the matrix. For the test conditions studied no detrimental effects are observed (i.e. voiding or cracking). Any

effects of this IDZ are expected to be reduced for real component wall thicknesses as the IDZ is small compared to real P92 pipe wall thicknesses.

- The Co-Cr-C coating appears to perform better than corresponding aluminide coated P92 samples from the literature. There is no evidence of Kirkendall porosity or coating substrate damage at accelerated service relevant tests. This is very encouraging for future application. This is explained because the diffusing species in the Co-Cr-C-P92 system all have similar atomic sizes and diffusion speeds. Therefore reducing the potential for Kirkendall porosity. There is also a series of practical advantages for industry application of the coating (i.e. low temperature application, non-line of sight, excellent reliability etc.).

CHAPTER 8

CONCLUSIONS AND FUTURE WORK

8.1 Summary and Conclusions

The main aim of this research project was to investigate the viability of the Co-Cr-C oxidation resistant coating for application to P92 ferritic steel substrate. The thesis serves as a feasibility study of Co-Cr-C coated P92 for the industrial sponsor before further more detailed testing. The main conclusions and the key results of the thesis are summarised below in this chapter.

8.1.1 Co-Cr-C Free-Standing Coating

Firstly the Co-Cr-C free-standing coating was studied before and after high temperature isothermal oxidation in air. This highlighted a number of promising oxidation and microstructural evolution properties.

- Equilibrium thermodynamic modelling of the Co-Cr-C free-standing coating shows that throughout the temperature range of likely future operation temperatures the Co-Cr-C coating remains stable (550-700 ^{o}C).

Modelling predicts there will be gradual transformation of the Cr_3C_2 phase to Cr_7C_3 between 500 and 735 ^oC and that this transformation will be most severe above 735 ^oC, where Cr_3C_2 will completely transform to Cr_7C_3. This transformation suggests alloying of the composite is occurring.

- The oxide formed on the Co-Cr-C coating following high temperature oxidation is shown to be multi-layered with a distinct inward and outward growth (50:50 ratio). Initially the fastest oxide to form is an outward growing layer of Co_3O_4; this is due to the ready availability of cobalt in the coating matrix. Slightly slower to form is the inward growth of chromium richer oxides. This inward growth contains embedded chromium carbides (Cr_3C_2) with 'halos' of Cr_2O_3 forming around them. After the very longest exposures these 'halos' are expected to extend into a distinct inner layer of Cr_2O_3. The remainder of the inward growth is made up of mixed spinel type oxides, namely $CoCr_2O_4$ and Co_2CrO_4. There is no evidence for oxide spallation during high temperature stress free testing.
- The oxidation kinetics of Co-Cr-C free-standing coating is shown to be parabolic in nature with an activation energy of 85.3 kJ/mol. This parabolic rate is explained by the oxide thickness increasing and therefore slowing the oxygen and metal ion transport across the oxide. The Cr_2O_3 is the most desirable phase for oxidation protection as it is slow growing and adherent. Its high density means that oxygen and metal ions diffuse through its structure very slowly. Formation of a distinct layer of Cr_2O_3 is highly desirable for oxidation protection and will have the effect of 'sealing' the oxidising surface. Oxidation kinetics of the Co-Cr-C coating are comparable to Co-Cr-C alloys studied in the literature and superior to Co-

Cr alloys. The oxidation kinetics value are shown to be similar to those for P92 steel, however the oxide for the Co-Cr-C is much more adherent and less prone to spallation.

- Cr_2O_3 is the slowest of the oxide layers to form because it is dependent on a supply of chromium from the embedded chromium carbides. The embedded Cr_3C_2 evolve slowly over time releasing their chromium and carbon into the cobalt matrix. Thermo-Calc modelling of the free-standing coating shows the Cr_3C_2 embedded in the inner oxide layer is beginning to transform into Cr_7C_3. The FCC microstructure of the cobalt matrix will be retained at high temperature and reverts to the low temperature HCP version on slow cooling from high temperature.
- Industrially representative high temperature oxidation testing (650-750 ^oC) in air shows that the multi-layered oxide on the Co-Cr-C free-standing coating remains intact and shows no signs of significant porosity or damage. The coating bulk also retains its integrity during testing. This is expected as the operation temperature is far below the temperature for which the coating was originally designed (1000 ^oC).

8.1.2 P92 Steel

Secondly the P92 substrate steel was studied, both microstructural and mechanical properties. This was important to establish reliable baseline data to compare coated mechanical testing to and also to establish how typical the P92 being studied in this project was.

- The DB P92 ferritic steel being used in this study is found to have a tempered martensitic structure; with $M_{23}C_6$ and MX type precipitates all being present in the as-received condition. $M_{23}C_6$ precipitates are seen to populate prior austenite grain boundaries whilst MX phase is seen to precipitate throughout the grain interior and along grain boundaries. This is typical of P92 presented in the literature.
- Thermodynamic modelling of DB P92 agrees with experimental characterisation and identifies: austenite (FCC), ferrite (BCC), the Laves Phase, MX and $M_{23}C_6$ as the main phases. The ferrite to austenite transformation temperature (Ae_1), on heating, for DB P92 is calculated to be 819 ^{o}C. Coating deposition temperatures and accelerated testing must remain well below this temperature to avoid detrimentally affecting the substrate DB P92 by the formation of austenite.
- Thermodynamic modelling of DB P92 precipitate phases identifies MX phase as (V, Nb) (N, C), $M_{23}C_6$ as $(Cr, Fe, Mo, W)_{23}C_6$ and Laves Phase as $(Fe, Cr)_2(Mo, W)$. Laves phase is expected to form during high temperature ageing and creep. MX and $M_{23}C_6$ precipitates (most important for creep resistance) remain stable for operation temperatures of up to 700 ^{o}C. Coating deposition temperatures and accelerated testing must remain below 700 ^{o}C to avoid detrimentally affecting precipitate phases and therefore P92 mechanical properties.
- P92 is characterised mechanically by performing tensile, creep and fatigue properties. Comparison to the literature shows that DB P92 is typical of grade P92 (within scatter) and can be used to provide representative results for coated P92 testing. The lowest stress, lowest temperature tests are most

industrially relevant for creep testing as they are typical of real in service conditions. Meanwhile the lowest stress, higher temperature tests are most relevant to observe effects of oxidation resistant coatings because the oxidation damage is greater.

- P92 is shown to be capable of operating at enhanced temperatures of 650-700 ^{o}C with good microstructural and mechanical properties. However the limiting factor, preventing temperatures of greater than 600 ^{o}C, is enhanced oxidation damage. This suggests that oxidation resistant coatings for P92 are a viable solution to allow higher temperature operation.

8.1.3 Co-Cr-C Coated P92 – Mechanical

Thirdly the coated P92 system was mechanically tested. This showed that the Co-Cr-C coated P92 steel has a number of promising mechanical properties, both creep and fatigue.

- Application of the 34-37 µm Co-Cr-C coating to DB P92 creep specimens appears to have a positive effect on the overall creep properties of the substrate P92 when tested in air at 650, 675 and 700 ^{o}C, for durations from ~ 200-4000 hours. This positive effect is caused by the preservation of the creep specimen cross-section diameter by the oxidation resistant coating preventing oxidation damage. This positive effect is expected to be reduced as real wall thicknesses are considered.
- Pre-deposition surface treatment (i.e. batch 1 – slurry grit blast or batch 2 – chemical etch) is shown to have no observable effect on the creep properties of the coated P92. Therefore entrapped alumina grit at the

interface appears not to be having a detrimental effect on creep life. However it is still recommended that chemical etch pre-treatment is used, simply to avoid any future longer term problems (i.e. fatigue behaviour).

- The Co-Cr-C coated P92 creep behaviour is superior to the aluminide coated P92 (current best in class coating) as it does not show a negative effect on the creep properties. The main advantage mechanically of the Co-Cr-C coating compared to previous coatings (i.e. aluminides) is that the low temperature deposition process (~ 45 ^{o}C) causes no microstructural distortion of the substrate P92. The ductility of the P92 is also not affected by the coating process. The coating and substrate are expected to have comparable mechanical properties at high temperature.
- Application of the Co-Cr-C coating to DB P92 is shown to have a small positive effect on the fatigue/creep-fatigue life when the total time is long enough to allow sufficient oxidation. This beneficial effect is most likely caused by the coating preserving the specimen surface and preventing crack initiation. The presence of the IDZ is also expected to slow down crack propagation, although more detailed work would be needed to fully understand this. The most encouraging result from the fatigue testing is that the coating application does not have a negative effect on the mechanical properties of P92.

8.1.4 Co-Cr-C Coated P92 – Microstructural

Finally the Co-Cr-C coating applied to P92 was considered in an oxidation and microstructural study of coated P92 samples. The coated system is shown to have a number of promising properties.

- The oxide on coated P92 coupons following high temperature exposure is shown to consist of an innermost layer of Cr_2O_3 which appears to be forming as more of a distinct continuous layer compared to free-standing coating samples (chapter 4). The outer layers are a more irregular mixture containing $CoCr_2O_4$, Co_2CrO_4 and Co_3O_4. The presence of the P92 substrate appears to be accelerating the oxidation processes compared to the Co-Cr-C free-standing coating study.
- The effect of the substrate is also that the oxidised layers are much less distinct compared to the free-standing coating and that the outer layer is a mixture of cobalt and chromium rich spinel rather than simply Co_3O_4. The substrate also causes the overall oxide to be thinner when compared to a corresponding free-standing coating sample. The reasons for these differences are due to the finite supply of active elements in the thin coating and also the effects of inter-diffusion between coating and substrate. It is possible that spallation of the outer oxidised layers is occurring during oxidation testing as coating bulk is being consumed.
- Mechanical creep loading, at higher stresses than would be experienced in service, causes cracking in the outer oxidised layer. This stress causes the outer layer to spall away in places; however in almost all cases the innermost Cr_2O_3 layer remains present. The quantity of spallation from the outer layer is shown to be significantly less than a corresponding uncoated P92 sample exposed to the same conditions and is therefore acceptable by industry.
- The Cr_3C_2 particles in the coating bulk are evolving from Cr_3C_2 to Cr_7C_3, which is vital to provide a chromium supply for oxidation (observed

experimentally and computationally). The presence of a substrate (elemental sink) has the effect of accelerating the diffusion processes and transformation rate. The cobalt matrix is again shown to retain its FCC structure at high temperature and reverts to HCP on slow cooling.

- Carbon and cobalt are both shown to be diffusing from the coating into the steel, whilst iron and chromium diffuses from the substrate into the coating. Diffusion of all elements is shown to be a function of temperature and time and diffusion of cobalt, chromium and iron results in the presence of an IDZ. Elements with a smaller atomic size, for example carbon, are shown to diffuse the furthest as they can diffuse interstitially. This could potentially affect the P92 properties even at real component wall thicknesses. Chromium, cobalt and iron all have similar atomic sizes and therefore diffuse to similar degrees (much less than carbon). At these test conditions there is no evidence of detrimental effects caused by diffusion processes. Any effect of the IDZ is expected to be reduced when real component wall thicknesses are considered. The Co-Cr-C coated P92 appears to have superior inter-diffusion properties compared to aluminide coated P92. This is primarily because the diffusing species all have similar atomic sizes and diffusion speeds, therefore reducing the potential for Kirkendall porosity to form.

8.1.5 General Conclusions

The conclusions and results presented in section 8.1.1-8.1.4 have allowed for some final conclusions about the overall suitability of the Co-Cr-C coating on P92 for industry application to be made:

- Electro-deposition of the Co-Cr-C coating onto DB P92 substrate is successful with good adherence of the coating to the substrate being observed. No interface cracking or defects were observed in the as-coated samples. Electro-deposition allows for consistent and reliable deposition onto both flat and curved surfaces. Electro-deposition is a viable method industrially for depositing the Co-Cr-C coating onto the inside surface of P92 pipework in a reliable, efficient and economical way. The main advantages are that it is low temperature and non-line of sight.
- The oxide formed on the Co-Cr-C coating is shown to be protective between 650 and 750 ^{o}C in air preventing oxidation damage of P92. Following high temperature oxidation and high temperature mechanical testing in air, at temperatures and stresses far above in service conditions, the desirable Cr_2O_3 phase is always present following all loading conditions. The quantity of any spalling outer layer oxide is expected to be far below the amount that would be spalling for uncoated P92.
- The inter-diffusion process is shown to provide good coating-substrate adherence with no detrimental diffusion effects being observed, for tests conducted that are representative of real service lives. This is superior to the current best in class aluminide type coating.
- The Co-Cr-C application is shown to have a positive effect on the creep properties of the DB P92 creep specimens. This is far superior to the current best in class, aluminide type coating and is mainly due to the low deposition temperature of the Co-Cr-C coating. Preliminary fatigue testing also shows that coating application has a small positive effect on P92 fatigue properties, this is promising for industry application.

- Overall the Co-Cr-C coated P92 shows a number of very promising oxidation, diffusion and mechanical properties which make it suitable for this power plant application. It also performs better in a number of tests than compared to the current 'best-in-class' aluminide type coating. Therefore this thesis concludes that industry sponsors (Doosan Babcock and Praxair Surface Technologies) should continue more detailed investigations of the coated system prior to potential commercialisation. Details of this future work are now presented.

8.2 Future Work

The results presented in chapters 4-7 of this thesis have served as a detailed feasibility study for the Co-Cr-C coated P92. The current work confirms that the Co-Cr-C coating is a viable coating technology with a number of promising properties and has therefore naturally created many areas for potential future work for industrial sponsors. The main areas requiring future work by industrial sponsors before full scale commercialisation are as follows:

- Steam Oxidation: An investigation of how the coated P92 system performs in a steam oxidation environment and compare this to the air oxidation work conducted in this thesis. This is a more aggressive environment and will therefore be important to truly test the assumptions made within this thesis.
- Coating Modification: An investigation into the potential beneficial effects of post-deposition heat treatment on the coating system prior to being put into service. These benefits would need to be clearly understood as heat

treatment could significantly increase the cost of coated components. Also any effect of surface preparation, for example grinding of the as-coated surface to improve oxidation behaviour, could be investigated. Also investigations of how the coating composition could be further improved.

- Mechanical: A mechanical study (tensile, creep, fatigue) of the free-standing coating material at 600-750 ^{o}C should be performed. This would allow for a more detailed understanding of the mechanical properties of the coating and substrate system. It would also be beneficial to establish how the coating composition could be modified to further improve mechanical properties. Computational modelling of coated mechanical behaviour could also be conducted.
- Thermodynamic Modelling: Further developments need to be made with the inter-diffusion modelling. For example creating a computational DICTRA diffusion model of the coated system [Chen, 2015]. In particular being able to simulate the effect that oxidation has on the diffusion of the elemental species. The system could be further extended by linking diffusion results from DICTRA with a finite element model of creep.
- Full Scale Testing: An investigation of full scale P92 pipework coating and comparison to the specimens examined in this work. Detailed welding trials of full size coated P92 pipework to assess any damage at full scale. Also the possibility of in-service trials of coated sections of the P92 pipework.

REFERENCES

Presented in this section is a comprehensive list of the literature used throughout this thesis, including: the literature review (chapter 2), experimental methods (chapter 3), results and discussion (chapter 4-7) and appendices (A-C).

Abe, F. (2004). Bainitic and martensitic creep-resistant steels. *Current Opinion in Solid State and Materials Science,* 8**,** pp. 305-311.

Abe, F., Kern, T. and Viswanathan, R. (2008). *Creep-resistant steels*. London: Woodhead Publishing.

Abe, F., Taneike, M. and Sawada, K. (2007). Alloy design of creep resistant 9Cr steel using a dispersion of nano-sized carbo-nitrides. *International Journal of Pressure Vessels and Piping,* 84**,** pp. 3-12.

Aguero, A., Garcia De Blas, J., Muelas, R., Sanchez, A. and Tsipas, S. (2001). Steam oxidation resistant coatings for steam turbine components: a feasibility study. *Materials Science Forum*, 369-372, pp. 939-946.

Aguero, A., Muelas, R. and Gonzalez, V. (2008). HVOF coatings for steam oxidation protection. *Materials and Corrosion,* 59**,** pp. 393-401.

Aguero, A., Muelas, R., Gutierrez, M., Van Vulpen, R., Osgerby, S. and Banks, J. (2007). Cyclic oxidation and mechanical behaviour of slurry aluminide coatings for steam turbine components. *Surface and Coatings Technology*, 201**,** pp. 6253-6260.

Aguero, A., Muelas, R., Pastor, A. and Osgerby, S. (2005). Long exposure steam oxidation testing and mechanical properties of slurry aluminide coatings for steam turbine components. *Surface and Coatings Technology,* 200**,** pp. 1219-1224.

Agyakwa, P. (2004). *Creep and microstructural development in P92 weldments at elevated temperature.* PhD, University of Nottingham, UK.

Anderson, P., Bellgardt, T. and Jones, F. (2003). Creep deformation in a modified 9Cr-1Mo steel. *Materials Science and Technology,* 19**,** pp. 207-213.

Armas, A., Petersen, C., Schmitt, R., Avalos, M. and Alvarez, I. (2004). Cyclic instability of martensite laths in reduced activation ferritic/martensitic steels. *Journal of Nuclear Materials,* 329**,** pp. 252-256.

Ashby, M. and Jones, D. (2013). *Engineering materials 1: an introduction to their properties and applications.* Oxford: Butterworth-Heinemann.

Bates, B., Zhang, Y., Dryepondt, S. and Pint, B. (2014). Creep behaviour of pack cementation aluminide coatings on grade 91 ferritic-martensitic alloy. *Surface and Coatings Technology,* 240**,** pp. 32-39.

Beeghly, H. (1952). Behaviour of nitrogen and some of its compounds in steel. *Analytical Chemistry,* 24**,** pp. 1095-1100.

Bellucci, A., Matera, S., Fry, A. and Seraffon, M. (2015). The steam oxidation and mechanical performance of a ferritic-martensitic steel coated with slurry and pack cementation aluminide coating. In*: EPRI, International Conference on Corrosion in Power Plants*, San Diego, USA, EPRI, pp. 1-12.

Berthod, P. (2013). High temperature oxidation behaviour of chromium-alloys containing high carbide fractions-part 1: nickel-based alloys. *Materials and Corrosion,* 64(7), pp. 567 – 577.

Betterridge, W. (1982). *Cobalt and its alloys.* Chichester: Ellis Horwood Limited.

Bhadeshia, H. and Honeycombe, R. (2006). *Steels-microstructure and properties.* Oxford: Butterworth-Heinemann.

Birks, N., Meier, G. and Pettit, F. (2006). *Introduction to the high temperature oxidation of metals*. London: Cambridge University Press.

Bose, S. (2011). *High temperature coatings*. Oxford: Butterworth-Heinemann.

Brett, S., Bates, J. and Thomson, R. (2004). Aluminium nitride precipitation in low strength grade 91 power plant steels. In: *ASM, 4th International Conference on Advances in Materials Technology for Fossil Power Plants*, South Carolina, USA, ASM International, pp. 1183-1197.

Brooman, E. (2004). Wear behaviour of environmentally acceptable alternatives to chromium coatings: cobalt-based and other coatings. *Metal Finishing,* 102**,** pp. 42-54.

Bugge, J., Kjaer, S. and Blum, R. (2006). High-efficiency coal-fired power plants development and perspectives. *Energy,* 31**,** pp. 1437-1445.

Callister, W. and Rethwisch, D. (2007). *Materials science and engineering: an introduction*. New York: Wiley.

Cameron, B., Foster, J. and Carew, J. (1979). The effect of carbide content and pre-heat treatment on the oxidation characteristics of cobalt-chromium carbide electrodeposits in air at 1000 ^{o}C. *Transactions of the Institute of Metal Finishing,* 57**,** pp. 113-118.

Chalk, K. (2013). *Weld consumables and PWHT for P92 power plant steel.* PhD, University of Nottingham, UK.

Chalk, K., Shipway, P. and Allen, D. (2011). Austenite formation during heat treatment of P92 power plant steel welds: dependence of Ae_1 temperature on compositional changes. *Science and Technology of Welding and Joining,* 16**,** pp. 613-618.

Chen, H. (2015). *Mechanical and chemical behaviour of thermally sprayed CoNiCrAlY bond coats.* PhD, University of Nottingham, UK.

Chen, R. and Yeun, W. (2003). Review of the high-temperature oxidation of iron and carbon steels in air or oxygen. *Oxidation of Metals,* 59**,** pp. 433-468.

Chescoe, D. and Goodhew, P. (1990). *The operation of transmission and scanning electron microscopes.* Oxford: Oxford University Press.

Chi, K. and Barnard, P. (2012). *BF2RA Project Meeting at Nottingham University: Doosan Power Systems Presentation* [Presentation]. UK: Doosan Babcock.

Clark, J. (2015). *Investigating chemical and microstructural evolution at dissimilar metal welds.* EngD, University of Nottingham, UK.

Clark, J., Glasson, D. and Jayaweera, S. (1986). Oxidation of chromium carbide. *Thermochimica Acta,* 103**,** pp. 193-199.

Colson, J. and Larpin, J. (1994). High temperature oxidation of stainless steels. *MRS Bulletin,* 19(10), pp. 23-25.

Connolley, T., Starink, M. and Reed, P. (2000). Effect of oxidation on high temperature fatigue crack initiation and short crack growth in Inconel 718. *Super-Alloys***,** pp. 435-444.

Cullity, B. and Stock, S. (2001). *Elements of x-ray diffraction*. London: Prentice Hall.

Czyrska-Filemonowicz, A., Zielinska-Lipiec, A. and Ennis, P. (2006). Modified 9% Cr steels for advanced power generation: microstructure and properties. *Journal of Achievements in Materials and Manufacturing Engineering,* 19**,** pp. 43-48.

Danielsen, H. and Hald, J. (2006). Behaviour of Z phase in 9-12% Cr steels. *Energy Materials,* 1**,** pp. 49-57.

Datta, A. (2010). *Electro-composite coating for flexible seals and method of applying the same*. Patent Number: US 7815784 B2.

David, S., Siefert, J. and Feng, Z. (2013). Welding and weldability of candidate ferritic alloys for future advanced ultra-supercritical fossil power plants. *Science and Technology of Welding and Joining,* 18**,** pp. 631-651.

DECC. (2014). *Technical assessment of the operation of coal and gas fired plants* [Technical Report]. London: DECC, pp. 1-50.

Dimmler, G., Weinert, P., Kozeschnik, E. and Cerjak, H. (2003). Quantification of the Laves phase in advanced 9-12% Cr steels using a standard SEM. *Materials Characterisation,* 51**,** pp. 341-352.

Ding, Y. (2009). *Effects of elevated temperature exposure on the microstructural evolution of Ni(Cr)-Cr_3C_2 coated 304 stainless steel.* PhD, University of Nottingham, UK.

Ding, Y., Hussain, T. and McCartney, D. (2015). High-temperature oxidation of HVOF thermally sprayed NiCr–Cr_3C_2 coatings: microstructure and kinetics. *Journal of Materials Science,* 50**,** pp. 6808-6821.

Durham, R., Gleeson, B. and Young, D. (1998a). Silicon contamination effects in the oxidation of carbide-containing cobalt-chromium alloys. *Materials and Corrosion,* 49**,** pp. 855-863.

Durham, R., Gleeson, B. and Young, D. (1998b). Factors affecting chromium carbide precipitate dissolution during alloy oxidation. *Oxidation of Metals,* 50**,** pp. 139-165.

Durham, R., Singheiser, L. and Quadakkers, W. (2008). Identification of degradation mechanisms in coatings for supercritical steam applications. *Materials and Corrosion,* 59**,** pp. 402-408.

Ehlers, J., Young, D., Smaardijk, E., Tyagi, A., Penkalla, H., Singheiser, L. and Quadakkers, W. (2006). Enhanced oxidation of the 9% Cr steel P91 in water vapour containing environments. *Corrosion Science,* 48**,** pp. 3428-3454.

Eiselstein, H. and Tillack, D. (1991). The invention and definition of alloy 625. *Super-Alloys,* 718**,** pp. 1-14.

El Dahshan, M., Stringer, J. and Whittle, D. (1975). The oxidation of cobalt-chromium-carbon alloys. *Anti-Corrosion Methods and Materials,* 22**,** pp. 10-14.

Ennis, P. and Czyrska-Filemonowicz, A. (2003). Recent advances in creep-resistant steels for power plant applications. *Sadhana,* 28**,** pp. 709-730.

Ennis, P. and Quadakkers, W. (2007). Implications of steam oxidation for the service life of high-strength martensitic steel components in high-temperature plant. *International Journal of Pressure Vessels and Piping,* 84**,** pp. 82-87.

Ennis, P., Zielińska-Lipiec, A. and Czyrska-Filemonowicz, A. (2000). Influence of heat treatments on microstructural parameters and mechanical properties of P92 steel. *Materials Science and Technology,* 16**,** pp. 1226-1233.

Ennis, P., Zielinska-Lipiec, A., Wachter, O. and Czyrska-Filemonowicz, A. (1997). Microstructural stability and creep rupture strength of the martensitic steel P92 for advanced power plant. *Acta Materialia,* 45**,** pp. 4901-4907.

ECCC. (2005). *Steel ASTM grade 92 - rupture formal assessment* [Master Equation]. London: ECCC.

Evans, R. and Wilshire, B. (1985). *Creep of metals and alloys*. London: Institute of Materials.

Evans, R. and Wilshire, B. (1993). *Introduction to creep*. London: Institute of Materials.

Falat, L., Vyrostkova, A., Homolova, V. and Svoboda, M. (2009). Creep deformation and failure of E911/E911 and P92/P92 similar weld-joints. *Engineering Failure Analysis,* 16**,** pp. 2114-2120.

Foster, J. (2007). *The Production and Application of Tribomet Electroplated Composite Coatings for Wear Resistance at Elevated Temperatures* [Presentation]. UK: Praxair Surface Technologies.

Foster, J. (2012a). *Tribomet Wear Control Coatings* [Leaflet]. UK: Praxair Surface Technologies.

Foster, J. (2012b). *Tribomet MCrAlY Coatings* [Leaflet]. UK: Praxair Surface Technologies.

Fournier, B., Dalle, F., Sauzay, M., Longour, J., Salvi, M., Caes, C., Tournie, I., Giroux, P. and Kim, S. (2011). Comparison of various 9-12% Cr steels under fatigue and creep-fatigue loadings at high temperature. *Materials Science and Engineering: A,* 528**,** pp. 6934-6945.

Fournier, B., Salvi, M., Dalle, F., De Carlan, Y., Caes, C., Sauzay, M. and Pineau, A. (2010). Lifetime prediction of 9-12% Cr martensitic steels subjected to creep-fatigue at high temperature. *International Journal of Fatigue,* 32**,** pp. 971-978.

Fournier, B., Sauzay, M., Caes, C., Noblecourt, M., Mottot, M., Bougault, A., Rabeau, V. and Pineau, A. (2008). Creep-fatigue-oxidation interactions in a 9Cr-1Mo martensitic steel-part 1: effect of tensile holding period on fatigue lifetime. *International Journal of Fatigue,* 30**,** pp. 649-662.

Gabriel, B. (1985). *SEM: a user's manual for materials science.* New York: American Society for Materials.

Gale, W. and Totemeier, T. (2004). *Smithell's metals reference book.* London: Elsevier Butterworth-Heinemann.

Gell, M. and Leverant, G. (1973). Mechanisms of high-temperature fatigue. *Fatigue at Elevated Temperatures,* ASTM International.

Giroux, P., Dalle, F., Sauzay, M., Caes, C., Fournier, B., Morgeneyer, T. and Gourgues-lorenzon, A. (2010). Influence of strain rate on P92 microstructural stability during fatigue tests at high temperature. *Procedia Engineering,* 2**,** pp. 2141-2150.

Gustafson, A. and Hattestrand, M. (2002). Coarsening of precipitates in an advanced creep resistant 9% chromium steel - quantitative microscopy and simulations. *Materials Science and Engineering: A,* 333**,** pp. 279-286.

Gu, Y., West, G., Thomson, R. and Parker, J. (2014). Investigation of creep damage and cavitation mechanisms in P92 steels. In: *ASM, Advances in Materials Technology for Fossil Power Plants: Proceedings from the Seventh International Conference,* Hawaii, USA, ASM International, pp. 596-606.

Hald, J. (1996). Metallurgy and creep properties of new 9-12% Cr steels. *Steel Research,* 67**,** pp. 369-374.

Hald, J. (2008). Microstructure and long-term creep properties of 9-12% Cr steels. *International Journal of Pressure Vessels and Piping,* 85**,** pp. 30-37.

Hald, J. and Korcakova, L. (2003). Precipitate stability in creep resistant ferritic steels - experimental investigations and modelling. *ISIJ International,* 43**,** pp. 420-427.

Hattestrand, M. and Andren, H. (2001). Evaluation of particle size distributions of precipitates in a 9 % chromium steel using energy filtered transmission electron microscopy. *Micron,* 32(8), pp. 789-797.

He, L., Xu, Z., Li, J., Mu, R., He, S. and Huang, G. (2009). Substrate effects on the high-temperature oxidation behaviour of thermal barrier coatings. *Journal of Materials Science & Technology,* 25**,** pp. 799-802.

Hoey, T., Chen, R., McCartney, D., Sun, W., Mansfield, J., Barnard, P. and Foster, J. (2015). Requirement for and use of coated P92 steel for enhanced structural integrity at high temperature. *Acta Physica Polonica A,* 128(4), pp. 514-519.

Hoglund, L. and Agren, J. (2001). Analysis of the Kirkendall effect, marker migration and pore formation. *Acta Materialia,* 49**,** pp. 1311-1317.

Honey, F., Kedward, E. and Wride, V. (1986). The development of electrodeposits for high-temperature oxidation/corrosion resistance. *Journal of Vacuum Science & Technology A,* 4**,** pp. 2593-2597.

Hosoi, Y., Wade, N., Kunimitsu, S. and Urita, T. (1986). Precipitation behaviour of laves phase and its effect on toughness of 9Cr-2Mo ferritic-martensitic steel. *Journal of Nuclear Materials,* 141**,** pp. 461-467.

Hussain, T. (2011). A study of bonding mechanisms and corrosion behaviour of cold sprayed coatings. PhD, University of Nottingham, UK.

Hyde, T., Becker, A., Sun, W. and Williams, J. (2006). Finite-element creep damage analyses of P91 pipes. *International Journal of Pressure Vessels and Piping,* 83**,** pp. 853-863.

Janjusevic, Z., Gulisija, Z., Mihailovic, M. and Pataric, A. (2009). The investigation of applicability of the Hollomon-Jaffe equation on tempering the HSLA steel. *Chemical Industry and Chemical Engineering Quarterly/CICEQ,* 15**,** pp. 131-136.

Jiang, R., Everitt, S., Gao, N., Soady, K., Brooks, J. and Reed, P. (2015). Influence of oxidation on fatigue crack initiation and propagation in turbine disc alloy N18. *International Journal of Fatigue,* 75**,** pp. 89-99.

Junak, G. and Ciesla, M. (2011). Low-cycle fatigue of P91 and P92 steels used in the power engineering industry. *Archives of Materials Science and Engineering,* 48**,** pp. 19-24.

Kamal, S., Jayaganthan, R. and Prakash, S. (2009). High temperature oxidation studies of detonation-gun-sprayed Cr_3C_2-NiCr coating on Fe-and Ni-based superalloys in air under cyclic condition at 900 ^{o}C. *Journal of Alloys and Compounds,* 472**,** pp. 378-389.

Kannan, R., Sankar, V., Sandhya, R. and Mathew, M. (2013). Comparative evaluation of the low cycle fatigue behaviours of P91 and P92 steels. *Procedia Engineering,* 55**,** pp. 149-153.

Kassner, M. and Hayes, T. (2003). Creep cavitation in metals. *International Journal of Plasticity,* 19, pp. 1715-1748.

Kedward, E. (1973). Electrodeposited composite coatings (wear resistant abrasive and dry lubricant cobalt-chromium carbide composite material coatings obtained by electrolytic co-deposition). *Cobalt***,** pp. 53-59.

Kedward, E. and Addison, C. (1976). Development of a wear-resistant electrodeposited composite coating for use on aero-engines. *Transactions of the Institute of Metal Finishing,* 54**,** pp. 8-15.

Kedward, E. and Wright, K. (1978). The wear control of aircraft parts using a composite electroplate (Tribomet T104C). *Surface Treatments for Protection***,** pp. 28-39.

Kedward, E., Wright, K. and Tennett, A. (1974). The development of electrodeposited composites for use as wear control coatings on aero-engines. *Tribology,* 7**,** pp. 221-227.

Klueh, R. (2005). Elevated temperature ferritic and martensitic steels and their application to future nuclear reactors. *International Materials Reviews,* 50**,** pp. 287-310.

Kosolapova, T. (1971). *Carbides: properties, production and applications.* London: Plenum Press.

Kowalewski, Z., Hayhurst, D. and Dyson, B. (1994). Mechanisms-based creep constitutive equations for an aluminium alloy. *The Journal of Strain Analysis for Engineering Design,* 29**,** pp. 309-316.

Laverde, D., Gomez-acebo, T. and Castro, F. (2004). Continuous and cyclic oxidation of T91 ferritic steel under steam. *Corrosion Science,* 46**,** pp. 613-631.

Lefton, S. and Besuner, P. (2006). The cost of cycling coal fired power plants. *Coal Power Magazine,* 4**,** pp. 16-20.

Li, H. and Mitchell, D. (2013). Microstructural characterization of P91 steel in the virgin, service exposed and post-service re-normalized conditions. *Steel Research International,* 84**,** pp. 1302-1308.

Liu, Y. and Murakami, S. (1998). Damage localization of conventional creep damage models and proposition of a new model for creep damage analysis. *JSME International Journal Series A,* 41**,** pp. 57-65.

Llewellyn, D. and Hudd, R. (1998). *Steels - metallurgy and applications.* London: Butterworth-Heinemann.

Mandrino, D., Godec, M., Kocijan, A., Lamut, M., Torkar, M. and Jenko, M. (2008). Oxide and nitride protective layers formed on stainless steel by thermal treatment: SEM, AES, WDS and corrosion measurement. *Metalurgija,* 47, pp. 119-123.

Masuyama, F. (2001). History of power plants and progress in heat resistant steels. *ISIJ International,* 41**,** pp. 612-625.

Mathiazhagan, P. and Khanna, A. (2011). High temperature oxidation behaviour of P91, P92 and E911 alloy steels in dry and wet atmospheres. *High Temperature Materials and Processes,* 30**,** pp. 43-50.

Mellor, B. (2006). *Surface coatings for protection against wear.* Oxford: Woodhead Publishing Limited.

Meyers, M. and Chawla, K. (2009). *Mechanical behaviour of materials*. Cambridge: Cambridge University Press.

Mogire, E., Higginson, R., Fry, A. and Thomson, R. (2011). Microstructural characterization of oxide scales formed on steels P91 and P92. *Materials at High Temperatures,* 28**,** pp. 361-368.

NIST. (2001). *X-ray form factor, attenuation, and scattering tables* [Table of Standards]. US: NIST.

Nawrocki, J., Dupont, J., Marder, A. and Robino, C. (2001). The post-weld heat-treatment response of simulated coarse-grained heat-affected zones in a new ferritic steel. *Metallurgical and Materials Transactions A,* 32**,** pp. 2585-2594.

N'Dah, E., Tsipas, S., Hierro, M. and Perez, F. (2007). Study of the cyclic oxidation resistance of Al coated ferritic steels with 9 and 12% Cr. *Corrosion Science,* 49**,** pp. 3850-3865.

Newman, P. (1977). *Surface coating for machine elements having rubbing surfaces.* Patent Number: US4005914A.

Nicholls, J. (2000). Designing oxidation-resistant coatings. *JOM,* 52**,** pp. 28-35.

Nieto Hierro, L., Rohr, V., Ennis, P., Schütze, M. and Quadakkers, W. (2005). Steam oxidation and its potential effects on creep strength of power station materials. *Materials and Corrosion,* 56**,** pp. 890-896.

Oakey, J., Pinder, L., Vanstone, R., Henderson, M. and Osgerby, S. (2003). *Review of status of advanced materials for power generation* [Technical Report]. London: Department of Trade and Industry, pp. 1-108.

Osgerby, S. (2000). Oxide scale damage and spallation in P92 martensitic steel. *Materials at High Temperatures,* 17**,** pp. 307-310.

Parker, J. (2013). In-service behaviour of creep strength enhanced ferritic steels grade 91 and grade 92 - part 1 parent metal. *International Journal of Pressure Vessels and Piping,* 101**,** pp. 30-36.

Payne, J., Beach, J., Datta, A., Cornett, K. and More, D. (2013). *Protective coating for metallic seals.* Patent Number: US 8431238 B2.

Pint, B. and Zhang, Y. (2011). Performance of Al-rich oxidation resistant coatings for Fe-base alloys. *Materials and Corrosion,* 62**,** pp. 549-560.

Reimer, L. (1998). *Scanning electron microscopy: physics of image formation and microanalysis.* London: Springer.

Richardot, D., Vaillant, J., Arbab, A. and Bendick, W. (2000). *The T92/P92 book*. London: Vallourec and Mannesmann Tubes.

Rosen, M. (2001). Energy and exergy based comparison of coal-fired and nuclear steam power plants. *Exergy, an International Journal,* 1**,** pp. 180-192.

Saber, M. (2011). *Experimental and finite element studies of creep and creep crack growth in P91 and P92 weldments.* PhD, University of Nottingham, UK.

Saber, M., Tanner, D., Sun, W. and Hyde, T. (2011). Determination of creep and damage properties for P92 at 675 ^{o}C. *The Journal of Strain Analysis for Engineering Design,* 46**,** pp. 842-851.

Sanchez, L., Bolivar, F., Hierro, M. and Perez, F. (2008). Iron aluminide coatings on ferritic steels by CVD-FBR modified process with Hf. *Intermetallics,* 16**,** pp. 1161-1166.

Saroja, S., Parameswaran, P., Vijayalakshmi, M. and Raghunathan, V. (1995). Prediction of microstructural states in Cr-Mo steels using phase evolution diagrams. *Acta metallurgica et materialia,* 43**,** pp. 2985-3000.

Saunders, N. and Miodownik, A. (1998). *CALPHAD (Calculation of Phase Diagrams): a comprehensive guide*. London: Elsevier.

Sawada, K., Kubo, K. and Abe, F. (2003). Contribution of coarsening of MX carbo-nitrides to creep strength degradation in high chromium ferritic steel. *Materials Science and Technology,* 19**,** pp. 732-738.

Scheefer, M., Knodler, R., Scarlin, B., Bruna, A. and Tsipas, D. (2005). New oxidation-resistant coatings for steam power plants at 650 °C. *Materials and Corrosion,* 56**,** pp. 907-915.

Shibli, A. and Starr, F. (2007). Some aspects of plant and research experience in the use of new high strength martensitic steel P91. *International Journal of Pressure Vessels and Piping,* 84**,** pp. 114-122.

Sourmail, T. (2001). Precipitation in creep resistant austenitic stainless steels. *Materials Science and Technology,* 17**,** pp. 1-14.

Srinivas Prasad, B., Rajkumar, V. and Hari Kumar, K. (2012). Numerical simulation of precipitate evolution in ferritic-martensitic power plant steels. *Calphad,* 36**,** pp. 1-7.

Sundararajan, T., Kuroda, S., Itagaki, T. and Abe, F. (2003a). Steam oxidation resistance of Ni-Cr thermal spray coatings on 9Cr-1Mo steel - part 1: 80Ni-20Cr. *ISIJ International,* 43**,** pp. 95-103.

Sundararajan, T., Kuroda, S., Itagaki, T. and Abe, F. (2003b). Steam oxidation resistance of Ni-Cr thermal spray coatings on 9Cr-1Mo steel - part 2: 50Ni-50Cr. *ISIJ International,* 43**,** pp. 104-111.

Sundararajan, T., Kuroda, S., Nishida, K., Itagaki, T. and Abe, F. (2004). Behaviour of Mn and Si in the spray powders during steam oxidation of Ni-Cr thermal spray coatings. *ISIJ International,* 44**,** pp. 139-144.

Taneike, M., Abe, F. and Sawada, K. (2003). Creep-strengthening of steel at high temperatures using nano-sized carbo-nitride dispersions. *Nature,* 424**,** pp. 294-296.

Taneike, M., Sawada, K. and Abe, F. (2004). Effect of carbon concentration on precipitation behaviour of $M_{23}C_6$ carbides and MX carbo-nitrides in martensitic 9Cr steel during heat treatment. *Metallurgical and Materials Transactions A,* 35**,** pp. 1255-1262.

Tanner, D., Puliyaneth, M., Sun, W. and Hyde, T. (2014). Creep damage modelling of P92 pipe weld at 675 ºC. *Materials Science and Technology,* 30(1), pp. 6-11.

Vaillant, J., Vandenberghe, B., Hahn, B., Heuser, H. and Jochum, C. (2008). T/P23, 24, 911 and 92: new grades for advanced coal-fired power plants - properties and experience. *International Journal of Pressure Vessels and Piping,* 85**,** pp. 38-46.

Vialas, N. and Monceau, D. (2006). Substrate effect on the high-temperature oxidation behaviour of a Pt-modified aluminide coating - part 1: influence of the initial chemical composition of the coating surface. *Oxidation of Metals,* 66**,** pp. 155-189.

Viswanathan, R. and Bakker, W. (2001). Materials for ultra-supercritical coal power plants - boiler materials: part 1. *Journal of Materials Engineering and Performance,* 10**,** pp. 81-95.

Viswanathan, R., Henry, J., Tanzosh, J., Stanko, G., Shingledecker, J., Vitalis, B. and Purgert, R. (2005). U.S. program on materials technology for ultra-supercritical coal power plants. *Journal of Materials Engineering and Performance,* 14**,** pp. 281-292.

Vyrostkova, A., Homolova, V., Pecha, J. and Svoboda, M. (2008). Phase evolution in P92 and E911 weld metals during ageing. *Materials Science and Engineering: A,* 480**,** pp. 289-298.

Viswanathan, R., Sarver, J. and Tanzosh, J. (2006). Boiler materials for ultra-supercritical coal power plants - steamside oxidation. *Journal of Materials Engineering and Performance,* 15**,** pp. 255-274.

Walton, P. (1990). *The factors controlling the composition and mechanical properties of heat treated electrodeposited composites.* PhD, South Bank Polytechnic, UK.

Wasmer, K., Nikbin, K. and Webster, G. (2006). Prediction of scatter in creep crack growth data from creep failure strain properties. *Journal of ASTM international,* 3, pp. 1-13.

Wood, G., Wright, I., Hodgkiess, T. and Whittle, D. (1970). A comparison of the oxidation of Fe and bond; Cr, Ni-Cr and Co-Cr alloys in oxygen and water vapour. *Materials and Corrosion,* 21**,** pp. 900-910.

Wright, I. and Dooley, R. (2010). A review of the oxidation behaviour of structural alloys in steam. *International Materials Reviews,* 55**,** pp. 129-167.

Xiang, Z. and Datta, P. (2006). Relationship between pack chemistry and aluminide coating formation for low-temperature aluminisation of alloy steels. *Acta Materialia,* 54**,** pp. 4453-4463.

Xiang, Z., Rose, S. and Datta, P. (2006). Long-term oxidation kinetics of aluminide coatings on alloy steels by low temperature pack cementation process. *Journal of Materials Science,* 41**,** pp. 7353-7360.

Yeh, S. and Rubin, E. (2007). A centurial history of technological change and learning curves for pulverized coal-fired utility boilers. *Energy,* 32**,** pp. 1996-2005.

Yoshizawa, M., Igarashi, M., Moriguchi, K., Iseda, A., Armaki, H. and Maruyama, K. (2009). Effect of precipitates on long-term creep deformation properties of P92 and P122 type advanced ferritic steels for USC power plants. *Materials Science and Engineering: A,* 510**,** pp. 162-168.

Young, D. (2008). *High temperature oxidation and corrosion of metals*. Oxford: Elsevier.

Zielinska-Lipiec, A. and Czyrska-Filemonowicz, A. (2007). Characterisation of the micro and nanoscale structure of new creep-resistant steels for use in advanced USC steam power plants. *Materials Transactions,* 48**,** pp. 931-935.

Zurek, J., Bruycker, E., Huysmans, S. and Quadakkers, W. (2014). Steam oxidation of 9% to 12% Cr steels: critical evaluation and implications for practical application. *Corrosion,* 70**,** pp. 112-129.

APPENDIX A

PUBLISHED DIFFRACTION DATA

Table A.1: A summary of published diffraction data for the relevant crystal structures (taken from the ICDD website: http://icsd.cds.rsc.org/)

Phase	PDF Number (ICDD)	Peak Positions (2Theta) [°]
Cr_3C_2	00-035-0804	35.2, 36, 36.5, 39.1, 39.6, 40.2, 42.7, 43, 45.6, 46.6, 47.6, 48.1, 48.7, 50.1, 51.3, 52.1, 54.1, 55.3, 56.5, 58.8, 59.6
Cr_7C_3	00-036-1482	25.4, 27.7, 29.6, 33.2, 37.9, 39.3, 39.8, 40.5, 42.2, 42.6, 44.3, 44.8, 46.2, 47.8, 48.5, 49.3, 50.3, 51.1, 52.2, 53.5, 54.5, 55.5, 56.8, 57.2, 58.8
Co - FCC	00-015-0806	44.3, 51.6
Co - HCP	00-005-0727	41.6, 44.3, 47.4
CoO	00-048-1719	19.3, 22.3, 31.8, 37.5, 39.2, 45.6, 50, 51.3, 56.7
Co_3O_4	00-042-1467	19, 31.3, 36.9, 38.6, 44.8, 55.7, 59.4
$CoCr_2O_4$	00-022-1084	18.4, 30.3, 35.7, 37.4, 43.4, 47.5, 53.9, 57.4
Co_2CrO_4	00-024-0326	18.8, 30.1, 36.5, 38.1, 44.3, 54.9, 58.6
Cr_2O_3	00-038-1479	24.5, 33.6, 36.2, 39.8, 41.5, 44.3, 50.3, 54.9, 57.2, 58.5

Given here are the published diffraction data for the common crystal structures used for analysing the XRD patterns in this thesis (table A.1). These phases are mainly concerned with the Co-Cr-C microstructure and the subsequent oxide formation following high temperature oxidation testing. XRD characterisation of samples is presented in chapters 4 and 7. EVA software (chapter 3) uses this diffraction data to identify crystal peaks in the XRD pattern.

APPENDIX B

X-RAY PENETRATION DEPTHS

Included below are the calculations (sections B.1-B.5) for the X-ray penetration depths in the coating bulk and the associated oxides, using the method presented by Ding [2009] and NIST [2001]. A summary of the penetration depths is presented in table B.1. These values allow for conclusions to be drawn about the distribution of phases identified from XRD. These values show that for some thick multi-layered oxide phases (chapter 4) a series of grinding stages are needed to reveal the innermost oxide layers by XRD.

B.1. Co-Cr-C Coating Bulk

Firstly the X-ray penetration depth in the coating bulk can be determined using the method shown below [Ding, 2009].

2θ = 25-60º, G_x = 90 %, CuK_α=1.542 Å

Composition = 32.6 % Cr + 5.0 % C + 62.3 % Co (taken from table 4.1)

The table of mass absorption coefficients, μ/ρ (cm^2/gm), and densities, ρ, for various elements can be looked up from Cullity [2001].

μ_{cr} = 252.3 x 7.19 = 1814.04 cm^{-1}

μ_c = 4.219 x 2.27 = 9.58 cm^{-1}

μ_{co} = 338.6 x 8.80 = 2979.68 cm^{-1}

μ_{total} = 32.6 % μ_{cr} + 5 % μ_c + 62.3 % μ_{co} = 2448.20 cm^{-1}

According to Cullity [2001] and Ding [2009] the penetration depth, x, is given by the equations:

$$G_x = (1 - e^{-\mu x/sin\theta}) \qquad \text{[Equation B.1]}$$

$$x = \frac{\ln\left(\frac{1}{1-G_x}\right).Sin\theta}{2\mu_{total}} \qquad \text{[Equation B.2]}$$

$x_{2\theta=25^o}$ = 1.02 µm

$x_{2\theta=60^o}$ = 2.35 µm

This shows that for the scan conditions used in this thesis (table 3.7) the X-rays will penetrate the Co-Cr-C coating material between 1.02 and 2.35 µm. This shows the coating has a relatively high density as penetration depth is small.

B.2. Co_3O_4 Oxide Phase

2θ = 10-60°, G_x = 90 %, CuK_α = 1.542 Å

Composition = 43 % Co + 57 % O (taken from table 4.7).

The mass absorption coefficients, μ/ρ, and the densities, ρ, for various elements can then be looked up from Cullity [2001] and used in equations B.1 and B.2.

μ_{co} = 338.6 x 8.80 = 2979.68 cm^{-1}

μ_o = 11.03 x 1.33 x 10^{-3} = 0.015 cm^{-1}

μ_{total} = 43 % μ_{co} + 57 % μ_o = 1281.27 cm^{-1}

$x_{2\theta=10^o}$ = 0.78 µm

$x_{2\theta=60^o}$ = 4.50 µm

This shows that for the above scan conditions used in this thesis (table 3.7) the X-rays will penetrate the Co_3O_4 oxide between 0.78 and 4.50 µm.

The mass absorption co-efficient, μ_{total}, for the Co_3O_4 phase can be found in the NIST [2001] databases when a phase density of 6.11 g/cm^3 is assumed. NIST [2001] gives μ_{total} for Co_3O_4 as 1.29 x 10^3 cm^{-1}. When inserting μ_{total} into equations B.1 and B.2 this gives a penetration depth of 0.78-4.47 µm. This is in good agreement with the values calculated above from elemental mass absorption coefficients.

B.3. Cr_2O_3 Oxide Phase

2θ = 10-60°, G_x = 90 %, CuK_α = 1.542 Å

Composition = 40 % Cr + 60 % O (taken from table 4.7).

The mass absorption coefficients, μ/ρ, and the densities, ρ, for various elements can then be looked up from Cullity [2001] and used in equations B.1 and B.2.

μ_{cr} = 252.3 x 7.19 = 1814.04 cm^{-1}

μ_o = 11.03 x 1.33 x 10^{-3} = 0.015 cm^{-1}

μ_{total} = 40 % μ_{cr} + 60 % μ_o = 725.63 cm^{-1}

$x_{2\theta=10^o}$ = 1.38 µm

$x_{2\theta=60^o}$ = 7.93 µm

This shows that for the above scan conditions used in this thesis (table 3.7) the X-rays will penetrate the Cr_2O_3 oxide between 1.38 and 7.93 µm.

The mass absorption co-efficient, μ_{total}, for the Cr_2O_3 phase can also be found in the NIST [2001] databases when a density of 5.22 g/cm^3 is assumed. NIST [2001] gives μ_{total} for Cr_2O_3 as 791 cm^{-1}. When inserting μ_{total} into equations B.1 and B.2 this gives a penetration depth of 1.27-7.28 µm. This is in good agreement with the values calculated above from elemental mass absorption coefficients.

B.4. Co_2CrO_4 Oxide Phase

2θ = 10-60°, G_x = 90 %, CuK_α = 1.542 Å

Composition = 29 % Co + 14 % Cr + 57 % O (taken from table 4.7).

The mass absorption coefficients, μ/ρ, and the densities, ρ, for various elements can then be looked up from Cullity [2001] and used in equations B.1 and B.2.

μ_{co} = 338.6 x 8.80 = 2979.68 cm^{-1}

μ_{cr} = 252.3 x 7.19 = 1814.04 cm^{-1}

μ_{o} = 11.03 x 1.33 x 10^{-3} = 0.015 cm^{-1}

μ_{total} = 29 % μ_{co} + 14 % μ_{cr} + 57 % μ_{o} = 1118.08 cm^{-1}

$x_{2\theta=10^o}$ = 0.90 μm

$x_{2\theta=60^o}$ = 5.15 μm

This shows that for the above scan conditions used in this thesis (table 3.7) the X-rays will penetrate the Co_2CrO_4 oxide between 0.90 and 5.15 μm.

B.5. $CoCr_2O_4$ Oxide Phase

2θ = 10-60°, G_x = 90 %, CuK_α = 1.542 Å

Composition = 14 % Co + 29 % Cr + 57 % O (taken from table 4.7).

The mass absorption coefficients, μ/ρ, and the densities, ρ, for various elements can then be looked up from Cullity [2001] and used in equations B.1 and B.2.

μ_{co} = 338.6 x 8.80 = 2979.68 cm^{-1}

μ_{cr} = 252.3 x 7.19 = 1814.04 cm^{-1}

μ_o = 11.03 x 1.33 x 10^{-3} = 0.015 cm^{-1}

μ_{total} = 14 % μ_{co} + 29 % μ_{cr} + 57 % μ_o = 943.24 cm^{-1}

$x_{2\theta=10^o}$ = 1.06 µm

$x_{2\theta=60^o}$ = 6.10 µm

This shows that for the above scan conditions used in this thesis (table 3.7) the X-rays will penetrate the $CoCr_2O_4$ oxide between 1.06 and 6.10 µm.

Table B.1 summarises the X-ray penetration depths for the main phases of interest in this thesis, calculated using the elemental mass absorption coefficients. Where possible the penetration depths have been confirmed using the phase mass absorption coefficients given by the NIST [2001] online database. In reality the penetration depths in the oxide phases are likely to be more complex because, as shown in chapters 4 and 7, the oxide is often an irregular mixture of several oxide phases.

The Co-Cr-C coating material is shown to have a penetration depth of 1.02-2.35 µm. Meanwhile the penetration depth is greater in oxide phases with an average penetration depth of 0.78-7.93 µm. This difference in penetration depth is primarily caused by a difference in phase density. Denser materials will cause the X-ray in the material to lose energy over a shorter distance and therefore the effective penetration depth is reduced. Pure cobalt and Cr_3C_2 have a density of 8.9 g/cm^3 and 6.68 g/cm^3 respectively. Whilst Cr_2O_3 has a density of 5.22 g/cm^3 and Co_3O_4 has a density of 6.11 g/cm^3.

Table B.1: Summary of the X-ray penetration depths for phases of interest.

Phase	**Scan Angles [º]**	**X-Ray Penetration Depth [µm]**
Co-Cr_3C_2 (bulk)	25 – 60	1.02 – 2.35
Co_3O_4	10 – 60	0.78 – 4.50
Cr_2O_3	10 – 60	1.38 – 7.93
Co_2CrO_4	10 – 60	0.90 – 5.15
$CoCr_2O_4$	10 – 60	1.06 – 6.10

APPENDIX C

THERMO-CALC MODELLING

C.1 Calculation of Phase Equilibria

The ability to model multi-component thermodynamic systems has always been important for materials science as it allows accurate thermodynamic predictions to be made about a materials behaviour. Modelling is especially important when there is limited or incomplete experimental data [Clark, 2015].

Thermo-Calc thermodynamic software utilises CALPHAD theory and can be used to calculate equilibrium phase behaviour of multi-component systems. Thermo-Calc works by calling on empirical databases for different alloy systems.

Thermo-Calc software was used to make predictions about the thermodynamic equilibrium in both the DB P92 and the Co-Cr-C coating before any experimental testing was conducted. It could also be used to understand inter-diffusion between the coating and substrate by calculating elemental activities in the coating and the substrate. All of these thermodynamic predictions could then be tested and verified during the experimental work [Clark, 2015].

C.2 CALPHAD Theory

Thermo-Calc is CALPHAD software [Saunders and Miodownik, 1998] which allows equilibrium thermodynamics of a system to be modelled. A phase within a material will exist in equilibrium if it has the lowest Gibbs free energy compared to other phases. Thermo-Calc calculations are performed by calculating the Gibbs energies of phases in a system, using information gained from empirical databases. The Gibbs free energy, G, of a phase is given by equations C.1 and C.2 [Clark, 2015]:

$$G\ (P,T) = U + PV - TS \qquad \text{[Equation C.1]}$$

$$G\ (P,T) = H - TS \qquad \text{[Equation C.2]}$$

In equations C.1 and C.2, U is the internal energy of the thermodynamic system (J), P is the pressure (Pa), V is the volume (m^3), T is the thermodynamic temperature (K), S is the entropy (J/K) and H is the enthalpy (J) [Callister and Rethwisch, 2007]. Gibbs energies can be plotted as a function of temperature (against composition) where the gradient of the free energy is the chemical potential, μ_{cp}. The chemical potential is a thermodynamic function and is defined as the ability of an atom in a chemical system to perform work. Clark [2015] states that the system will be in equilibrium when the sum of all the chemical potentials is zero. The chemical potential is related to the activity (measure of the effective concentration of a species in a mixture) by equation 7.1. Activity and chemical potential values can be used to determine the direction of elemental diffusion (from high to low activity).

The CALPHAD method calculates the Gibbs free energy for every phase in a system for a certain composition. It then adjusts the composition and calculates the change in Gibbs energy for each phase, it does this until the energies of all the phases have been minimised. This gives the phase equilibrium of a system at a given composition, temperature and pressure. The stepping process can also be employed to calculate equilibrium as one of these conditions is varied (composition, temperature or pressure). If two conditions are varied, in a process called mapping, then a binary phase diagram can be plotted [Clark, 2015]. Variables such as chemical potential, activity and entropy can also be determined by the CALPHAD approach [Clark, 2015; Saunders and Miodownik, 1998]. As the number of phases in the system or the number of elements in the system are increased the computational power needed is greater. Therefore it is advisable to start with simplified systems (i.e. excluding minor elements) and gradually increase the complexity.

All Thermo-Calc calculations must obey the Gibbs phase rule, given in equation C.3 as:

$$F_{DF} = C - P + 2 \qquad \text{[Equation C.3]}$$

In equation C.3, F_{DF} is the number of degrees of freedom, C is the total number of components and P is the number of phases in thermodynamic equilibrium. The number of degrees of freedom is the largest number of thermodynamic parameters (temperature, pressure) that can be varied simultaneously without influencing one another [Clark, 2015].

C.3 Thermo-Calc Modelling Methods

C.3.1 P92 Equilibrium Modelling

For DB P92 Thermo-Calc was used along with the TCFE7 steels database to model equilibrium behaviour. The composition values used in the calculation were taken from the elemental composition provided by Doosan Babcock and presented in table 3.1. The only elements excluded from the calculations were boron and sulphur as they were only present in small quantities and removing them reduced computational complexity. The following phases were included in the calculation according to the phase equilibria for P92 presented in chapter 2:

- BCC (α-Fe/ferrite)
- FCC (γ-Fe/austenite)
- Laves Phase ($(Fe, Cr)_2(Mo, W)$)
- MX Phase (M = V or Nb, X = C or N)
- $M_{23}C_6$ (M = Cr, Mo, Fe, W)

Thermo-Calc software was used to plot volume phase fraction against temperature for the DB P92, over a range of typical future service temperatures (500-950 ^{o}C). This allowed for main transformation points to be determined and for predictions to be made about high temperature behaviour. The software was also used to plot the specific compositions of the precipitate phases, mole fraction of the element plotted against temperature. This allowed for potential evolution and stability of the precipitates to be predicted. Predictions of the

model were verified by comparison to experimental testing as well as the published literature.

C.3.2 Co-Cr-C Coating Equilibrium Modelling

For the Co-Cr-C coating Thermo-Calc was used along with the SSOL5 alloys database. The composition values used in the calculation were taken from experimentally determined values presented in table 4.1, determined using image analysis. ImageJ software was used to measure the area fraction of Cr_3C_2 from a series of SEM images, which is assumed to be approximately equal to volume fraction. Volume fraction could then be converted to weight percentage using the densities of Cr_3C_2 and cobalt from the literature. The stoichiometric composition of Cr_3C_2 could then be used to approximate the elemental composition of the coating.

Thermo-Calc was used to plot ternary phase diagrams (isothermal sections) of the Co-Cr-C system at 650 ^{o}C. In this case all of the phases suggested as being present in the system by Thermo-Calc were included in the calculation. The ternary diagrams could be used to predict how varying the elemental composition of the coating would affect the equilibrium phases.

Thermo-Calc was also used to plot mole fraction against temperature for the specific composition of the Co-Cr-C coating, over a full range of temperatures (500-900 ^{o}C). These plots could be used to predict the evolution of the Co-Cr-C coating with temperature and identify any potential transformation temperatures. To reduce computational time only the following phases were included in the calculation. These phases were chosen based on the ternary

phase diagram (isothermal section) findings and the phase equilibria literature for Co-Cr-C presented in chapter 2.

- Liquid
- BCC
- FCC
- Graphite
- HCP
- M_3C_2
- M_7C_3
- $M_{23}C_6$
- SIGMA

C.3.3 Activity Modelling

For both DB P92 substrate and the Co-Cr-C coating the TCFE7 and SSOL5 databases could again be used to plot elemental activities (or chemical potential) against temperature for the main elements of interest to diffusion. This modelling can give an indication of the direction of elemental diffusion (following chemical potential gradients) and also the relative speed compared to other diffusing elements (gradients of chemical potential). The same assumptions and modelling methods were used, as detailed above, to plot graphs of elemental activity against temperature for carbon, chromium, cobalt and iron. Diffusion behaviour determined from chemical potential (diffusion from high to low potential) is considered more accurate than calculating diffusion from concentration profiles [Saunders and Miodownik, 1998].

APPENDIX D

MCrAlY COATED P92

As well as the Co-Cr-C coating, that has been considered extensively in this work, an MCrAlY type coating (M = Co, Ni or Co/Ni) was also investigated in the very early stages of this research project (following consultation with Praxair Surface Technologies) to also assess its viability for application to P92. The coating tradename is TM312S and is also manufactured by Praxair Surface Technologies using the patented Tribomet deposition process (as detailed in chapter 3) [Foster, 2012b]. A schematic of the microstructure is given in figure D.1, with gas atomised MCrAlY powder particles being electrodeposited within a cobalt/nickel matrix to a thickness of ~ 30 μm. This coating is typically used for high temperature oxidation and corrosion resistance and also bond coats in TBC coating systems, typically for gas turbine components (~ 1000 ^{o}C). On paper this coating was expected to perform better than the Co-Cr-C type because of its higher composition of chromium and aluminium in the MCrAlY particles. However when a series of isothermal oxidation tests in air were conducted, for the TM312S coated P92, the oxide was seen to advance

through the matrix of the coating very quickly in the form of cobalt and nickel rich oxides. The MCrAlY particles remained intact, almost as inert particles, showing no signs of evolution or release of chromium or aluminium to form protective oxide scales. This shows that at these low temperatures (~ 650 ^{o}C) the MCrAlY particles seem insensitive to the exposure. A solution would be to perform a post-deposition heat treatment to induce alloying, prior to being used in service. Following consultation with Praxair Surface Technologies this is expected to need to be at around 1000 ^{o}C. Not only is this prohibitively expensive for power plant application but also would have significant detrimental effects on the P92 substrate mechanical properties (as discussed in chapter 5 and 6). Therefore it was decided that the MCrAlY type coating would not be investigated any further. Especially as the Co-Cr-C type coating showed such promising behaviour in the as-coated condition, without the need for heat treatment. More details of this work can be provided on request.

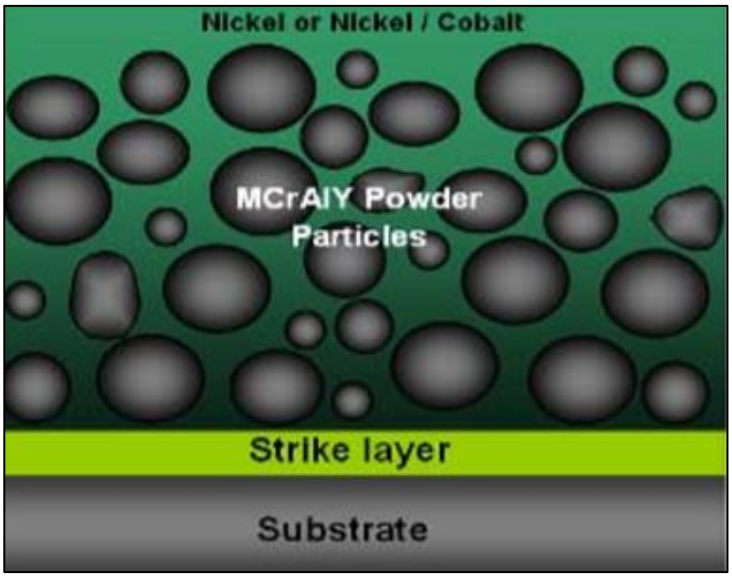

Figure D.1: Schematic to show the microstructure of the TM312S MCrAlY type coating, without heat treatment [Foster, 2012b: p1].